SCALING OF TURBULENCE AND TURBULENT MIXING USING TERASCALE NUMERICAL SIMULATIONS

A Thesis
Presented to
The Academic Faculty

by

Diego A. Donzis

In Partial Fulfillment
of the Requirements for the Degree
Doctor of Philosophy in the
School of Aerospace Engineering

Georgia Institute of Technology
December 2007

SCALING OF TURBULENCE AND TURBULENT MIXING USING TERASCALE NUMERICAL SIMULATIONS

Approved by:

Prof. P.K. Yeung, Advisor
School of Aerospace Engineering
Georgia Institute of Technology

Prof. Katepalli R. Sreenivasan
Institute for Physical Sciences & Technology
University of Maryland

Prof. Suresh Menon
School of Aerospace Engineering
Georgia Institute of Technology

Prof. Timothy Lieuwen
School of Aerospace Engineering
Georgia Institute of Technology

Prof. Donald Webster
School of Civil and Environmental Engineering
Georgia Institute of Technology

Prof. Paul Neitzel
School of Mechanical Engineering
Georgia Institute of Technology

Date Approved: December 2007

To Vane,

ACKNOWLEDGMENTS

This work was supported by the National Science Foundation (grant numbers CTS-0121030, CTS-0328314 and CBET-0553867). Our simulations were performed on computer resources provided by San Diego Supercomputer Center (SDSC), Pittsburgh Supercomputing Center (PSC), the National Energy Research Scientific Computing Center (NERSC), and IBM T.J. Watson Research Center through the BGW Consortium Days program.

I would like to express my gratitude to those who directly or indirectly made this work possible. First of all, I would like to thank Prof. P. K. Yeung, my thesis advisor, for his guidance during my years of doctoral research. I also thank him for stimulating discussions in topics of fundamental importance in the field, and also for allowing me to explore aspects of my own interest. I learned a lot from both his pursuit of rigor, and his ability and desire to push the frontiers of large-scale simulations using the most powerful computers available.

I am also grateful to him for providing the opportunities to interact with many highly respected researchers in the field, which contributed to my understanding of turbulence, and therefore to this work. I have had the opportunity to learn from and contribute to discussions with Drs. R.A. Antonia, A. Bershadskii, M. Farge, C. Meneveau, M. Nelkin, J.J. Niemela S.B. Pope, B.L. Sawford, K. Schneider, J. Schumacher and V. Yakhot all of whom I thank. I would like to express my gratitude especially to Dr. K.R. Sreenivasan for his hospitality during my visits to ICTP in Italy during my years at Georgia Tech. His deep understanding of the field, creativity, humility, and thirst for better physical understanding are all sources of inspiration.

I would like to thank the help from strategic consultants at the different supercomputing

centers: D.E. Skinner (NERSC) and D.C. O'Neal (PSC) for their constant help and support in large-scale simulations; D. Pekurovsky (SDSC) for his contributions to the development of a new domain decomposition; and J.A. Gunnels (IBM) for his help in running and tuning the code on the BGW computer.

I would like to thank Drs. S. Menon, D.R. Webster, T.C. Lieuwen, G.P. Neitzel and K.R. Sreenivasan for taking the time to be in my committee. I am also thankful to my lab mates, Dr. Shuyi Xu, Elizabeth Kurth, Jason Hackl and Kartik Iyer for their help. The list of friends who shared their lives with me during these years is too long to enumerate, but they will always be with me. I also would like to express my gratitude to Rosi and Arnoldo whose generosity and help cannot be overstated. To them and to my family in law I am thankful for making the distance less significant.

My parents, Aldo and Graciela, and my siblings Pabli and Sabri deserve my deepest gratitude not only for their love, constant support and encouragement but also for simply always being such a big part of my life.

Finally, I would like to thank the most important person of all, Vane, my wife, to whom this thesis is dedicated. Her boundless love, understanding and strength make everything possible.

TABLE OF CONTENTS

LIST OF TABLES

LIST OF FIGURES

SUMMARY

Fundamental aspects of turbulence and turbulent mixing are investigated using direct numerical simulations (DNS) of stationary isotropic turbulence, with Taylor-scale Reynolds numbers (R_λ) ranging from 8 to 650 and Schmidt numbers (Sc) from 1/8 to 1024. The primary emphasis is on important scaling issues that arise in the study of intermittency, mixing and turbulence under solid-body rotation.

Simulations up to 2048^3 in size have been performed using large resource allocations on Terascale computers at leading supercomputing centers. Substantial efforts in algorithmic development have also been undertaken and resulted in a new code based on a two-dimensional domain decomposition which allows the use of very large number of processors. Benchmark tests indicate very good parallel performance for resolutions up to 4096^3 on up to 32768 processors, which is highly promising for future simulations at higher resolutions and processor counts eventually to approach Petascale levels.

Investigation of intermittency through the statistics of dissipation and enstrophy in a series of simulations at the same Reynolds number but different resolution indicate that accurate results in high-order moments require a higher degree of fine-scale resolution than commonly practiced. However, statistics up to fourth order are satisfactory if the grid spacing is not larger than Komogorov scale, without the requirement of a clear analytic range for corresponding structure functions as suggested by recent theories. Results from highly resolved simulations provide support for a modified resolution criterion derived in this work for structure functions of different orders and as a function of R_λ. At the highest Reynolds

number in our simulations (400 and 650) dissipation and enstrophy exhibit extreme fluctuations of $O(1000)$ the mean which have not been studied in the literature before. The far tails of the probability density functions of dissipation and enstrophy appear to coincide, suggesting a universal scaling of small scales.

Simulations at $R_\lambda \approx 650$ on 2048^3 grids with scalars at $Sc = 1/8$ and 1 have allowed us to obtain the clearest evidence of attainment of $k^{-5/3}$ inertial-convective scaling in the scalar spectrum (as function of wavenumber k) in numerical simulations to date. In addition, results at high Sc appear to support k^{-1} viscous-convective scaling. Intermittency for scalars as measured by the tail of the PDF of scalar dissipation and moments of scalar gradient fluctuations is found to saturate at high Sc. This asymptotic state is reached at lower Sc when R_λ is high. Statistics of scalar gradients in different directions are used to address the scaling of anisotropy due to the imposed mean scalar gradient. Persistent departures from isotropy are observed as R_λ increases. However, results suggest a return to isotropy at high Schmidt numbers, a tendency that appears to be stronger at high Reynolds numbers.

The effects of the Coriolis force on turbulence under solid-body rotation are investigated using simulations at 1024^3 resolution on enlarged solution domains which reduce the effects of periodic boundary conditions due to the growth of integral scales. Anisotropy at all scales is observed, and is strongest at intermediate rotation rates. Spectra, structure functions and different alignments show strong departures from classical scaling. At high rotation rates the nonlinear terms are damped which help explain the observed decrease in intermittency. The basic property of enstrophy production through vortex stretching in non-rotating flows is also reduced at high rotation rates. Results from DNS do not appear to support some of the assumptions leading to the classical form of the Taylor-Proudman theorem. A mechanism for mixing and a scaling for structure functions is proposed for rapidly rotating flows.

CHAPTER I

INTRODUCTION

1.1 Background

Turbulence characterized by disorderly fluctuations in time and three-dimensional space is the most common state of fluid motion in nature and engineering, with diverse applications including aerospace vehicles, combustion devices, and the environmental sciences. The apparent randomness and nonlinearity of the turbulent fluctuations make a deterministic approach almost impossible and also causes well-known closure difficulties in equations that govern the statistical properties of the flow. The complexities of turbulence are such that even after over a century of research effort (Lumley & Yaglom 2001) the subject is still a major "unsolved" problem in physics (Nelkin 1992, Sreenivasan 1999). It is clear that progress in understanding turbulence requires the careful use of both experiments and (increasingly) numerical simulation. In many applications of interest e.g turbulent combustion in a jet engine, efficient mixing of substances carried by the turbulent flow is very important, and the turbulence itself may be occurring in a rotating frame of reference subjected to Coriolis forces.

Because of the presence of a wide range of scales in the flow, a fundamental question in the study of turbulence is how fluctuations at different scale sizes behave and interact with each other. The concept of similarity scaling is thus to discover how the various important statistics of the flow vary with scale size as well as with the range of scales present, and to attempt to devise a systematic description of the observed behavior. A very well-known theory in this regard is that represented by Kolmogorov (1941a)'s hypotheses of small-scale universality, which leads to well-known results including predictions of the functional form of

velocity structure functions and energy spectra at different scale sizes, provided the Reynolds number is sufficiently high. In particular, Kolomogorov introduced the concept of local isotropy, which implies that the small-scale motions (e.g. velocity gradient fluctuations) are statistically homogeneous and isotropic, with no preferential orientation regardless of the geometry of the large scales or the flow domain in consideration. A similar description has been extended to passive scalars in turbulent mixing, where an additional nondimensional parameter is the Schmidt number (Sc), which is the ratio of the kinematic viscosity of the fluid (ν) to the molecular diffusivity (D) of the transported scalar (e.g. concentration of a contaminant, or a small temperature fluctuation). In addition, effects of a rotating frame are represented by the Rossby number (Ro), which is the ratio of the time scale of rotation to the time scale of the turbulence. As further discussed below, the research reported in this thesis is centered around the use of large-scale computation on state-of-the-art computers to address important scaling issues over a range of Reynolds, Schmidt and Rossby numbers, including departures from Kolmogorov's original theory or extensions therefrom.

In the study of turbulence scaling there is great interest in intermittency, which is the property of intense and localized fluctuations especially at high Reynolds numbers (see e.g. Obukhov 1962, Frisch 1995, Sreenivasan & Antonia 1997). These fluctuations are closely related to the concept of *anomalous scaling* which is usually manifested as departures from the classical theory of Kolmogorov (1941a). A practical consequence is that for small-scale quantities the scaling relations for moments of different orders have to be obtained individually (Sreenivasan 1999) since they cannot be related to low order moments in a trivial way and cannot be deduced from dimensional considerations alone. Incorporation of effects of intermittency is very important in devising stochastic or subgrid-scale models appropriate for application in high Reynolds number turbulence. At the small scales, intermittency can be characterized by fluctuations of velocity gradients which can be decomposed into strain

and rotation rates, whose quadratic invariants are represented by the dissipation rate and enstrophy (vorticity squared) respectively. Local fluctuations of the energy dissipation rate are especially important in the intermittency corrections needed for Kolmogorov (1941a). Enstrophy, on the other hand, is related to rotating motions which are easily seen in any turbulent flow in nature. Several attempts have been made to understand its role in the dynamics of turbulence (see e.g. Tsinober 1998) or to further describe turbulent flows as collection of vortical structures (see e.g. Pullin & Saffman 1998).

A distinguishing feature of turbulence is efficient transport of momentum, heat and mass, which can be orders of magnitude faster than in a laminar flow which rely only on slow molecular diffusion processes. This is a very desirable feature in combustion where reaction rates depend on the mixing of multiple chemical species and in the environment where pollutants in both air and water are dispersed into the surroundings. The fundamental mechanisms of turbulent mixing are best illustrated by the study of *passive scalars* which are defined as diffusive quantities that are convected by but do not modify the flow (Warhaft 2000). In practice the Schmidt number varies over a wide range, from $O(0.01)$ in liquid metals, to order one in gaseous flames, and $O(1000)$ for industrial applications involving organic liquids. The dynamics of moderately diffusive scalars with $Sc \leq 1$ (Obukhov 1949, Corrsin 1951) and weakly diffusive scalars with $Sc \gg 1$ (Batchelor 1959) are governed by distinct processes and characterized by different scaling behaviors. Because scalars of high Sc possess scales much smaller than those for the velocity field (Batchelor 1959) they impose further resolution requirements in both experiment and simulation (Bogucki *et al.* 1997, Yeung *et al.* 2004). As a result, less data is available (Antonia & Orlandi 2003), and the scaling is less understood.

In most of our work we have focused on the idealized flow configuration of forced stationary isotropic turbulence, because it allows better sampling, is readily amenable to high-performance computing (through the use of pseudo-spectral methods), and, most importantly, its small-scale features are of wide relevance as suggested by Kolmogorov (1941a) theory. However, we are also interested in non-equilibrium situations where the presence of a different physical process, such as uniform solid-body rotation, may change the turbulence structure substantially such that Kolmogorov's hypotheses do not apply. Rotating turbulent flows occur in diverse fields such as engineering (e.g. turbomachinery and reciprocating engines with swirl), geophysics, and astrophysics. It is known that rotation causes initially isotropic turbulence to develop anisotropy at both large and small scales (e.g. Morinishi *et al.* 2001, Yang & Domaradzki 2004). Strong rotation (represented by low Rossby number) is also known to reduce the cascade of energy and lead to the growth of the integral scales (e.g. Jacquin *et al.* 1990, Mansour *et al.* 1991a, Cambon *et al.* 1997, Yeung & Zhou 1998). However, many aspects of the scaling with respect to the Rossby number are still not understood. In addition to anisotropies at all scales we observe a decrease in intermittency (Yeung *et al.* 2003) which could be explained by a strong damping of the nonlinear terms in the governing equations.

While there is a variety of approaches in which supercomputers can be used to study turbulent flows (Moin & Kim 1997) we focus on Direct Numerical Simulations (DNS, see Moin & Mahesh 1998, for a review) where all scales are computed according to the instantaneous form of the Navier-Stokes equations. The primary advantage of this approach is that it can provide tremendous detail about the flow physics: e.g. with the full velocity field computed at every grid point, many quantities that are extremely difficult to measure in experiments can be extracted from the DNS database with relative ease. In addition, the relative ease of systematic variation of parameters such as the Reynolds, Schmidt or Rossby

numbers allows one to address important scaling issues. It is well known, however, that the range of scales of a turbulent flow increases with the Reynolds number (e.g. Tennekes & Lumley 1972). Therefore, if one is to solve all the scales, the computational power required also increases with the Reynolds number.

Rapid advances in computing power at aggregate speeds in the Teraflop range (10^{12} operations per second, see figure 1.1) have made very large simulations possible, typically aimed at reaching higher Reynolds numbers (e.g. Kaneda *et al.* 2003's, world-record resolution of 4096^3 for isotropic turbulence and Hoyas & Jiménez 2006 for fully-developed channel flow). Reynolds numbers currently achievable on terascale computers are comparable to those in controlled laboratory experiments. This is the case with our recent DNS of turbulent mixing on a 2048^3 grid which is the largest in the US, at Taylor-scale Reynolds number ($R_\lambda \equiv u'\lambda/\nu$ where $\lambda^2 = \langle u^2 \rangle / \langle (\partial u/\partial x)^2 \rangle$ is the Taylor microscale) almost 700, which is close to that (800) in experiments performed by Mydlarski & Warhaft (1998) in a setup designed to reach relatively high Reynolds numbers in an active-grid wind-tunnel.

As to be described in more detail later in Chapter 2, we have performed simulations with a massively parallel implementation of the pseudo-spectral algorithm of Rogallo (1981) at up to 2048^3 resolution at multiple national supercomputer centers. To prepare for 4096^3 and higher we have undertaken significant efforts to implement a new domain decomposition that will allow us to take advantage of future machines with ever-larger processor counts. The new code has been benchmarked successfully using up to 32768 processors of an IBM BlueGene at IBM Watson Research Center (currently ranked No 4 in the world according to the "top500" list in June 2007). The nature of turbulence as a Grand Challenge problem in high-performance computing is clearly recognized in its selection as one of three model problems in a recent solicitation by the National Science Foundation[1] to create a computer

[1] http://www.nsf.gov/pubs/2006/nsf06573/nsf06573.html

capable of sustained performance at one Petaflop/s (10^{15} operations per second) by the year 2011.

Below we give a more detailed review of the important recent developments in our field of research, followed by a summary of objectives and an outline for the structure of subsequent Chapters in this thesis.

1.2 Motivation and Literature Review

Because turbulent flows are extremely common in nature and engineering devices, its fundamental understanding is of utmost importance. Turbulence theories, models and applications permeate a very large number of other fields. The wide scope of turbulence can be seen from recent reviews in different fields: from classical problems such as flow in pipes (Jiménez 2004, Eckhardt *et al.* 2007), the scaling of anisotropy (Biferale & Procaccia 2005) or turbulent mixing (Dimotakis 2005) to dispersion in the ocean (Garrett 2006), combustion problems such as droplet evaporation (Birouk & Gokalp 2006) or modeling (Veynante & Vervisch 2002), problems involving marine organisms (Sanford 1997, Abraham 1998, Franks 2005), magnetohydrodynamics turbulence (Zhou *et al.* 2004), or relatively novel applications such as quantum and classical turbulence in cryogenic flows (Vinen & Niemela 2002, Nimela & Sreenivasan 2006). This list, which is far from comprehensive, is aimed at giving an example of the scope of applicability of achievements at the fundamental level and therefore its importance.

The review by Lumley & Yaglom (2001) gives a broad view of the last hundred years of turbulent research pointing out the lack of a comprehensive theory (see also e.g. Nelkin 1992, Sreenivasan 1999). An interesting historical review about the work of O. Reynolds was recently published (Jackson & Launder 2007). Sreenivasan & Antonia (1997) review the knowledge and importance of studying small scale intermittency. Direct numerical simulation has a history of about 35 years, beginning with the work of Orszag & Patterson

(1972) using pseudo-spectral methods and 32^3 grid points. Past reviews include Rogallo & Moin (1984) and Moin & Mahesh (1998). The more recent review by Jiménez (2003) compares simulations and experiments and speculates that in the future, understanding of key concepts of wall-bounded flows would be better supported by simulations. At the time of this writing, the largest DNS known for isotropic turbulence is that by Kaneda *et al.* (2003) which used 4096^3 grid points achieving a Taylor-based Reynolds number of about 1200, although the simulation was relatively short and statistical sampling may not be fully adequate. In our studies of turbulent mixing we have focused on reaching the highest Reynolds number for Schmidt number unity (Yeung *et al.* 2005), as well as the highest Schmidt number at very low Reynolds number (Yeung *et al.* 2004).

In order to push the envelope of the largest simulation possible (e.g. to investigate scaling at ever-higher Reynolds numbers), one has to use the most powerful state-of-the-art supercomputers available to the scientific community. This, in turn, requires porting the code to new architectures where new challenges often arise. As the resolution increases (e.g. 4096^3) memory limitations, I/O and communications performance all have to be considered and may present serious additional challenges. These issues are the driving force behind an extensive effort in algorithm development as described in Chapter 2.

Intermittency has been an active field of research for several decades (see e.g. Obukhov 1962, Frisch 1995). In order to characterize small-scale intermittency many studies have focused on high-order moments of velocity gradients or equivalently the tail of their probability density functions (PDF). Intermittency in the inertial range is usually characterized by statistics of velocity increments whose PDF tails become wider at smaller scale sizes. It is also observed that scaling exponents of structure functions in the inertial range show non-trivial departures from the classical theory of Kolmogorov (1941a). Obukhov (1962)

suggested using local averages of energy dissipation over a domain of linear size r to understand its spatial fluctuations. According to this theory, the moments of local averages scale as power laws in r with exponents that characterize the intermittent behavior in departure from Kolmogorov (1941a) prediction. Kolmogorov (1962) further suggested that moments of local averages of dissipation are linked to those of velocity structure functions in the inertial range. A review of results on both dissipative and inertial range intermittency can be found in Sreenivasan & Antonia (1997).

Two common descriptors of small scale intermittency are the fluctuations of dissipation rate and enstrophy. Theoretical arguments (L'vov & Procaccia 1996, He *et al.* 1998, Nelkin 1999) have been given that suggest identical scaling for these two quantities at high Reynolds numbers. However, almost all sources of data available (e.g. Siggia 1981, Kerr 1985, Yeung & Pope 1989, Sreenivasan *et al.* 1995, Chen *et al.* 1997a, Zhou & Antonia 2000) show that enstrophy is more intermittent than dissipation. These data include high-order moments, scaling exponents of local averages, tails of PDF's. The clarification of this issue is important because the hope for a universal behavior of the small scales will be strengthened if dissipation and enstrophy can be described by the same set of scaling exponents. At the same time, it could help distinguish the roles of local straining versus rotation in the modeling of turbulent dispersion (Borgas & Yeung 2004). We use our DNS database to address the scaling of both dissipation and enstrophy, including whether the observed differences are due to the effect of finite Reynolds number. The study of intermittency requires that the simulations be able to capture the smallest scales (steepest gradients) in the flow. Recent theories (e.g. Yakhot & Sreenivasan 2005) suggest stricter constraints in resolution requirements for DNS to capture extreme fluctuations whose contribution to high order moments is substantial. Therefore, it is important to address the effect of resolution in the study of intermittency in turbulence. Depending on the quantities of interest, a better

degree of resolution of the small scales than commonly practiced may be necessary.

The range of scales at which mixing occurs depends on the Sc. For moderately diffusive scalars ($Sc \lesssim 1$) the smallest scale is the Obukhov-Corrsin scale $\eta_{OC} \equiv \eta Sc^{-3/4}$ (Obukhov 1949, Corrsin 1951) where η is the Kolmogorov scale. For weakly diffusive scalars ($Sc > 1$) the smallest scale is given by the Batchelor scale $\eta_B = \eta Sc^{-1/2}$ (Batchelor 1959). The processes dominating the mixing of the scalar at the smallest scales also depends on Sc. The review by Warhaft (2000) focuses on experimental data at $Sc \sim O(1)$ and presents evidence suggesting that local isotropy is violated even at very high Reynolds numbers, that intermittency is stronger than for the velocity field at both inertial and dissipative scales, and that there seems to be a strong interaction between large and small scales making simple concepts of spectral cascade inadequate. For scalars of high Schmidt number, the recent review by Antonia & Orlandi (2003) points out the existence of scalar "sheets" where scalar dissipation concentrates, and the good collapse of spectra when normalized with Batchelor scales. Although not completely conclusive, a k^{-1} scaling of the spectrum seems plausible. The very fine structure of the scalar field appears to be better represented by models that take into account fluctuations in the strain rate (absent in Batchelor's model). It is not known whether departures from local isotropy would vanish in the limit $Sc \to \infty$. Extensions to active scalars and reacting flows are reviewed by Dimotakis (2005).

We study in detail the scaling of the mean scalar dissipation rate although high order statistics are also presented to characterize intermittency. Because Batchelor scale is smaller than Kolmogorov scale, more stringent resolution requirements are imposed in both simulations and experiments for high-Sc scalars. Therefore, knowledge about the scaling of weakly diffusive scalars is less developed. Batchelor (1959) predicted a k^{-1} behavior for the spectrum by assuming that the scalars are mixed by a slowly varying strain field. Although an important theoretical result (Nelkin 1994), Batchelor k^{-1} scaling is not well established.

While some experiments and simulations do support it (e.g. Gibson & Schwarz 1963, Garrett 1985, Prasad & Sreenivasan 1990, Bogucki *et al.* 1997, Antonia & Orlandi 2003) some other data do not (e.g. Miller & Dimotakis 1996, Williams *et al.* 1997, Dasi 2004). One of the difficulties in obtaining unambiguous scaling is the attainment of a clear viscous-convective range in DNS and experiments due to resolution constraints. Intermittency at small scales is usually studied through fluctuations of the scalar dissipation rate. This is important in, e.g., reacting flows (Sreenivasan 2004, Bilger 2004) where reaction rates are proportional to scalar dissipation and large values can lead to local extinction of the flame. It has been observed that scalar dissipation is more intermittent than dissipation (see e.g. Sreenivasan & Antonia 1997, Yeung *et al.* 2005). However, due to the constraints mentioned above, the nature of Sc scaling is less understood.

The structure of turbulence is profoundly modified by uniform solid-body rotation (e.g. Cambon & Jacquin 1989, Cambon *et al.* 1997). The basic picture of a spectral cascade is disrupted and has to be revised. It was found that in addition to the usual cascade from low wavenumbers to high wavenumbers, there is transfer between wavenumbers parallel to the axis of rotation to wavenumbers perpendicular to it, the so-called "slow manifold" (Cambon *et al.* 1997). If rotation is sufficiently strong, the latter "cascade" could entirely replace the former (e.g. Morinishi *et al.* 2001). The combined effect of these transfers has subtle consequences which include growth of integral length scales along the axis of rotation, reduced decaying rates of kinetic energy, anisotropy at both large and small scales. Following (Jacquin *et al.* 1990) it is possible to define different regimes for rotation based on the values of the Rossby number. Although some effects are monotonic with rotation (e.g. reduced spectral transfer to small scales), some others are strongest at intermediate rotation rates. Due to the growth of integral scales, effect of domain size associated with

periodic boundary conditions are a significant concern, which has led us to perform simulations at domain sizes $(4\pi)^3$ and $(8\pi)^3$ versus the usual $(2\pi)^3$. Different spectral slopes has been proposed in the literature (Cambon *et al.* 2004, see e.g.). However, evidence from simulations and experiments is mixed. It is also known that, although the anisotropy tensor remains isotropic, its different components present deviations from an isotropic state (Morinishi *et al.* 2001, Yang & Domaradzki 2004) especially at intermediate rotation rates. In addition, experimental results (Simand *et al.* 2000, Baroud *et al.* 2002) show anomalous scaling for velocity structure functions which, however, suggest a possible self-similar behavior. Quasi-two-dimensional features are expected based on the Taylor-Proudman theorem for rapidly rotating flows (Greenspan 1968). However, this result has to be re-examined as some assumptions may not be satisfied in turbulent flows.

1.3 Objectives and Outline

Our objectives in this thesis are to:

1. develop efficient simulation capabilities to perform large simulations (e.g. at 4096^3) using very large number of processors;

2. study the issue of resolution in DNS for the study of intermittency. For this purpose we investigate moments of dissipation and enstrophy as well as structure functions as they approach the so-called analytic range;

3. study the scaling of small-scale intermittency through both dissipation and enstrophy. We investigate whether the difference in scaling is due to Reynolds number effects with particular attention to extreme values of the fluctuations;

4. investigate the scaling of passive scalars. We test the hypothesis that scalar dissipation is independent of molecular properties, which is necessary for the extension of

Kolmogorov theory to passive scalars. We also address the scaling of the spectrum as well a plausible saturation of intermittency with increasing Sc; and

5. study the effect of the addition of the Coriolis force in the governing equations. In particular we study the scaling of anisotropy and intermittency and possible mechanisms for the observed homogeneity along the axis of rotation.

The rest of this thesis is organized as follows.

In Chapter 2 we describe the numerical method for our direct numerical simulations. The parallel algorithm is briefly summarized followed by a description of a new scheme developed to allow for larger simulations. Some benchmarks are presented and future issues are also discussed.

Chapter 3 deals with the issue of resolution and high-order statistics. High-order moments of dissipation and enstrophy are used to investigate the need for resolving small scales batter than usually done. We further derive expressions for the error incurred by computing moments of gradients from structure functions and its departure from the analytic range. Results are compared with recent theories on the smallest scales to be resolved in simulations.

In Chapter 4 we investigate the scaling of dissipation and enstrophy in the context of small scale intermittency. Extreme fluctuations of order 1000 times the mean value are found which tend to occur in clusters. The nature of these fluctuations is investigated further in terms of local isotropy. A possible universal state for these extreme fluctuations is discussed.

Turbulent mixing is studied in Chapter 5. The commonly accepted view that scalar dissipation is independent of molecular properties is analyzed. The scaling of the scalar spectrum in the inertial-convective and viscous-convective range is discussed. Intermittency in small-scale mixing is investigated through fluctuations of the scalar dissipation rate.

In Chapter 6 we study turbulence subject to solid-body rotation. We first investigate the effects of domain size. Then, using new simulations at higher Reynolds number we address the scaling of the spectrum, anisotropy and intermittency with respect to the two relevant parameters, namely the Reynolds and Rossby numbers.

Chapter 7 summarizes the conclusions and explore possible extensions of the work presented in this thesis.

In the appendices we include the abstract of related publications which contain part of the material presented in this thesis.

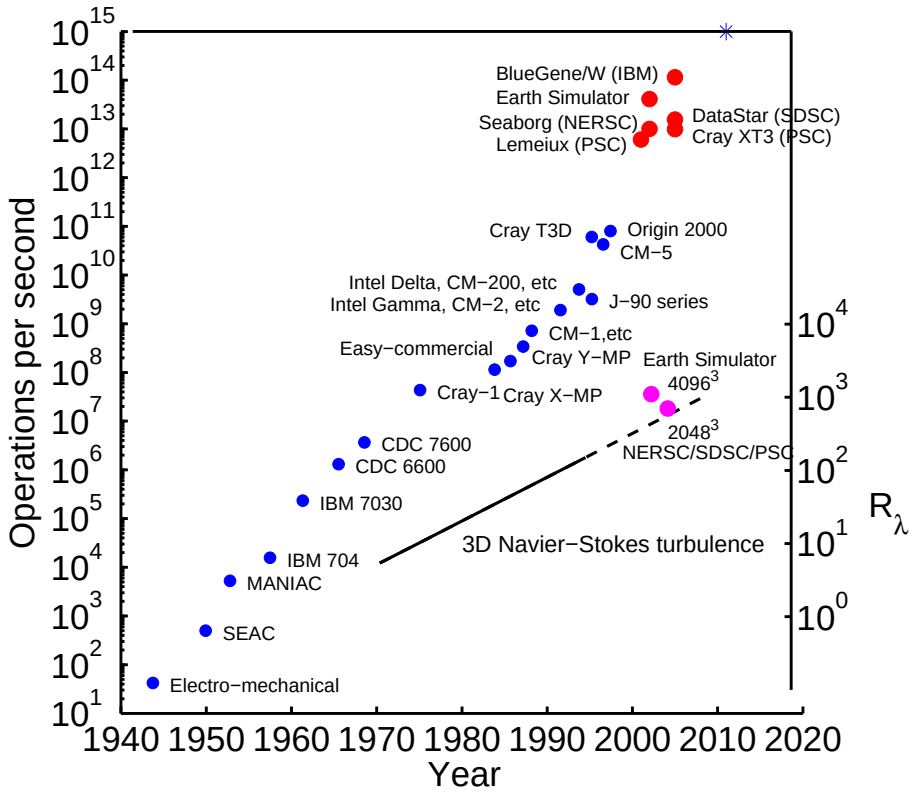

Figure 1.1: Evolution of computational power (left axis) and R_λ achievable (right axis) as a function of calendar year. Figure originally by K.R. Sreenivasan (NRC Report 1999). Today's machines seem to continue the trend. The symbol $*$ represent a Petascale machine expected to be available by the year 2011.

CHAPTER II

DIRECT NUMERICAL SIMULATIONS AND HIGH-END COMPUTING

In this chapter we describe the numerical scheme, parallel implementation and benchmarking of the code used for the simulations in this work. To date, our accumulated database comprises more than 20 Terabytes. A summary listing for isotropic turbulence is shown in Table 2.1. The Reynolds and Schmidt numbers ranges span about 3 and 4 decades respectively. This wide range of parameters allows us to address some scaling issues, such as dissipative anomaly or intermittency scaling, more reliably than possible before.

2.1 Numerical Method

Direct numerical simulation is a powerful tool in turbulence research (Moin & Mahesh 1998). It consists of solving the exact Navier-Stokes equations for the instantaneous velocity field representing the laws of conservation of mass and momentum for all the relevant time and length scales in the problem. With no mean flow the velocity fluctuations evolve by the equation

$$\frac{\partial u_i}{\partial t} + u_j \frac{\partial u_i}{\partial x_j} = -\frac{1}{\rho}\frac{\partial p}{\partial x_i} + \nu \frac{\partial^2 u_i}{\partial x_j \partial x_j}, \tag{2.1}$$

with the conservation of mass for an incompressible fluid given by

$$\frac{\partial u_i}{\partial x_i} = 0. \tag{2.2}$$

Equations (2.1) and (2.2) can be transformed to Fourier space as

$$\frac{\partial \hat{u}_i(\mathbf{k},t)}{\partial t} = -\iota k_l P_{im}(\mathbf{k}) \int_{\mathbf{k}'} \hat{u}_m(\mathbf{k}',t)\hat{u}_l(\mathbf{k}-\mathbf{k}',t)d\mathbf{k}' - \nu k^2 \hat{u}_i(\mathbf{k},t) \tag{2.3}$$

$$k_i \hat{u}_i(\mathbf{k},t) = 0 \tag{2.4}$$

where $\hat{u}_i(\mathbf{k}, t)$ is the velocity Fourier coefficient at wavenumber vector $\mathbf{k}$ and time t, $\iota \equiv \sqrt{-1}$ and $P_{im}(\mathbf{k}) \equiv \delta_{im} - k_i k_m / k^2$ (with $k = |\mathbf{k}|$) is the solenoidal projection tensor. This leads to a set of coupled ordinary differential equations which can be integrated in time using an explicit second-order Runge-Kutta method. If equation (2.3) is written as

$$\frac{d\hat{\mathbf{u}}(\mathbf{k}, t)}{dt} = \hat{\mathbf{a}}[\hat{\mathbf{u}}(\mathbf{k}, t)] \tag{2.5}$$

where $\hat{\mathbf{a}}$ represents the acceleration given by the right-hand side of Eq. 2.3, then to advance the solution from time t_n to t_{n+1} we compute a first-order approximation in the predictor step as

$$\hat{\mathbf{u}}^*(\mathbf{k}) = \hat{\mathbf{u}}(\mathbf{k}, t_n) + \Delta t \; \hat{\mathbf{a}}[\hat{\mathbf{u}}(\mathbf{k}, t_n)] \tag{2.6}$$

and then an improved solution is obtained in the corrector step as

$$\hat{\mathbf{u}}(\mathbf{k}, t_{n+1}) = \hat{\mathbf{u}}(\mathbf{k}, t_n) + \frac{\Delta t}{2} \left\{ \hat{\mathbf{a}}[\hat{\mathbf{u}}(\mathbf{k}, t_n)] + \hat{\mathbf{a}}[\hat{\mathbf{u}}^*(\mathbf{k})] \right\} \tag{2.7}$$

The time step Δt is restricted by numerical stability considerations expressed by a Courant number in explicit schemes. Although for spectral schemes stability constraints are less established (see, e.g. Peyret & Taylor 1983) it is common to use the Courant number to determine the time step. In three dimensions the Courant number is defined as

$$C \equiv \Delta t \max_{\mathbf{x}} \left\{ \frac{|u_1(\mathbf{x}, t)|}{\Delta x_1} + \frac{|u_2(\mathbf{x}, t)|}{\Delta x_2} + \frac{|u_3(\mathbf{x}, t)|}{\Delta x_3} \right\} \tag{2.8}$$

where the maximum is taken over all grid points. Tests conducted by Eswaran & Pope (1988) showed that values of C greater than unity produce unacceptable results. Typically, for second-order explicit schemes if $C < 1$ the time-stepping error decreases as C^2. It is clear that a small C enhances accuracy in time but (via number of time steps) also increases the overall computational cost. In our simulations we typically use $C = 0.6$. Smaller values are necessary for simulations involving scalars of high Sc which possess scales finer than the velocity field.

To maintain a stationary state an additional forcing term is added to Eq. 2.3. The forcing used in this work, which uses a combination of six independent Uhlenbeck-Ornstein random processes (Eswaran & Pope 1988), is nonzero for wavenumbers with magnitudes in the interval $k_0 \leq k \leq k_F$ where k_0 is the lowest wavenumber represented in the calculation (equal to unity in the case of a standard periodic cube of length 2π in each direction) and k_F is typically chosen to be either $\sqrt{2}$, 2 or $2\sqrt{2}$. There have been many forcing schemes proposed in the literature although there is no consensus on which one is the best (Overholt & Pope 1998). However, the details of forcing do not appear to affect small scale statistics (Eswaran & Pope 1988, Sreenivasan 1998).

A fully-spectral method for evaluating the convolution term in Eq. 2.3 would require N^6 operations since for each wavenumber N^3 multiplications are involved. To avoid this large cost the nonlinear terms are computed in physical space and then transformed back to Fourier space (Orszag 1969, 1971). This scheme, called pseudo-spectral, reduces the cost to $O(N^3 \ln_2 N)$ but aliasing errors arise which however, are carefully controlled by a combination of truncation and phase shifting techniques (Rogallo 1981).

The highest wavenumber resolvable in the pseudo-spectral scheme used here is $k_{max} = \sqrt{2}N/3$ where N is the number of grid points in each direction. A convenient non-dimensional parameter of resolution is $k_{max}\eta$ where $\eta = (\nu^3/\langle\epsilon\rangle)^{1/4}$ is the Kolmogorov scale. In most published work aimed at achieving the highest Reynolds number on a given grid, $k_{max}\eta$ is between 1.0 and 2.0 (Eswaran & Pope 1988, Wang *et al.* 1996, Gotoh *et al.* 2002, Kaneda *et al.* 2003, Biferale *et al.* 2004) with 1.4-1.5 being most common which corresponds to a grid spacing of about 2η. At the same time, in order to capture the largest scales, the domain size should be several times larger than the longitudinal integral scale L_1. Typically, the ratio box-size to L_1 is between 5 and 6. If that is not the case, a larger domain should be used, as in simulations of rotating turbulence (see Chapter 6).

Classical scale estimates (Kolmogorov 1941a) imply that the number of grid points necessary to resolve all scales in a three-dimensional domain (N^3) varies as $N^3 \sim (L_1/\eta)^3$ which is proportional to ${R_\lambda}^{9/2}$. Since the number of time steps M should be enough to span several eddy-turnover times T_E we can estimate $M \propto T_E/\Delta t$. If, as a first order approximation, the term in brackets in Eq. 2.8 is assumed to be proportional to the rms velocity, u', then a fixed Courant number would imply $\Delta t \propto \Delta x/u'$. As a result, M would scale as $T_E u'/\Delta x \sim L/\Delta x$ where $L \sim T_E u'$ is a large-eddy length scale. Because the grid spacing should be of the order of Kolmogorov scale (i.e. $\Delta x \sim \eta$), we finally obtain the number of times steps as $M \sim L/\eta \sim {R_\lambda}^{3/2}$. The overall computational power needed, therefore, scales as

$$N^3 M \sim {R_\lambda}^6 \tag{2.9}$$

which shows clearly why simulations at high Reynolds numbers are highly CPU-intensive. Recent work by Yakhot & Sreenivasan (2005) suggests an even stricter constraint of the form ${R_\lambda}^8$ at higher R_λ due to intermittency, which is investigated further in Chapter 3.

2.2 Parallel Algorithms

We use a massively parallel implementation of the pseudo-spectral algorithm by Rogallo (1981) in which the most time-consuming task is the three-dimensional Fourier transform. The code was originally written to work on IBM machines using the Fast Fourier Transforms (FFT) included in the IBM-optimized ESSL libraries, but it also has been ported to non-IBM machines (such as Cray XT3, see Table 2.2) by using the portable FFTW package. The FFTW implementation showed performance comparable to the ESSL (even on IBM machines). The post-processing codes, which are also parallel, needed to be changed as well. Given the severe computational requirements (see Eq. 2.9) it is clear that simulations of high Reynolds number turbulence require the use of the most powerful computing resources available to the research community. We have used significant resources at three national

supercomputing centers, namely San Diego Supercomputer Center (SDSC), Pittsburgh Supercomputing Center (PSC), and the National Energy Research Scientific Computing Center (NERSC). A summary of the major characteristics of the computers we use at these sites is given in Table 2.2.

According to *www.top500.org* as of June 2007, the most powerful computer in the world is an IBM BlueGene. The remaining machines in Table 2.2 are also based on top-ranked architectures. In addition to production calculations carried out on machines at SDSC, PSC and NERSC, we have ported and benchmarked our codes on a BlueGene (called BGW) at IBM Watson Research Center which has 40960 processors and is ranked number four with 114 Tflops/s. This machine is highly scalable and has sufficient capacity for supporting production calculations at 4096^3 resolution.

The data structure in the code is organized in "slabs" as shown in figure 2.1(a). For an N^3 grid, each processor holds N/N_P planes of data where N_P is the number of processors (and is equal to the number of slabs). In the pseudo-spectral algorithm used here, to advance the solution in time, some quantities are needed in both Fourier and physical space. They are obtained by a three-dimensional FFT implemented as below. In physical space, since each processor holds data in the form of XZ-planes, FFTs are first applied in the X and Z directions. To transform in Y, it is necessary that each processor hold all grid points in that direction. Therefore, processors have to exchange data among themselves to re-partition the domain. This *transpose* takes places among all processors with collective communication calls (using MPI_ALLTOALL from the MPI software library) which incurs significant overhead. Indeed, because all processors are involved, these operations are the bottleneck for improved performance especially at large processor counts. The three-dimensional transform is completed by transforming in the Y-direction since after the transpose, processors hold data in XY-planes as shown in figure 2.1(b).

While the scheme described above has worked well and was used for most of our production runs to date, it has the disadvantage that the number of processors that can be used is limited to N (i.e. number of planes in an N^3 domain). Two issues arise for very large problem sizes. First, for $N = 4096$ or higher, the memory requirements for just one plane may exceed the memory available per processor. (This is especially true for IBM BlueGene which has small memory per processor as seen in Table 2.2). Second, even if sufficient memory is available (e.g. on DataStar at SDSC) the wall clock time when using only N processors is likely to be too long for a production simulation spanning 10^4 or 10^5 time steps to be feasible.

To overcome the limitations above, we have devised, with help from strategic consultants at SDSC, a new code which divides the solution domain in two directions as shown in figure 2.2(a). The processors form a two-dimensional *processor grid* as each processor is identified by two coordinates that specify which parts of the domain it holds. For example, in figure 2.2(a), processor 0 (P0 in the figure) is located at (Y,Z)=(1,1) whereas processor 6 at (2,3). It is clear that the *slabs* code (figure 2.1a) corresponds to the special case of a one-dimensional processor grid. In the example shown in the figure the two-dimensional processor grid is, for simplicity, square with $N_{P1} = N_{P2} = 4$ where N_{P1} and N_{P2} are the number of processors in each direction of the processor grid such that $N_{P1}N_{P2} = N_P$. The size of each pencil is $N \times (N/N_{P1}) \times (N/N_{P2}) = N^3/N_P$ and it is clearly seen that this code allows the use of up to N^2 processors. Our implementation allows for cases where N_{P1} and N_{P2} are not equal, as well as cases where N_{P2} is not an integer factor of N. In the latter case, some processors carry a slightly larger amount of workload but departure from perfect load balance is small.

The three-dimensional FFTs in the *pencils* code are performed with *two* collective communication operations as follows. First, each processor transforms in the direction that

contains all the grid points, X in physical space (figure 2.2a). To transform in another direction, say Z, communication must take place so that each processor can hold all grid points in that direction. This is done by a collective communication among processors in the same *row* on the computational grid. In the case illustrated in the figure, say, processor 0, exchanges data only with processors 1, 2 and 3 to re-partition the data as pencils aligned with the Z direction. Then, FFT's are applied to data along Z. The last collective communication is among processors in the same *column* on the computational grid after which processors hold all grid points along Y as shown in figure 2.2(b). Finally, the transforms in Y are performed.

As described above, for each three-dimensional FFT the code requires two collective communication calls (as opposed to only one in the *slabs* code.) However, since these communication calls occur on fewer processors (of the order $\sim \sqrt{N_P}$), the code is expected to scale better than the *slabs* code when the number of processors becomes very large.

2.3 Performance and Benchmarking

It is useful to address the efficiency of the code via several performance measures as one changes the number of processors and problem size. The so-called *strong scaling* consists in changing the number of processors with problem size held fixed. Perfect strong scaling implies a wall clock time inversely proportional to the number of processors. *Weak scaling*, on the other hand, consists in varying both processor count and problem size so that the load per processor remains constant. Since the cost of FFTs is proportional to $N^3 \ln_2 N$, then perfect weak scaling would imply a wall clock time proportional to $N^3 \ln_2 N/N_P$. A summary of benchmarking data on BG at SDSC is presented in Table 2.3 in terms of the wall clock time per time step per processor (t/s/p) for a range of processor counts and problem sizes. From the timings at $N = 1024$ we can see that strong scaling from 1024 to 2048 processors for the *pencils* code is as high as 98%. Since the FFT cost scales

as $N^3 \ln_2 N$, perfect weak scalability (fixed load per processor) would imply, for example, that the time taken per step per processor for a 2048^3 grid on 2048 processors would be $\ln_2(2048)/\ln_2(1024) = 1.1$ times longer than a 1024^3 on 256 processors. We can see, however, from Table 2.3 that in this case, the *pencils* code seems to achieve superlinear scaling. This is not the case in general but only for a few combinations of resolutions and processor counts. This behavior is a consequence of two factors. First, it depends on how the two-dimensional domain decomposition is mapped onto a three-dimensional torus architecture (like BG). If the grid decomposition is such that processors in one direction fit exactly in that dimension of the torus, communications can use wraparound links and are faster than the case in which collective communications have to use the network tree. The second factor is related to effects of the processor cache size. For some processor grid geometries the first dimension of the main arrays containing the flow variables is 32 bytes long. The innermost loops over X (first dimension) then fit exactly in one line on Level 1 (L1) cache (L1 has 32KB on BG). Outside this loop, there are other loops over the other directions as well as over flow variables which means that the code needs to read from another location in memory. If the first dimension, however, is a few times greater than 32 bytes, then the processor would prefetch those lines at the same time it is computing on the first cache line with the consequent increase in performance. More details on the scaling of the DNS code on BG and DS were recently presented at a conference (Pekurovsky *et al.* 2006). We also conducted benchmarks at 4096^3 resolution on 2048 processors on DataStar where we obtained (t/s/p)=110 secs and 133 secs for the *slabs* and *pencils* codes respectively. However, this is not good enough for production purposes since a run with $O(10^5)$ time steps would cost more than 6 million CPU-hours using almost all of the entire machine for more than 4 months.

Benchmark runs were also conducted on the 114 Tflops BlueGene at IBM's Watson

Research Center (called BGW). The architecture of this machine is similar to the BG at SDSC (see Table 2.2) but it has 40960 processors. Results of this series of benchmarks on BGW, BG at SDSC, and DataStar are shown together in figure 2.3. Each node on BlueGene is composed of two cores and can run in two different modes: co-processor (CO) mode in which one core performs computations while the other is responsible only for communications, and virtual node (VN) mode in which each core performs both computation and communication. In CO mode the computing node has access to twice as much memory as in VN mode. The code was tested in both modes and VN was found to be better. In part (a) of figure 2.3 perfect scaling would imply a Flop rate per processor independent of N_P. We see that although the scaling is not perfect, strong scaling of 85% is achieved from 16384 to 32768 processors for a 4096^3 run . The code is also seen to attain about 10% of the theoretical peak performance which is comparable to the performance of most large user codes. Benchmarks on DataStar (DS) are also included to compare the scaling on other architectures. It is seen that on both BG and DS, the scaling is a weak function of the number of processors. Figure 2.3(b) shows the aggregate Flop rates for the same cases as in part (a). Perfect scaling would imply a straight line with slope unity and is shown as a dashed line. Simulations using 32768 processors apparently reach about 5 Tflops/sec with very good scalability. The good scaling seen in figure 2.3(b) is likely to persist for even higher processor counts.

For a given problem size, performance of the *pencils* code depends not only on N_P but the geometry of the processor grid (i.e. N_{P1} and N_{P2}). Although the code can automatically generate a processor grid as "square" as possible, we found that other combinations lead to better results. Table 2.4 shows (t/s/p) for a 4096^3 on 32768 processors using different processor grids. The best performance in this case is obtained apparently with the choice $N_{P1} = 32$ and $N_{P2} = 1024$. As shown in Pekurovsky *et al.* (2006), this result can be

explained by considering how the data are mapped into the 3D torus along with cache effects. As discussed earlier, these effects can also lead to superlinear scaling on BlueGene's for certain combinations of resolutions and processor grids. An example is seen in figure 2.3(a) at $N_P = 512$. Note that the results shown in figure 2.3 presented earlier were all obtained with processor grids close to a square configuration. Therefore, actual Flop rates and scaling better than those shown in the figure are possible. For example, for a 4096^3 we obtain (t/s/p) $\approx$ 20 secs on 32768 processors and 39 secs on 16384 processors using the best processor grids in each case with almost perfect strong scaling.

Velocity fields are saved regularly during production DNS runs for post-processing and/or checkpointing. For example, in a 4096^3 simulation, the size of a set of restart files is 768 GB (1.25 TB if two scalars are included). The I/O scheme we use is such that all processors write their own files simultaneously . When thousands or tens of thousands of processors are involved, however, some challenges arise. It is often the case that processors share part of the I/O system (e.g. I/O nodes, network, disks) which may lead to severe bottlenecks. BlueGene architecture is based on *psets* which are units containing a number of computing nodes and one I/O node. The larger the ratio of number of computing nodes to number of I/O nodes, the greater is the potential for a bottleneck. While this ratio is 8:1 on BG at SDSC and leads to good I/O performance, it is 64:1 on BGW. Originally, our code on BGW using 32768 processors took about 3 hours to write the files. The scheme implemented to alleviate this problem consists on scheduling the processors in batches. Within a *pset* only a number of processors write simultaneously thus reducing the number of cores accessing the I/O node. For that purpose, it is necessary to identify the location of each MPI task within a given *pset* which is done through BlueGene "personality" functions for which C wrappers were created. It was further necessary to create batches according to the location of each MPI task in the 3D torus for which more wrappers had to be created.

The resulting scheme consists of batches of a number of processors writing simultaneously. Some tests on BGW showed that the optimum batch size within a *pset* was 4 while the batches according to location in the torus have a size of 8192 processors. With all these improvements, the time to write the restart files has been reduced recently to approximately 25 minutes.

2.4 Future Issues

The *pencils* code was written from scratch with the active help of consultants at SDSC, and optimized for use with very large number of processors. Although we ran benchmarks mainly on BG architectures, it is important to address the scaling on other machines since communication times on different architectures can vary substantially. For example, time spent in communication for a 1024^3 on 512 processors with the *slabs* code is approximately 36% of the total time on BG at SDSC whereas it is greater than 50% on an XT3 at PSC. Since communication is the main bottleneck preventing better scaling, it will also be worthwhile to explore the possibility of overlapping communication and computation. This task may also be platform-dependent for which different solutions could be found. Regarding I/O, it may also be interesting to explore the possibilities of MPI-IO which could help us create a portable solution (although may not be the best for all architectures) using the concept of *view* of a file. MPI-IO allows many processors to access the same file although each processor have a different *view* of it. This *view* determines for example the location in the file each processor has access to. Creating batches using MPI-IO schemes may help reduce bottlenecks especially when many processors have to read the same file. Furthermore, since both blocking and non-blocking versions of writing/reading calls are available, it could be possible to overlap I/O and computations (during checkpoints for example). As was described in the previous Section, a very specific solution for I/O performance was found on BlueGene architectures. Fine tuning the code for a given architecture is a very important

task when state-of-the-art supercomputers are used to push the limits of today's standards.

It is important to address the scaling of all parts of the code especially taking into account the National Science Foundation solicitation to create a Petascale machine for which one of the model problems is turbulence simulation on a periodic domain. The configuration is the same as we study in this thesis and the aim is to simulate 10000 time steps at $R_\lambda \sim O(2000)$ on a 12288^3 grid in 40 hours with 50 checkpoints. It is clear that I/O performance needs improvement to meet this goal. The estimated memory required for such a problem is about 67.5 Terabytes which exceeds machine capacities available today but should be feasible by 2011. Although actual tests cannot be conducted at this time, the scaling performance presented in figure 2.3 suggests that our *pencils* code can, with certain modifications, scale up to the challenge of a 12288^3 simulation.

In any production run of stationary turbulence it is necessary to achieve a physically meaningful stationary state starting from some initial conditions. The time spent between the start of the simulation and the attainment of a stationary state has to be minimized as it could represent millions of CPU hours for a 4096^3 and much more for a 12288^3. The closer the initial conditions are to a stationary state at a given Reynolds number, the shorter the time to reach stationarity (e.g. Rosales & Meneveau 2006). An initial velocity field could be generated using Gaussian random fields with a given spectrum (Rogallo 1981). In our simulations we generate the initial spectrum by both interpolating and extrapolating a time-averaged spectrum from a stationary state at a lower R_λ using concepts of Kolmogorov (1941a) according to which the normalized spectrum

$$\frac{E(k\eta)}{\langle\epsilon\rangle^{2/3}k^{-5/3}} = f(k\eta) \tag{2.10}$$

is universal for the small scales. To understand this scheme, we first note that $\langle\epsilon\rangle$ is independent of viscosity and is determined by the large scale forcing which is the same at different resolutions whereas viscosity is changed to achieve a target Reynolds number. To

increase the Reynolds number, one has to increase the number of grid points from say N_1 to $N_2 = 2N_1$ (subscripts are used here to denote different simulations). In this example, twice as many modes are available but $\eta = (\nu^3/\langle\epsilon\rangle)^{1/4}$ is reduced (through changes in viscosity) so that resolution at small scales remains the same (i.e. $\eta_2 \approx \eta_1/2$). The normalized wavenumbers in the N_1^3 simulation are then

$$(k\eta)_1 = \eta_1,\ 2\eta_1,\ 3\eta_1,\ \ldots,\ N_1\eta_1/2 \tag{2.11}$$

whereas at N_2^3 they are

$$(k\eta)_2 = \eta_2,\ 2\eta_2,\ 3\eta_2,\ \ldots,\ N_2\eta_2/2\ \approx\ \eta_1/2,\ \eta_1,\ 3\eta_1/2,\ \ldots,\ N_1\eta_1/2. \tag{2.12}$$

It is clear that since $f(k\eta)$ in Eq. 2.10 is only known at the wavenumbers given in Eq. 2.11, both interpolation and extrapolation are needed to obtain values of $f(k\eta)$ at the wavenumbers given in Eq. 2.12. In figure 2.4 we show a typical result obtained using this scheme for a spectrum at 4096^3 from a 2048^3 time-averaged spectrum. A well established stationary state using this scheme is attained within 4 or 5 eddy turnover times. However, at 4096^3 resolution, this could cost of the order of 10^6 CPU-hours.

We have developed a new scheme in which both an interpolated/extrapolated initial spectrum and an *instantaneous* velocity field of fully developed turbulence at a lower resolution and R_λ are used to generate the initial conditions. The Fourier coefficients from a N_1^3 simulation are read by the code and used at the same wavenumbers on a N_2^3 grid ($N_2 = 2N_1$). For example, $\hat{\mathbf{u}}(\mathbf{k})$ at $\mathbf{k} = (2, 2, 2)$ on the N_1^3 grid is used as the Fourier coefficient at wavenumber $\mathbf{k} = (2, 2, 2)$ on the N_2^3 grid. We also noted that because at N_1^3 fewer modes are available, the new high-resolution initial velocity field will contain $7N_2^3/8$ zero-valued coefficients at high wavenumbers. Those coefficients are initialized with a Gaussian

field (Rogallo 1981). In other words,

$$\hat{\mathbf{u}}^{(2)}(\mathbf{k}^{(2)}) = \begin{cases} \hat{\mathbf{u}}^{(1)}(\mathbf{k}^{(2)}) & \text{if } |\mathbf{k}^{(2)}| < k_{max}^{(1)} \\ \text{Gaussian field} & \text{otherwise} \end{cases}, \tag{2.13}$$

where superscripts (1) and (2) denote simulations at N_1^3 and N_2^3 respectively. Becasue the Fourier coefficients are equal at the same wavenumber $\mathbf{k}$ but not the same *normalized* wavenumber $\mathbf{k}\eta$ (since $\eta_2 \approx \eta_1/2$), the spectrum obtained at N_2^3 using this scheme (say $E_{lr}(k)$) would not correspond to the universal form Eq. 2.10. To produce a velocity field with a "target" spectrum $E_t(k)$, we multiply each Fourier coefficient by the factor $\sqrt{E_t(k)/E_{lr}(k)}$. The spectrum $E_t(k)$ is obtained from a time-averaged spectrum at lower resolutions as described below Eq. 2.10.

The scheme just described involves intensive I/O which was optimized for BGW according to the discussion in Section 2.3. Preliminary tests conducted at lower resolutions suggest that the new scheme allows a stationary state to be developed in only about one eddy-turnover time. Part of the success of the new proposed scheme in reducing transient periods is related to the forcing. After multiplying Eq. 2.1 by u_i and taking averages, one obtains the kinetic energy budget with the energy input by the forcing given by $\langle f_i u_i \rangle$. It is clear that the energy input depends on the correlation between $\mathbf{f}$ and $\mathbf{u}$. The stochastic forcing used in this work (Eswaran & Pope 1988) requires an initial random number seed at the start of the simulation. However, the level of correlation between forcing and velocity cannot be determined a priori. In general, simulations which start with a randomly chosen seed initially undergo a decay of kinetic energy due to the lack of correlation between $\mathbf{f}$ and $\mathbf{u}$ before the energy input increases and leads to a stationary state. With the new proposed scheme, the random number seed from the lower resolution simulation can be used to generate a forcing field which is already well correlated with the velocity field at large scales (where the forcing is applied). Therefore, the initial decay of kinetic energy is

avoided. This scheme is currently being used as initial condition for a target 4096^3 simulation with $R_\lambda \approx 1100$.

Table 2.1: DNS database of isotropic turbulence. The simulations were performed at the three supercomputer centers in Table 2.2 using up to 2048 processors.

R_λ	Sc	grids up to
8	1/8,1, 4, 16, 32, 64, 128, 256, 512, 1024	512^3
38	1/8, 1, 4, 8, 16, 32, 64	512^3
140	1/8, 1, 4, 64	2048^3
240	1/8, 1	2048^3
400	1/8, 1	1024^3
650	1/8, 1	2048^3

Table 2.2: Terascale computers used for simulations.

Computer	**DataStar**	**BlueGene**	**XT3 BigBen**	**Seaborg**	**Bassi**
Center	SDSC	SDSC	PSC	NERSC	NERSC
Procs.	IBM Power4	PowerPC	AMD Opteron	IBM Power3	IBM Power5
Peak perf.	1.5 Gflop/s	700 Mflop/s	2.6 Gflop/s	1.5 Gflop/s	7.6 Gflops/s
NO_PROCS	2176	6144	4136	6080	976
Procs/node	8	2	4	16	8
Mem/proc.	16 GB	512 MB	4 GB	16 GB	32GB
Total perf.	15.6 Tflops/s	17.2 Tflops/s	21.5 Tflops/s	9.12 Tflops/s	7.4 Tflops/s

Table 2.3: Benchmark on BlueGene (BG) and DataStar (DS) at SDSC using the *slabs* code (1D processor grid) and the *pencils* code (2D processor grid). Numbers are in seconds per step per processor. Note that *slabs* code cannot run with $N_P > N$.

N	N_P	1D	2D	Machine
512	512	2.05	1.5	BG
1024	256	22.3	34.4	BG
1024	512	13	17	BG
1024	1024	5.3	6.6	BG
1024	2048	—	3.84	BG
2048	2048	29.2	32.3	BG
4096	2048	110	130	DS

Table 2.4: Time per step per processor for a 4096^3 on 32768 processors with different processor grids. Timings were obtained on BGW at Watson Research Center.

processor grid ($N_{P1} \times N_{P2}$)	$t/s/p$ (secs)
256 x 128	27.8
128 x 256	26.1
64 x 512	24.6
32 x 1024	20.0
16 x 2048	22.6

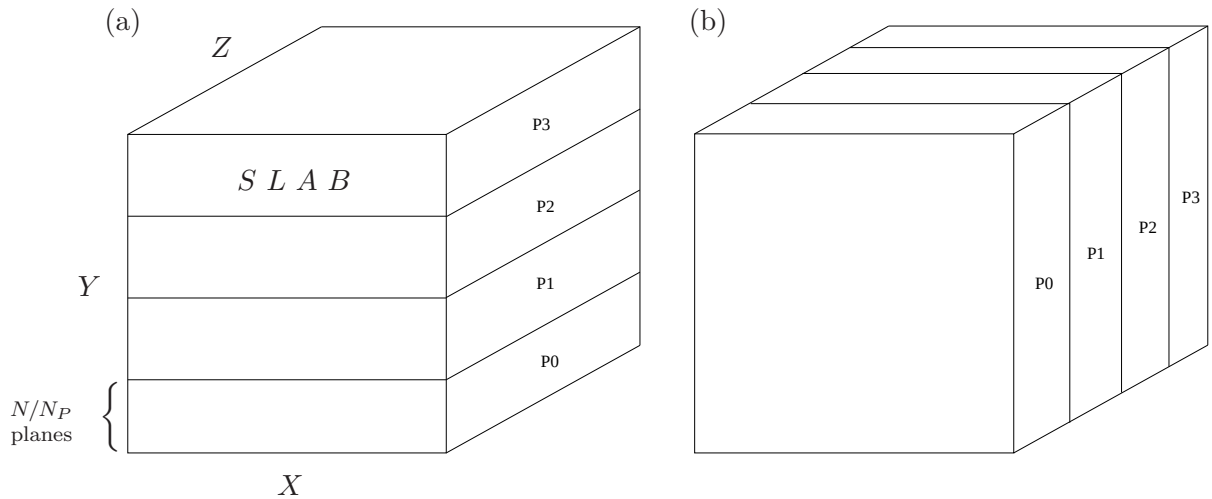

Figure 2.1: Data layout for a N^3 grid with $N_P = 4$ for the *slabs* code . Each processor holds N/N_P planes of data.

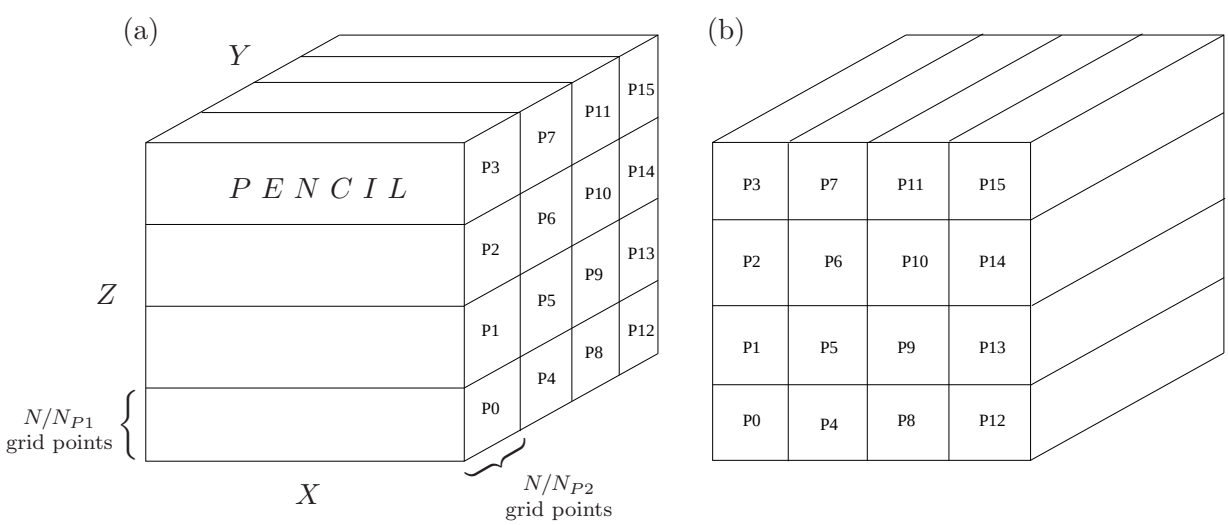

Figure 2.2: Data layout for a N^3 grid with $N_P = 16$ for the *pencils* code . Each processor holds $(N/N_{P1}) \times (N/N_{P2})$ lines of data.

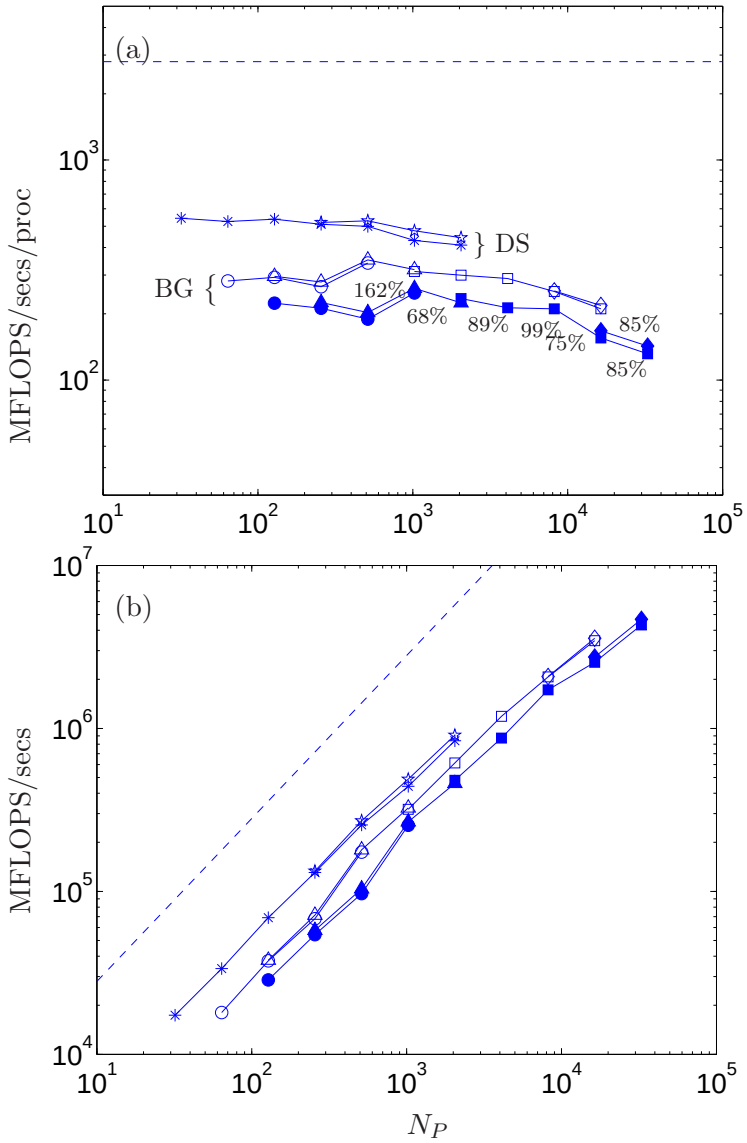

Figure 2.3: Performance per processor (a) and aggregate (b) of the 2d DNS code on BlueGene at resolutions 512^3 (circles), 1024^3 (triangles), 2048^3 (squares) and 4096^3 (diamonds) on up to 32768 processors. Open and closed symbols correspond to CO and VN mode respectively. Timings on DataStar are also included for 1024^3 (asterisk) and 2048^3 (stars). Dashed lines are theoretical peak performance for BlueGene. Percentages between data points correspond to parallel scalability which are presented only for VN mode runs.

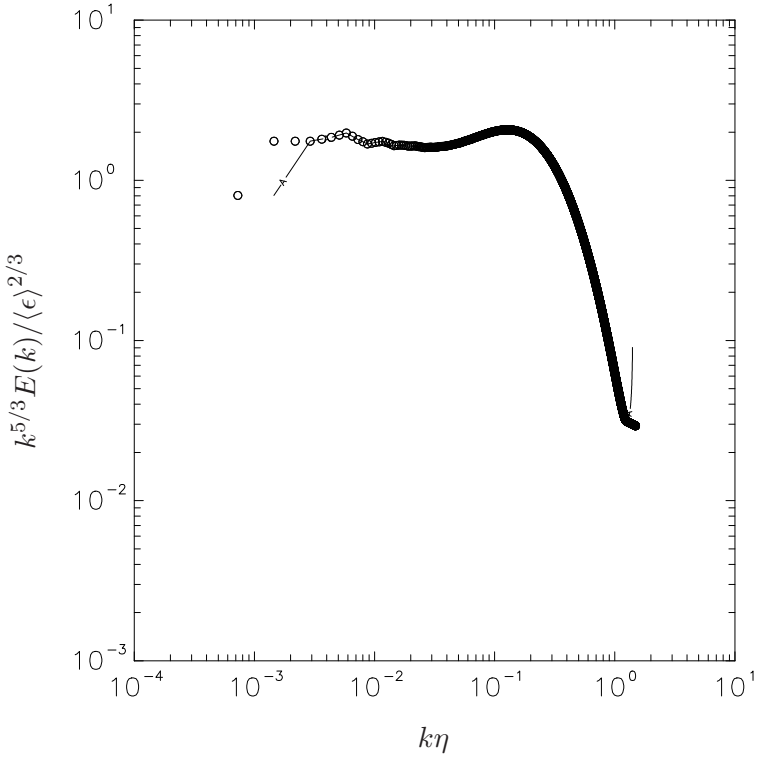

Figure 2.4: Spectrum at $R_\lambda \approx 1100$ on a 4096^3 grid (◯) interpolated/extrapolated from an average spectrum from $R_\lambda \approx 650$ simulations on a 2048^3 grid (solid line).

CHAPTER III

EFFECTS OF RESOLUTION

Our interest in this Chapter is to quantify the effects of finite resolution on DNS results through the statistics of dissipation and enstrophy, which are closely connected to velocity gradients and, more generally, velocity increments as a function of scale size r in viscous and inertial ranges. Below we first show the effects on single-point moments and then present an analysis based on velocity increments which can be compared with recent theoretical estimates by Yakhot & Sreenivasan (2005). Table 3.1 provides a listing of some of the basic parameters in the simulations used in this Chapter, including those where increasing computational power was used to resolve the small scales better instead of increasing the Reynolds number. As in a number of past publications (e.g. Vedula & Yeung 1999, Yeung *et al.* 2002, Donzis *et al.* 2005b) we average the results over a certain number of realizations (N_r) taken from instantaneous velocity fields saved at regular time intervals within a simulation time (T) typically of several eddy-turnover times (T_E). Our present focus on strong but short-lived events at the small scales allows us to take realizations closer in time than otherwise, without compromising the desired statistical independence among different datasets. Nevertheless, since samples of the most intense fluctuations are inherently few in number, a clear distinction between errors due to finite resolution and uncertainties due to finite sampling is not always possible.

3.1 Moments of Dissipation and Enstrophy

Well-known concepts of dissipative anomaly (Sreenivasan 1984, 1998, Donzis *et al.* 2005b) imply that in our simulations the mean dissipation $\langle\epsilon\rangle$ (and $\langle\Omega\rangle$) is determined by the large

scales subject to stochastic forcing and quite insensitive to small-scale resolution. It is convenient to normalize both dissipation and enstrophy by the mean, i.e. to define

$$\epsilon' \equiv \epsilon/\langle\epsilon\rangle; \qquad \Omega' \equiv \Omega/\langle\Omega\rangle, \tag{3.1}$$

and to examine their moments at order $p = 2$ onwards. We show these moments for $p = 2, 3, 4$ in figure 3.1 (a,b) and Table 3.2 at different grid resolutions with Reynolds numbers held fixed at $R_\lambda \approx 140$ and 240 as indicated in Table 3.1. As expected, the effect of finite resolution is seen in underestimation of these moments, and increasingly so at higher orders. However, for $k_{max}\eta$ from about 3 onwards these effects appear to be weak and within statistical error bounds indicated by 90% confidence intervals, suggesting little further gain in accuracy if the grid spacing were reduced further to a value smaller than η.

An important check on the statistical reliability of the data above is to examine the statistical convergence of moments via integrands of the form $(\epsilon')^p f_\epsilon(\epsilon')$ contributing to each moment of order p (and similarly for Ω'), where $f_\epsilon(\epsilon')$ is the PDF of the normalized dissipation. In figure 3.2 we show these integrands for $p = 4$ at different resolutions with $R_\lambda \approx 140$. The area under each curve gives the normalized fourth-order moment, which may be considered converged if the curve falls to nearly zero in the limit of the largest sampled ϵ' and Ω'. This behavior is well attained for all the curves shown, which suggests satisfactory convergence or alternatively reliable estimates of the moments can be obtained by integration from the PDF. At the same time this figure shows clearly that a grid at resolution $k_{max}\eta \approx 1.5$ misses many samples of large ϵ' or Ω'. On the other hand, resolution does not appear to affect samples of ϵ or Ω close to the mean: curves for dissipation and enstrophy show little difference for ϵ' up to about 7 and Ω' up to about 10 respectively. However, both the location and height of the peak are underestimated in simulations at $k_{max}\eta \approx 1.4$.

It is interesting to note from Table 3.2 that normalized moments of the form $\langle\epsilon^4\rangle/\langle\epsilon^2\rangle^2$

are considerably less sensitive to resolution than "unnormalized" moments of the same order (in this case, $\langle \epsilon'^4 \rangle$ which is proportional to $\langle \epsilon^4 \rangle$). This behavior can be understood by noting that effects of resolution increase with the order of the moment, which implies that some partial cancellation occurs when taking normalized ratios of moments of order close to each other and hence leading to reduced sensitivity to resolution. Another interpretation is that although finite resolution changes the shape of the observed dissipation and enstrophy PDFs by failing to capture the farthest tails, the results may — as to be seen below — still retain the correct functional form albeit with different values of parameters or coefficients involved.

Although moments of both ϵ' and Ω' are (as seen in results above) significantly affected by resolution, whether ratios between their corresponding moments, such as $\langle (\Omega')^p \rangle / \langle (\epsilon')^p \rangle$ (for $p = 2, 3, 4$, etc) behave similarly is a different issue. Table 3.3 shows these ratios for the same simulation datasets as in Table 3.2. It can be seen that the sensitivity is considerably less: e.g., although at $R_\lambda \approx 140$ both $\langle (\epsilon')^4 \rangle$ and $\langle (\Omega')^4 \rangle$ (from Table 3.2) change by a factor of more than 2.5 between $k_{max}\eta \approx 1.4$ and 2.8, the ratio $\langle (\Omega')^4 \rangle / \langle (\epsilon')^4 \rangle$ varies by less than 10%. Likewise, resolution effects on the ratio

$$\frac{\langle \Omega^4 \rangle / \langle \Omega^2 \rangle^2}{\langle \epsilon^4 \rangle / \langle \epsilon^2 \rangle^2}$$

are much weaker than on each quantity taken separately. The value 4.8 for this ratio from our least-resolved simulation at $R_\lambda \approx 240$ in Table 3.3 is also in reasonable agreement with 5.26 reported by Chen *et al.* (1997a) in simulations at $R_\lambda = 216$ with $k_{max}\eta < 2$ on a 512^3 grid. These observations suggest resolution tends to affect statistics of dissipation and enstrophy similarly, which in turn imply that conclusions on the scaling of dissipation versus enstrophy based on DNS data at modest resolution (Yeung *et al.* 2005) may remain at least qualitatively valid. In particular, as we discuss later in Chapter 4, qualitative comparisons between the PDFs of dissipation and enstrophy at modest resolution can still be made even

when their tails individually are underestimated.

Recently Yakhot & Sreenivasan (2005) proposed a theory of small-scale statistics which suggests, in part, that resolution of n-th order moments of dissipation requires an analytic range in velocity structure functions of order $4n$. For $n = 4$ (as we considered above) this would point to structure functions of order 16, which are rarely available in the literature and certainly cannot be captured reliably at the resolution level of $k_{max}\eta \approx 3$. In other words, our data suggest that (for the present purposes) results of acceptable accuracy in higher order moments of dissipation (and enstrophy) are possible under conditions less stringent than proposed by Yakhot & Sreenivasan (2005). This observation calls for a careful study of the resolution requirements applicable to the structure functions, or more generally, the statistics of velocity increments in space as a function of scale size.

3.2 Statistics of Velocity Increments and Gradients

The importance of velocity increments in space in describing turbulence structure has been well known since Kolmogorov (1941a); e.g. the third-order longitudinal structure function is often used as a test for inertial-range behavior (Yeung & Zhou 1997, Yeung *et al.* 2005) Analytic behavior at the small scales is (with an implied assumption of local isotropy) indicated if in the limit of small r the longitudinal and transverse structure functions were to scale as

$$\langle(\Delta_r u)^p\rangle/r^p = \langle(\partial u/\partial x)^p\rangle \quad ; \quad \langle(\Delta_r v)^p\rangle/r^p = \langle(\partial v/\partial x)^p\rangle \ . \tag{3.2}$$

In practice exact equality is not available but our goal is to develop a systematic estimate of departures due to finite resolution at each order p and for the smallest r available (i.e. the grid spacing, Δx). We also check whether inertial-range statistics at intermediate r can be affected substantially by resolution. While both longitudinal and transverse gradients are considered, the latter are more intermittent and thus provide a more rigorous test of data quality.

Figure 3.3(a,b) shows the PDFs of transverse velocity increments for a range of scale sizes r in our highly resolved 2048^3 simulation at $R_\lambda \approx 140$, at $k_{max}\eta \approx 11$ and $\Delta x/\eta \approx 0.3$. Two different normalizations are used: namely by the standard deviation (which increases with r) in (a), and by using r and the Kolmogorov time scale (τ_η) in (b) as explained below. In (a) we observe that, as expected, the increment at small r is highly non-Gaussian with wide tails reflecting strong intermittency at the small scales, while Gaussian behavior at large r is the result of the increment behaving as the difference between two uncorrelated velocities at a large distance apart. However, for a test of resolution in view of Eq. 3.2, it is useful to first divide $\Delta_r v$ by r, and then to non-dimensionalize by the r.m.s. of velocity gradient fluctuations, which is proportional to $1/\tau_\eta$. Unlike the standardized PDFs in (a), curves in (b) are expected to converge as r is made even smaller towards the limit of analytic behavior. Clearly, the curve for data obtained at the "standard" resolution $k_{max}\eta \approx 1.5$ differs significantly from the others, thus showing the effects of finite resolution. However there is little further change as $k_{max}\eta$ is increased further beyond 3; in fact, for clarity, we have removed the curve for $k_{max}\eta \approx 5.7$ since it is virtually indistinguishable from that for $k_{max}\eta \approx 11$. These comparisons suggest contributions to velocity gradients from scale sizes smaller than $\eta/2$ are small, and that for many purposes adequate results on velocity gradient statistics can be obtained with $k_{max}\eta \approx 3$, i.e. $\Delta x/\eta$ close to 1.0.

In analogy to the moments of dissipation considered earlier in figure 3.1 and 3.2, the quality of statistical sampling of the tails of the velocity increment PDFs in figure 3.3 can be checked via a test for the convergence of integrals for moments of increasing order. Since the transverse increments are statistically symmetric we define

$$C_p(z) = \int_{-z}^{z} (z')^p f(z') dz' \tag{3.3}$$

where z is the normalized velocity increment $\delta_r^* v \equiv (\Delta_r v)/(r\tau_\eta)$, $f(\cdot)$ is its PDF, and by definition $C_p(0) = 0$, $C_p(\infty) = \langle(\Delta_r v/r)^p\rangle {\tau_\eta}^p$ for any $p > 0$. Figure 3.4 shows the data,

for $p = 4, 6, 8, 10, 12$ and $k_{max}\eta \approx 1.5$, 3 and 11 at $R_\lambda \approx 140$ in our simulations. (Data for $k_{max}\eta \approx 6$ are, as in figure 3.3 above, indistinguishable from $k_{max}\eta \approx 11$ and omitted for clarity.) Statistical convergence is indicated if curves shown reach asymptotic values in the limit of large z. This convergence is attained reasonably well up to order 8, but is less satisfactory at higher orders or smaller scale sizes where stronger intermittency effects are expected. Within each group of curves at fixed p we also observe convergence of a deterministic nature in the limit of small r/η. In particular, using relations based on local isotropy one can show that in the limit of $r \ll \eta$ the value of $C_p(\infty)$ defined above should be equal to $(2/15)^{p/2}\langle(\partial v/\partial x)^p\rangle/\langle(\partial v/\partial x)^2\rangle)^{p/2}$, which increases strongly with p.

In the study of resolution effects there is much interest (Yakhot & Sreenivasan 2005) in how small the grid spacing must be (compared to η) in order to observe analytic behavior in velocity structure functions of order p, depending on both p and the Reynolds number. To illustrate this issue we show in figure 3.5 the compensated longitudinal structure functions $\langle(\Delta_r u)^p\rangle/r^p$ at even orders $p = 2, 4, 6, 8, 10, 12$, from the $R_\lambda \approx 140$ simulation with $k_{max}\eta \approx 11$ (2048^3). (The solid-square symbols are from the theory of Yakhot & Sreenivasan (2005), to be described below.) Analytic range behavior is indicated if the curves reach $\langle(\partial u/\partial x)^p\rangle$ (dashed horizontal lines) as r is decreased towards the smallest value available (i.e., the grid spacing Δx). As expected, the minimum r required for an analytic range decreases with increasing order p of the structure functions. In particular, analytic behavior for orders 8 and upwards requires r/η substantially smaller than 1, which is the smallest scale resolved in simulations at $k_{max}\eta \approx 3$. In other words, although in figure 3.1 we saw that statistics for the fourth-order moment of dissipation in simulations at $k_{max}\eta \approx 3$ appear to be accurate, this is being achieved without satisfying the corresponding of analytic range in structure functions of order 16 suggested in theory by Yakhot & Sreenivasan (2005).

In figure 3.5 it is evident that at any given r/η departure from analytic behavior increases

systematically with order p of the structure functions: e.g. in our data at $R_\lambda = 140$ and $k_{max}\eta \approx 2.8$ we find at $r/\eta \approx 1$ about 1% error for $p = 2$ but 24% for $p = 12$. Solid squares in the figure denote the theoretical estimate by Yakhot & Sreenivasan (2005) for the scale needed to accurately capture structure functions of order p, as

$$\eta_p/\eta \approx ({R_\lambda}^2/15)^{3/4+d_p} \tag{3.4}$$

where $d_p = 1/(\zeta_p - \zeta_{p+1} - 1)$ with ζ_p being the inertial-range scaling exponents of structure functions of order p. It should be noted that this estimate does not distinguish between longitudinal and transverse structure functions, and we have used $R_\lambda^2/15$ in place of a large-eddy or integral-scale Reynolds number, while following Yakhot & Sreenivasan (2005) in taking $\zeta_p = 0.383p/(1 + 0.05p)$. Since the inertial range exponents possess the anomalous-scaling properties $\zeta_p < p/3$ (especially at larger p) the exponent $3/4 + d_p$ in Eq. 3.4 is negative with magnitude increasing with p, such that the predicted η_p/η decreases with increasing p and increasing R_λ, as required. In practice, of course, statistics at different orders taken from a simulation with given Reynolds number and resolution will always be at different degrees of accuracy, such that some compromise at the highest orders of interest is inevitable.

We are interested in developing an alternative estimate of the resolution required for a given deviation from analytic range behavior, using a Taylor-series approach (Stolovitzky & Sreenivasan 1993) that can also distinguish between longitudinal and transverse statistics. For transverse velocity increments a standard Taylor-series expansion gives

$$\frac{\Delta_r v}{r} = v_x + \frac{r}{2} v_{xx} + \frac{r^2}{6} v_{xxx} + O(r^3) \tag{3.5}$$

where, for brevity, coordinate subscripts are used to denote differentiation. Taking the p-th power and assembling terms in ascending powers of r gives

$$\left(\frac{\Delta_r v}{r}\right)^p - v_x^p = r\frac{p}{2} v_x^{p-1} v_{xx} + r^2 p \left(\frac{1}{6} v_x^{p-1} v_{xxx} + \frac{p-1}{8} v_x^{p-2} v_{xx}^2\right) + O(r^3). \tag{3.6}$$

It is useful to note the identities

$$v_x^{p-1} v_{xx} = \frac{1}{p}(v_x^p)_x \tag{3.7}$$

and

$$v_x^{p-1} v_{xxx} = (v_x^{p-1} v_{xx})_x - (p-1) v_x^{p-2} v_{xx}^2 \tag{3.8}$$

which imply that some of the contributions on the right of Eq. 3.6 vanish by homogeneity when averaged in space. Accordingly we obtain

$$\left\langle \left(\frac{\Delta_r v}{r} \right)^p \right\rangle - \langle v_x^p \rangle = -\frac{1}{24} p(p-1) r^2 \left\langle v_x^{p-2} v_{xx}^2 \right\rangle + O(r^4). \tag{3.9}$$

With $\langle v_x^{p-2} v_{xx}^2 \rangle$ being non-negative for all even integers p, this result is consistent with the observation that finite resolution causes underestimation of higher-order moments. We also see that, to leading order, the error involved decreases as r^2 for structure functions at all orders (p) but increases with p through the factor $p(p-1)$ as well as the quantity $\langle v_x^{p-2} v_{xx}^2 \rangle$.

To investigate the Reynolds number dependence in Eq. 3.9 it is useful to divide both sides by $\langle v_x^p \rangle$ and express the right hand side in terms of Kolmogorov variables. Upon some further rearrangement a non-dimensional result can be written as

$$\frac{\langle v_x^p \rangle - \langle (\Delta_r v / r)^p \rangle}{\langle v_x^p \rangle} = \frac{p(p-1)}{24} Q_p^T \left(\frac{r}{\eta} \right)^2 + O(r^4) \tag{3.10}$$

where effects of small-scale intermittency are expressed by the quantity defined as

$$Q_p^T \equiv \frac{\langle v_x^{p-2} v_{xx}^2 \rangle}{\langle v_x^p \rangle / \eta^2} \ . \tag{3.11}$$

A similar expression can be written for second-order longitudinal structure functions involving an analogous quantity Q_p^L in terms of longitudinal velocity gradients. Exact results for Q_p^T (and Q_p^L) are not available, although its numerator is subject to Cauchy-Schwarz inequality for the covariance between two random variables (v_x^{p-2} and v_{xx}^2) whereas the denominator $\langle v_x^p \rangle$ can be analyzed using intermittency models such as those based on log-normality or multifractal concepts. In any case these quantities are readily computed from

our DNS database but because they involve second derivatives and higher powers of the first derivatives we use only results from the best-resolved simulation at each Reynolds number.

Figure 3.6 shows DNS data on both Q_p^L and Q_p^T at $R_\lambda \approx 140$ and 240, using simulations at $k_{max}\eta \approx 11$ and 6 respectively. Since transverse gradients are statistically symmetric data points for Q_p^T are available for even orders only. Although there is some scatter it can be seen that, at each given p, both Q_p^L and Q_p^T increase with Reynolds number as the turbulence becomes more intermittent; and Q_p^T is likewise larger than Q_p^L for longitudinal gradients. However, except for $p = 2$ and perhaps $p = 3$, there appears to be no clear dependence on p from 4 onwards. Taking an average from $p = 4$ through $p = 12$ produces the values 0.0476 and 0.0548 for Q_p^L and Q_p^T respectively for $R_\lambda \approx 140$ compared with 0.0563 and 0.0703 for $R_\lambda \approx 240$.

It may be noted that some support for the observed quasi-constancy (with respect to p) of Q_p^L and Q_p^T can be obtained by using a simple scaling argument for the second derivative (Stolovitzky & Sreenivasan 1993)

$$v_{xx} \sim c\frac{v_x}{\eta} \tag{3.12}$$

where c is a random coefficient of order unity. This estimate is also consistent with the so called p-model of intermittency (Meneveau & Sreenivasan 1987) and leads to the result

$$Q_p^T = \frac{\langle v_x^{p-2} v_{xx}^2 \rangle}{\langle v_x^p \rangle / \eta^2} \approx \frac{\langle c^2 \rangle \langle v_x^{p-2} v_x^2 \rangle / \eta^2}{\langle v_x^p \rangle / \eta^2} = \langle c^2 \rangle \tag{3.13}$$

which is indeed independent of p but can retain a dependence on the Reynolds number.

It is clear that a Q_p^T taken as quasi-constant as suggested above leads to $p(p-1)$ scaling for the normalized error in Eq. 3.10. In figure 3.7 we show the resulting estimated error at each p for data at both $R_\lambda \approx 140$ and $R_\lambda \approx 240$, computed at degrees of resolution at $k_{max}\eta$ nominally 1.5, 3 and 6 (see Table 1). We show only transverse data in this figure since if transverse gradients are resolved adequately then results on longitudinal gradients will also

be satisfactory (in fact, slightly better). At all three levels of resolution very good agreement can be seen for order $p = 4$ onwards between actual (open and closed symbols) and estimated (dashed and solid lines, correspondingly) errors from order 4 onwards. The agreement is in general less close for higher orders, where there is greater statistical uncertainty and possibly a need to retain more terms in the Taylor-series expansions we use in the paper.

Using Eq. 3.10 and data on the quantity Q_p, as shown in figure 3.6, it is now possible to compute a quantitative estimate of the value of r/η where structure functions at each order p can capture the p-th order velocity gradient moment to within a specified error tolerance. In particular if the fractional error allowed at order p is e, then Eq. 3.10 gives

$$(r/\eta)_{1-e} \approx \left[\frac{24\ e}{p(p-1)Q_p}\right]^{1/2} \tag{3.14}$$

as an estimate of the scale that must be resolved. As a working definition we take $e = 5\%$ here and denote the pertinent scale as $(r/\eta)_{95}$, which, in practice, would be a reasonable criterion for how small $\Delta x/\eta$ needs to be in order to provide accurate results on velocity gradient moments up to order p.

Figure 3.8 shows a comparison of $(r/\eta)_{95}$ obtained directly from structure function data in DNS using the LHS of Eq. 3.10, its estimated value based on Eq. 3.14 using quasi-constant values of Q_p^T from figure 3.6, and the theoretical estimate η_p/η (Eq. 3.4) by Yakhot & Sreenivasan (2005). It is clear the size of the smallest scale (compared to η) that must be resolved decreases with increasing order of the moment as well as (less strongly) the Reynolds number. As expected from the discussions in figure 3.6 and 3.7 results from Eq. 3.14 based on a quasi-constant Q_p^T are close to the actual DNS data except for the highest orders $p = 10$ and 12 mainly at higher Reynolds number ($R_\lambda \approx 240$). Although the 95% criterion (i.e. 5% error) proposed in Eq. 3.14 is somewhat arbitrary, a change to, say, 99% would produce only a roughly 2% decrease in the size of the smallest scale that must be resolved. The comparisons here suggest that the resolution criterion proposed by

Yakhot & Sreenivasan (2005) may be overly restrictive at low and moderate orders, but (importantly) more realistic at higher orders.

While we have focused primarily on resolution concerns for intermittency at the smallest scales, another important question is whether inferences of inertial-range behavior and scaling constants in DNS can be affected quantitatively by resolution. For this latter issue our main interest would be in velocity increment statistics at scale size r in the range identified empirically as showing behavior closest to classical inertial scaling, via (for example Yeung *et al.* 2005), plots of the third-order longitudinal structure function normalized by Kolmogorov variables. Figure 3.9 shows standardized PDFs of transverse velocity increments at $r/\eta \approx 2$ and 17, which are in the dissipative and inertial ranges respectively, at $k_{max}\eta \approx 1.4$, 2.8 and 5.5 for $R_\lambda \sim 240$. The differences are seen to be small even for $r/\eta = 2$, which is not surprising since even with the usual resolution $k_{max}\eta = 1.5$ scales down to $r \approx 2\eta$ are resolved. The implication of these results is that statistics in the inertial range are not greatly affected by resolution, such that $k_{max}\eta \approx 1.5$ would be adequate for such purposes even though the small scales are not captured perfectly. In other words resolution at $k_{max}\eta \approx 1.5$ is sufficient for studies of scaling exponents in relations such as $\langle \Delta_r u^p \rangle \sim r^{\zeta_p}$ in the inertial range (although statistics of local averages of dissipation at these scales can still be affected by resolution).

3.3 Summary

Results at fixed Reynolds numbers but different grid resolutions indicate that moments of dissipation and enstrophy are accurate up to fourth order if the product of highest resolvable wavenumber (k_{max}) and Kolmogorov length scale (η) is at least 3, or equivalently if the grid spacing (Δx) is not larger than η. This result is achieved despite the absence of an analytic range in velocity structure functions at the corresponding order predicted by Yakhot & Sreenivasan (2005). A Taylor-series expansion is used to quantify the degree of departure

from analytic range in the structure functions at different orders and as a function of the Reynolds number. This analysis leads to a resolution estimate (applicable to the structure functions) which is not as restrictive as Yakhot & Sreenivasan (2005) at lower orders but similar at higher orders. Effects of finite resolution on inertial-range statistics of velocity increments are found to be relatively weak. Likewise, although use of the "standard" resolution $k_{max}\eta \approx 1.5$ (as in most DNS aimed at reaching high Reynolds number) leads to underestimation of high-order moments and the tails of PDFs of dissipation and enstrophy, statements comparing the qualitative behaviors of these quantities still appear to be reliable.

Table 3.1: DNS parameters: Taylor-microscale Reynolds number $R_\lambda = u'\lambda/\nu$, number of grid points N^3, viscosity ν, resolution measured by $k_{max}\eta$ and $\Delta x/\eta$, number of independent realizations N_r and length of the simulation T normalized by eddy turnover time $T_E = L/u'$.

R_λ	140	140	140	140	240	240	240
N^3	256^3	512^3	1024^3	2048^3	512^3	1024^3	2048^3
ν	0.0028	0.0028	0.0028	0.0028	0.0011	0.0011	0.0011
$k_{max}\eta$	1.4	2.8	5.7	11.1	1.4	2.8	5.4
$\Delta x/\eta$	2.10	1.05	0.52	0.27	2.08	1.04	0.55
N_r	11	16	18	11	13	12	14
T/T_E	10.0	7.2	8.5	6.0	9.4	5.4	5.4

Table 3.2: Ensemble averaged moments of dissipation and enstrophy at $R_\lambda \approx 140$ (top) and 240 (bottom) with 90% confidence intervals.

$R_\lambda \approx 140$

$k_{max}\eta$	1.4	2.8	5.7	11.1
$\langle(\epsilon')^2\rangle$	2.53 ± 0.04	2.85 ± 0.07	2.77 ± 0.06	2.82 ± 0.08
$\langle(\epsilon')^3\rangle$	14.1 ± 0.6	21.5 ± 1.6	19.9 ± 1.4	20.7 ± 2.1
$\langle(\epsilon')^4\rangle$	153 ± 14	388 ± 58	341 ± 48	364 ± 81
$\langle\epsilon^4\rangle/\langle\epsilon^2\rangle^2$	23.9	47.8	44.5	45.8
$\langle(\Omega')^2\rangle$	4.52 ± 0.09	5.19 ± 0.18	5.07 ± 0.19	5.20 ± 0.23
$\langle(\Omega')^3\rangle$	63.0 ± 3.1	100.0 ± 9.3	94.2 ± 9.9	97.6 ± 13.1
$\langle(\Omega')^4\rangle$	2022 ± 179	5315 ± 989	4920 ± 965	4751 ± 1200
$\langle\Omega^4\rangle/\langle\Omega^2\rangle^2$	99.2	197.1	191.3	175.9

$R_\lambda \approx 240$

$k_{max}\eta$	1.4	2.8	5.4
$\langle(\epsilon')^2\rangle$	3.07 ± 0.05	3.17 ± 0.07	3.15 ± 0.06
$\langle(\epsilon')^3\rangle$	25.3 ± 1.3	29.1 ± 1.8	28.8 ± 1.7
$\langle(\epsilon')^4\rangle$	488 ± 53	696 ± 83	697 ± 89
$\langle\epsilon^4\rangle/\langle\epsilon^2\rangle^2$	51.9	69.3	70.4
$\langle(\Omega')^2\rangle$	5.81 ± 0.13	5.99 ± 0.18	5.93 ± 0.12
$\langle(\Omega')^3\rangle$	133 ± 8	150 ± 14	142 ± 9
$\langle(\Omega')^4\rangle$	8364 ± 1017	11222 ± 1869	10211 ± 1503
$\langle\Omega^4\rangle/\langle\Omega^2\rangle^2$	247.7	312.8	290.6

Table 3.3: Ratios of moments of dissipation and enstrophy with different resolutions at $R_\lambda \approx 140$ and 240. Values differ slightly from those obtained using data in Table 3.2 since ensemble average is perform after taking ratios for each realization.

R_λ	140	140	140	140	240	240	240
$k_{max}\eta$	1.4	2.8	5.7	11.1	1.4	2.8	5.4
$\langle(\Omega')^2\rangle/\langle(\epsilon')^2\rangle$	1.8	1.8	1.8	1.8	1.9	1.9	1.9
$\langle(\Omega')^3\rangle/\langle(\epsilon')^3\rangle$	4.5	4.6	4.7	4.6	5.2	5.1	4.9
$\langle(\Omega')^4\rangle/\langle(\epsilon')^4\rangle$	13.3	13.8	14.1	12.7	17.2	15.7	14.5
$(\langle\Omega^4\rangle/\langle\Omega^2\rangle^2)/(\langle\epsilon^4\rangle/\langle\epsilon^2\rangle^2)$	4.2	4.2	4.2	3.7	4.8	4.4	4.1

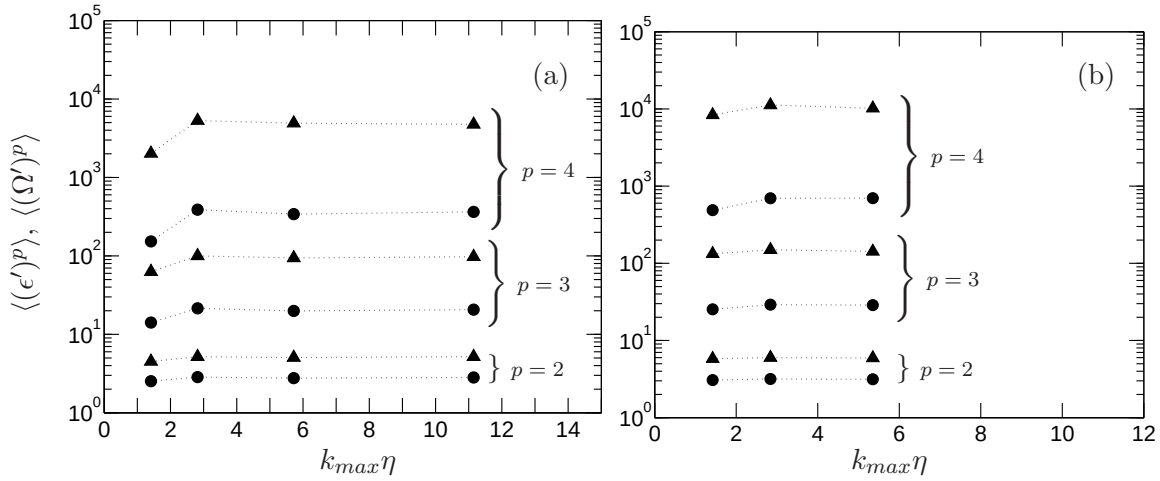

Figure 3.1: Ensemble-averaged moments of normalized dissipation rate and enstrophy: $\langle \epsilon'^p \rangle$ (●) and $\langle \Omega'^p \rangle$ (▲) for orders $p = 2, 3, 4$ at different resolutions for (a) $R_\lambda \approx 140$ and (b) $R_\lambda \approx 240$ as listed in Table 1. Also included 90% confidence intervals.

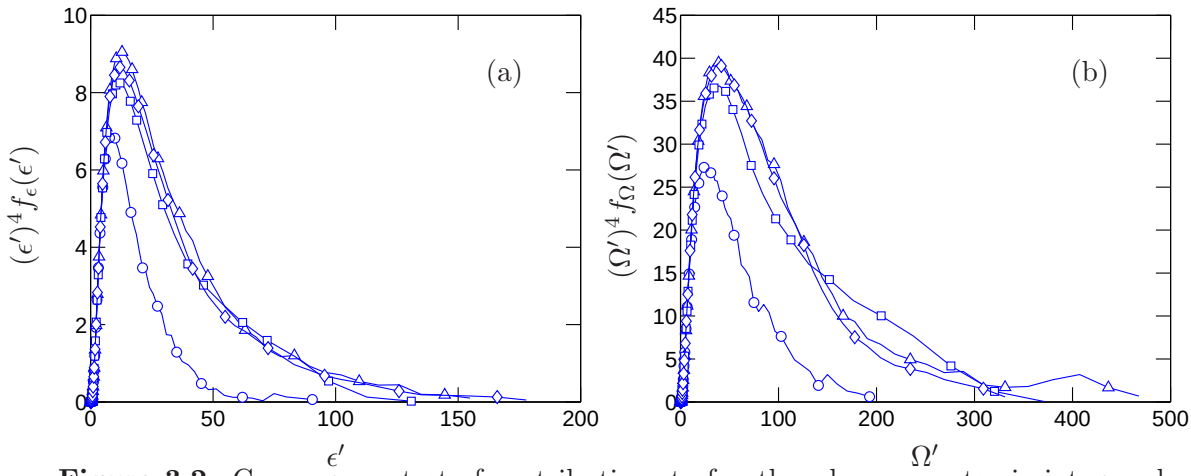

Figure 3.2: Convergence test of contributions to fourth order moments via integrands of PDFs of (a) normalized dissipation $\epsilon' \equiv \epsilon/\langle\epsilon\rangle$ and $\Omega' \equiv \Omega/\langle\Omega\rangle$, from data at $R_\lambda \approx 140$ with $k_{max}\eta \approx 1.4$ (◯), 2.8 (△), 5.7 (□) and 11 (◇).

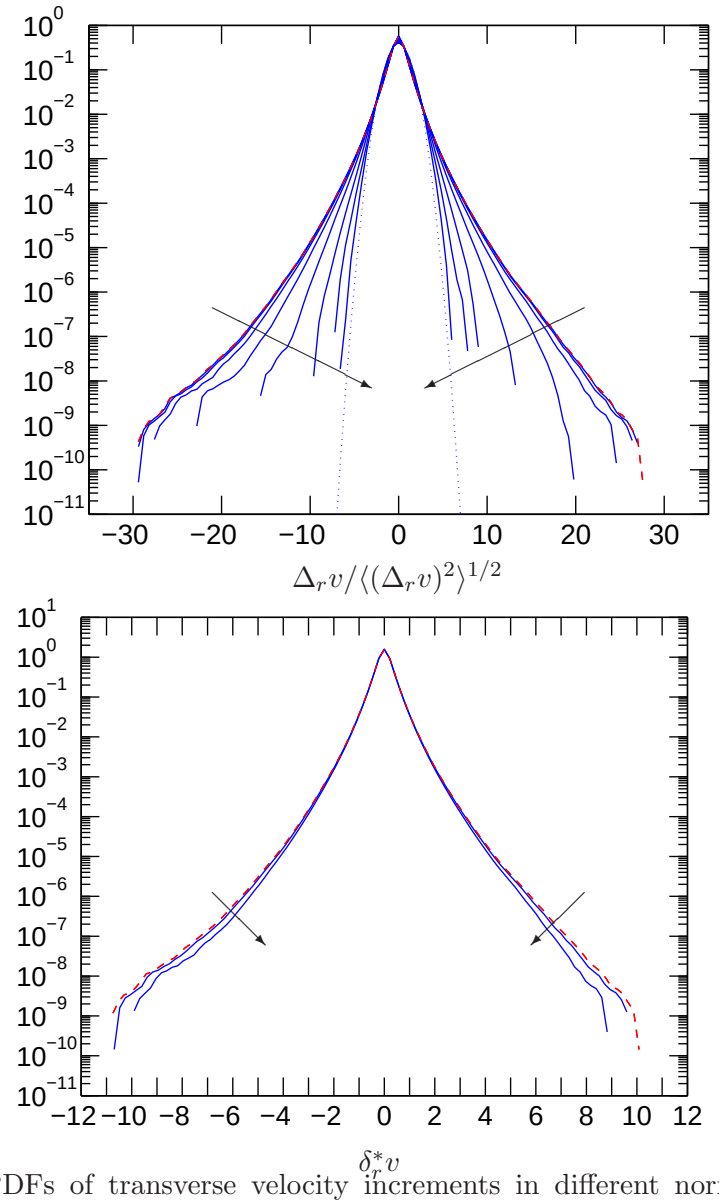

Figure 3.3: PDFs of transverse velocity increments in different normalizations, from DNS data at $R_\lambda \approx 140$ with $k_{max}\eta \approx 11$, and arrows indicating trends in the direction of increasing scale size r. In (a) $\Delta_r v$ is normalized by its r.m.s., i.e. $\langle(\Delta_r v)^2\rangle^{1/2}$, for $r/\Delta x = 1, 2, 4, 8, 16, 32, 64, 128, 256$, and a standard Gaussian (dashed curve) is included for comparison. In (b) $\Delta_r v$ is normalized by r/τ_η, for $r/\Delta x = 1, 4, 8$ ($r/\eta \approx 1/4, 1, 2$).

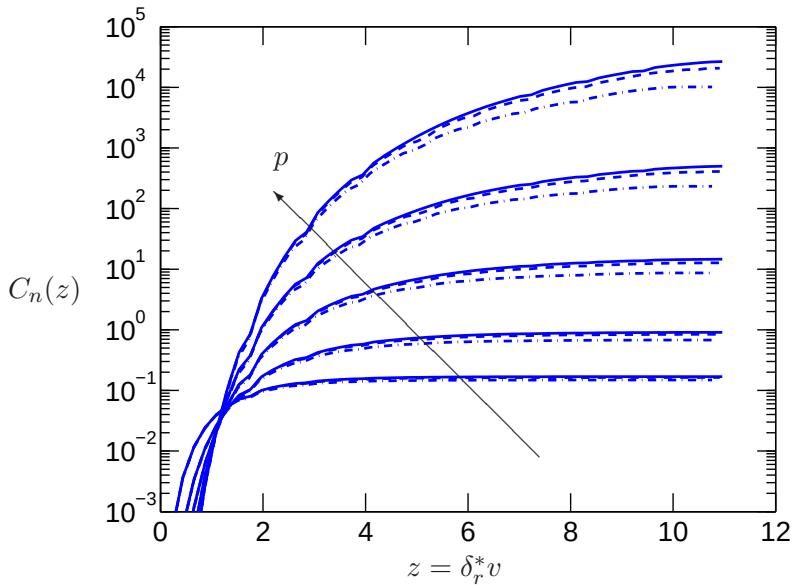

Figure 3.4: Convergence test of contributions to moments of $\delta_r^* v = (\Delta_r v/r)/\tau_\eta$ through $C_p(\delta_r^* v)$ (see Eq. 3.3) at $r/\eta \approx 1/4$ (solid line), 1 (dashed line) and 2 (dash-dotted line), from simulation at $R_\lambda \approx 140$ with $k_{max}\eta \approx 11$ (2048^3). Arrow points in the direction of increasing p (4,6,8,10,12).

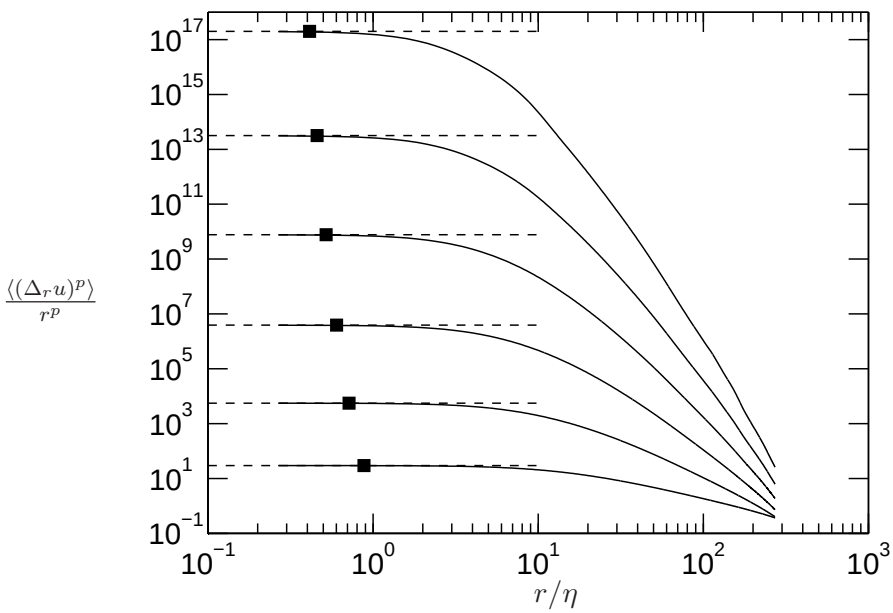

Figure 3.5: Normalized longitudinal structure functions of even order: $\langle(\Delta_r u)^p\rangle/r^p$ for p =2, 4, 6, 8, 10 and 12 (bottom to top) from simulation at $R_\lambda \approx 140$ and $k_{max}\eta \approx 11$ (2048^3). Horizontal dashed lines indicate analytic limit as moments of longitudinal velocity gradients. Solid squares denote η_p/η as defined in Yakhot & Sreenivasan (2005).

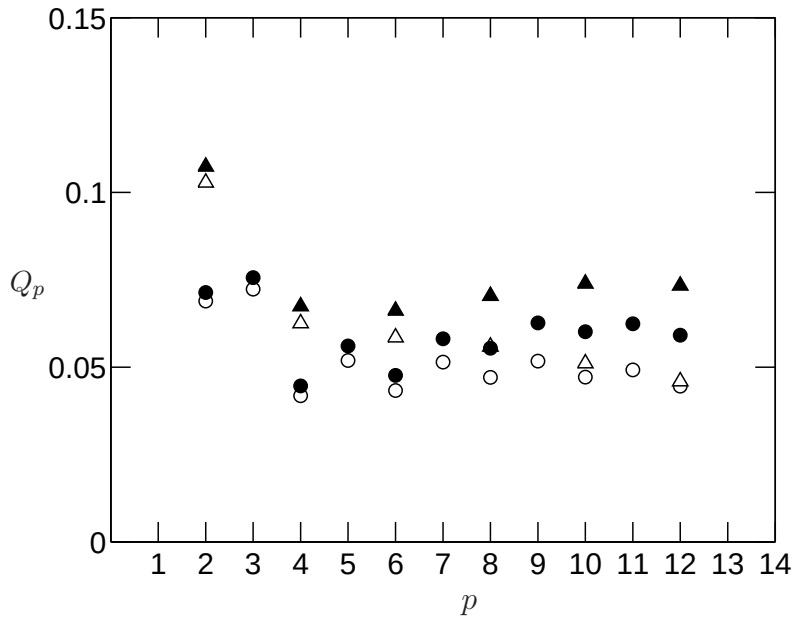

Figure 3.6: Variation of Q_p^T (triangles) defined by Eq. 3.11 and its longitudinal counterpart (Q_p^L, circles) with order p, from simulations at $R_\lambda \approx 140$ with $k_{max}\eta \approx 11$ (open symbols) and $R_\lambda \approx 240$ with $k_{max}\eta \approx 5.5$ (closed symbols).

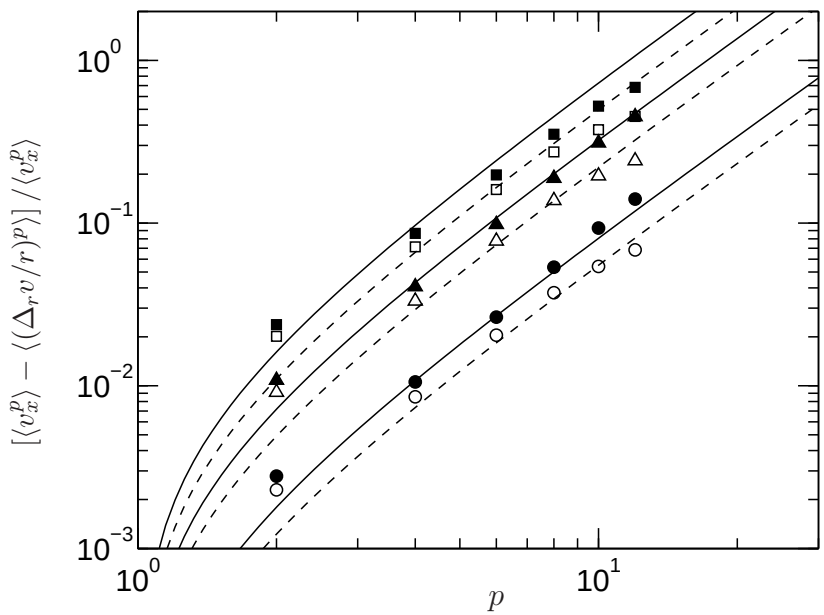

Figure 3.7: Normalized departures from analytic behavior of transverse structure functions measured directly from DNS, at $R_\lambda \approx 140$ with $k_{max}\eta \approx 11$ (open symbols) and $R_\lambda \approx 240$ with $k_{max}\eta \approx 5.5$ (closed symbols), compared to estimates based on Eq. 3.10 with quasi-constant values of Q_p^T. Circles, triangles, and squares denote data points at $r/\eta \approx 0.5$, 1 and 1.6 respectively. Dashed lines denote result from Eq. 3.10 for $R_\lambda \approx 140$; solid lines for $R_\lambda \approx 240$.

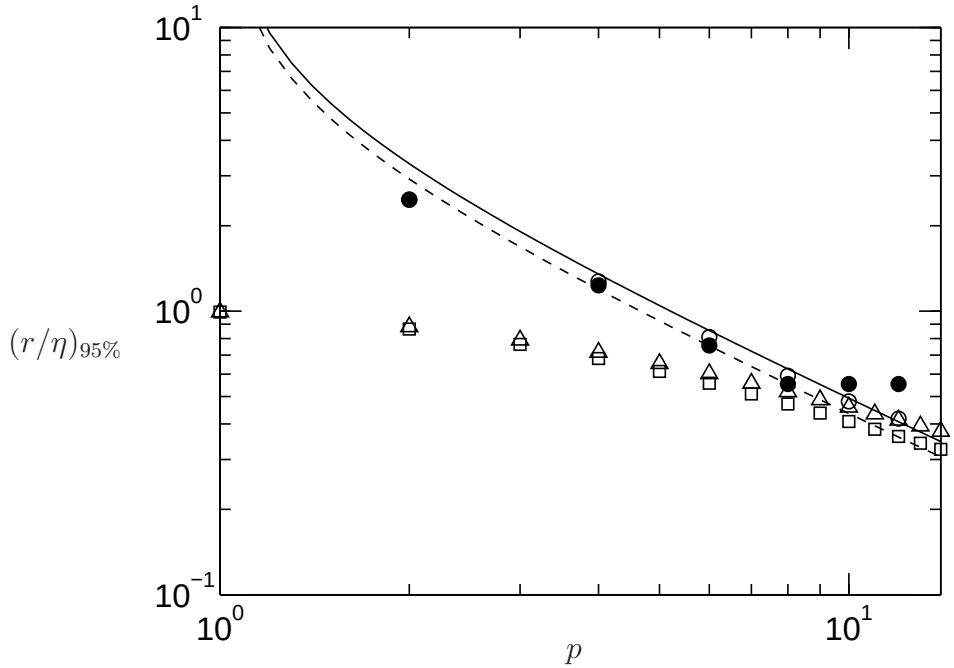

Figure 3.8: Normalized scale size $(r/\eta)_{95}$ for 5% deviation from analytic behavior for different orders of moments of transverse velocity increments. DNS data from simulations at $R_\lambda \approx 140$ with $k_{max}\eta \approx 11$ (open circles) and 240 with $k_{max}\eta \approx 5.5$ (closed circles) are compared with results from Eq. 3.14 at $R_\lambda \approx 140$ (solid line) and 240 (dashed line). Also included are the scales η_p/η for $R_\lambda \approx 140$ ($\triangle$) and 240 ($\square$).

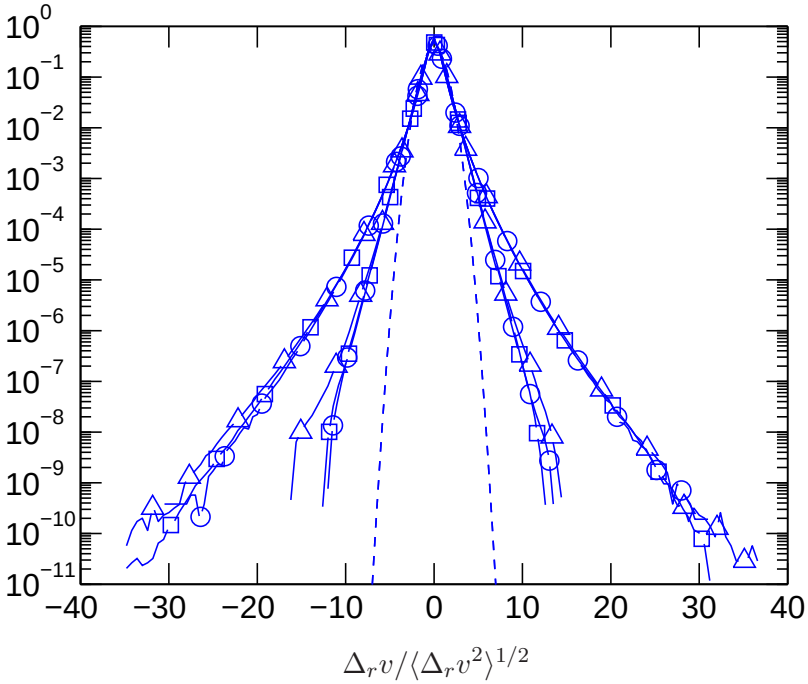

Figure 3.9: Standardized PDFs of transverse velocity increment from $R_\lambda \approx 240$ simulations with $k_{max}\eta \approx 1.4$ (◯), 2.8 (△) and 5.5 (□). Outer and inner groups of lines are for $r/\eta \approx 2$ and 17 respectively. The dashed curve shows a standardized Gaussian for comparison.

CHAPTER IV

INTERMITTENCY AND REYNOLDS NUMBER SCALING

4.1 Background

The notion of small-scale similarity originated with Kolmogorov (1941a). He suggested that at high Reynolds numbers, the statistics of velocity differences over a distance r much smaller than the integral scale ($r \ll L$) are only a function of r, ν and $\langle\epsilon\rangle$. For even higher Reynolds numbers there is an intermediate range of scales ($\eta \ll r \ll L$), called the inertial range, in which statistics of velocity increments depend only on r and $\langle\epsilon\rangle$. Kolmogorov (1941b) derived from the N-S equations an exact relation for the third-order structure function in the inertial range (commonly referred to as the "four-fifths law"), namely

$$\langle \Delta u_r^3 \rangle = -(4/5)\langle\epsilon\rangle r. \tag{4.1}$$

Since this relation is exact, it is often used as a direct test of inertial range scaling. In figure 4.1 we show that in our recent $R_\lambda \approx 650$ simulations there is good attainment of the theoretical value 4/5 for the third-order structure function (lower curve on the left figure). We also include vertical dashed lines to delimit the inertial range.

Following the reasoning behind Kolmogorov (1941a) (subsequently referred to as K41), one could expect that in the inertial range the structure functions scale as

$$\langle \Delta u_r^n \rangle = C_n(\langle\epsilon\rangle r)^{n/3} \tag{4.2}$$

where C_n are universal constants. Attempts to test this scaling have shown that there are significant departures from Eq. 4.2 especially for large n (see e.g. Frisch 1995, Sreenivasan & Antonia 1997). Obukhov (1962) anticipated that these departures are partly due to the

fluctuations of ϵ. Instead of using $\langle\epsilon\rangle$ in Eq. 4.2, he suggested using local averages,

$$\epsilon_r = \frac{1}{V_r}\int_{V_r} \epsilon(\mathbf{x})d\mathbf{x} \tag{4.3}$$

where $V_r \sim r^3$ is a volume of linear size r. The variable $\epsilon_r/\langle\epsilon\rangle$ is random and its statistics are functions of r/L according to Obukhov's picture. Therefore, if one uses a local average instead of the global average in Eq. 4.2 the structure functions are still expected to scale as

$$\langle \Delta u_r^n \rangle \sim r^{\zeta_n} \tag{4.4}$$

although the exponents ζ_n may be *anomalous*, that is, different from the classical prediction of $n/3$. Equation 4.1 implies that $\zeta_3 = 1$.

In figure 4.1 we show longitudinal structure functions normalized such that validity of K41 would imply that all the curves present a plateau at intermediate scales. It is clear that there is anomalous scaling for high-order moments. It was also suggested that anomaly is also present for low order moments (e.g Chen *et al.* 2005). The exponents ζ_n in Eq. 4.4 can be obtained by fitting a power law in the regions where the third-order structure function shows a plateau. The result of this calculation is shown in figure 4.2 where we see that departures from K41 are apparent. We also include the experimental data by Anselmet *et al.* (1984). Good agreement between our simulations and experiments is observed despite the mean shear present in the experiments.

As suggested by Obukhov, anomalous scaling may in part be due to the strong fluctuations of ϵ. Indeed, the energy dissipation is highly intermittent as seen in figure 4.3 where contours of $\epsilon/\langle\epsilon\rangle$ at three arbitrary planes are shown. Very large localized fluctuations can be of the order of 100 times the mean value or higher while large regions of space show relatively weak activity.

More generally, small-scale intermittency can be characterized by the velocity gradient tensor whose quadratic invariants are represented by the dissipation and enstrophy. Several

theoretical arguments are known (L'vov & Procaccia 1996, He *et al.* 1998, Nelkin 1999) implying that both dissipation and enstrophy should scale similarly at high enough Reynolds numbers. However, almost all sources of available data (e.g Siggia 1981, Kerr 1985, Yeung & Pope 1989, Sreenivasan *et al.* 1995, Chen *et al.* 1997a, Zhou & Antonia 2000) suggest that enstrophy is more intermittent than dissipation. Evidence from both simulation and experiment have included larger skewness and flatness factors, probability density functions (PDFs) with wider tails, and larger intermittency exponents for local averages (ϵ_r and Ω_r) taken over a domain of linear size r in the inertial range. A better understanding of this issue is important, in order to, say, avoid ambiguities in the choice of variable used to represent the small scales (Sreenivasan & Antonia 1997), and to clarify the roles of local straining versus rotation in the modeling of turbulent dispersion (Borgas & Yeung 2004).

In the rest of this Chapter we compare statistics of dissipation and enstrophy and address their Reynolds number scaling. We recently found (Yeung *et al.* 2005) that for intermediate values of ϵ and Ω the differences seen in the PDFs may be due to finite Reynolds number. We first re-examine the PDFs with special focus on extreme events, which may have not been reported in the literature before, followed by conditional statistics to help understand the relation between ϵ and Ω. To characterize the extreme fluctuations, dissipation and enstrophy are decomposed into longitudinal, transverse and cross-term gradients and their scaling are studied in regions of high versus low enstrophy and dissipation.

4.2 Scaling of Dissipation and Enstrophy

Here we examine the issue of how the tails of the PDFs of dissipation and enstrophy behave and compare with each other at increasing Reynolds number, given our latest understanding of resolution effects on numerical simulation data as seen in Chapter 3. We present the PDF data and use conditional sampling of velocity gradient contributions to investigate the nature of extreme fluctuations at $O(10^3)$ times the mean which are observed in our highest

Reynolds number datasets but may not have been reported before in the literature.

Many studies in the past (Hosokawa 1991, Meneveau & Sreenivasan 1991, Bershadskii *et al.* 1993) have suggested that the dissipation PDF f_ϵ can be well represented by a stretched exponential fit of the form

$$f_\epsilon(\epsilon') \sim \exp[-b_\epsilon(\epsilon')^{c_\epsilon}] \ , \tag{4.5}$$

where the prefactor b_ϵ and exponent c_ϵ may depend on the Reynolds number. Stronger intermittency at the tails of the PDF may be indicated by either a smaller prefactor or smaller exponent with the other parameter held fixed. A similar functional form can also been proposed (with prefactor b_Ω and exponent c_Ω) for f_Ω, the PDF of enstrophy (Zhou *et al.* 2005a). Table 4.1 shows, for DNS data at different Reynolds numbers and grid resolutions, the parameters which provide the best fits for the range $5 \leq \epsilon', \Omega' \leq 100$, which covers fluctuations large compared to the mean but yet is not greatly contaminated by sampling noise.

Underestimation of PDF tails in simulations at $k_{max}\eta \approx 1.4$ as noted in Chapter 2 is reflected in Table 4.1 by the decrease of the exponents with increasing $k_{max}\eta$ at a given Reynolds number. Although the past literature (Ruetsch & Maxey 1991, Bershadskii *et al.* 1993, Zeff *et al.* 2003) suggested exponents not far from 1/2, data from our high-resolution datasets suggest values close to 1/4 for both energy dissipation and enstrophy. In figure 4.4 we show the PDFs of dissipation and enstrophy from our high-resolution datasets at R_λ 140 and 240 ($k_{max}\eta \approx 5.5$ and 11 respectively). Very good agreement is seen with fits of the form (dashed lines)

$$f_\epsilon(\epsilon') \sim \exp[-{b_\epsilon}'(\epsilon')^{1/4}] \tag{4.6}$$

with the exponent held fixed at 1/4 and Reynolds number dependence expressed solely by the associated prefactor ${b_\epsilon}'$. Values of ${b_\epsilon}'$ and ${b_\Omega}'$ are also shown in Table 4.1 where it is clear that they both decrease with increasing Reynolds number or grid resolution but are

about the same from $k_{max}\eta \approx 3$ onwards. Incidentally, the closeness of fit shown in the figure (using Eq. 4.6) is virtually the same as that obtained using Eq. 4.5 (Table 4.1) for moderately large fluctuations which are typical of measurements reported in the past. We also note that Reynolds number dependence on the ratio between ${b_\epsilon}'$ and ${b_\Omega}'$ is apparently weak, which suggests if the PDFs f_ϵ and f_Ω are to approach each other in this range of values of ϵ' and Ω' with increasing Reynolds number then this approach must be very slow.

In figure 4.5 we compare dissipation and enstrophy PDFs in our datasets at highest Reynolds numbers available ($R_\lambda \approx 390$ and 650). Despite modest resolution at $k_{max}\eta \approx 1.4$ it is clear that the tails stretch very wide, towards ϵ and Ω several thousands times the mean or higher. These extreme tails are not described well by fits of the forms of Eqs. 4.5 and 4.6 with parameters based on more moderate values of ϵ' or Ω'. However, we find that a uniformly good fit for essentially all values of ϵ' can be obtained by using a double stretched-exponential of the form

$$f_\epsilon(\epsilon') \sim s_1 \exp[-t_1(\epsilon')^{1/4}] + s_2 \exp[-t_2(\epsilon')^{1/4}] \tag{4.7}$$

(and similarly for $f_\Omega(\Omega')$). The best fit coefficients corresponding to the dashed lines in Eq. 4.7 for dissipation and enstrophy are shown in Table 4.2. It is apparent from the contrasts between the magnitudes of these parameters the second exponential is significant primarily at the far tails. However, the most remarkable feature in this figure is that the PDFs of ϵ and Ω appear to collapse onto each other at extremely large values of ϵ' and Ω' — of order 1000 or greater, which is a data range of very rare events probably not reported or at least not given much attention in the literature before. Furthermore, this collapse appears to occur in the same way at $R_\lambda \sim 390$ and 650 but is not observed at lower Reynolds numbers. It is clear that further investigation is warranted, since this suggests the possibility of a universal scaling of extreme events — such that high-order moments of energy dissipation and enstrophy could scale similarly although low order moments may

still differ at finite Reynolds numbers.

A question that arises from the observation above is whether those extreme values of ϵ' and Ω' of order 10^3 occur together, i.e., at the same locations in space. It should be noted that two random variables can have the same PDF (i.e. be identically distributed) without being related to each other. However, the correlation between dissipation and enstrophy is known to be positive and increasing with Reynolds number (see e.g. Yeung *et al.* 2007, for data inferable from studies of Langrangian cross-correlation functions). In Table 4.3 we show the correlation coefficient obtained from the present datasets. It is clear that resolution effects are weak but an approach towards an asymptotic value seems possible. Evidently, it is reasonable to expect that likelihood for the largest values of dissipation and enstrophy to be in close proximity to each other increases with Reynolds number. However, the question of whether they coincide can be examined more directly via the conditional distribution of the ratio ϵ'/Ω' (or Ω/ϵ') given the local value of ϵ' or Ω': if events of extreme ϵ' and Ω' are collocated in space then a peak in the conditional PDF close to 1.0 is expected.

In figure 4.6 we show the conditional PDFs of the ratio ϵ'/Ω' in the $R_\lambda \sim 650$ simulation, given a range of values of ϵ' in geometric progression. In general, as ϵ' increases smaller values of ϵ'/Ω' become less likely, and the conditional PDF shifts to the right. However, as ϵ' increases beyond the mean, the probability of large ϵ'/Ω' first reaches a maximum (lines D to G) and then eventually decreases. Furthermore at values of ϵ' considered to be extreme (lines H and I, in inset) the conditional PDF is seen to be forming a peak in the neighborhood of $\epsilon'/\Omega' \approx 1$. This observation indicates that very large values of dissipation are likely to be accompanied by similarly large enstrophy. In other words the local mechanisms that cause extreme dissipation are likely to lead to extreme enstrophy as well.

To test the converse of the scenario suggested above we examine in figure 4.7 the conditional PDF of the ratio ϵ'/Ω' again, now given Ω' instead of ϵ'. At low values of conditioning enstrophy the ratio ϵ'/Ω' tends to be large, as expected. At conditioning enstrophy equal to the mean (line D) the likelihood of small ϵ'/Ω' is almost the same as in the unconditional distribution (dashed line). This implies that events of stronger-than-average dissipation are unlikely to develop in regions of small or average enstrophy. At very large enstrophy (lines H and I) we see that the conditional PDF shifts steadily towards smaller values of ϵ'/Ω'. This means, in contrast to statements made in the preceding paragraph, that intense enstrophy is often not accompanied by intense dissipation. In other words the mechanisms that cause extreme enstrophy either contribute less to dissipation or are subject to partial cancellation by other competing effects.

Additional information can be obtained from the conditional averages of ϵ and Ω given one another, as shown in figure 4.8. At low ϵ or Ω the conditional dependences are seen to be relatively weak. A dashed line of slope 1 is drawn to indicate the limiting condition of large ϵ and Ω being coincident. It can be seen that for $\epsilon > \langle\epsilon\rangle$ the behavior of $\langle\Omega|\epsilon\rangle$ is close to this limit: i.e. large dissipation is most likely accompanied by large enstrophy, as discussed above based on conditional PDFs in figure 4.6. On the other hand, $\langle\epsilon|\Omega\rangle$ falls below the slope 1 line for Ω' between 10 and 1000 which indicates enstrophy values in this range are quite often accompanied by smaller values of the dissipation. However $\langle\epsilon|\Omega\rangle$ appears to approach the slope 1 line again when Ω' reaches higher than 1000, indicating that the most extreme events of high enstrophy may be accompanied by events of extreme dissipation as well. The trends noted are also consistent with the unconditional PDFs shown in figure 4.5, namely that dissipation and enstrophy scale differently for ϵ' and Ω' in the range 10-1000 but possibly the same for extreme fluctuations greater than 1000 times the mean.

Although the discussion above based on single-point statistics indicate that events of

extreme dissipation and enstrophy are, in general, not coincident, a significant overlap in space is still possible (and, in fact, likely). A simple but direct test for such overlaps is to examine the coordinate locations of either ϵ' or Ω' exceeding some threshold (h). Figure 4.9 shows a typical cluster of points above a normalized threshold $h = 800$, in an instantaneous velocity field taken from our 2048^3 R_λ 650 simulation. Points of high ϵ' and high Ω' are indicated by asterisks and open circles respectively, with a color map used to illustrate intensity. A substantial overlap is indicated by the presence of asterisks placed in a circle, especially in the core regions of the cluster shown. Recently Moisy & Jiménez (2004) studied the geometry and spatial distribution of regions of high levels of dissipation and enstrophy in detail. However, the threshold levels they used are much smaller that those presented in this work. This can be explained by the fact that their Reynolds number was smaller ($R_\lambda \approx 168$) at which samples in the range where the PDFs collapse (see figure 4.5) do not exist.

Although the results are difficult to quantify, it is clear that the size of clusters of the type shown here decreases with the threshold level chosen. In practice we can estimate the average volume of the cluster by first identifying a sub-domain that just completely encloses the cluster (as in figure 4.9). A volume (V_h) can be defined by multiplying the number of samples with $\epsilon' > h$ within the sub-domain by the volume of a grid cell (nominally, $(\Delta x)^3$). Without making detailed assumptions (which would require further study) about the topology of each cluster, a rough measure of linear size can be obtained as $\Lambda_\epsilon(h) = V_h^{1/3}$, and similarly Λ_Ω for regions of high enstrophy. Our results suggest power-law dependences of the form $\Lambda_\epsilon \sim h^{-0.54}$ and $\Lambda_\Omega \sim h^{-0.68}$ at threshold levels corresponding to extreme events in the dissipation and enstrophy PDFs. While these relations involve proportionality factors that (as expected) increase with the Reynolds number it is quite remarkable that the exponents deduced from simulations at R_λ 400 and 650 simulations are nearly the same,

thus suggesting a degree of asymptotic universality. Similar results are obtained also for an alternative (and larger) estimate of linear size, as the maximum distance between any two points with $\epsilon' > h$ or $\Omega > h$ within the same cluster, with the best-fit exponents being approximately -0.81 and -0.89.

It is important to note that regions of high ϵ or Ω are (especially in the case of worm or filament-like vortex structures) likely to have at least one linear dimension significantly shorter than the linear-size estimates considered above. For example although at $h = 1000$ in our R_λ 650 simulation Λ_ϵ/η and Λ_Ω/η typically lie in the range 10-50 and can certainly be detected, capturing the shortest linear dimension may be questionable. In other words, a simulation conducted at the "standard" grid resolution ($k_{max}\eta \approx 1.5$) with spacing $\Delta x \approx 2\eta$ is expected to detect certain characteristics of high-intensity clusters satisfactorily but at the same time some of the details will not be fully captured.

4.3 Conditional Sampling of Velocity-Gradient Contributions

To characterize the nature of flow conditions in regions of extremely high dissipation and/or enstrophy it is useful to distinguish between longitudinal velocity gradients, which contribute to the dissipation only, and transverse gradients, which contribute to both. We write

$$\epsilon/\nu = L + T + C \quad ; \qquad \Omega = T - C \tag{4.8}$$

where, with the usual summation convention suppressed,

$$L = 2\sum_{i=1,3} u_{i,i}^2 \quad , \qquad T = \sum_{i,j=1,3}^{i\neq j} u_{i,j}^2 \quad , \quad \text{and} \quad C = \sum_{i,j=1,3}^{i\neq j} u_{i,j}u_{j,i} \ . \tag{4.9}$$

with the term C representing cross-terms among different transverse components. It is well known (e.g. Dhruva *et al.* 1997, Gotoh *et al.* 2002, Zhou *et al.* 2005b) that the PDF of transverse gradients (hence T and C) presents wider tails than for longitudinal gradients (L). While L and T are by definition always positive, the sign of C carries useful information

on the local kinematics. A positive value of C contributes to higher dissipation via the off-diagonal strain rates, whereas a negative value contributes to enstrophy via the difference between off-diagonal velocity gradients. This suggests the conditional average of C should be positive in strain-dominated regions of high dissipation but negative in rotation-dominated regions of high enstrophy, and small if high values of ϵ and Ω occur simultaneously.

For incompressible isotropic turbulence with $\langle\epsilon\rangle = \nu\langle\Omega\rangle$ it is readily shown that

$$\langle L\rangle = (2/5)\langle\epsilon\rangle/\nu \tag{4.10}$$

while the other two contributions can be written as

$$\langle T\rangle = 2\langle L\rangle; \quad \langle C\rangle = -\langle L\rangle/2 \ . \tag{4.11}$$

These relations suggest that two possible scenarios in which extreme events of dissipation and enstrophy would scale similarly are (i) for Eqs. 4.10 and 4.11 to hold locally for the largest fluctuations, or (ii) squares of transverse gradients to dominate overwhelmingly, i.e. $T \gg (L, |C|)$. Conditional statistics presented below give support to scenario (i) but not (ii).

Basic results including a resolution check on the averages of L, T and $-C$ conditioned upon the local dissipation rate are given in figure 4.10, using data from simulations at $R_\lambda \approx 240$ with three different values of the resolution parameter $k_{max}\eta$. Since $\langle C|\epsilon\rangle$ is found to be negative for all ϵ we have plotted $\langle -C|\epsilon\rangle$ instead. The data have been checked to satisfy the requirement (from Eq. 4.9) that $\langle L|\epsilon\rangle + \langle T|\epsilon\rangle + \langle C|\epsilon\rangle = \epsilon/\nu$ which however may not (because of the use of logarithmic scales) be obvious from the figure. Except for better capture of samples at large ϵ the effect of grid resolution on these quantities is apparently weak (which is true for many conditional statistics in general, e.g. Yeung *et al.* 2006). A dashed line of slope 1 on logarithmic scales shows that the conditional average of longitudinal gradients scales in almost the same way as in the unconditional result of

Eq. 4.10, i.e.

$$\langle L|\epsilon\rangle = \frac{2}{5}\epsilon/\nu \tag{4.12}$$

for all values of ϵ. In Appendix A we provide a derivation which gives theoretical support to this result. The other terms $\langle T|\epsilon\rangle$ and $\langle C|\epsilon\rangle$ follow a similar scaling with different coefficients for ϵ' about 4 or higher but approaches a constant in the limit of low ϵ. More detailed results show that samples of C in regions of low ϵ are exclusively negative and contribute to a strong (yet incomplete) cancellation in $T + C$. Such a cancellation, which corresponds to small off-diagonal strain rates and may be accompanied by high local enstrophy, has a kinematic origin, which can be seen by writing ϵ as $2\nu s_{ij}s_{ij}$ and noting that as ϵ tends to zero so must each square term in this definition. For example, $s_{12}^2 = (u_{1,2}^2 + u_{2,1}^2 + 2u_{1,2}u_{2,1}) \to 0$ when $\epsilon \to 0$ which implies, after taking conditional averages and adding different components, that $\langle T|\epsilon'\rangle \to -\langle C|\epsilon'\rangle$ as $\epsilon' \to 0$.

Figure 4.11 shows corresponding data on the conditional averages from our highest Reynolds number simulation (R_λ 650). Although many of the features are broadly similar to those at lower Reynolds number (see preceding figure) there are significant differences in the behavior of $\langle -C|\epsilon'\rangle$ from about $\epsilon = 100\langle\epsilon\rangle$ onwards, and in the comparison among L, T and C in the limit of extreme dissipation. To understand this, we note that as $\epsilon/\langle\epsilon\rangle$ increases from small to moderately large and ultimately extreme values the conditional distribution of C changes from having negative samples only to having a small number of positive samples, and ultimately a wide range of both positive and negative samples with the conditional mean remaining negative. The "kink" seen in $\langle -C|\epsilon\rangle$ at $\epsilon/\langle\epsilon\rangle$ around 300 is a result of partial cancellation between positive and negative samples which also leads to increased sampling noise persisting to very large dissipation. However, despite these uncertainties it can be seen that the ratio of $T : L : C$ becomes closer to the isotropic value of $2 : 1 : -1/2$ from $\epsilon/\langle\epsilon\rangle \approx 10^3$ and upwards. This suggests that motions contributing to

events of extreme dissipation are, within sampling uncertainty, close to isotropic in their statistical properties.

For the nature of contributions from L, T and C in regions of low versus high enstrophy we show conditional averages given enstrophy in figure 4.12. Since by definition $\Omega = T - C$ it is not surprising that $\langle C|\Omega\rangle$ is positive at low Ω (solid line with circles) and negative at high Ω (dashed line). In the limit of very low Ω we observe $T \approx C$ (which can again be explained by kinematics as $\Omega \to 0$) while L (which contributes only to ϵ) is nearly constant. In a narrow range of Ω' around unity the ratio between $\langle T|\Omega\rangle$ and $-\langle C|\Omega\rangle$ is close to 4 as suggested by Eq. 4.11. Larger values of Ω' up to about 400 are seen to be the result of C approaching $-T$ as the magnitudes of both terms increase. Remarkably, however, as Ω' approaches values of 1000 or higher the ratio between $\langle T|\Omega\rangle$ and $-\langle C|\Omega\rangle$ becomes close to 4 again. In other words, these results suggest that the local flow structure is close to statistically isotropic in regions of extreme enstrophy, as it is for extreme dissipation as noted above.

Finally, in figure 4.13(a,b,c) we compare directly the conditional averages of L, T and C given dissipation, and given the enstrophy, replotted from Figures 4.11 and 4.12. Conditioning on ϵ and Ω yields almost the same results, which is not surprising since T appears in the same form in both $\epsilon = L + T + C$ and $\Omega = T - C$. For both L and C it is clear that averages conditioned on ϵ and on Ω are quite different in form, with agreement around $\epsilon' \approx 1$ and then again for ϵ from about 1000 and upwards. For regions of above-average ϵ or Ω the greatest discrepancy between averages conditioned on ϵ versus those conditioned on Ω is observed for ϵ and $\Omega \sim$ around 200, which is consistent with observations noted in figures 4.5, 4.11 and 4.12.

4.4 Summary

A common indicator of intermittency in dissipation and enstrophy is in the wide tails in their probability density functions (PDFs), which are well represented by stretched-exponential fits in the range of values up to 100 times the mean. However data at the two highest Reynolds numbers available ($R_\lambda \approx 390$ and 650) reveal extreme fluctuations as large as several thousands times the mean. We find that the PDF tails can be described as the sum of two exponentials which dominate respectively in regions of moderate or high dissipation and enstrophy. At extreme values of ϵ' and Ω' the PDFs appear to coincide within statistical error, suggesting the possibility of a universal behavior of extreme fluctuations although low order statistics may still differ. Results from conditional averaging indicate that large dissipation is often accompanied by large enstrophy but intense enstrophy is not usually accompanied by intense dissipation. However, in the range of "extreme" fluctuations noted above very large dissipation and enstrophy appear to possess a significant degree of overlap. The dimensions of clusters of points with dissipation or enstrophy above a certain threshold suggest that they can be detected readily even with $k_{max}\eta$ only about 1.5, although some of the details will not be fully captured. The nature of the extreme fluctuations is studied further by decomposing (Eq. 4.9) both dissipation and enstrophy into longitudinal (L), transverse (T), and cross terms (C). In general C is positive in strain-dominated regions, negative in rotation-dominated regions, and small compared to L and T if large dissipation and enstrophy occur simultaneously. In regions of extreme dissipation (more than 1000 times the mean) the ratio L:T:C is found to approach the value 2:1:-1/2 which is consistent with a state of local isotropy.

Table 4.1: Best fit coefficients for Eqs. 4.5 and 4.6 for the range $5 < \epsilon', \Omega' < 100$.

R_λ	$k_{max}\eta$	b_Ω	b_ϵ	c_Ω	c_ϵ	${b_\Omega}'$	${b_\epsilon}'$	${b_\Omega}'/{b_\epsilon}'$
140	1.4	5.23	6.04	0.29	0.33	7.11	10.54	0.67
140	2.8	7.04	8.27	0.24	0.25	6.42	8.51	0.75
140	5.7	6.46	9.54	0.25	0.23	6.54	8.51	0.77
140	11.1	7.25	8.79	0.23	0.25	6.44	8.57	0.75
240	1.4	6.96	6.75	0.23	0.28	6.14	8.41	0.73
240	2.8	7.40	8.55	0.22	0.24	6.07	7.92	0.77
240	5.4	6.78	8.62	0.24	0.24	6.12	7.91	0.77
390	1.4	8.30	8.58	0.20	0.23	5.59	7.22	0.77
650	1.3	8.53	8.04	0.19	0.23	5.34	6.73	0.79

Table 4.2: Best fit coefficients for Eq. 4.7 for data at $R_\lambda \approx 390$ and 650 for ϵ', $\Omega' \geq 5$.

R_λ	$k_{max}\eta$	variable	s_1	t_1	s_2	t_2
390	1.4	ϵ'	27.7	5.40	4.05×10^{-6}	2.09
390	1.4	Ω'	466.1	7.21	8.19×10^{-6}	2.28
650	1.3	ϵ'	14.2	5.03	1.04×10^{-6}	1.84
650	1.3	Ω'	177.5	6.59	0.79×10^{-6}	1.85

Table 4.3: Correlation coefficient between dissipation and enstrophy.

R_λ	$k_{max}\eta$	$\rho(\epsilon, \Omega)$
140	1.4	0.50
140	2.8	0.51
140	5.8	0.51
140	11.1	0.51
240	1.4	0.52
240	2.8	0.53
240	5.4	0.53
390	1.4	0.54
650	1.3	0.55

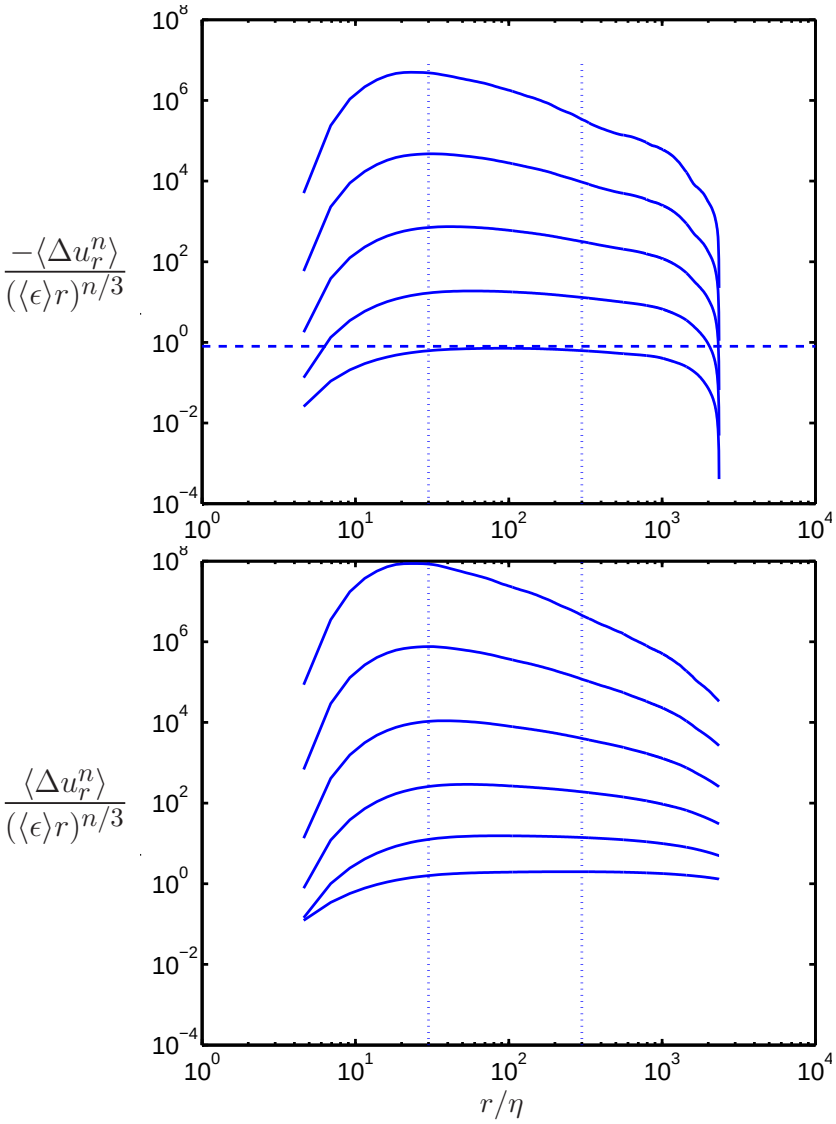

Figure 4.1: Structure functions at $R_\lambda \approx 650$ normalized according to K41 (Eq. 4.2). The inertial range is taken between vertical dotted lines. Top: Odd order. From bottom to top $n = 3$ to 11. Exact result for $n = 3$ in the inertial range is shown as an horizontal dashed line. Bottom: Even order. From bottom to top $n = 2$ to 12.

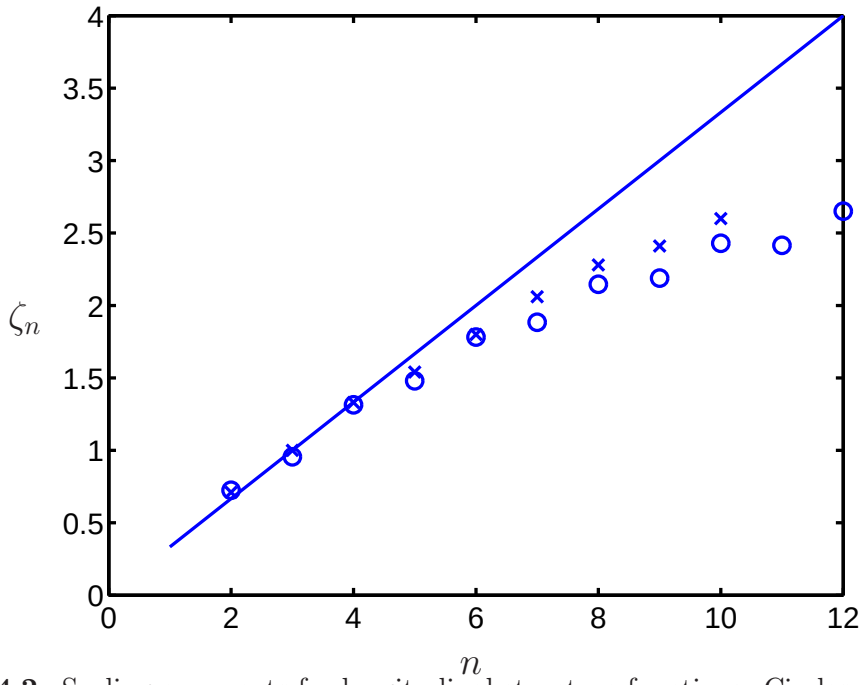

Figure 4.2: Scaling exponents for longitudinal structure functions. Circles: DNS at $R_\lambda \approx 650$ (2048^3). Crosses: Jet at $R_\lambda = 536$ from Anselmet *et al.* (1984). Solid line: $\zeta_n = n/3$ according to K41.

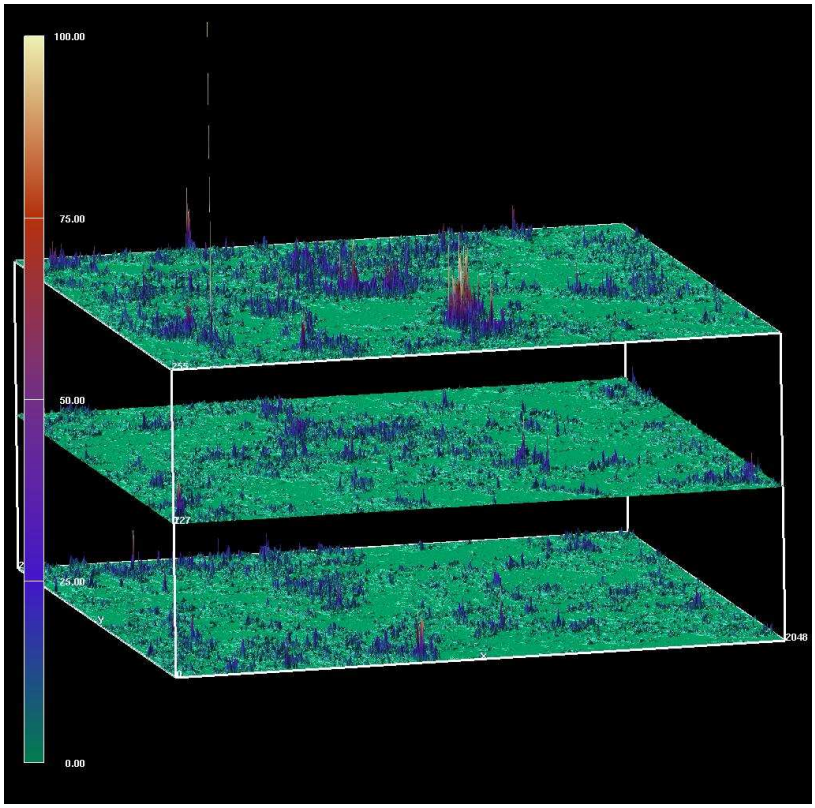

Figure 4.3: Spatial distribution of energy dissipation rate shown as elevated surfaces for $R_\lambda \approx 650$ (2048^3). Courtesy of Cristina Siegerist of NERSC.

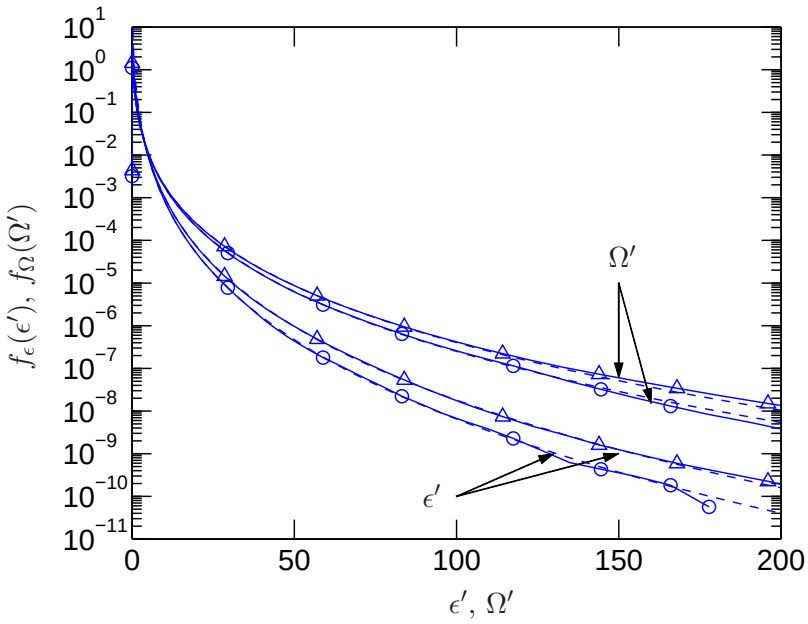

Figure 4.4: PDFs of $\epsilon' \equiv \epsilon/\langle\epsilon\rangle$ and $\Omega' \equiv \Omega/\langle\Omega\rangle$ at $R_\lambda \approx 140$ with $k_{max}\eta \approx 11$ (◯) and $R_\lambda \approx 240$ with $k_{max}\eta \approx 5.5$ (△). Dashed lines represent stretched-exponential fits of the form in Eq. 4.6 which almost coincide with the DNS data.

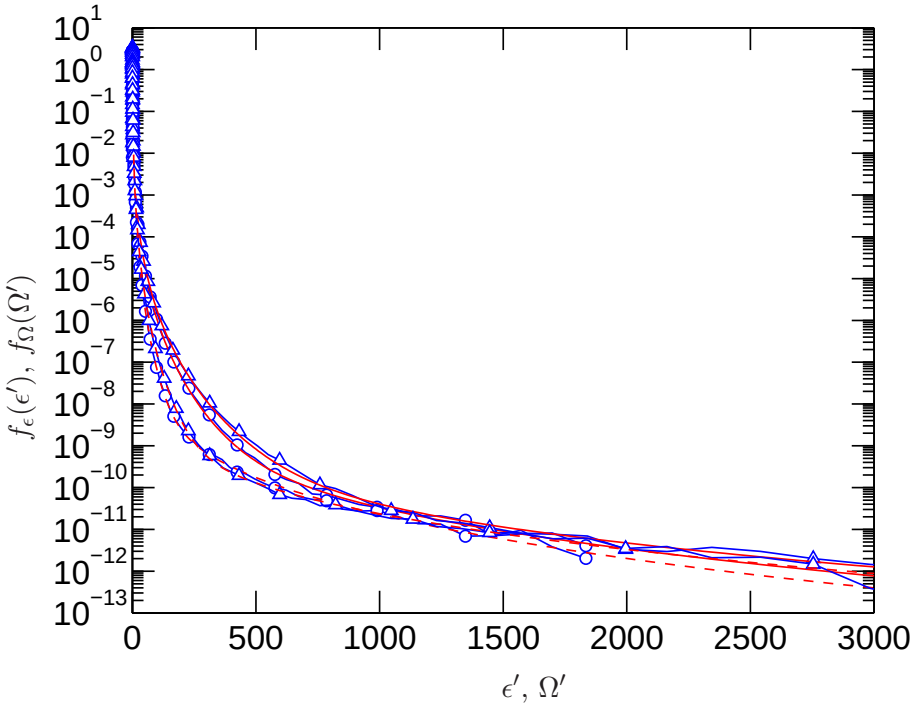

Figure 4.5: PDF of dissipation (lower curves) and enstrophy (upper curves) from simulations at the highest two Reynolds numbers: $R_\lambda \approx 390$ at 1024^3 (◯) and $R_\lambda \approx 650$ at 2048^3 (△), both with $k_{max}\eta \approx 1.4$. Dashed and solid lines represent fits according to Eq. 4.7 for dissipation and enstrophy respectively.

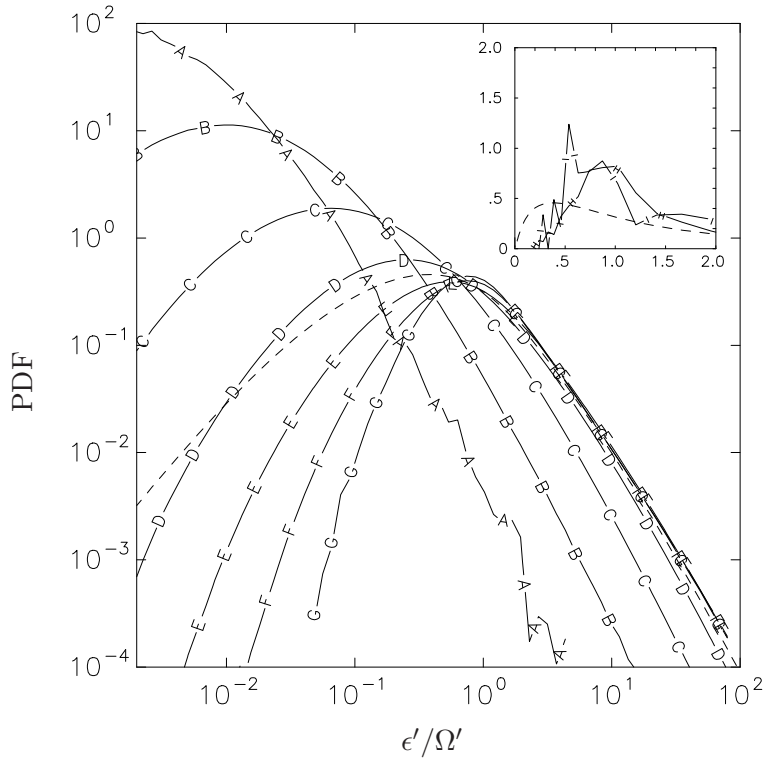

Figure 4.6: Conditional PDF of the ratio ϵ'/Ω' given ϵ' in the $R_\lambda \approx 650$ simulation. Lines A-I correspond to $\epsilon' = 2^n$ with $n = -12, -9, -6, -3, 0, 3, 6, 9, 12$ (note lines H and I are in inset and plotted in different scales). Dashed lines correspond to the unconditional PDF.

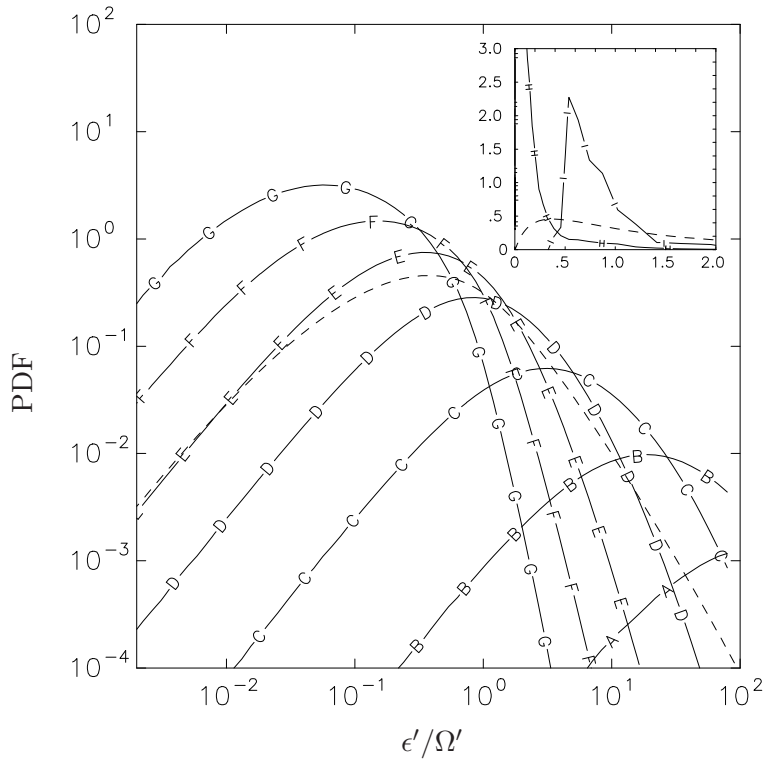

Figure 4.7: Same as figure 4.6, but conditioned on Ω'.

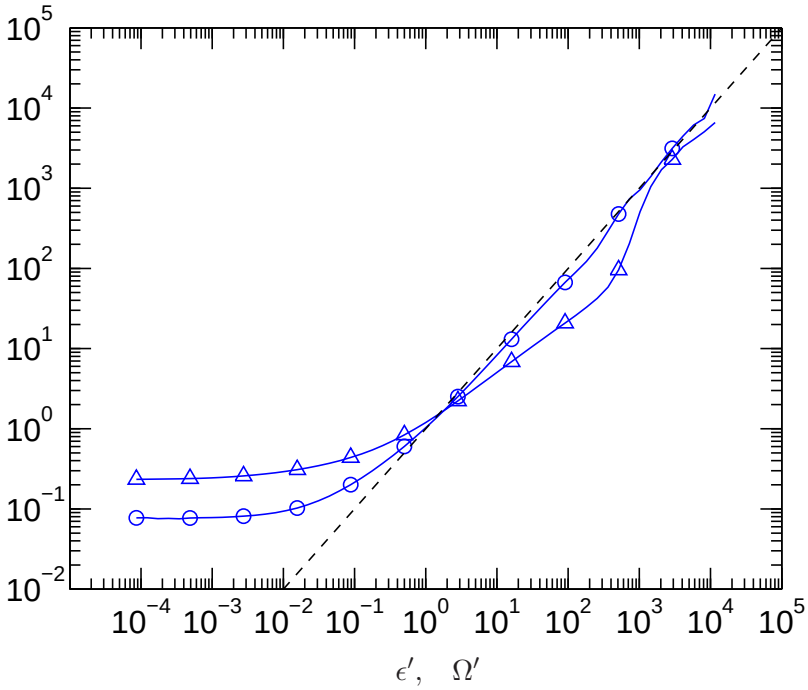

Figure 4.8: Conditional means $\langle \epsilon' | \Omega' \rangle$ (◯) and $\langle \Omega' | \epsilon' \rangle$ (△) at $R_\lambda \approx 650$ with $k_{max}\eta \approx 1.4$. A dashed line at slope 1.0 is included for comparison.

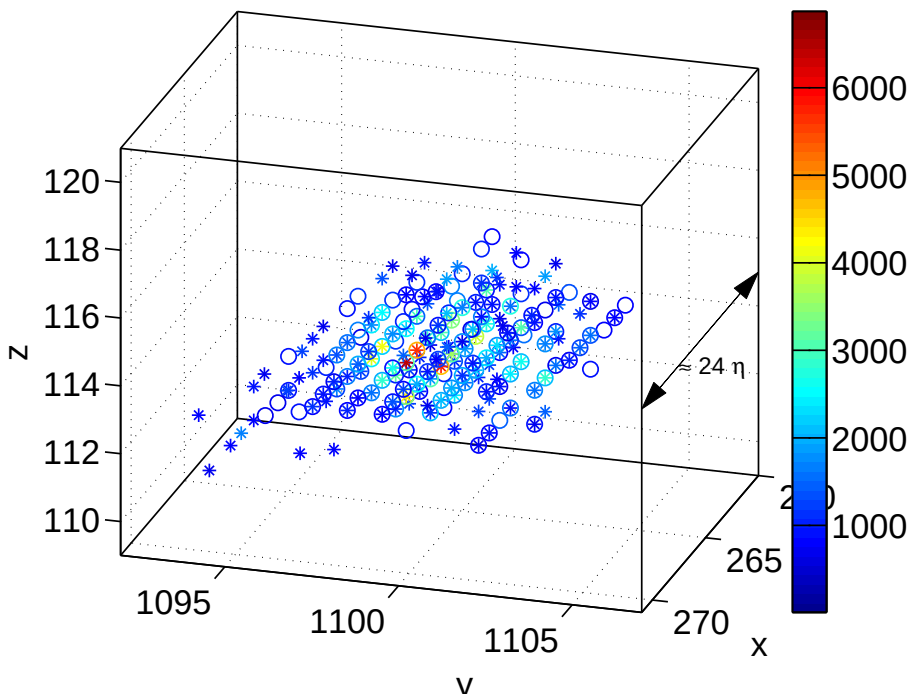

Figure 4.9: Sample of cluster of grid points with $\epsilon' > 800$ (circles) and $\Omega' > 800$ (crosses) at $R_\lambda \approx 650$ with $k_{max}\eta \approx 1.4$. Colors indicate intensity of ϵ' and Ω'.

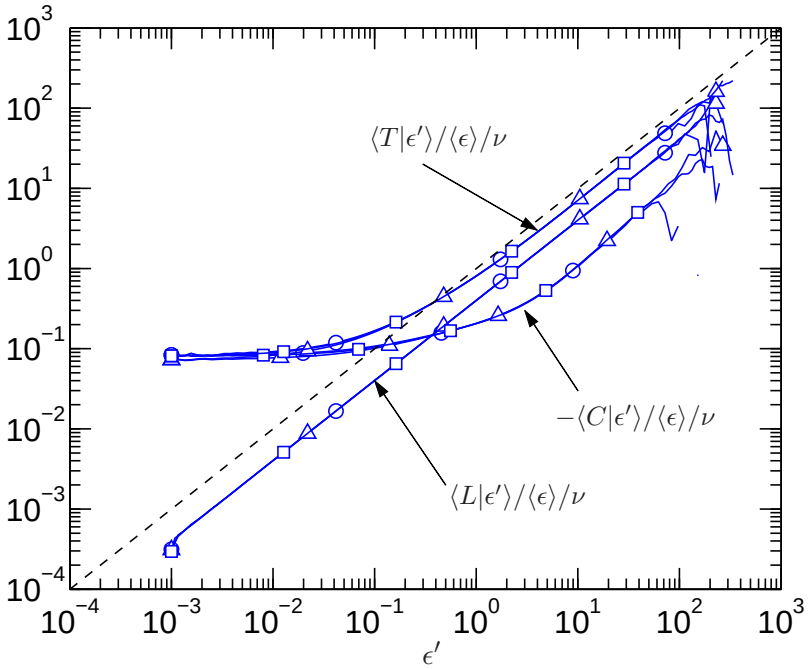

Figure 4.10: Conditional averages $\langle L|\epsilon'\rangle$, $\langle T|\epsilon'\rangle$ and $-\langle C|\epsilon'\rangle$, all normalized by $\langle\epsilon\rangle/\nu$, from simulations at at $R_\lambda \approx 240$ and different degrees of resolution: $k_{max}\eta \approx 1.4$ (◯), 2.8 (△) and 5.5 (□). A dashed line at slope 1.0 is included for comparison.

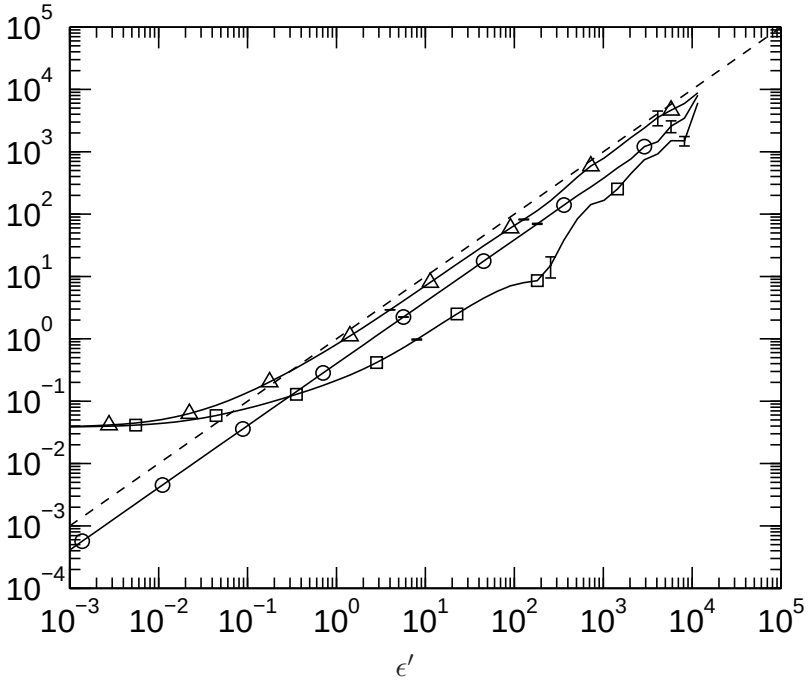

Figure 4.11: Conditional averages $\langle L|\epsilon'\rangle/\langle\epsilon\rangle/\nu$ (◯), $\langle T|\epsilon'\rangle/\langle\epsilon\rangle/\nu$ (△) and $-\langle C|\epsilon'\rangle/\langle\epsilon\rangle/\nu$. (□) at $R_\lambda \approx 650$ with $k_{max}\eta \approx 1.3$. Dashed line has slope 1.0.

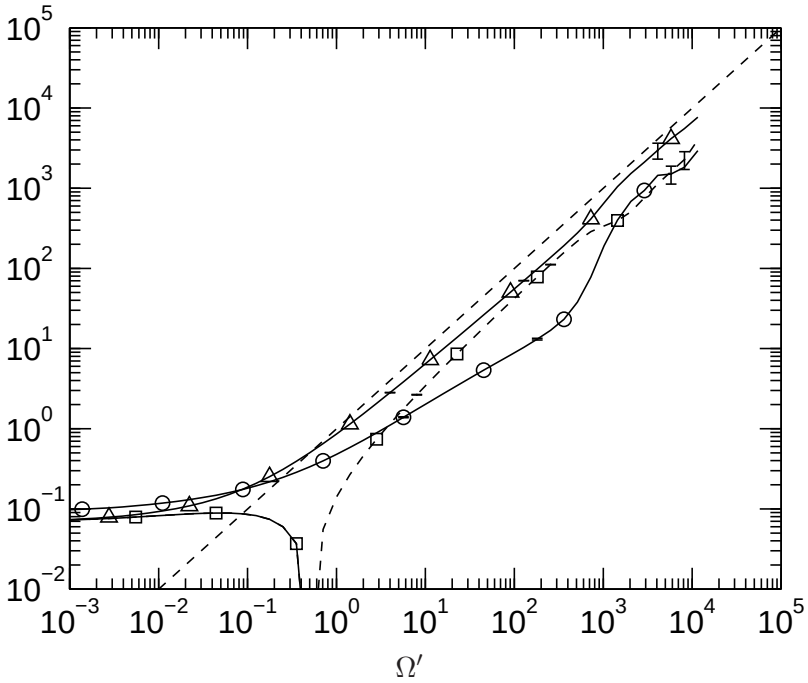

Figure 4.12: Same as figure 4.11 but conditioned on normalized enstrophy instead of dissipation.

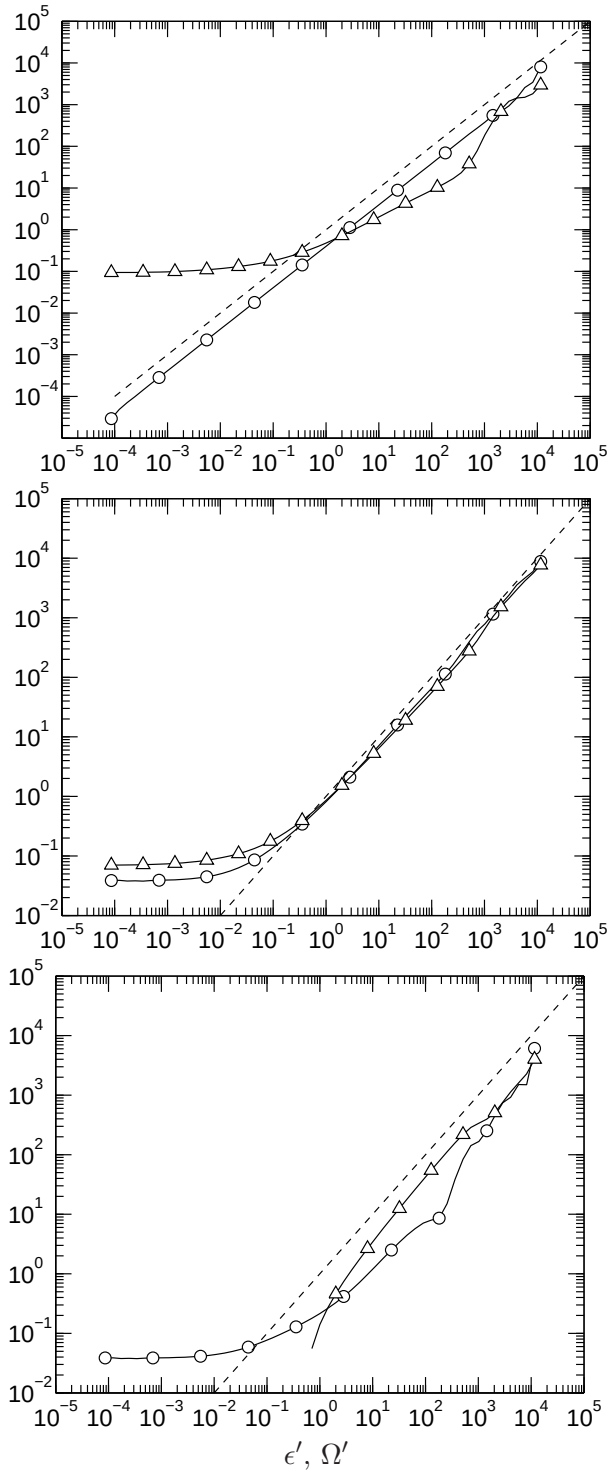

Figure 4.13: Conditional averages at $R_\lambda \approx 650$ with $k_{max}\eta \approx 1.4$. From top to bottom: (a) $\langle L|\epsilon'\rangle/\langle\epsilon\rangle/\nu$ (◯) and $\langle L|\Omega'\rangle/\langle\Omega\rangle$ (△); (b) $\langle T|\epsilon'\rangle/\langle\epsilon\rangle/\nu$ (◯) and $\langle T|\Omega'\rangle/\langle\Omega\rangle$ (△); and (c) $-\langle C|\epsilon'\rangle/\langle\epsilon\rangle/\nu$ (◯) and $-\langle C|\Omega'\rangle/\langle\Omega\rangle$ (△). Dashed lines of slope 1.0 are included for comparison.

CHAPTER V

PASSIVE SCALARS

In this chapter we study the scaling of turbulent mixing of passive scalars. In addition to Eqs. 2.1 and 2.2, we solve for the scalar fluctuations in the presence of an imposed mean gradient (e.g. Pumir 1994, Overholt & Pope 1996, Brethouwer *et al.* 2003) according to the advection-diffusion equation

$$\frac{\partial \phi}{\partial t} + \mathbf{u}\cdot\nabla\phi = -\mathbf{u}\cdot\nabla\Phi + D\nabla^2\phi, \tag{5.1}$$

where $\nabla\Phi$ is the mean scalar gradient. The numerical scheme is the same as described in Chapter 2. A spatially uniform $\nabla\Phi$ allows the scalar fluctuations to remain homogeneous and attain a statistically stationary state. This is made possible because of the destruction of scalar variance by the molecular dissipation is balanced by production through the action of velocity fluctuations on the mean gradient. Because Eq. 5.1 is linear, the magnitude of $\nabla\Phi$ has no effect on normalized statistics of the scalar field.

The important non-dimensional parameter for a scalar is the Schmidt number $Sc = \nu/D$ where D is the molecular diffusivity. For $Sc \leq 1$ the smallest scale is given by the Obokhov-Corrsin scale $\eta_{OC} = \eta Sc^{-3/4}$ (Obukhov 1949, Corrsin 1951) and for $Sc \gg 1$ it is the Batchelor scale $\eta_B = \eta Sc^{-1/2}$ (Batchelor 1959). For $Sc > 1$ less is known because more resolution is needed to resolve up to η_B in both experiments and simulations. In our simulations we resolve the scalars up to $k_{max}\eta_B$ at least 1.5.

The rest of the Chapter is organized as follows. In the next Section we investigate the scaling of the scalar spectrum with Reynolds and Schmidt number. We compare our results with the theoretical predictions of Batchelor (1959) and Kraichnan (1968). In Section

5.2 we examine the assumption that the mean scalar dissipation rate is independent of molecular properties of the fluid and the scalar (i.e. ν and D). For this purpose we use data from simulations and experiments and find theoretical limits in terms of R_λ and Sc at which the mean scalar dissipation rate achieve an asymptotic state. In Section 5.3, we study the scaling of intermittency for passive scalars with emphasis in Schmidt number effects. Small-scale intermittency is characterized through the tail of the PDF of the scalar dissipation, whereas inertial-convective intermittency is studied using scaling exponents of three-dimensional local averages. Departures from local isotropy are investigated as both R_λ and Sc vary through statistics of scalar gradient fluctuations parallel and perpendicular to the imposed mean scalar gradient. We conclude the Chapter with a summary of the findings, further analysis of the results and issues yet to be resolved.

5.1 Scalar Spectrum

The same ideas behind K41 has been extended to passive scalars with $Sc \leq 1$ independently by Obukhov (1949) and Corrsin (1951). Following Kolmogorov (1941a) they suggested there is a range of scales much smaller than L but larger than diffusive scales for the scalars (i.e. $1/L \ll k \ll 1/\eta_{OC}$) in which the dynamics are determined by the transfer rate of energy and scalar through a cascade process—the *inertial-convective range*. One of the consequences in this range is a scalar spectrum of the form

$$E_\phi(k) = C_{OC}\langle\chi\rangle\langle\epsilon\rangle^{-1/3}k^{-5/3} \tag{5.2}$$

where $\langle\chi\rangle = 2D\langle\nabla\phi\cdot\nabla\phi\rangle$ is the mean scalar dissipation rate. The existence of an inertial-convective range requires high R_λ although as suggested by experiments and simulation this condition seems to be weaker for scalars than for the velocity field (Sreenivasan 1996). Our recent simulations at $R_\lambda \approx 650$ (Yeung *et al.* 2005) show clear inertial-convective scaling for $Sc = 1/8$ and 1 as seen in figure 5.1. The value of C_{OC} is represented by the

height of the plateau at intermediate scales. Sreenivasan (1996) surveyed the available data on the Obukhov-Corrsin constant and obtained a mean value of 0.4 from one-dimensional spectra from experiments. Using isotropic relations one obtains $C_{OC} = 0.67$ for the three-dimensional scalar spectrum which is shown in the figure as a dashed line. As can be seen there is excellent agreement with experiments which supports the universality of the constant. For $Sc = 1$ we also see a bump which is a consequence of viscous effects and may also be regarded as a precursor for a k^{-1} Batchelor scaling (Yeung *et al.* 2002).

Batchelor (1959) studied scalars with $Sc \gg 1$ and argued that for scales much smaller than η, the scalar fluctuations are driven by the strain rate $\gamma \approx (\langle\epsilon\rangle/\nu)^{1/2}$ which varies slowly at these scales. Therefore, for $Sc \gg 1$ there is a range of scales $1/\eta \ll k \ll 1/\eta_B$, —the viscous-convective range— where diffusivity is not important and the only relevant parameters are γ, k and $\langle\chi\rangle$. Dimensional arguments then yield

$$E_\phi(k) = C_B\langle\chi\rangle(\nu/\langle\epsilon\rangle)^{1/2}k^{-1}. \tag{5.3}$$

If R_λ is also large there is a $k^{-5/3}$ inertial-convective range for scales $1/L \ll k \ll \eta$. Batchelor (1959) also showed that for $Sc \gg 1$, high-wavenumbers scalar modes ($k > 1/\eta$) tend to align to the compressive axis of the rate of strain tensor and are compressed to scales of the order η_B where the thinning is balanced by diffusion effects. This compression occurs at a time scale $\sim \ln(D/\nu)^{1/2}/\gamma$. The final expression for the spectrum is

$$E_\phi(k) = C_B\langle\chi\rangle(\nu/\langle\epsilon\rangle)^{1/2}k^{-1}\exp[-C_B(k\eta_B)^2]. \tag{5.4}$$

Kraichnan (1968) modified Batchelor's theory to take into account fluctuations in space and time of the strain rate γ. The result of this analysis yields a spectrum of the form

$$E_\phi(k) = C_B\langle\chi\rangle(\nu/\langle\epsilon\rangle)^{1/2}k^{-1}(1 + (6C_B)^{1/2}k\eta_B)\exp[-(6C_B)^{1/2}(k\eta_B)]. \tag{5.5}$$

It is clear that both Eq. 5.4 and 5.5 predict a k^{-1} scaling (Eq. 5.3) in the viscous-convective range ($1/\eta \ll k \ll 1/\eta_B$). The DNS from Bogucki *et al.* (1997) at R_λ up to 77, show that

Kraichnan's prediction is more accurate than Batchelor's although the highest Schmidt number in their simulation was moderate ($Sc = 7$). We have performed simulations at very high Sc (of order 1000) but low R_λ (≈ 8) to investigate further viscous-convective scaling (Yeung *et al.* 2004). Because Batchelor scale is much smaller than Kolmogorov scale, high Schmidt numbers are only attainable at the expense of low Reynolds numbers if one is to resolve down to the smallest scales for the scalars. As shown in figure 5.2 we find that there is a trend toward k^{-1} scaling with Sc. However, some concerns are present at $R_\lambda \approx 8$ because the range of scales where the energy cascade proceeds (through non-linear interactions) is too narrow. Forcing applied at low wavenumbers can in fact affect dissipative scales and the strain at scales smaller than η may not be accurately estimated by the high-Reynolds number Kolmogorov prediction $\gamma \sim (\langle\epsilon\rangle/\nu)^{1/2}$ as assumed by Batchelor. Even at $R_\lambda \approx 38$, the velocity field may not be considered completely developed for some purposes as it does not exhibit an inertial range. This is shown in figure 5.3 where velocity spectra at $R_\lambda \approx 8$, 38, 140 and 650 are presented. It is only at $R_\lambda \approx 140$ that an inertial range is attained (Yeung & Zhou 1997) and a wider separation of scales achieved.

We recently performed simulations of high-Sc mixing at $R_\lambda \approx 140$ and $Sc = 4$ and 64 on a 2048^3 grid at $k_{max}\eta_B \approx 5.5$ and 1.4 respectively. . The un-normalized scalar spectra are presented in figure 5.4 along with data for $Sc = 1/8$ and 1 at 256^3. Consistent with results at lower R_λ (see figure 5.2) the increase in high-wavenumber content with Sc appears to support a trend towards k^{-1} scaling at intermediate scales.

In figure 5.5 we show data normalized according to Eq. 5.3 for a wide range of Reynolds numbers (8 to 650) and Schmidt numbers (1/8 to 1024). It is interesting to note the degree of universality at small scales ($k\eta_B \gtrsim 0.1$) which includes both low and high Schmidt numbers. It has been suggested that other mechanisms (involving the strain rate γ used by Batchelor 1959) are important in the mixing of scalars (Gibson 1968, Gibson *et al.* 1988).

A consequence of this theory is the implication of a universal scaling (i.e. for any Sc) in the viscous-diffusive range. Similar results has been reported by Bogucki *et al.* (1997) and Antonia & Orlandi (2003) although the for narrower ranges for R_λ and Sc. For high-Sc scalars a k^{-1} scaling is best observed at $R_\lambda \approx 140$ (lines G and H) with about one decade of scaling range. Scalars with low Schmidt numbers (1/8 and 1) at $R_\lambda \approx 650$ (lines C and D), show also an inertial-convective range (already seen in figure 5.1) given by $k^{-2/3}$ under the present normalization.

In figure 5.5 we also include the predictions in Eq. 5.4 and Eq. 5.5 with $C_B = 5.0$ to fit the DNS data. We note that this value is consistent with $C_B = 2\sqrt{5}$ by Qian (1995) and the results based on structure function in Borgas *et al.* (2004). It is clear that Batchelor's spectrum underpredicts the spectral content at high wavenumbers ($k\eta_B \gtrsim 1$) and that Eq. 5.5 gives a better approximation even for scalars with $Sc \lesssim 1$. A careful examination of the spectra presented in figure 5.5, suggests an increase in high-wavenumber content with Reynolds number especially for $Sc \lesssim 1$ (see e.g. lines A and C). This effect, however, could be incorporated in Kraichnan's model with C_B being a (weak) decreasing function of R_λ. The variation of the C_B with both R_λ and Sc was also observed in Yeung *et al.* (2002, 2004).

A basic premise in the phenomenology of turbulence, including the spectral results analyzed above, is that the mean dissipation is independent of molecular processes (see e.g. Sreenivasan & Antonia 1997, Sreenivasan 1998). In the case of the velocity field, the mean energy dissipation rate should be independent of viscosity in the high-Reynolds number limit. In the case of a passive scalar, the mean scalar dissipation rate should not depend on either the viscosity of the fluid or the diffusivity of the scalar as long as both are sufficiently small. Since the results in this Section rely on this assumption, the next subsection is devoted to the scaling of the mean scalar dissipation rate with R_λ and Sc.

5.2 Dissipative Anomaly

After some fifty years of accumulated work (e.g. Batchelor 1953, Sreenivasan 1984, 1995, 1998, Zocchi *et al.* 1994, Kaneda *et al.* 2003) it has now become empirically clear that the mean dissipation rate of turbulent energy away from the walls, $\langle\epsilon\rangle \equiv \frac{\nu}{2}\left\langle \left(\frac{\partial u_j}{\partial u_i} + \frac{\partial u_i}{\partial u_j}\right)^2 \right\rangle$, is independent of the fluid viscosity, ν, as long as ν is small, or a suitably defined Reynolds number is large. This property of turbulence (Taylor 1938, Kolmogorov 1941a), known as the dissipative anomaly, has the consequence that the normalized energy dissipation, i.e., the function $f \equiv \langle\epsilon\rangle L/u'^3$, where L and u' are some viscosity-independent length and velocity scales respectively, approaches an asymptotic constant in the limit of high Reynolds numbers. This behavior of f is consistent with rigorous bounds for $\langle\epsilon\rangle$ deduced from the Navier-Stokes equations (Constantin 1994). In particular, a functional form motivated by the results of Doering & Foias (2002), namely

$$f \equiv \frac{\langle\epsilon\rangle L}{u'^3} = A(1 + \sqrt{1 + (B/R_\lambda)^2}), \tag{5.6}$$

where $u'^2 \equiv \langle u^2\rangle$, is found to provide, as seen in figure 5.6, a good fit for the Reynolds number dependence of f. Here, L is the longitudinal integral length scale evaluated from the energy spectrum function $E(k)$ in wavenumber space as

$$L = \frac{\pi}{2u'^2}\int_0^\infty \frac{E(k)}{k}dk \ . \tag{5.7}$$

With this choice, the fit in figure 5.6 gives $A \approx 0.2$ and $B \approx 92$, yielding an asymptotic value of 0.4 for f.

While the behavior shown in figure 5.6 is universal for all turbulent flows away from the solid wall (see Sreenivasan 1995), it must be stressed that the coefficients A and B are not universal, even if ones fixes the operational definitions of L and u'. They depend on the type of flow, and, for a given flow, on detailed initial conditions—for example the geometry of the grids in grid-generated turbulence and the nature of large-scale forcing in simulations.

Similar issues can be explored for $\langle\chi\rangle \equiv 2D\left\langle \left(\frac{\partial\phi}{\partial x_i}\right)^2 \right\rangle$, which is the mean "dissipation" rate of the scalar variance $\langle\phi^2\rangle$, ϕ being the fluctuating scalar and D its diffusion coefficient. Specifically: (a) what is the "asymptotic" nature of $\langle\chi\rangle$ when ν and D are both small? (b) What is the analogue of equation (1.1) for $\langle\chi\rangle$ as a function of R_λ and the Schmidt number Sc ($\equiv \nu/D$)? Answering these questions is the goal of this Section. Aside from their intrinsic interest, the findings are of practical value for reacting flows in which the products in the fast-chemistry limit bear a direct proportion to χ (see, e.g., Bilger 2004, Sreenivasan 2004).

The questions outlined above are not entirely new, but the available data are scattered in the literature and the effect of Schmidt number, especially for $Sc \gg 1$, has received less attention than warranted. Monin & Yaglom (1975) discussed (a) above, while both (a) and (b) were addressed by Sreenivasan & Yeung (2000) at an earlier conference. A short paper addressing some of these same issues (Xu *et al.* 2000) has also appeared. We believe, however, that this work is the first comprehensive evaluation of the questions mentioned above, besides incorporating new data from direct numerical simulations and presenting related correlations. We provide a brief overview of numerical and experimental datasets from various sources used in our discussion. Next, we present results and theoretical considerations, which lead us to infer the circumstances under which the scalar dissipation becomes independent of molecular properties, for $Sc < 1$ and $Sc > 1$.

5.2.1 The Data

As described in Chapter 1, we have accumulated a significant DNS database from simulations previously performed in which the Reynolds and Schmidt numbers were varied independently. Table 5.1 lists the data from Yeung *et al.* (2004, 2002) and Yeung & Sawford (2002). We have also included data from a 1024^3 resolution. In this Section, we use data at R_λ from about 8 to about 390 while keeping Sc fixed at unity; similarly, we varied Sc from 1/4 to 1024 for R_λ fixed at 8 as well as 38. These parameter combinations are

shown in Table 5.1. The adequacy of numerical resolution in DNS is often expressed for the velocity field by the non-dimensional parameter $k_{max}\eta$. For high-Sc scalar fields, the resolution requirement is expressed by $k_{max}\eta_B$, where $\eta_B \equiv \eta Sc^{-1/2}$ is the Batchelor scale (Batchelor 1959). For a given computational size, this requirement is met only by keeping the Reynolds number appropriately low. For reference, we have included in Table 5.1 the values of u'^2, the scalar variance related to its spectral density E_ϕ through

$$\phi'^2 \equiv \langle \phi^2 \rangle = \int_0^\infty E_\phi(k) dk, \tag{5.8}$$

the integral scale for velocity, L, the integral scale for the scalar, L_ϕ, defined through the relation

$$L_\phi = \frac{\pi}{2\langle \phi^2 \rangle} \int_0^\infty \frac{E_\phi(k)}{k} dk, \tag{5.9}$$

as well as $\langle \epsilon \rangle$, $\langle \chi \rangle$, R_λ and Sc.

In addition to the present, we incorporate data from Overholt & Pope (1996), Bogucki *et al.* (1997), Wang *et al.* (1999), and Watanabe & Gotoh (2004). All these studies were for stationary isotropic turbulence though some of them differ in the method of forcing the turbulence and in ways by which scalar fluctuations are maintained against scalar dissipation. Bogucki *et al.* (1997) forced both the velocity and scalar field by keeping the energy constant in a few low-wavenumber modes. The forcing of the velocity field by Overholt & Pope was the same as the present, as was manner of maintaining stationarity of the scalar field through the mean gradient. Wang *et al.* maintained both the velocity and scalar fields stationary by forcing wavenumbers with $k < 3$ such that the energy and scalar spectra followed a $k^{-5/3}$ power law. Watanabe & Gotoh forced both the velocity and scalar field with Gaussian random solenoidal forces that were delta-correlated in time, and applied the forcing in the wavenumber range $1 \leq k \leq 2$. The relevant parameters from these references are summarized in Tables 5.2 to 5.5, making sure (except when explicitly noted otherwise) that they conform to the definitions used here.

We also consider the experimental data from Mills *et al.* (1958), Yeh & Van Atta (1973), Warhaft & Lumley (1978), Sreenivasan *et al.* (1980), Tavoularis & Corrsin (1981), Sirivat & Warhaft (1983), Mydlarski & Warhaft (1998) and Antonia *et al.* (2000). Most of the measurements were made at low Reynolds numbers and for nearly passive temperature fluctuations in air ($Sc \approx 0.7$) in decaying grid-turbulence, generated by heating either the turbulence-generating grid itself, or an auxiliary screen placed downstream; the experimental configurations and conditions are succinctly summarized by Sreenivasan *et al.* (1980). The recent experiments of Mydlarski & Warhaft (1998) stretch the Reynolds number range substantially using the so-called active grid. The definitions of length and velocity scales used in experiments are sometimes different from those of numerical simulations, which complicates precise comparisons, though these differences do not appear to be critical. In any case, we have provided a list of the different definitions used by the authors wherever necessary or appropriate.

5.2.2 The Scaling of Scalar Dissipation

5.2.2.1 Unity Schmidt Number

In analogy to the energy dissipation rate, one can examine the R_λ-variation of $\langle\chi\rangle L/\langle\phi^2\rangle u'$. No general results are known on bounds on scalar dissipation, comparable to those of Doering & Foias (2002) for the energy dissipation, though Schumacher *et al.* (2003) studied related issues with the assumption of rapid straining at small scales. The data culled from Table 5.1 for $Sc = 1$, plotted in figure 5.7, indeed have the form

$$\frac{\langle\chi\rangle L}{\langle\phi^2\rangle u'} = A'(1 + \sqrt{1 + (B'/R_\lambda)^2}) \tag{5.10}$$

which is a direct extension of Eq. 5.6. For our own DNS data (circles in the figure) we have $A' \approx 0.4$ and $B' \approx 31$. The value of B' in Eq. 5.10 is significantly smaller than B in Eq. 5.6, which suggests that the asymptotic value of the normalized scalar dissipation is

attained faster in R_λ than the normalized energy dissipation. This is evident also from a comparison of figures 5.6 and 5.7. In analogy with the energy dissipation, we expect the form of the equation to be the same for all initial conditions, though the numerical values could be different.

In plotting figure 5.7, we have used L as the relevant length scale because the ratio L_ϕ/L is of the order unity for these data (0.7 ± 0.06). Further, instead of using L/u' as the indicator of the large-eddy time scale, one can consider the time scale $K/\langle\epsilon\rangle$, which is used to define the so-called "mechanical-to-scalar time scale ratio" (r_ϕ) often used in the modeling of reacting flows (see, e.g., Fox 2003). (Some results on r_ϕ were given in Yeung & Sawford 2002). The time scales L/u' and T are related from definitions as

$$\frac{L}{Tu'} = \frac{2}{3}f, \tag{5.11}$$

where f is given by Eq. 5.6. Because their ratio becomes a constant only for large R_λ, the use of the time scale T, instead of L/u', changes the form of the normalized data for low R_λ but its constancy for high Reynolds numbers is assured, as seen from the inset to figure 5.7. The use of T as a time scale possesses an advantage as we shall see further below.

In summary, it appears from the data just considered that dissipative anomaly applies to passive scalar fields as well. Following the idealized notion of cascades, the implication is also that the time taken by the scalar variance to reach the dissipative scales is of the same order as the time scale of the large eddies. In particular, the present evidence does not support the idea of a cascade short-circuit (Villermaux *et al.* 2001), though it is possible that the present homogeneous flows and the jet flow studied by Villermaux *et al.* could be different in this respect. We have focused here on homogeneous flows partly because the large body of data available allows definitive conclusions to be drawn, and partly because—based on our experience with the energy dissipation (Sreenivasan 1995)—each inhomogeneous flow has to be studied carefully on its own merit. While we do not expect a large qualitative

difference, this is clearly work for the future.

5.2.2.2 Non-unity Schmidt Numbers

We can now plot available data for all Sc in a similar manner (figure 5.8). The data for different conditions tend to approach constant values of the order unity for large R_λ, though without collapsing, because of the additional parameter, Sc. There is, in particular, no discernible order for low R_λ. Instead of examining the R_λ-variation, one may plot the data against the microscale Péclet number

$$P_{\lambda\phi} \equiv \frac{u'\lambda_\phi}{D} = R_\lambda Sc \frac{\lambda_\phi}{\lambda}, \tag{5.12}$$

where the scalar microscale λ_ϕ is defined through the relation

$$\lambda_\phi^2 = 6D\frac{\langle\phi^2\rangle}{\langle\chi\rangle}. \tag{5.13}$$

That, too, does not collapse the data although the dependence on Sc emerges more clearly (figure 5.9). This is not surprising because the Péclet number does not distinguish between the case of low Sc and high R_λ on the one hand and that of high Sc and low R_λ on the other—which are two different problems in mixing. Even if T were used instead of L/u', the data do not collapse against R_λ or $P_{\lambda\phi}$ (see figures 5.10 and 5.11). While a reasonable conclusion may still be that an asymptotic state is reached for large R_λ or $P_{\lambda\phi}$, this limit is not the same for all the data.

For the data used in figure 5.7, the ratio L_ϕ/L is about 0.7±0.06, so it is reasonable to assume that the scalar field is forced at essentially the same scale as the velocity field. As shown in figure 5.12, the length scale ratio for our data depends on Sc, even if not very strongly. (This dependence may seem surprising at first but the increasing importance with Sc of the -1 part of $E_\phi(k)$ makes it quite plausible. There is practically no dependence on R_λ for fixed Sc.) If L_ϕ/L is small compared to unity so that the scalar forcing occurs within

the inertial range of the velocity field, the appropriate time scale for normalizing $\langle\chi\rangle/\langle\phi^2\rangle$ is not L/u' or T, but their products with the factor $(L_\phi/L)^{2/3}$. This conclusion follows if we assume that the characteristic time scale for the inertial range is given by the Kolmogorov scenario, and that the time scale needed for scalar variance to reach the dissipative scales is diminished because the forcing occurs in the inertial range at $L_\phi < L$. It would thus seem appropriate to multiply the ordinates in figures 5.8-5.11 by $(L_\phi/L)^{2/3}$. We have prepared these plots but do not present them because they do not make a qualitative difference. We surmise the reason to be that, while the length scale ratio is not strictly unity, its variation is not sufficiently strong for it to matter in the present context.

To understand the Sc-dependence of $\phi^2/\langle\chi\rangle T$, we consider large Sc and small Sc separately. For the former case, we may approximate the scalar spectrum by (see Section 5.1)

$$E_\phi(k) = C_{OC}\langle\chi\rangle\langle\epsilon\rangle^{-1/3}k^{-5/3} \tag{5.14}$$

below a crossover wavenumber and by

$$E_\phi(k) = C_B\langle\chi\rangle(\nu/\langle\epsilon\rangle)^{1/2}k^{-1} \tag{5.15}$$

above the crossover. Here, C_{OC} is the Obukhov-Corrsin constant (Corrsin 1951) and C_B is the Batchelor constant (Batchelor 1959). The natural crossover scale is $k_\eta \sim 1/\eta$, where $\eta = (\nu^3/\langle\epsilon\rangle)^{1/4}$ is the Kolmogorov scale. By integrating the scalar spectrum it is then easy to show that

$$\frac{\langle\phi^2\rangle}{\langle\chi\rangle} = \frac{(3/2)C_{OC}}{\langle\epsilon\rangle^{1/3}k_0^{2/3}}\left[1-\left(\frac{k_0}{k_\eta}\right)^{2/3}\right] + (1/2)C_B\left(\frac{\nu}{\langle\epsilon\rangle}\right)^{1/2}\ln(Sc), \tag{5.16}$$

which can be written as

$$\frac{\langle\phi^2\rangle}{\langle\chi\rangle T} = c_1\ \tilde{f} + c_2\ \frac{\ln(Sc)}{R_\lambda} \tag{5.17}$$

with

$$\tilde{f} = f^{2/3} - \frac{c_3}{R_\lambda}, \tag{5.18}$$

where f comes from (5.6), $c_1 = C_{OC}$, $c_2 = C_B\sqrt{15}/3$ and $c_3 = \sqrt{15}$. It should be noted that taking the crossover scale as a multiple of k_η different from unity—as is indeed suggested by the numerical constants C_{OC} and C_B (determined, e.g., from the simulations of Yeung *et al.* (2002)—does not alter any of the conclusions drawn here. The appearance of terms of the form $1/R_\lambda$ and $\ln(Sc)/R_\lambda$ in Eq. 5.18 and and Eq. 5.17 is also in agreement with a separate analysis by Borgas *et al.* (2004, ; see equation (15) therein).

The first term of (5.17) depends on both R_λ and the flow (through constants A and B that are implicit in f), and the second term is a linear function of $\ln(Sc)/R_\lambda$. The advantage of using T instead of L/u' is that the prefactor for the second term is a constant in the former case instead of being a function of R_λ and of A and B in the latter. Equation 5.17 shows that the meaning of large Reynolds number for large Sc is that $\ln(Sc)/R_\lambda$ must be small (in addition to the usual criterion that R_λ itself be large).

In simulations listed in table 5.1, it is generally the case that $\ln(Sc)/R_\lambda$ is not small (as we shall discuss further below), and so the asymptotic state has not been reached. Nevertheless, for some sets of data, the $\tilde{f}$-term is small compared with the $\ln(Sc)/R_\lambda$-term, which suggests that the data for those cases may collapse if plotted against $\ln(Sc)/R_\lambda$. This is indeed the case, as shown infigure 5.13.

For $Sc < 1$, we can get an approximate spectrum from (5.14) but using the high-wavenumber cut-off at the Obukhov-Corrsin scale ($\eta_{OC} \equiv \eta Sc^{-3/4}$). Proceeding as before, we integrate the spectrum using (1.1) for $\langle\epsilon\rangle$ and obtain

$$\frac{\langle\phi^2\rangle}{\langle\chi\rangle T} = c_1 \left(f^{2/3} - \sqrt{15}\frac{1}{R_\lambda Sc^{1/2}} \right). \tag{5.19}$$

The first term is a function of both the flow geometry (or forcing scheme in simulations) and R_λ, while the second is a linear function of the parameter $(R_\lambda Sc^{1/2})^{-1}$. However, since the first term is in general not small, especially for high R_λ, the straight lines would depend on flow features and R_λ. It is clear that the asymptotic state is attained only when $R_\lambda Sc^{1/2}$

is large (in addition to R_λ being large)—this being different from the large-Sc case.

As an aside, it is worth remarking that (5.19) can be rewritten, using (5.6) for f, as

$$\frac{\langle\phi^2\rangle}{\langle\chi\rangle T'} = \frac{3}{2}c_1\left(1 - 15^{-1/6}\frac{1}{{R_{L'}}^{1/3}Sc^{1/2}}\right), \tag{5.20}$$

where a new time scale $T' = L^{2/3}/\langle\epsilon\rangle^{1/3}$ and a new Reynolds number $R_{L'} = (u'L^2/\lambda)/\nu$ have been introduced. To obtain this equation, we have also used the relation $R_\lambda f^{2/3} = 15^{2/3}{R_{L'}}^{1/3}$. The important feature of (5.20) is that it does not contain any flow-dependent parameters (unlike (5.19) through f). If we now plot $\frac{\langle\phi^2\rangle}{\langle\chi\rangle T'}$ against $({R_{L'}}^{1/3}Sc^{1/2})^{-1}$ we expect a straight line with a negative slope. In figure 5.14 we show all the relevant data and compare the best fit (dotted line) with the line given by (5.20) (dash-dotted line with $C_{OC} = 0.6$ and $C_B = 5$). The comparison is not unreasonable. This scaling is a consequence of Obukhov-Corrsin spectrum, according to which the scalar dissipation rate, when normalized by T', should scale with ${R_{L'}}^{-1/3}Sc^{-1/2}$, thus independent of all other details. If we plot the data using R_λ, or another time scale, then the dependencies on the flow and R_λ will reappear.

Finally, for $Sc = 1$, we can put Sc to unity in both estimates (5.17) and (5.19), the corresponding form turns out to be the same:

$$\frac{\langle\chi\rangle T'}{\langle\phi^2\rangle} = \frac{2}{3c_1}\left(1 - \frac{15^{-1/6}}{{R_{L'}}^{1/3}}\right)^{-1}. \tag{5.21}$$

We can express Eq. 5.21 in terms of L/u' and R_λ as $\langle\chi\rangle L/\langle\phi^2\rangle u' = 2f/[3\ c_1(f^{2/3} - \sqrt{15}/R_\lambda)^{-1}]$. This functional form, although different from (5.10), can also be fitted to compare with the DNS data. In figure 5.7 we included this theoretical prediction using the values of A and B obtained from our DNS data. This trend of the curve is similar to Eq. 5.10 though it yields a somewhat higher value than that observed for the data.

5.2.2.3 Limits

The results of the preceding Section can be summarized as follows:

$$\frac{\langle\phi^2\rangle}{\langle\chi\rangle T}\frac{1}{c_1} = f^{2/3} - \frac{1}{R_\lambda} \times \begin{cases} c_3 - c_4 \ln(Sc) & Sc > 1 \\ \sqrt{15}\ Sc^{-1/2} & Sc < 1 \end{cases} \tag{5.22}$$

where $c_4 = c_2/c_1$. We are now interested in the limiting behaviors of $\frac{\langle\phi^2\rangle}{\langle\chi\rangle T'}$ with respect to R_λ and Sc. In particular, from the above equation it is easy to find the following results:

$$\lim_{R_\lambda\to\infty} \frac{\langle\phi^2\rangle}{\langle\chi\rangle T} = c_1(2A)^{2/3} \qquad 0 < Sc < \infty, \tag{5.23}$$

$$\lim_{R_\lambda\to 0} \frac{\langle\phi^2\rangle}{\langle\chi\rangle T} = -c_1\frac{1}{R_\lambda} \begin{cases} c_3 - c_4 \ln(Sc) & Sc > 1 \\ \sqrt{15}\ Sc^{-1/2} & Sc < 1, \end{cases} \tag{5.24}$$

$$\lim_{Sc\to\infty} \frac{\langle\phi^2\rangle}{\langle\chi\rangle T} = \frac{1}{R_\lambda} c_2 \ln(Sc) \qquad R_\lambda < \infty, \tag{5.25}$$

$$\lim_{Sc\to 0} \frac{\langle\phi^2\rangle}{\langle\chi\rangle T} = -\frac{c_1\sqrt{15}}{R_\lambda Sc^{1/2}} \qquad R_\lambda < \infty. \tag{5.26}$$

Some comments on these limits are now in order. According to (5.23), as R_λ approaches infinity, the normalized scalar dissipation rate tends to a constant. As already remarked, this constant is flow-dependent. However, the limiting behavior appears to be independent of the diffusivity of the scalar. In figure 5.10, this is what would be expected for higher R_λ. In the opposite limit of vanishing R_λ, Eq. 5.24 shows that the behavior at small R_λ depends upon Sc (and this dependence is different for scalars with Sc greater or less than unity). Moreover, $\langle\phi^2\rangle/(\langle\chi\rangle T)$ decreases for $Sc < 1$, while it increases for high Sc (the numerical value depending on c_1 and c_2). This can also be seen in figure 5.10. For low-Sc

scalars the normalized scalar dissipation increases as R_λ decreases, while high-Sc scalars do the opposite. This limit presents no dependence on the flow (or forcing in DNS). The third limit, Eq. 5.25, implies that no flow and forcing effects are felt when Sc is very high. This feature cannot be tested here since the only high-Sc data available are our own, for which a common forcing scheme was used. Finally, Eq. 5.26 suggests an R_λ-dependence, but no flow-dependence, as $Sc \to 0$.

We have seen that, according to the Obukhov-Corrsin scaling, there is a universal behavior of $\langle\chi\rangle/\langle\phi^2\rangle$ when normalized by T' and plotted against $R_{L'}$. This is seen in the recast form of (5.22) as

$$\frac{\langle\phi^2\rangle}{\langle\chi\rangle T'}\frac{2}{3c_1} = 1 - \frac{15^{-2/3}}{{R_{L'}}^{1/3}} \times \begin{cases} c_3 - c_4 \ln(Sc) & Sc > 1 \\ \sqrt{15}\ Sc^{-1/2} & Sc < 1. \end{cases} \tag{5.27}$$

Using this form of normalization and remembering that, because of the relation $R_\lambda f^{2/3} = 15^{2/3}{R_{L'}}^{1/3}$, one Reynolds number tends to infinity when the other does, we see that the $R_\lambda \to \infty$ limit preserves the asymptotic constancy even if it yields a different limit from (3.12). The limit in this case is

$$\lim_{R_\lambda\to\infty} \frac{\langle\phi^2\rangle}{\langle\chi\rangle T'} = \frac{3}{2}c_1 \equiv \frac{3}{2}C_{OC} \qquad 0 < Sc < \infty. \tag{5.28}$$

In particular, the constant $\frac{3}{2}C_{OC}$ is independent of the flow details and hence universal. The replot of the data using this scaling, shown in figure 5.15, seems to confirm the conclusion. The lack of strict universality could be due to, among other effects, contaminations from the large scale details, especially taking into account the variety of flows we are analyzing.

5.2.2.4 The Overall Picture

Equations 5.17 and 5.21 can be used to address the following question: how close is a given flow, characterized by given values of R_λ and Sc, to being asymptotic? To illustrate this

point, we take the operational view that the asymptotic state is attained when the second term in each of these equations, which depends on both viscosity and diffusivity, is 10% of the respective first terms. A choice of some other similar percentage will not affect the conclusions qualitatively, as we shall see.

In figure 5.16, we have plotted in the R_λ-Sc plane the condition just spelled out, implementing it as follows. The full curve to the right side of the plot is the locus of points for which the first term in Eq. 5.17 is 10 times larger than the log-term, while that to the left is the locus for which the first term of Eq. 5.19 is 10 times the second one. The dash-dotted lines mean that the R_λ-parts in the first term (which are small for large R_λ in any case) are neglected. The horizontal dotted line represents the R_λ at which the asymptotic state for $\langle\epsilon\rangle$ has been attained (at this R_λ the difference between Eq. 5.6 and its asymptotic value is 10 times smaller than the latter). The behaviors bound the asymptotic state and, as long as a point resides above these lines, it can be regarded, to this rough approximation, as belonging to the asymptotic state. The diagram reinforces the statement that such an asymptotic state is governed by both Reynolds and Schmidt numbers, and that the precise criteria depend on whether Sc is large or small. The high-R_λ approximations (dash-dotted lines in the diagram) are very close to the solid lines. The former only depend on the flow-specific constant A (see Eq. 5.6). But, since A does not depend too strongly on the flow, these limits can be regarded to provide the qualitative indication for all flows. Moreover, if this diagram were redrawn using $R_{L'}$ instead of R_λ (to make the result flow-independent), the result would still look very similar.

Figure 5.16 also shows where all the data from our tables lie on this phase plane. It is clear that all the high-Sc data from simulations are not asymptotic, as some of the older experiments. This is not a new revelation but the diagram is the first attempt made to quantify this feature.

5.2.2.5 Other Correlations

We may write from dimensional considerations that

$$E_\theta(k) = C\langle\chi\rangle\langle\epsilon\rangle^{-1/3}k^{-5/3}f(k\eta, Sc), \tag{5.29}$$

and

$$E_\theta(k) = C\langle\chi\rangle(\nu/\langle\epsilon\rangle)^{1/2}k^{-1}f(k\eta, Sc), \tag{5.30}$$

depending on whether $Sc < 1$ or $Sc > 1$. We can then integrate these expressions to obtain $\langle\phi^2\rangle$

$$\frac{\langle\phi^2\rangle/\langle\chi\rangle}{\tau_\phi} = \int_0^\infty f(k\eta, Sc)d(k\eta_B) \tag{5.31}$$

where τ_ϕ is equal to $\tau_\eta = (\nu/\langle\epsilon\rangle)^{1/2}$ or $\tau_B = \langle\epsilon\rangle^{-1/3}{\eta_B}^{2/3}$ depending on whether we use Eq. 5.29 or 5.30. Following the arguments leading to Eq. 5.19, we may expect that the right hand side is a function of R_λ and Sc. Or, using $R_{L'}$ instead of R_λ, we have

$$\frac{\langle\phi^2\rangle/\langle\chi\rangle}{\tau_\phi} = F(R_{L'}, Sc). \tag{5.32}$$

We may now naively expect that F will be in the form of power-laws in $R_{L'}$ and Sc, and hence write

$$\frac{\langle\phi^2\rangle/\langle\chi\rangle}{\tau_\phi} = \alpha {R_{L'}}^n Sc^m. \tag{5.33}$$

By an optimization procedure, we obtain $n = 0.35$ and $m = 0.57$ (when using τ_B) and $n = 0.36$ and $m = 0.23$ (when using τ_η) as best fits to the data. This is confirmed in figure 5.17. The prefactor α in Eq. 5.33 is 1.55 for τ_B and 1.43 for τ_η (and the additive constants in both cases are negligibly small).

Using the fact that $\tau_B = (\nu/\langle\epsilon\rangle)^{1/2}Sc^{-1/3} = T'/(15\ {R_{L'}}^2Sc^2)^{1/6}$, Eq. 5.33 can also be written as

$$\frac{\langle\phi^2\rangle}{\langle\chi\rangle T'} \sim {R_{L'}}^{n-1/3}Sc^{m-1/3}. \tag{5.34}$$

The closeness of the best estimate of 1/3 for n suggests that the R_λ-variation must indeed be negligible. The weak power of Sc is qualitatively similar to a logarithmic dependence on Sc as $Sc \to \infty$.

5.2.3 Summary and Conclusions

In this Section we investigated the asymptotic independence of the scalar dissipation on scalar diffusivity. One of the problems faced while attempting to understand the large-Reynolds number behavior for non-unity Schmidt numbers is the lack of a suitable criterion of what constitutes the asymptotic state. Without that rough guideline, one can come to varying conclusions from simulations and experiments. In this Section we have arrived at empirical criteria based on the analysis of existing data and summarized them in figure 5.16.

We wish to note that the flows analyzed here are homogeneous. This choice was deliberate because the situation with inhomogeneous flows is more complex. At the least, the meaning of how high a Reynolds number is high enough depends on the flow. The presence of solid boundaries introduces additional complexities: the role of viscosity in the boundary layer is different from that in the jet (or wake) because the viscosity effects in the former will not vanish at any Reynolds number (though Schmidt number effects may vanish at high enough Sc). Our expectation is that the asymptotic independence discussed here will hold for all flows far from a solid boundary, but that the rate at which this state is attained will be different for different flows. And, as we have already noted, the asymptotic value of the normalized scalar dissipation will depend on the flow.

5.3 Intermittency and Anisotropy Scaling for Passive Scalars

5.3.1 Scalar Dissipation Rate

The mean scalar dissipation rate $\langle\chi\rangle$, which was discussed at length in the previous Section, is simply the first order moment of the distribution of χ. However, like the energy dissipation, the scalar dissipation is an intermittent variable for which the first few moments are not sufficient to characterize its behavior. In fact, as we will see in this Section, χ is even more intermittent than ϵ. It is therefore necessary to study high-order moments of χ or even the complete PDF, f_χ. Fluctuations in energy-dissipation rates are important in combustion problems in which, for example, reaction rates are proportional to χ and extreme fluctuations can lead to local extinction/reignition of the flame (Sreenivasan 2004, Bilger 2004). A useful way to characterize large fluctuations is by studying the tail of the PDFs which are particularly wide for intermittent variables. In the case of passive scalars, it is important to distinguish between Reynolds and Schmidt number effects as was done previously in this Chapter.

In figure 5.18(a) we show the PDF of scalar dissipation normalized by its mean value ($\chi' \equiv \chi/\langle\chi\rangle$) at different Reynolds numbers with $Sc = 1$. As expected, as R_λ increases (at fixed Sc) finer scales are present for both velocity and scalar fields and larger gradients become more likely. Accordingly, we see that the tail of f_χ widens at large R_λ. The scaling of intermittency with Sc can be seen in 5.18(b) where we show the PDF of χ at $R_\lambda \approx 140$ for a range of Sc. We can see wider tails for $Sc = 1$ than $1/8$ and even wider for $Sc = 4$. However, at $Sc = 64$ the PDF is almost coincident with that at $Sc = 4$. This phenomenon, known as *saturation of intermittency*, was also observed at $R_\lambda \approx 8$ in Yeung *et al.* (2004) and $R_\lambda \approx 38$ in Yeung *et al.* (2002) by studying moments of scalar gradients.

It has been suggested (Holzer & Siggia 1994, Overholt & Pope 1996) that the PDF of

scalar dissipation can be approximated by a stretched exponential of the form

$$f_\chi(\chi') \sim (\chi')^{-1/2} \exp[-b_\chi (\chi')^{c_\chi}] \tag{5.35}$$

which does in fact produce good fits to our data for all R_λ and Sc. In figure 5.19 and Table 5.7 we show the parameters that provide the best fit in the range $1 < \chi' < 50$. Stronger intermittency is seen as smaller values of b_χ and c_χ. To help understand Reynolds and Schmidt number scaling, in Table 5.7 we also include the resolution N, since as found in Chapter 3, modest resolution leads to underestimation of the tails or equivalently, larger exponents c_χ. For a given R_λ and resolution N, the simulations are performed with 2 or 3 scalars (see the table) with the resolution criterion $k_{max}\eta_B \approx 1.5$ applied to the scalar with highest Schmidt number in the simulation. These scalars are identified in Table 5.7 with an asterisk (*) next to the resolution. It is not surprising then, that for those scalars, the coefficients may appear slightly larger than what the overall trend suggests.

For a fixed Schmidt number, we see in Table 5.7 that increasing R_λ leads to a smaller exponent c_χ consistent with an increased intermittency. For a fixed Reynolds number, on the other hand, the data suggest that the exponents c_χ approach an asymptotic value at some Sc which is consistent with the saturation of intermittency mentioned above. For $R_\lambda \approx 8$, saturation occurs at Sc between 64 and 256 (Yeung *et al.* 2004), whereas for $R_\lambda \approx 38$ it occurs at $Sc \sim O(4)$ (Yeung *et al.* 2002). Taking into account the fact that due to resolution effects, c_χ for $Sc = 1$ at $R_\lambda \approx 140$ may be overestimated, our recent simulations suggest that saturation may occur at $Sc \sim O(1)$. We can also see that the difference between the coefficients at $Sc = 1/8$ and 1 is smaller at high R_λ being almost equal for $R_\lambda \geq 240$.

In figure 5.19(b) we included $c_\chi = 1/3$ (dashed line) which was derived analytically for large Péclet and Schimdt numbers under the so called Kraichnan model for the velocity field in Eq. 5.1 (see e.g. Falkovich *et al.* 2001). The details of these calculations can be

found, for velocity fields with different statistics, in Chertkov *et al.* (1998b,a), Gamba & Kolokolov (1998) and Balkovsky & Fouxon (1999). As seen from the figure, DNS data does not support this result as the asymptotic state at large Sc appears to depend on R_λ.

Intermittency of passive scalars at different scales can be studied using local averages similar to that defined in Section 4.1 for energy dissipation (i.e. Eq. 4.3):

$$\chi_r = \frac{1}{V_r} \int_{V_r} \chi(\mathbf{x}) d\mathbf{x} \tag{5.36}$$

Using the concept of multipliers and multifractals (see e.g. Frisch 1995) we can expect a scaling of the form

$$\langle \chi_r^q \rangle \sim r^{-\nu_q} \tag{5.37}$$

Note that the exponents ν_q are all zero in the absence of scalar dissipation intermittency. Prasad *et al.* (1988) found the (nontrivial) exponents in the inertial-convective range (roughly for $\eta < r < L$) for $R_\lambda \approx 200$ while Sreenivasan & Prasad (1989) found that in the viscous-convective range at $R_\lambda \approx 150$, the exponents are all zero (i.e. no intermittency). However, the Sc scaling of this result is less understood. In figure 5.20 we show the moments $\langle \chi_r^q \rangle$ for $Sc = 4$ and 64 at $R_\lambda \approx 140$ on a 2048^3 grid. At this resolution, $k_{max}\eta$ is approximately 11 which implies, according to our findings in Chapter 3, a very well resolved velocity field. The exponents ν_q in Eq. 5.37 were obtained by fitting power laws shown as dotted lines in figure 5.20. In figure 5.21 we show $\nu_q/(q-1)$ (instead of ν_q) which are equal to the "generalized" dimensions D_q defined by Hentschel & Procaccia (1983) and are usually found in the literature. Data at the same Reynolds number and $Sc = 1/8$ and 1 are also included for comparison. We can see that there is a decrease of intermittency at inertial-convective scales as Sc increases for $Sc > 1$. Although there may be some ambiguity in the choice of the scaling range, the decrease in inertial-convective range intermittency is robust to changes in the fitting interval. We also include results for energy dissipation

at the same R_λ. It is clear from figure 5.21 that the exponents for scalar dissipation are greater than those for energy dissipation (dashed line) indicating that χ is more intermittent and less space filling than ϵ in agreement with results found in the literature (e.g. Sreenivasan & Antonia 1997). Our results suggest that the scaling of intermittency of χ in the inertial-convective range may behave similar to energy dissipation at very high Sc.

5.3.2 Scalar Gradients

An essential element in the phenomenology of Kolmogorov (1941a), and subsequent applications to passive scalars, is that at high Reynolds numbers the small scales become locally isotropic. However, a large body of evidence from both experiments and simulations (see summary in e.g. Sreenivasan 1991, Warhaft 2000) indicates that departures from local isotropy persists even for very large R_λ. One measure of anisotropy is given by the skewness of scalar gradients fluctuations parallel to the imposed mean gradient ($\nabla_\parallel \phi$) which according to local isotropy concepts (reflectional symmetry) should vanish. In figure 5.22 we show this quantity (denoted by $\mu_3(\nabla_\parallel \phi)$) as a function of Reynolds number for $Sc = 1/8$, 1, 4 and 64. At the highest Reynolds number in our simulations there is a persistent anisotropy consistent with the data of Warhaft (2000) for moderately diffusive scalars. At $Sc = 64$, however, μ_3 appears to decrease with R_λ but an asymptotic value at high R_λ cannot be ruled out from our data. Due to the difficulty in studying high-Sc scalars in both experiments and simulations, less is known about the Sc scaling of anisotropy. Yeung *et al.* (2002) studied the Sc scaling of gradients at $R_\lambda \approx 38$ and found that there is a systematic decrease of $\mu_3(\nabla_\parallel \phi)$ when Sc was varied from 1/4 for 64. The same trend was found in (Yeung *et al.* 2004) as Sc was increased up to 1024 at fixed $R_\lambda \approx 8$. In figure 5.23(a) we show $\mu_3(\nabla_\parallel \phi)$ from our database at $R_\lambda \approx 8$ (Yeung *et al.* 2004), 38 (Yeung *et al.* 2002) and new results at $R_\lambda \approx 140$. For all Reynolds numbers, the data suggest that the skewness decreases with Sc although as already pointed out in Yeung *et al.* (2004) careful examination of the results

in figure 5.23(a) reveals a Reynolds number dependence. In particular, it is seen that at high Reynolds numbers, the skewness decreases faster with Sc. A power law dependence of the form $Sc^{-\beta}$ is found to represent the data at high Schmidt numbers reasonably well although more data at $R_\lambda \approx 140$ is highly desirable. Nonetheless, best fits to the data in figure 5.23(a) for $Sc \geq 4$ result in exponents $\beta \approx 0.27$, 0.39 and 0.43 for $R_\lambda \approx 8$, 38 and 140 respectively which imply a faster return to isotropy with Sc in high Reynolds number flows.

In figure 5.23(b) we show the flatness factor (μ_4) of $\nabla_\parallel \phi$ for the same cases as in part (a) in the figure. It was also found in Yeung *et al.* (2002, 2004) that scalar gradients become more intermittent as Sc increases but reach an asymptotic value in the high-Sc limit. Data from our recent simulations at $R_\lambda \approx 140$ support this conclusion and show that both the asymptotic value for the flatness and the Sc necessary to attain this high-Sc limit, depend on R_λ. The asymptotic value of $\mu_4(\nabla_\parallel \phi)$ is found to be about 10, 13 and 20 at $R_\lambda \approx 8$, 38 and 140 respectively. The ratio between flatness factors of scalar gradients fluctuations parallel and perpendicular to the mean scalar gradient is shown in figure 5.24. Local isotropy requires $\mu_4(\nabla_\parallel \phi)/\mu_4(\nabla_\perp \phi) = 1$ which is seen to be a better approximation as Sc increases.

5.4 Summary, Discussion and Further Questions

In this Chapter we have investigated the Reynolds and Schmidt number scaling of passive scalars in isotropic turbulence with an imposed mean scalar gradient. Using our DNS database with a wide range of R_λ and Sc we first addressed the scaling of the spectrum for scalar fluctuations. We found that at high R_λ (650), inertial-convective range scaling (Obukhov 1949, Corrsin 1951) is clearly seen for $Sc = 1/8$ and 1. A bump in the spectrum similar to the energy spectrum is observed for $Sc = 1$ which may be a transition to k^{-1} scaling. At high Schmidt number, our data supports Batchelor k^{-1} scaling for $R_\lambda \approx 8$, 38 and recent simulations at 140 for which high-Sc data are available. In the viscous-diffusive

range, Kraichnan's form of the spectrum is a better approximation than Batchelor's which suggests that fluctuations in the strain rate are important in mixing at scales smaller than η.

It was further found that the normalized scalar spectrum according to Batchelor's scales (i.e. Eq. 5.3) appears to present some universal features for all Sc studied here (including scalars with $Sc < 1$). This result, which was also observed in Bogucki *et al.* (1997), implies that other mechanisms involving the strain rate may play an important role in turbulent mixing as suggested by Gibson (1968), Gibson *et al.* (1988). The study of alternative mechanisms leading to a unified treatment of scalars capable of explaining, for example, the collapse of the spectrum seen in figure 5.5, is an important task for the future.

A basic premise of Kolmogorov (1941a) is that the mean dissipation rate becomes independent of molecular properties when R_λ is sufficiently high. The same assumption is needed for the mean scalar dissipation rate when Kolmogorov's ideas are extended to passive scalars. We investigated this phenomenon, known as dissipative anomaly, and found limits in terms of R_λ and Sc at which the mean scalar dissipation can be considered independent of molecular properties, namely ν and D. Different analytic expressions were derived depending on whether $Sc > 1$ or $Sc < 1$.

Intermittency for scalars at small scales was found to increase with both R_λ and with Sc although for sufficiently high Sc, indicators of intermittency such as high-order moments of gradients and the PDF of scalar dissipation approach an asymptotic state. New simulations at $R_\lambda \approx 140$ (2048^3) with $Sc = 4$ and 64 support previous claims about saturation of intermittency and show that the asymptotic state is reached at lower Sc when R_λ is high. Departures from anisotropy are also found to decrease with Schmidt number and the Reynolds number effect was discussed. In particular, it is found that return to isotropy with Sc is faster in high Reynolds number flows.

Some further comments about the results found above are in order. In terms of the

scaling of scalar dissipation, the findings can be summarized as follows:

(a) The mean scalar dissipation rate $\langle\chi\rangle$ reaches an asymptotic state at large R_λ and Sc. The higher the Sc, the higher the R_λ needed to reach the asymptotic state (see e.g. figure 5.16).

(b) For a fixed R_λ the PDF of χ presents wider tails as Sc is increased (i.e. intermittency increases with Sc) but saturates (reaches an asymptotic state) at some Sc. This asymptotic state seems to require a higher value of Sc when R_λ becomes small (see e.g. Table 5.7 and figure 5.23b).

(c) Intermittency in the inertial-convective range measured by scaling exponents of moments of local averages of χ decreases with Sc.

Clearly the Sc at which the asymptotic state is reached scales differently with R_λ according to (a) and (b). This suggests that the mechanisms determining low-order moments (a) such as the mean value are different from those determining high-order moments (b). As was seen in Section 5.2, the mean scalar dissipation is determined by large scales through a classical "cascade" process in the high R_λ and Sc limit (dissipative anomaly). The processes leading to intermittency, on the other hand, are not completely understood and may be due to a direct interaction between large and small scales (see e.g. Warhaft 2000). For example, the phenomenon of saturation of intermittency (b) may be explained as follows. Large scalar gradients are formed when a scalar blob is in proximity to another blob with very different concentration. This could be realized by large scales bringing these two blobs together from large distances (e.g. its integral length scale L_ϕ so that their concentration is very different) at a time scale much shorter than that needed by diffusion processes to smooth out scalar differences. A diffusive time scale T_D for a scalar moving a distance of the order of L_ϕ, would scale as $T_D \sim L_\phi^2/D$. Large gradients will form if a flow time scale

(e.g. L_ϕ/u') is much shorter than this diffusive time scale, i.e. $L_\phi/u' \ll T_D$. Decreasing diffusivity (increasing Sc) would not lead to stronger gradients since according to this mechanism, the scalar gradient is determined by large scales bringing together two scalar blobs. Using the definitions above, the condition for asymptotic state can be re-written as ${R_\lambda}^2 Sc(L_\phi/L) \gg 1$. However, in our simulations the ratio L_ϕ/L scales as $Sc^{-\alpha}$ with $\alpha \ll 1$ (see figure 5.12). Therefore, we can ignore this variation and write

$$ {R_\lambda}^2 Sc \gg 1 \tag{5.38} $$

This condition should be met in order for the mechanism suggested above to generate large gradients. If this is not met, for example for large D (low Sc), sharp fronts are smoothed out by diffusivity and a reduction of intermittency is seen as Sc is decreased. To test Eq. 5.38 we observe that at $R_\lambda \approx 8$ saturation of intermittency occurs at $Sc \sim 64$ which implies ${R_\lambda}^2 Sc \sim O(5000)$. Meeting this condition at $R_\lambda \approx 38$ would imply a Schmidt number of about 78 which is not far from $O(64)$ found from our DNS data. We stress that given the crude approximations made in this analysis, condition Eq. 5.38 gives reasonable results. At $R_\lambda \approx 140$, according to this estimate, saturation would occur at $Sc \sim O(0.25)$ which cannot be ruled out as a possibility using our DNS data. Simulations at the Reynolds numbers presented in this work with both higher and lower Sc scalars would be desirable. This is especially so for $R_\lambda \approx 140$.

It is interesting that although small-scale intermittency, as measured by high-order moments of χ, reaches an asymptotic state at high Sc (b), there is a decrease of intermittency in the inertial-convective range (c). These results suggest that the trend (c) is not a result of large fluctuations of χ being less likely but a change in its geometric distribution. In particular, it may imply a more even distribution in space of high-dissipation structures at scales between L and η. In figure 5.25 we show three-dimensional volume renders of scalar dissipation rate at $R_\lambda \approx 140$ on a 2048^3 grid for $Sc = 4$ and 64. Qualitatively, in addition

to finer scales, we see that the large scale structure of regions of high χ, is more evenly distributed in space at $Sc = 64$ consistent with smaller exponents ν_q. The characterization of these structures (as done in Chapter 4 for energy dissipation and enstrophy) should help clarify the role of these large scales in the scaling of intermittency with Sc. It would be interesting in particular to address the role of large scales in the asymptotic state reached in the high-Sc limit.

Table 5.1: DNS data in our own simulations: including Yeung *et al.* 2002 for R_λ 8, Yeung *et al.* 2004 for R_λ 38-240, and results at R_λ 390 and 650.

R_λ	N	u'	L	$\langle\epsilon\rangle$	ν	Sc	ϕ'	L_ϕ	$\langle\chi\rangle$
8	128	1.122	1.498	2.537	0.159	1	1.029	1.174	1.410
8	128	1.122	1.498	2.537	0.159	8	1.667	0.847	1.656
8	128	1.122	1.498	2.537	0.159	64	2.208	0.613	1.670
8	128	1.144	1.518	2.588	0.159	4	1.384	0.944	1.449
8	128	1.144	1.518	2.588	0.159	16	1.739	0.765	1.434
8	128	1.144	1.518	2.588	0.159	32	1.897	0.691	1.404
8	256	1.197	1.575	2.697	0.159	64	2.570	0.661	2.177
8	256	1.197	1.575	2.697	0.159	128	2.737	0.601	2.141
8	256	1.197	1.575	2.697	0.159	256	2.895	0.550	2.103
8	512	1.182	1.576	2.760	0.159	256	3.161	0.555	2.494
8	512	1.182	1.576	2.760	0.159	512	3.321	0.511	2.455
8	512	1.182	1.576	2.760	0.159	1024	3.471	0.473	2.416
38	64	1.625	1.077	2.822	0.025	0.25	1.029	0.935	2.106
38	64	1.625	1.077	2.822	0.025	0.5	1.197	0.838	2.285
38	64	1.625	1.077	2.822	0.025	1	1.355	0.751	2.397
38	256	1.589	1.007	2.802	0.025	0.25	1.108	0.994	2.240
38	256	1.589	1.007	2.802	0.025	1	1.433	0.801	2.500
38	256	1.589	1.007	2.802	0.025	4	1.716	0.649	2.568
38	256	1.584	1.064	2.665	0.025	4	1.758	0.628	2.720
38	256	1.584	1.064	2.665	0.025	8	1.893	0.566	2.724
38	256	1.584	1.064	2.665	0.025	16	2.024	0.511	2.723
38	512	1.645	1.214	2.787	0.025	16	2.145	0.530	2.969
38	512	1.645	1.214	2.787	0.025	32	2.271	0.483	2.935
38	512	1.645	1.214	2.787	0.025	64	2.391	0.443	2.903
90	128	1.295	1.366	0.763	0.006546	0.125	1.601	1.102	2.573
90	128	1.295	1.366	0.763	0.006546	0.25	1.750	1.003	2.694
90	128	1.295	1.366	0.763	0.006546	1	2.017	0.829	2.835
140	256	1.404	1.095	1.169	0.0028	0.125	1.263	0.924	1.875
140	256	1.404	1.095	1.169	0.0028	1	1.458	0.731	1.934
240	512	1.480	1.164	1.201	0.0011	0.125	1.807	0.955	3.235
240	512	1.480	1.164	1.201	0.0011	1	1.943	0.827	3.245
390	1024	1.534	1.254	1.302	0.000437	0.125	1.641	0.896	2.579
390	1024	1.534	1.254	1.302	0.000437	1	1.714	0.819	2.588

Table 5.2: DNS data from Watanabe & Gotoh (2004).

R_λ	N	u'	L	$\langle\epsilon\rangle$	ν	Sc	ϕ'	L_ϕ	$\langle\chi\rangle$
258	512	1.077	1.180	0.507	0.0006	1	1.421	0.407	1.116
427	1024	1.146	1.180	0.591	0.00024	1	1.407	0.413	1.196

Table 5.3: DNS data from Overholt & Pope (1996). The integral scalar length in their paper is taken to be $L_\phi = \langle \phi^2 \rangle^{1/2} / \beta$, which is reproduced here.

R_λ	N	u'	L	$\langle \epsilon \rangle$	ν	Sc	ϕ'	L_ϕ	$\langle \chi \rangle$
28	32	0.902	1.260	0.519	0.025	0.7	1.424	1.424	1.539
52	64	2.497	1.091	8.703	0.025	0.7	1.476	1.477	4.136
84	128	6.266	0.965	132.300	0.025	0.7	1.421	1.421	9.856
84	128	6.187	0.970	126.500	0.025	0.7	1.375	1.375	9.012

Table 5.4: DNS data from Wang *et al.* (1999).

R_λ	N	u'	L	$\langle\epsilon\rangle$	ν	Sc	ϕ'	L_ϕ	$\langle\chi\rangle$
132	256	0.676	1.072	0.179	0.001	0.7	0.766	0.752	0.345
68	256	0.256	1.049	0.014	0.001	0.7	0.141	0.883	0.004
100	128	0.857	1.530	0.201	0.004	1	1.090	0.956	0.419
151	256	0.855	1.514	0.177	0.002	1	1.090	0.937	0.440
195	512	0.874	1.412	0.246	0.001	1	1.100	0.918	0.501

Table 5.5: DNS data from Bogucki *et al.* (1997).

R_λ	N	u'	L	$\langle\epsilon\rangle$	ν	Sc	ϕ'	L_ϕ	$\langle\chi\rangle$
36	162	0.450	1.310	0.047	0.01	3	0.905	0.711	0.160
36	162	0.450	1.310	0.047	0.01	5	0.984	0.506	0.190
36	162	0.450	1.310	0.047	0.01	7	1.001	0.648	0.160
74	240	0.560	1.090	0.080	0.0033	3	1.010	0.715	0.260
74	240	0.560	1.090	0.080	0.0033	5	1.060	0.650	0.260
74	240	0.560	1.090	0.080	0.0033	7	1.080	0.642	0.270

Table 5.6: Experimental data. The scalar integral length scale in Mydlarski & Warhaft (1998) is $L_\phi = \langle \phi^2 \rangle^{1/2}/\beta, \beta$ being the mean gradient.

Source	R_λ	u'	L	$\langle \epsilon \rangle$	ν	Sc	ϕ'	L_ϕ	$\langle \chi \rangle$
MKOC	22	0.0529	0.0157	0.016	1.5	0.72	0.075	0.0142	0.0199
YV	35	0.0872	0.02	0.0456	1.55	0.725	0.2776	0.0184	0.308
WL	45	0.121	0	0.0951	1.65	0.73	0.0687	0	0.01298
	45	0.121	0	0.0951	1.65	0.73	0.1105	0	0.0558
STHC	34	0.1	0.014	0.0856	1.5	0.71	0.0549	0.0116	0.0203
	34	0.1	0.014	0.0856	1.5	0.71	0.135	0.0111	0.132
TC	128	0.4227	0.044	1.94	1.5	0.71	0.1091	0.031	0.128
	147	0.4889	0.051	2.65	1.5	0.71	0.1158	0.038	0.154
	160	0.5441	0.057	3.42	1.5	0.71	0.1249	0.0435	0.1773
SW	26	0.0432	0.02	0.00531	1.65	0.7	0.02963	0.0156	0.00222
	36	0.08	0.02	0.0393	1.65	0.7	0.0576	0.0164	0.0176
MW	85	0.1249	0.056	0.0314	1.6	0.71	0.249	0.052	0.124
	140	0.1703	0.11	0.0418	1.55	0.69	0.4195	0.17	0.277
	247	0.3162	0.17	0.164	1.5	0.67	0.5797	0.16	0.581
	306	0.3018	0.3	0.0833	1.6	0.71	0.8944	0.33	0.799
	407	1.0198	0.16	6.13	1.6	0.71	0.2828	0.079	0.466
	582	0.7635	0.43	0.94	1.6	0.71	1.0344	0.29	1.74
	731	1.2	0.4	3.88	1.5	0.67	1.4318	0.28	4.96
AZX	30	0.0594	0.0212	0.018	1.5	0.7	0.061	0	0.01
	51	0.1125	0.0465	0.117	1.5	0.7	0.076	0	0.03
	62	0.1809	0.0372	0.4	1.5	0.7	0.061	0	0.032
	78	0.2657	0.0349	1.412	1.5	0.7	0.044	0	0.026

Table 5.7: Best fit coefficients for Eq. 5.35 for the range $1 < \chi' < 50$. Scalars with an asterisk (*) next to the resolution correspond to those with $k_{max}\eta_B \approx 1.5$ in each simulation.

R_λ	Sc	N	b_χ	c_χ
8	1	128	0.43	0.74
8	8	128	0.53	0.58
8	64	128*	0.55	0.55
8	256	512	0.65	0.49
8	512	512	0.73	0.46
8	1024	512*	0.65	0.49
38	0.25	256	0.49	0.63
38	1	256	0.69	0.48
38	4	256*	0.77	0.44
38	4	256	0.74	0.44
38	8	256	0.85	0.40
38	16	256*	0.85	0.40
38	16	512	0.89	0.40
38	32	512	0.79	0.42
38	64	512*	0.70	0.45
140	0.125	256	0.72	0.46
140	1	256*	0.73	0.43
140	4	2048	1.24	0.29
140	64	2048*	1.17	0.30
240	0.125	512	0.98	0.35
240	1	512*	1.05	0.33
400	0.125	1024	1.39	0.27
400	1	1024*	1.07	0.31
680	0.125	2048	1.63	0.24
680	1	2048*	1.71	0.23

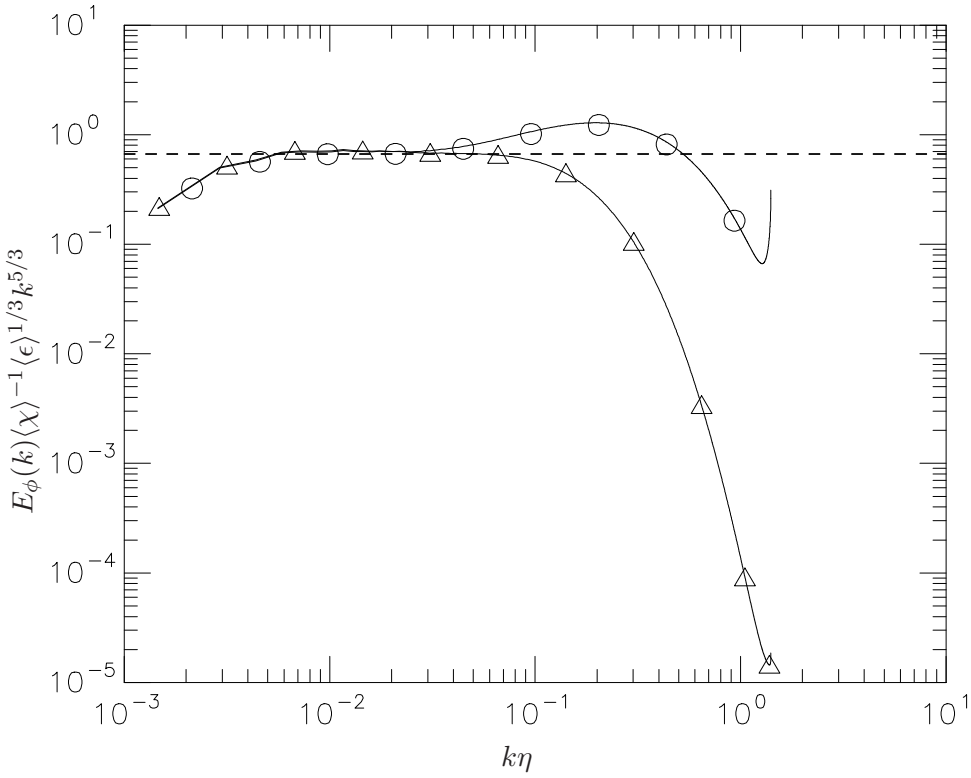

Figure 5.1: Compensated scalar spectrum according to Obukhov-Corrsin scaling in 2048^3 DNS at $R_\lambda \approx 650$ and $Sc = 1/8$ (triangles) and 1 (circles). The dashed line at 0.67 is to compare with experiments of Sreenivasan 1996.

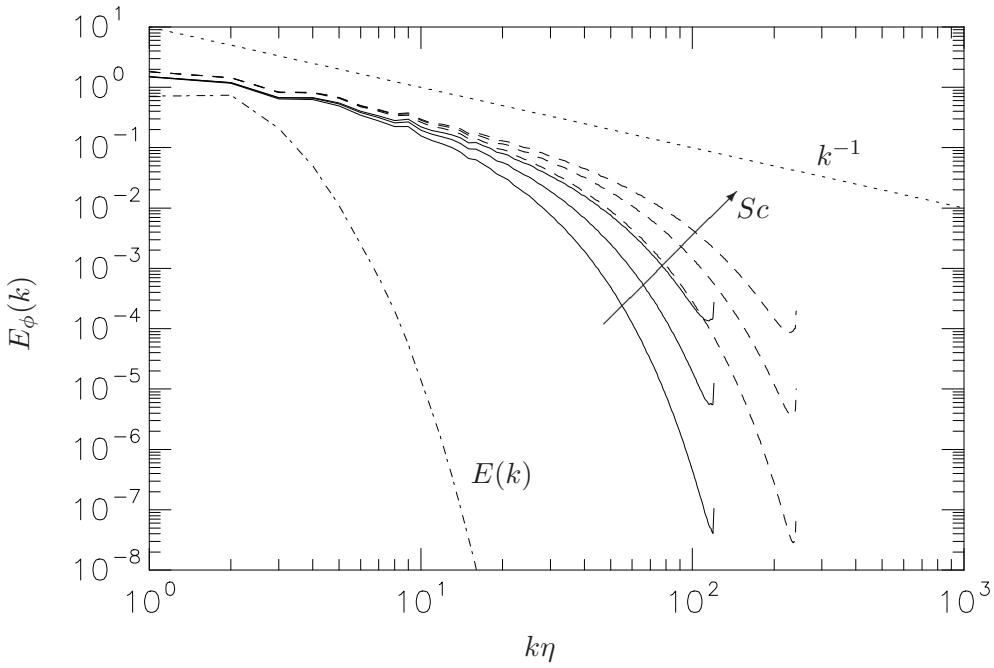

Figure 5.2: Un-normalized 3D spectra for scalars at $R_\lambda \approx 8$. $E(k)$ (chain-dotted line), $E_\phi(k)$ for $Sc = 64$, 128, 256 from 256^3 simulation (solid lines), and $E_\phi(k)$ for $Sc = 256$, 512, 1024 from 512^3 simulation (dashed lines). The dotted line shows slope -1 for reference.

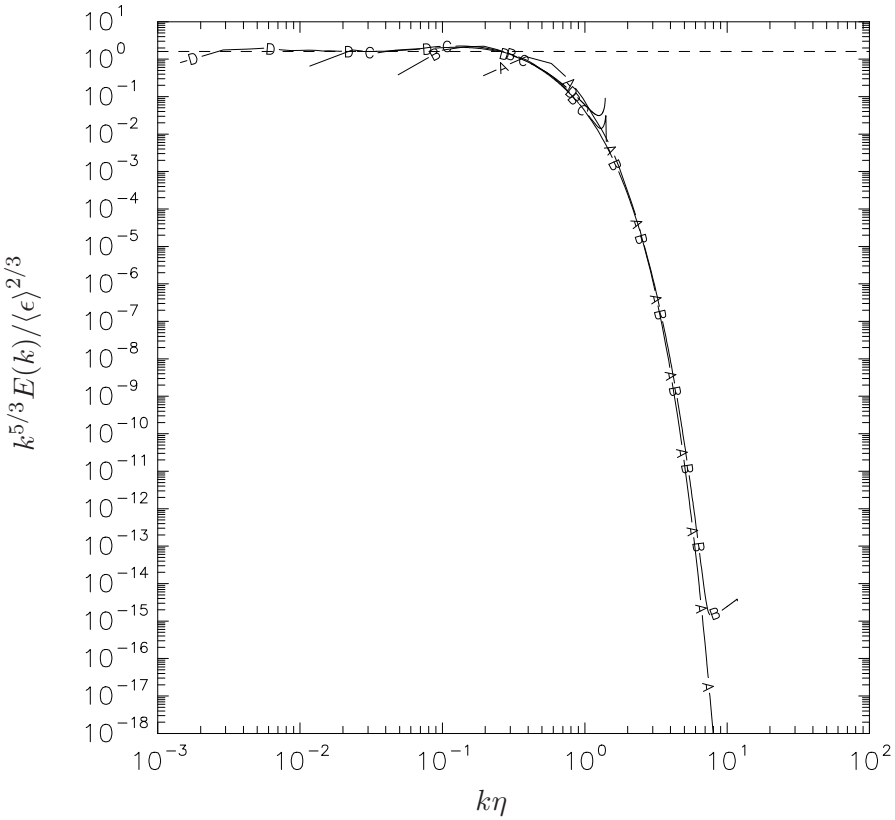

Figure 5.3: Energy spectrum normalized according to Kolmogorov (1941a). Lines A-D corresponds to $R_\lambda \approx 8$ (512^3), 38 (512^3), 140 (256^3) and 650 (2048^3). Dashed line corresponds to a Kolmogorov constant of 0.6.

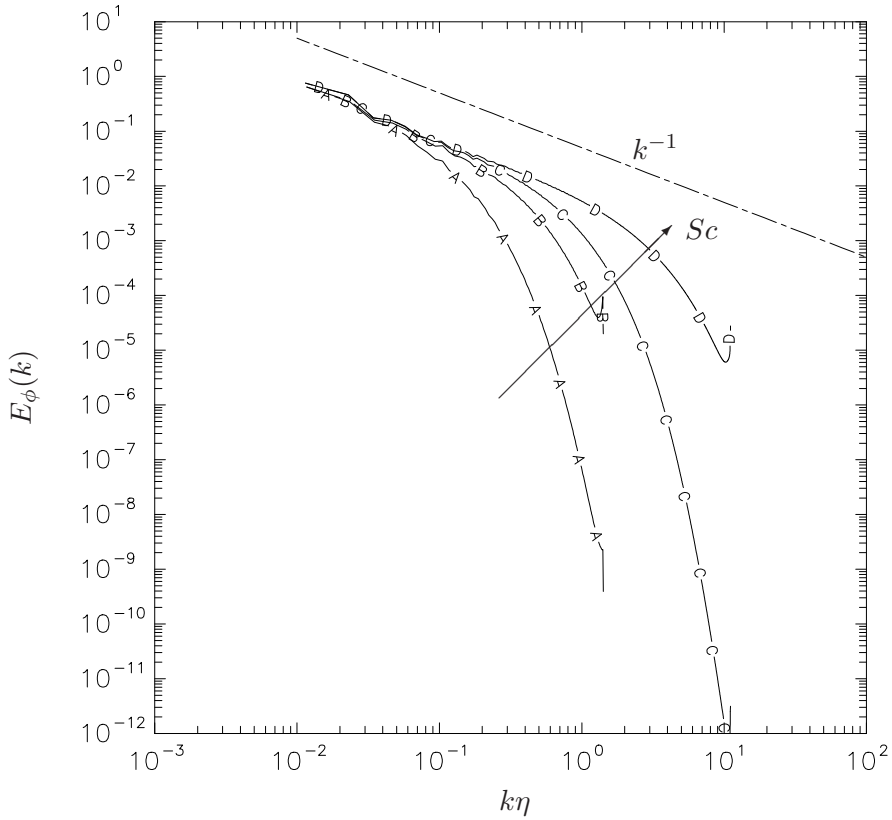

Figure 5.4: Un-normalized 3D spectrum for scalars at $R_\lambda \approx 140$. Lines correspond to $Sc = 1/8$ (A) and 1 (B) at 256^3 and $Sc = 4$ (C) and 64 (D) at 2048^3. The dotted line shows slope -1 for reference.

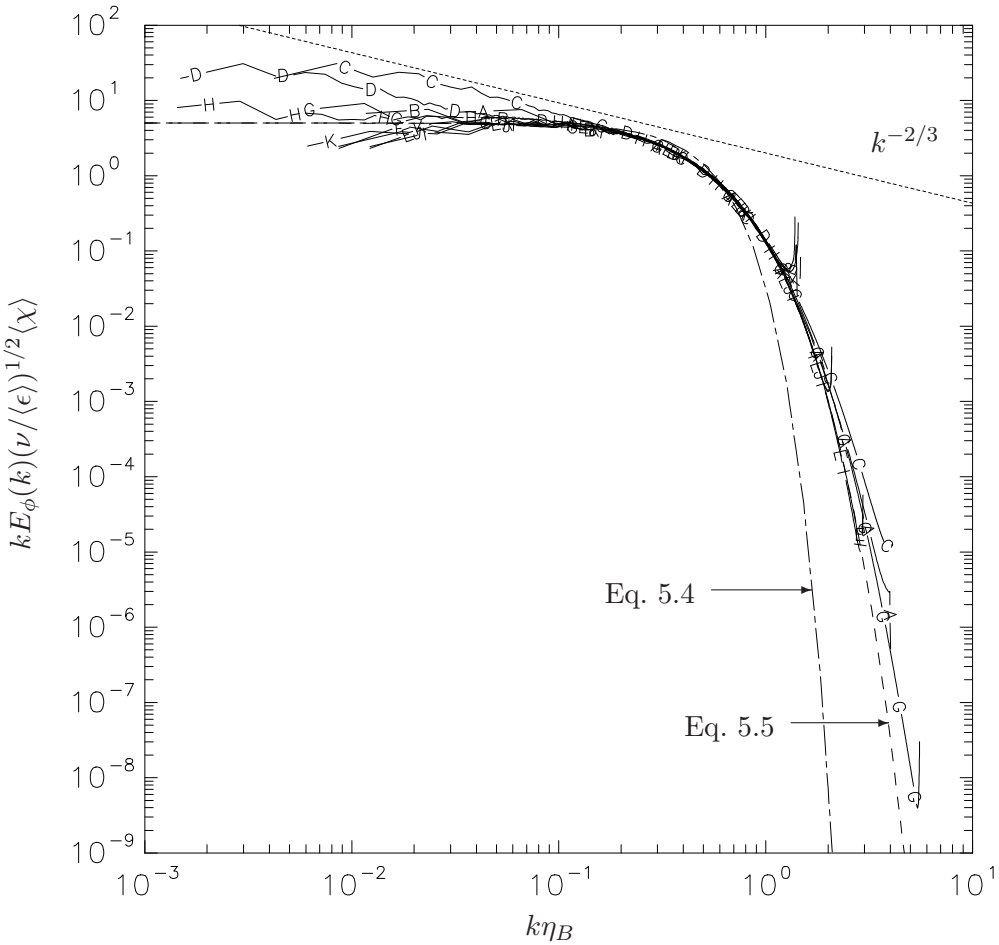

Figure 5.5: Normalized spectrum according to Batchelor's Eq. 5.3. Lines correspond to $Sc = 1/8$ (A) and 1 (B) at $R_\lambda \approx 140$ (256^3); $Sc = 1/8$ (C) and 1 (D) at $R_\lambda \approx 650$ (2048^3); $Sc = 16$ (E) and 32 (F) at $R_\lambda \approx 38$ (512^3); $Sc = 4$ (G) and 64 (H) at $R_\lambda \approx 140$ (2048^3); $Sc = 256$ (I), 512 (J) and 1024 (K) at $R_\lambda \approx 8$ (512^3). Dash-dotted and dashed lines are Batchelor's (Eq. 5.4) and Kraichnan's (Eq. 5.5) predictions with $C_B = 6$. Dotted line with slope $-2/3$ corresponds to $k^{-5/3}$ under the present normalization.

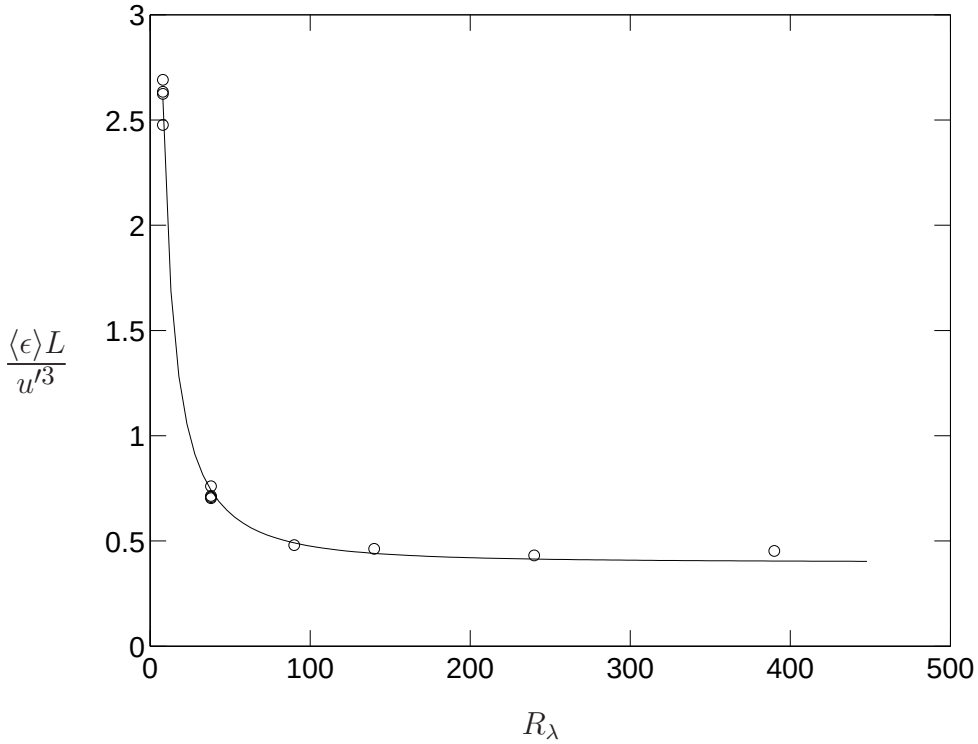

Figure 5.6: Normalized energy dissipation rate from the direct numerical simulations of isotropic turbulence. Solid line represents Eq. 5.6 with $A \approx 0.2$ and $B \approx 92$.

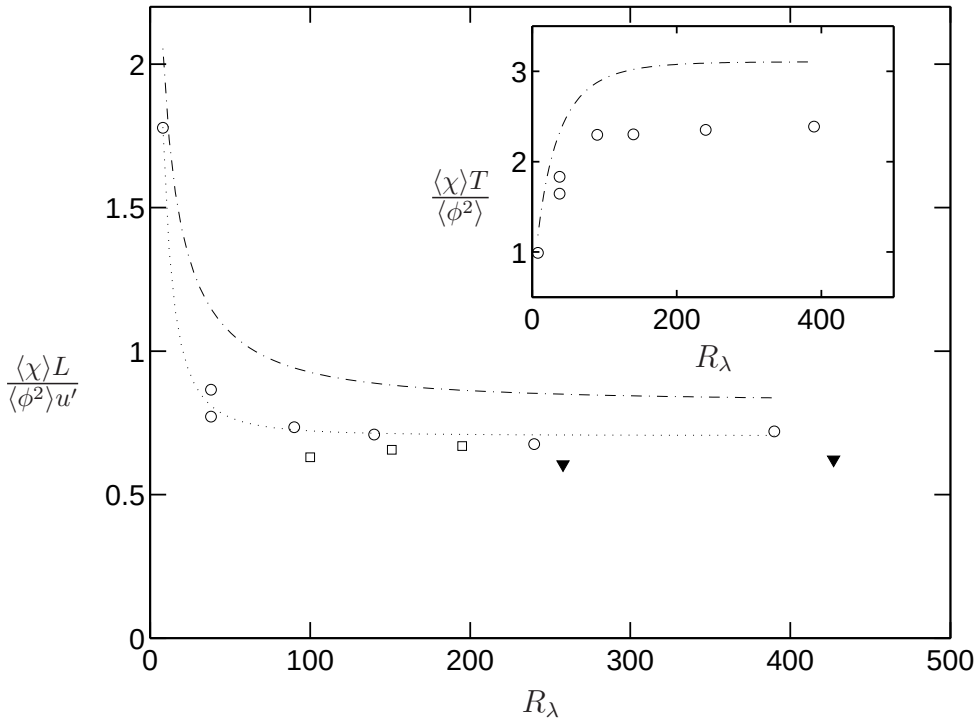

Figure 5.7: Scalar dissipation rate normalized with L/u' for $Sc = 1$. Symbols: ◯, present data; □, Wang *et al.* (1999); ▼, Watanabe & Gotoh (2004). Dotted line: Eq. 5.10 as the best fit for the present data. Dash-dotted line: theoretical prediction of Eq. 5.21, which will be described in Section 5.2.2.2. Inset shows the present data using the normalization of T instead of L/u', as well as Eq. 5.21. While the asymptotic constancy holds for both normalizations, the direction of approach of this constancy is different.

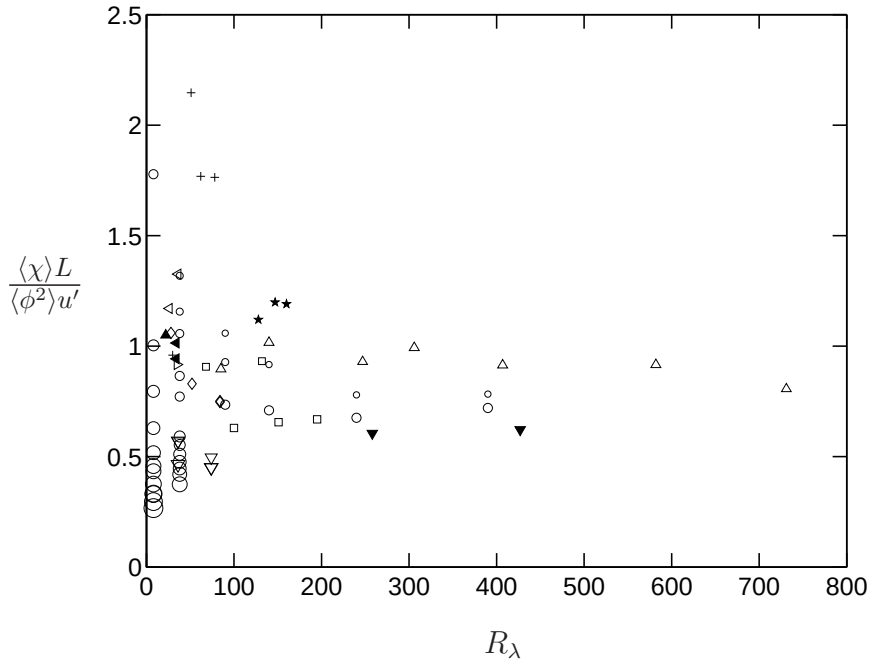

Figure 5.8: Scalar dissipation rate normalized with L/u'. Symbols: ◯, present data; ▼, Watanabe & Gotoh (2004); □, Wang *et al.* (1999); ◊, Overholt & Pope (1996); △, Mydlarski & Warhaft (1998); ★, Tavoularis & Corrsin (1981); ◁, Sirivat & Warhaft (1983); ◀, Sreenivasan *et al.* (1980); ▷, Yeh & Van Atta (1973); ▶, Warhaft & Lumley (1978); ▲, Mills *et al.* (1958); +, Antonia *et al.* (2000); ▽, Bogucki *et al.* (1997). The relative sizes of symbols of the same type illustrate the relative magnitudes of Sc.

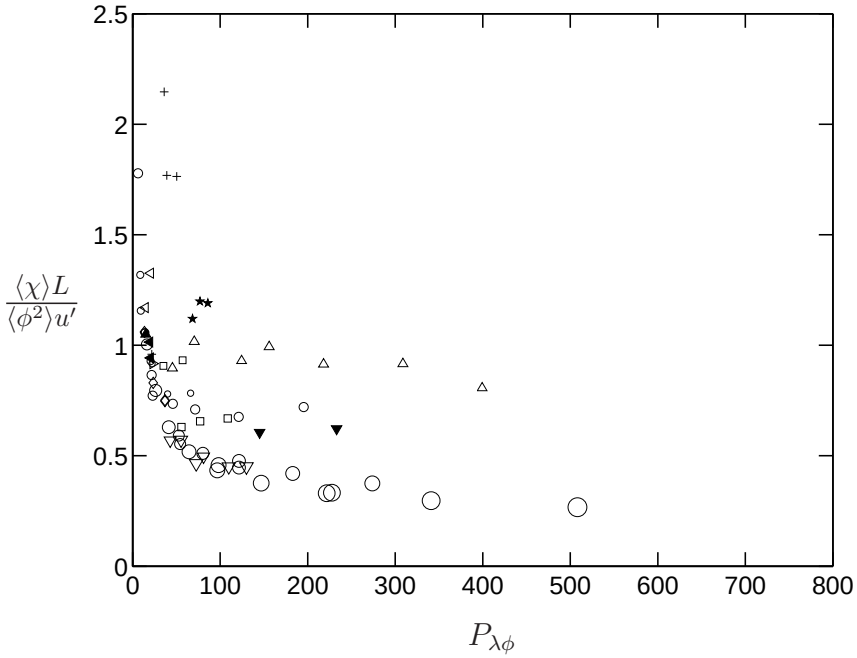

Figure 5.9: Scalar dissipation rate normalized with L/u'. Symbols as in figure 5.8.

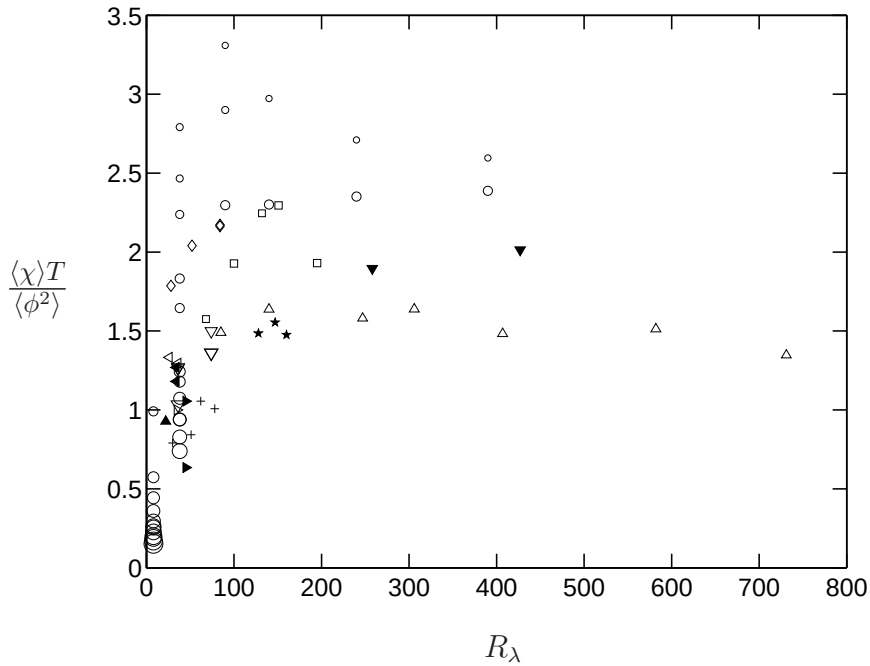

Figure 5.10: Scalar dissipation rate normalized with $T = K/\langle\epsilon\rangle$. Symbols as in figure 5.8.

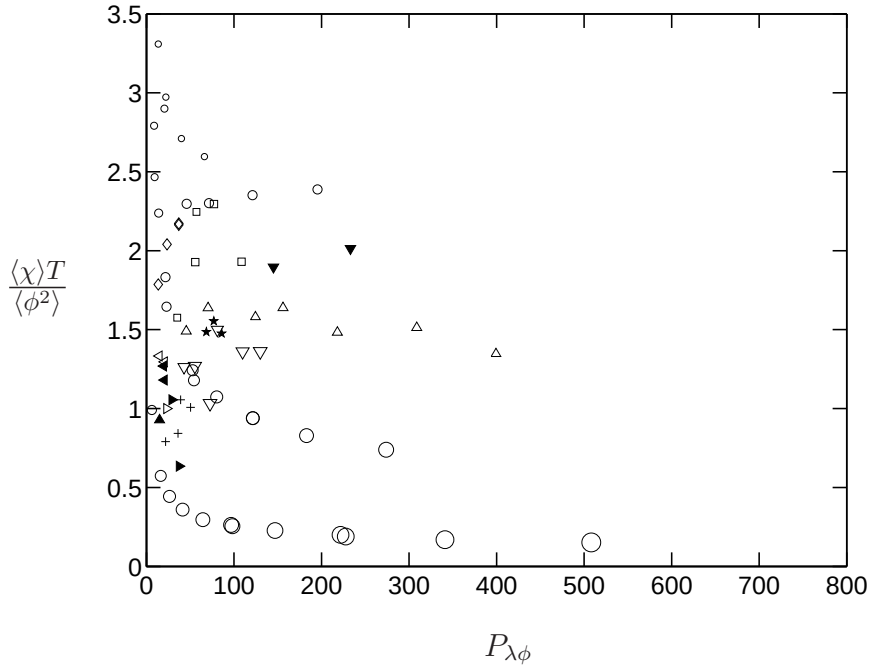

Figure 5.11: Scalar dissipation rate normalized with $T = K/\langle\epsilon\rangle$. Symbols as in figure 5.8.

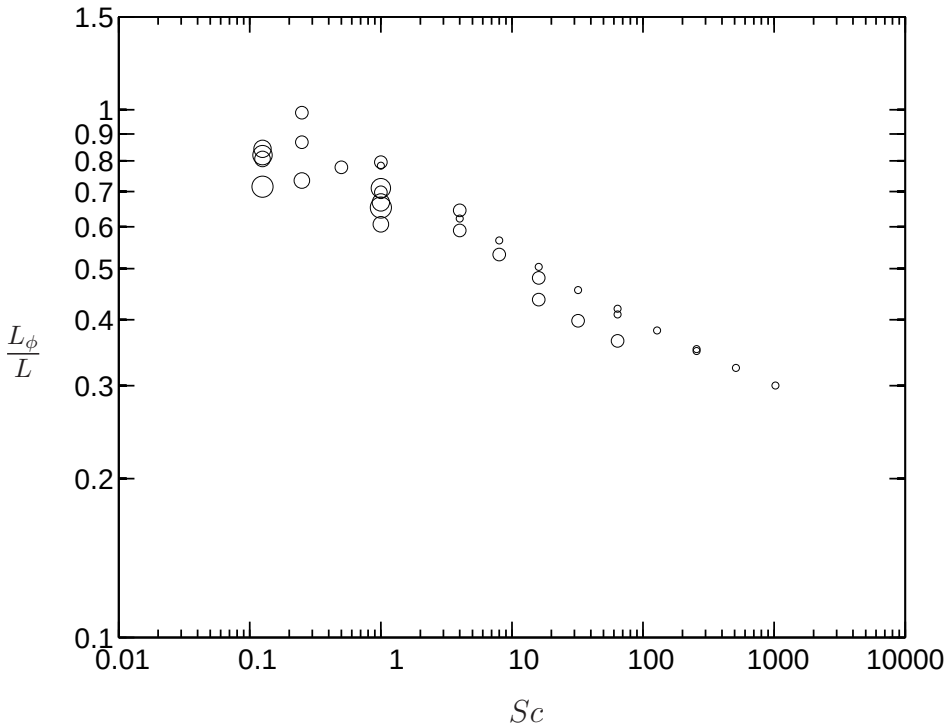

Figure 5.12: Ratio of integral length scales for present data. The relative size of the symbol illustrates the relative magnitude of R_λ.

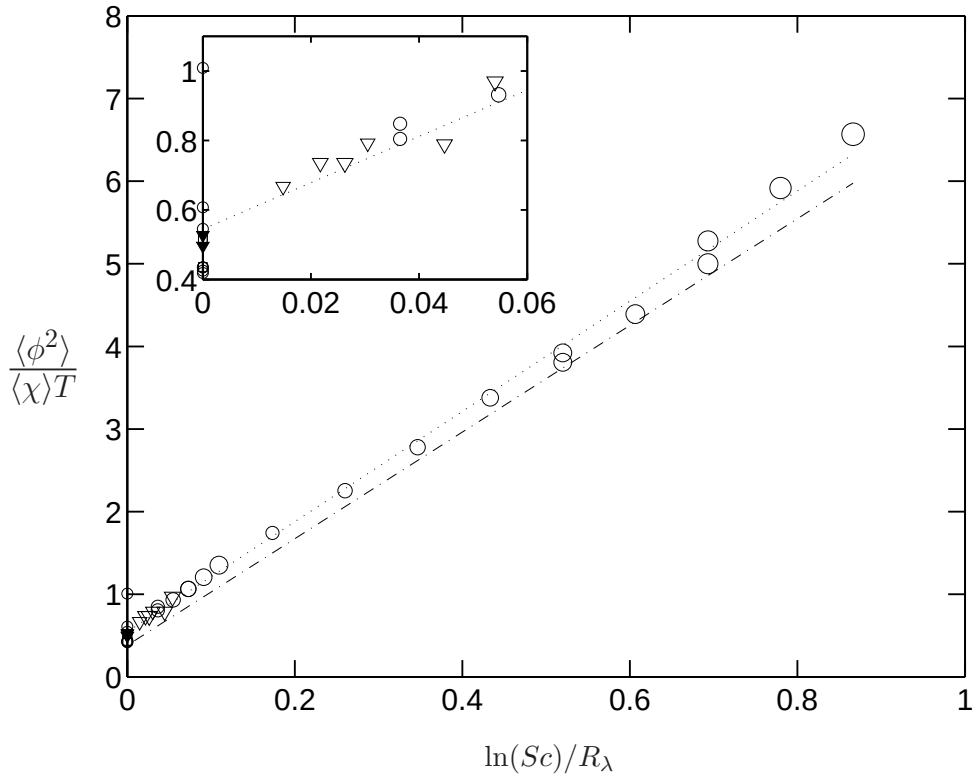

Figure 5.13: High Schmidt number scaling for low and moderate Reynolds numbers. Symbols as in figure 5.8. Dotted line: best fit for data with $Sc \geq 1$. Dash-dotted: Eq. 5.17 with $C_{OC} = 0.6$ and $C_B = 5$. Inset is an expanded view near the origin. As in figure 5.8, the relative size of the symbol illustrates the relative magnitude of Sc.

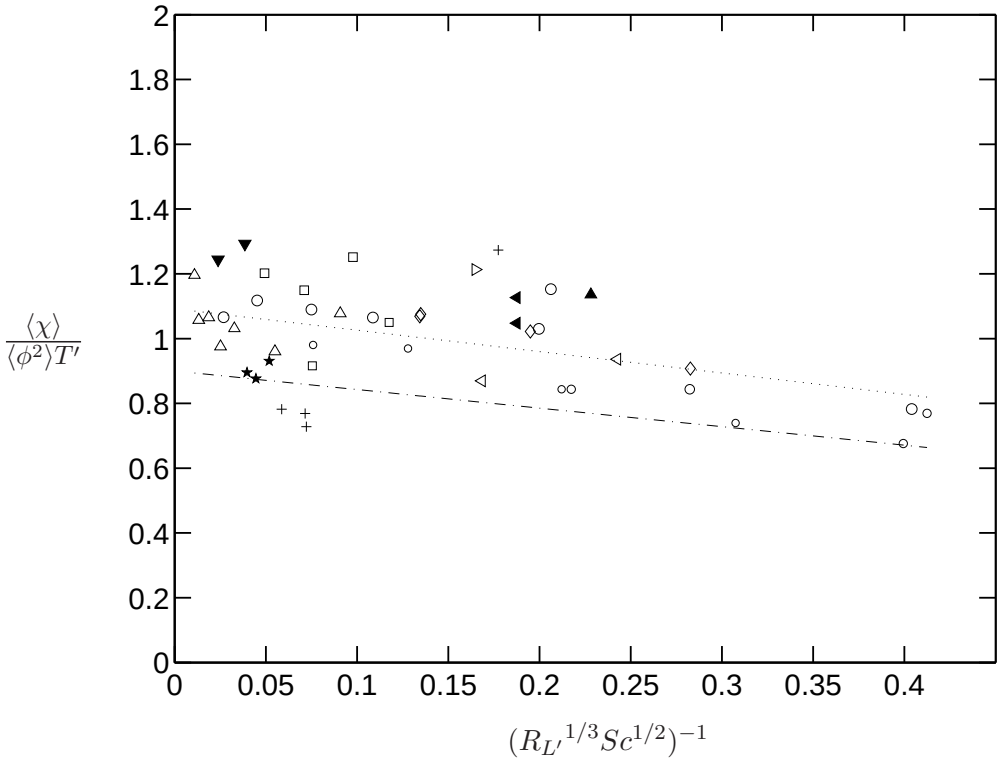

Figure 5.14: Low Schmidt number scaling. Symbols as in figure 5.8. Dotted line: best fit for data with $Sc < 1$. Dash-dotted: Eq. 5.20 with $C_{OC} = 0.6$ and $C_B = 5$.

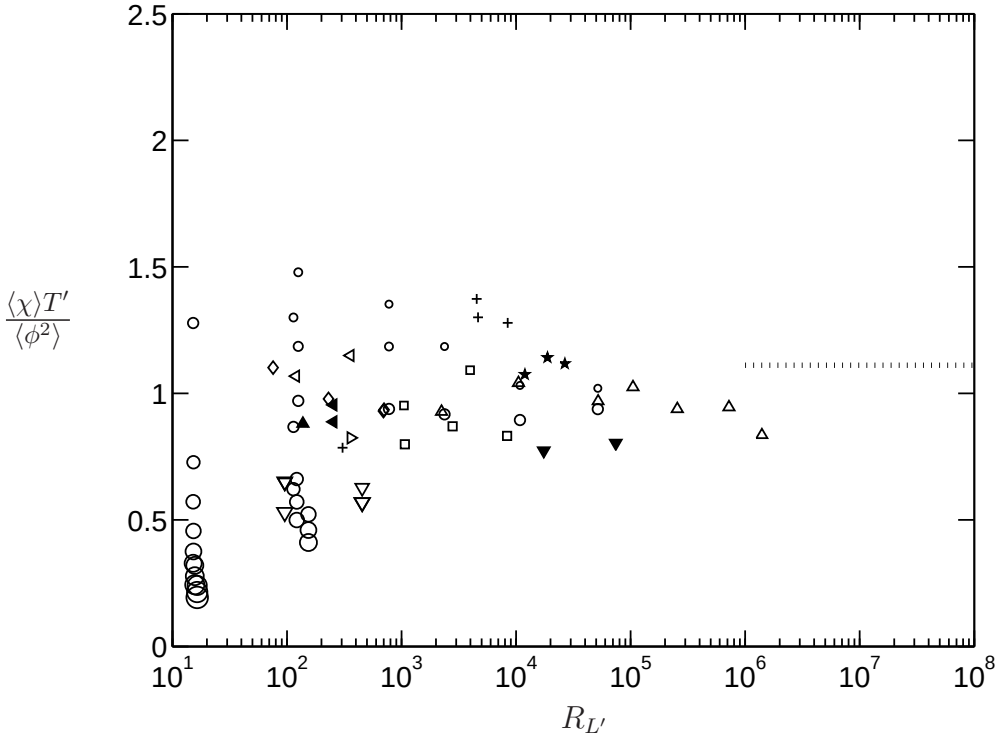

Figure 5.15: Scalar dissipation rate normalized by $T' = L^{2/3}/\langle\epsilon\rangle^{1/3}$. Symbols as in figure 5.8. The relative size of the symbol illustrate the relative magnitude of Sc. Dotted line: the limit $\frac{2}{3C_{OC}}$ predicted by Eq. 5.28 with $C_{OC} = 0.6$.

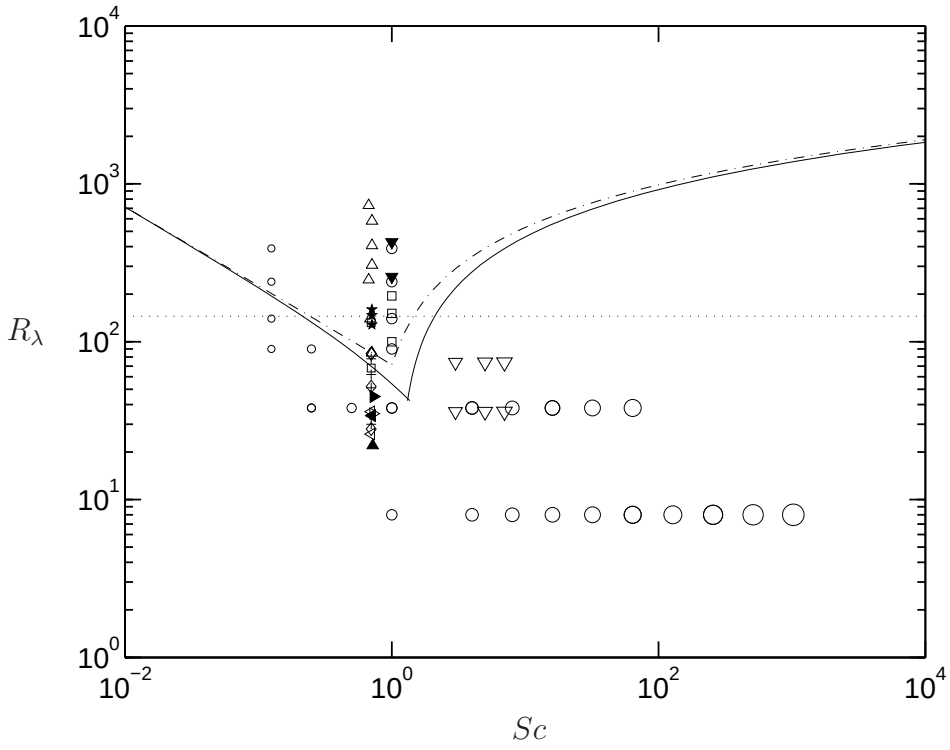

Figure 5.16: Theoretical limits for asymptotic state. See text for explanation on different lines. Symbols as in figure 5.8.

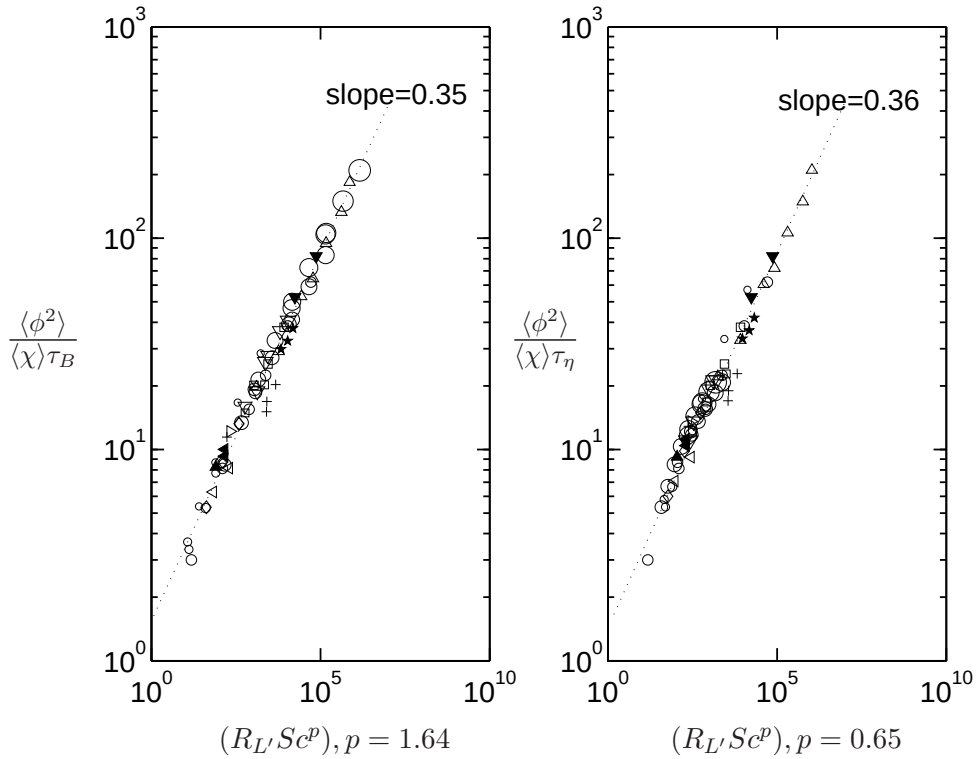

Figure 5.17: Scalar dissipation rate normalized with τ_B and τ_η for all data. Dotted lines are best fits. Symbols as in figure 5.8. The relative size of the symbols illustrate the relative magnitude of Sc.

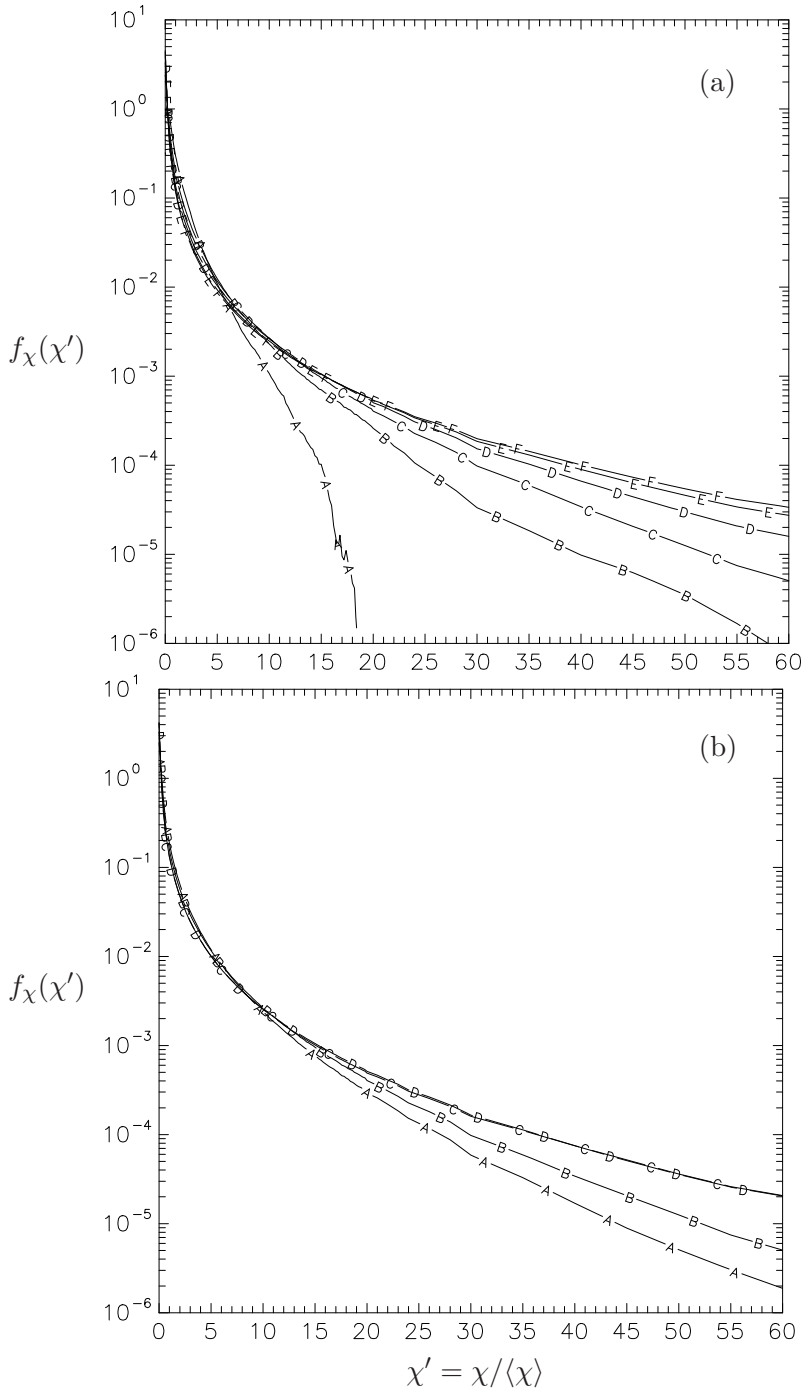

Figure 5.18: PDF of scalar dissipation. (a) $Sc = 1$, lines A-F correspond to $R_\lambda \approx 8$, 38, 140, 240, 400 and 650. (b) $R_\lambda \approx 140$, lines A-D $Sc = 1/8$, 1, 4 and 64.

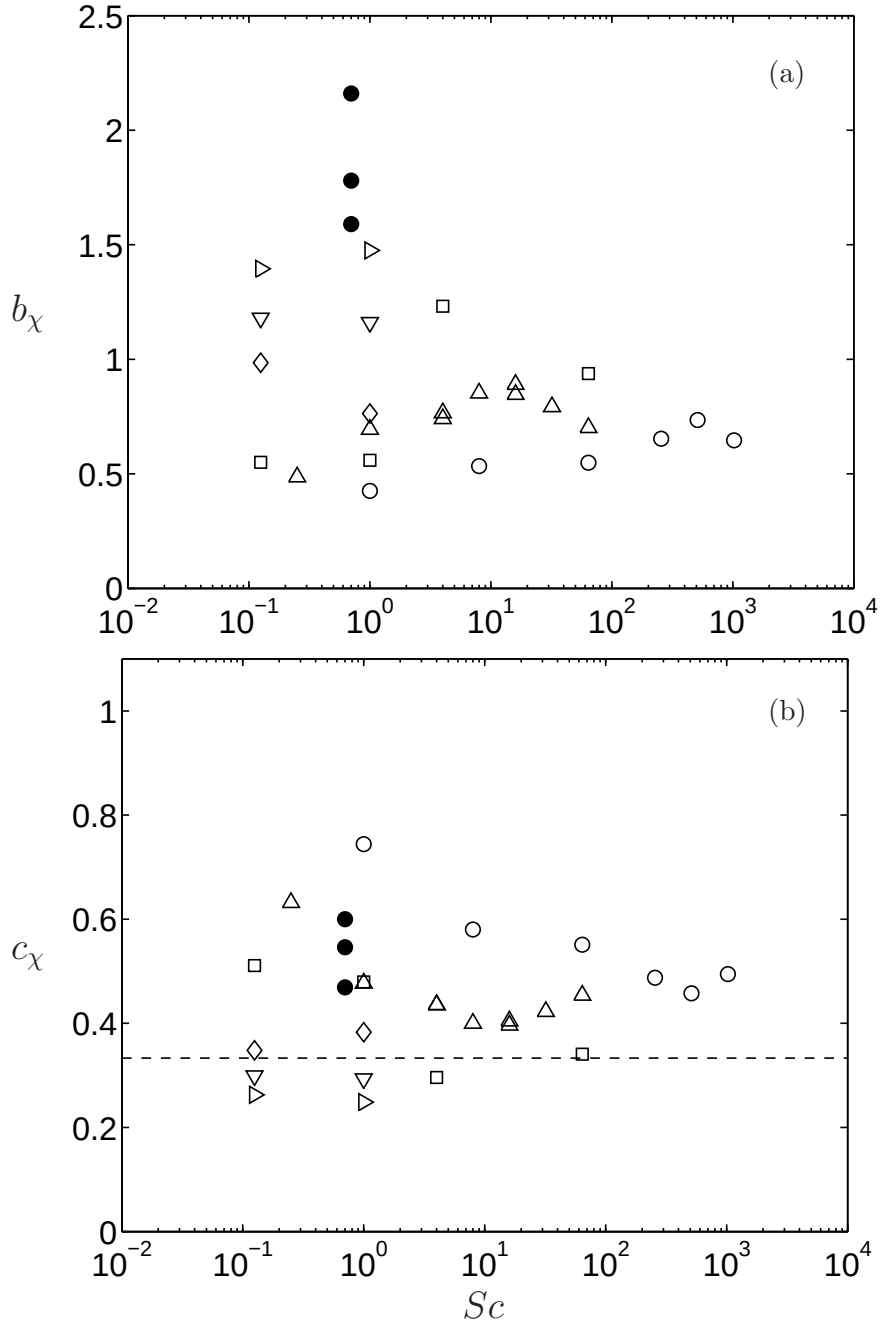

Figure 5.19: Best fit coefficients b_χ (a) and c_χ (b) in Eq. 5.35 at $R_\lambda \approx 8$ (◯), 38 (△), 140 (□), 240, 400 and 650. (b) $R_\lambda \approx 140$, lines A-D $Sc = 1/8$, 1, 4 and 64. Dashed line corresponds to 1/3.

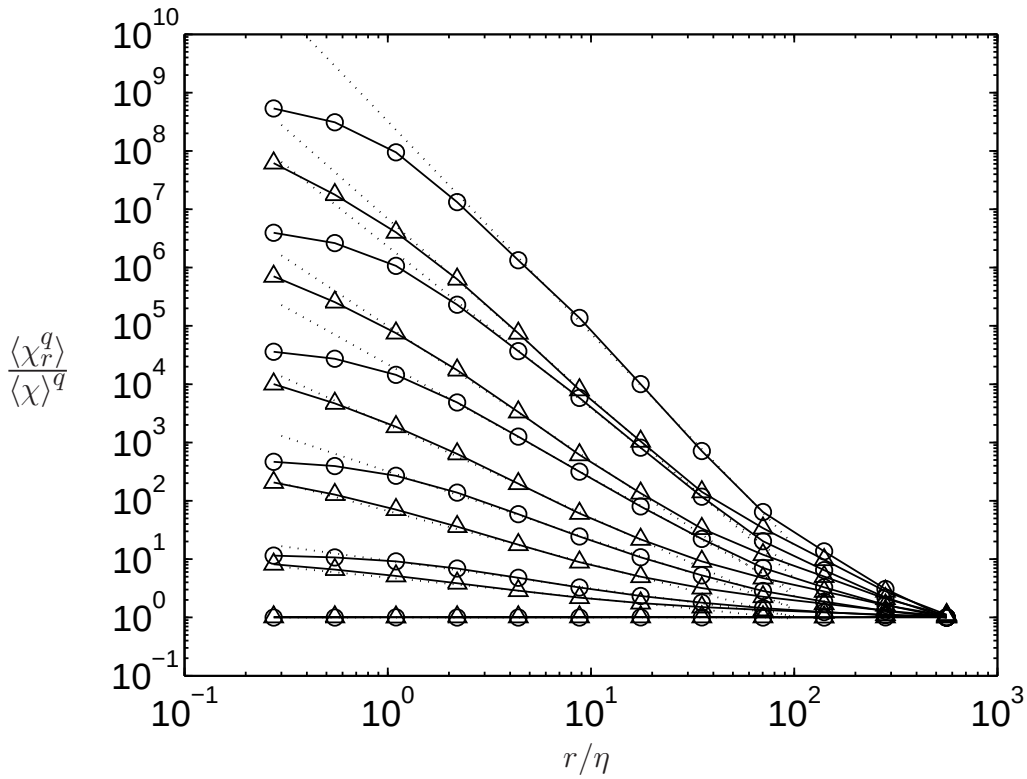

Figure 5.20: Moments $\langle \chi_r^q \rangle / \langle \chi \rangle^q$ as a function of r/η for scalars with $Sc = 4$ (◯) and 64 (△) at $R_\lambda \approx 140$. From bottom to top, curves correspond to $q = 1$ to 6. Dotted lines show the scaling range used to obtain the exponents ν_q.

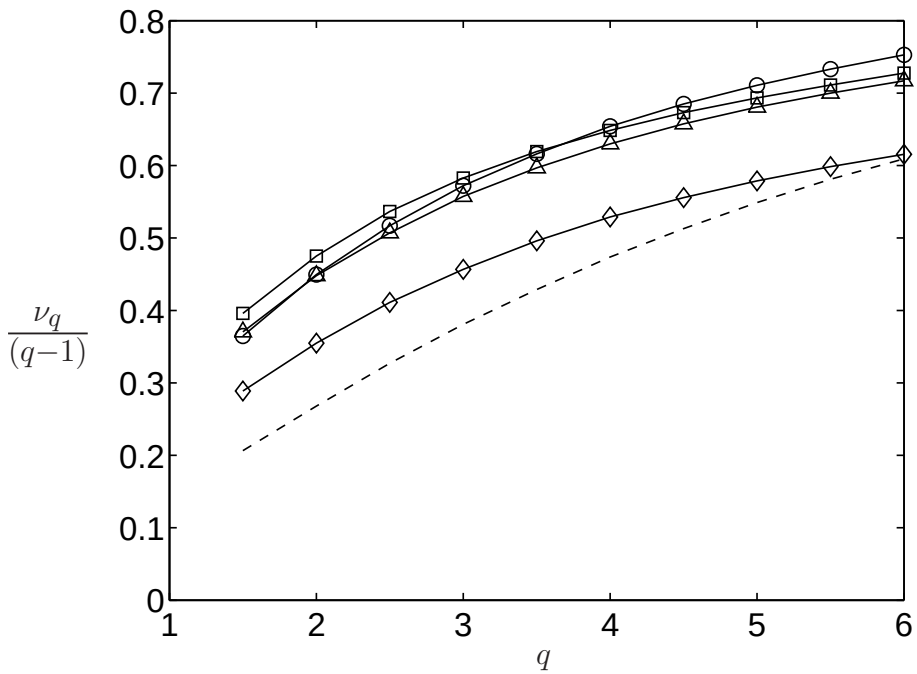

Figure 5.21: The scaling exponents for χ_r defined in Eq. 5.37 at $R_\lambda \approx 140$ with $Sc = 1/8$ (◯), 1 (△), 4 (□) and 64 (◇). Dashed line: exponents for the energy dissipation rate.

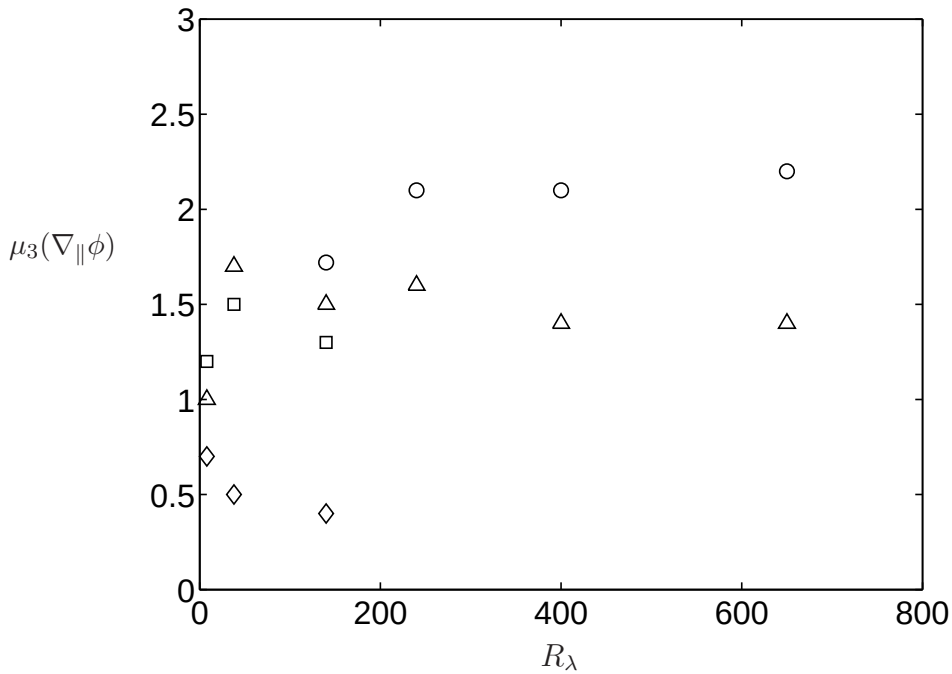

Figure 5.22: Skewness of scalar gradient fluctuations parallel to the imposed mean with $Sc = 1/8$ (◯), 1 (△), 4 (□) and 64 (◇). Data at $R_\lambda \geq 140$ correspond to simulations at $k_{max}\eta \approx 1.5$.

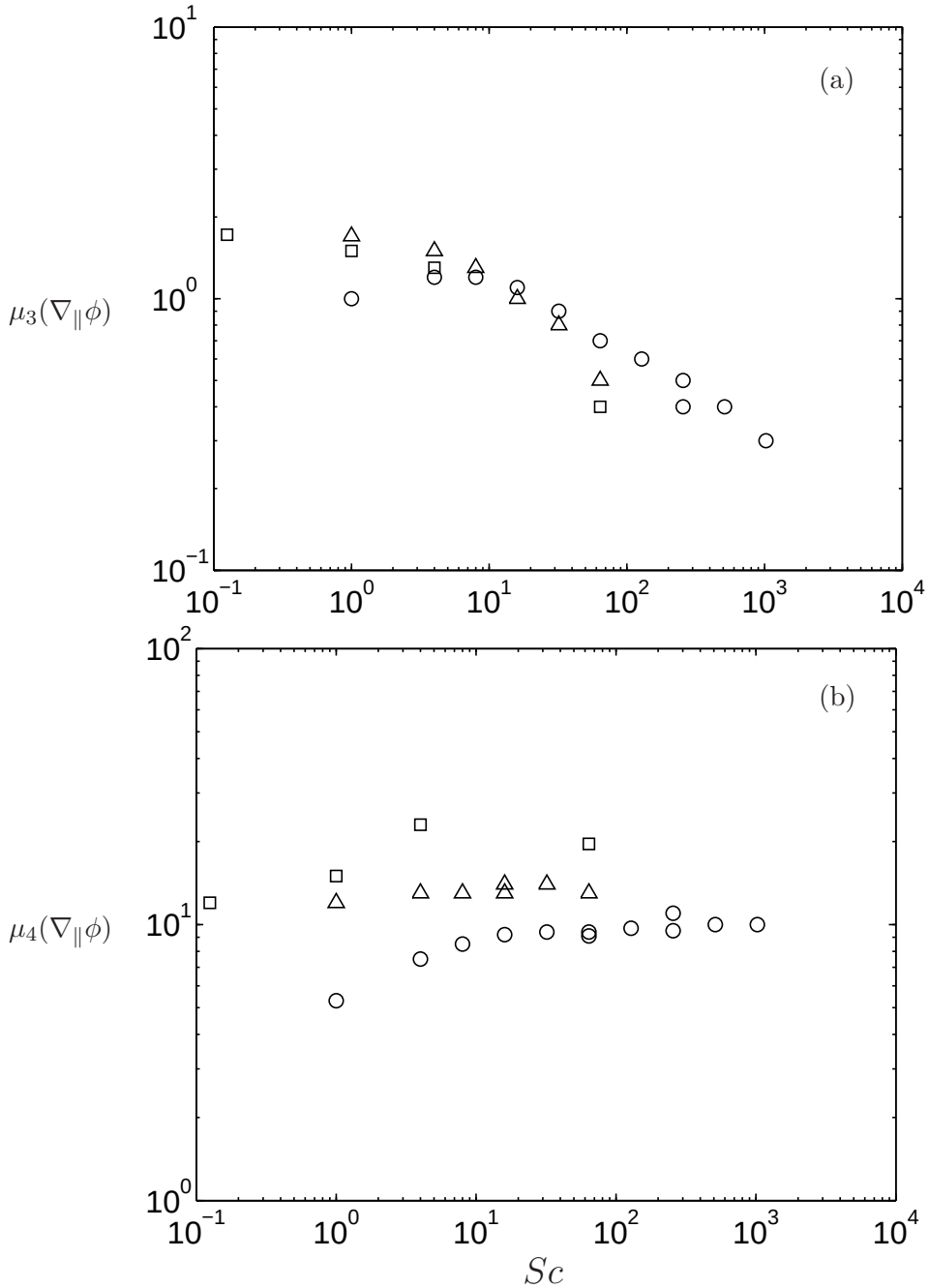

Figure 5.23: Skewness (a) and flatness (b) factors of scalar gradients fluctuations parallel to the imposed mean at $R_\lambda \approx 8$ (◯), 38 (△) and 140 (□).

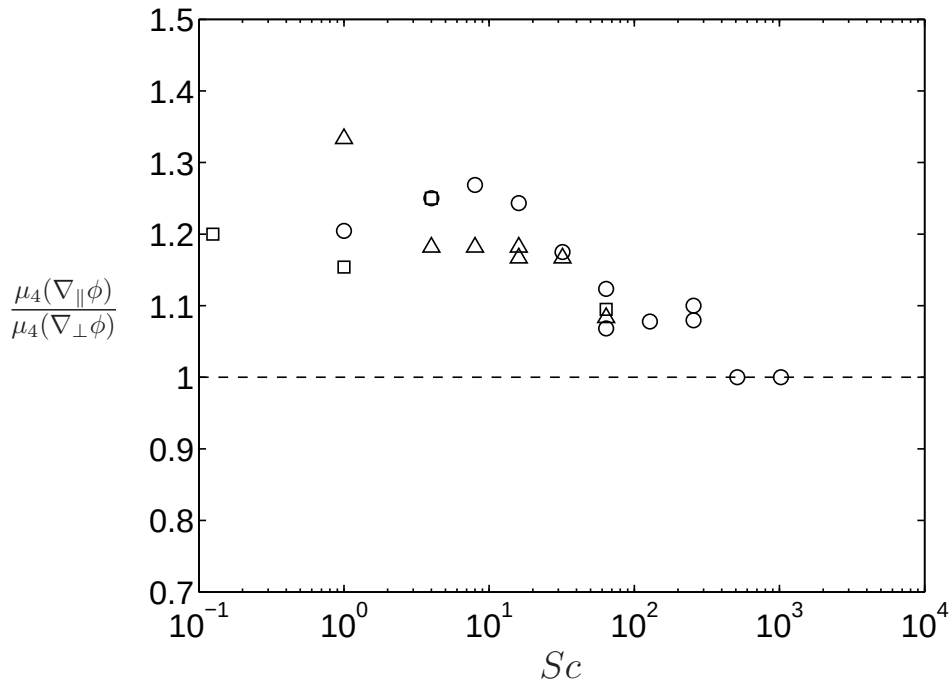

Figure 5.24: Ratio of flatness factors of scalar gradients fluctuations parallel and perpendicular to the imposed mean at $R_\lambda \approx 8$ (◯), 38 (△) and 140 (□).

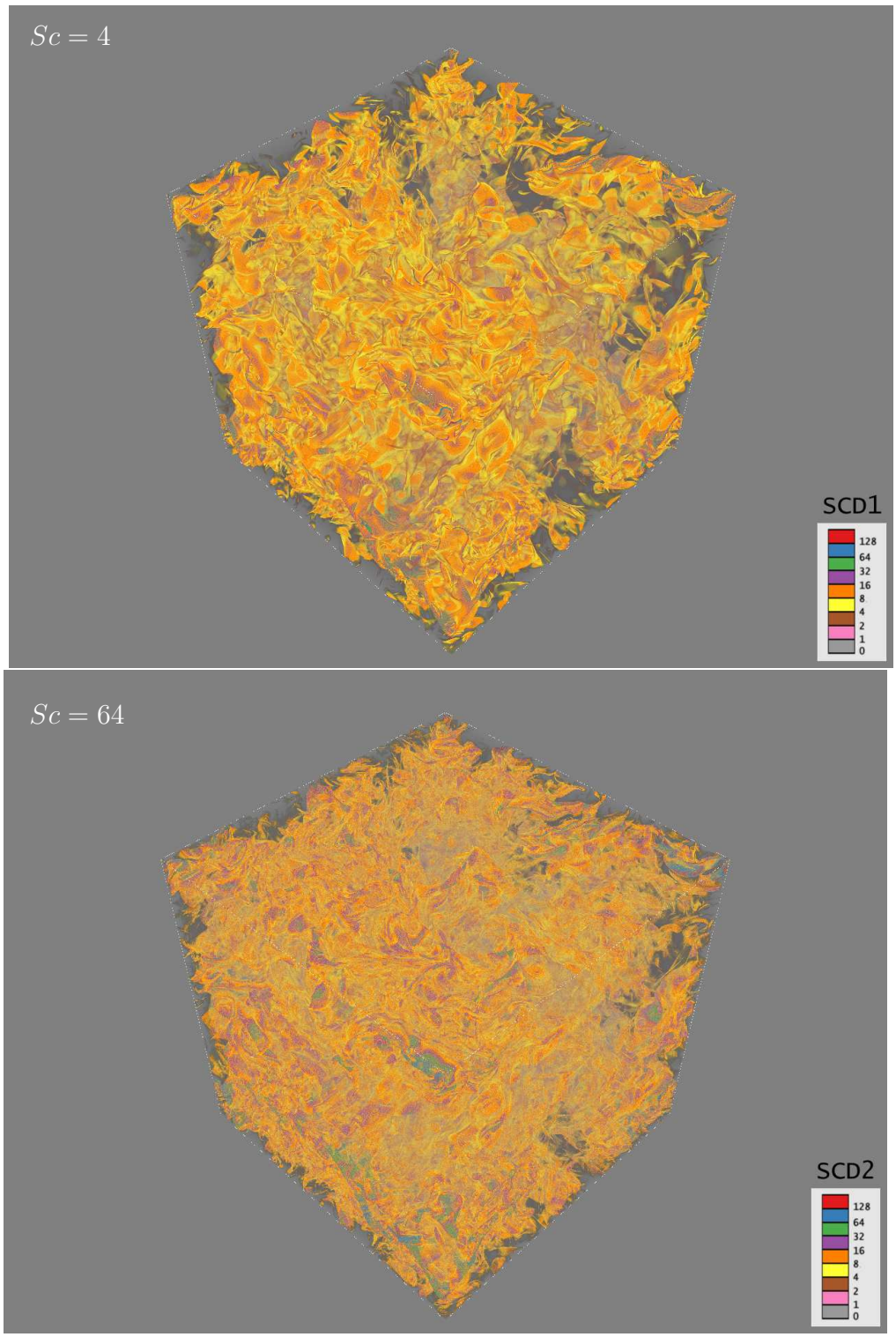

Figure 5.25: Three-dimensional volume renders for scalar dissipation rate normalized by its mean χ' for $Sc = 4$ (top) and 64 (bottom) at $R_\lambda \approx 140$ (2048^3). Courtesy of Amit Chourasia of SDSC.

CHAPTER VI

ROTATING TURBULENCE

In this Chapter we study the effect of solid-body rotation on the scaling of turbulence which is found in many problems in engineering (e.g. turbomachinery, reciprocating engines with swirl) geophysics and astrophysics. The effects of rotation on the turbulence structure, through the Coriolis term in the equations or motion, are known to be profound although not completely understood. It is known, for example, that although the Coriolis term does not appear explicitly in the kinetic energy budget equation it weakens the fundamental property of an energy cascade from large to small scales. Therefore, solid-body rotation modifies the scaling of turbulence through a coupling with the nonlinear interactions responsible for this transfer. The simplest flow in which the effects of rotation can be isolated and studied more clearly is the case of initially isotropic turbulence subjected to solid-body rotation.

In the next Section we give some background on the subject and the additional numerical constraints that have to be considered in simulations. In Section 6.1 we focus on the scaling of anisotropies developed due to the introduction of rotation. For this purpose we look at the behavior of integral length scales, the anisotropy tensor (and its components) and component spectra. In Section 6.2 we study the effect of rotation on intermittency through moments of velocity gradients and the basic scaling of structure functions. The fundamental Taylor-Proudman theorem for rapidly rotating flow is investigated in Section 6.4 and we found a more accurate representation of the observed behavior with an alternative version of the theorem which is derived here. The theoretical results are used to study further anisotropy and the scaling of structure functions. The conclusions and further issues are discussed in Section 6.5.

6.1 Background and Numerical Simulations

In general, rotation gives rise to both Coriolis and centrifugal accelerations. However, if the equations of motion are written in a rotating frame of reference only the Coriolis acceleration is important. The Navier-Stokes equations in a such a frame can be written as:

$$\frac{\partial u_i}{\partial t} + u_j \frac{\partial u_i}{\partial x_j} = -\frac{1}{\rho}\frac{\partial p}{\partial x_i} - 2\epsilon_{ijk}\Omega_j u_k + \nu \frac{\partial^2 u_i}{\partial x_j \partial x_j} + f_i, \tag{6.1}$$

where ϵ_{ijk} is the alternating symbol and the vector $\mathbf{\Omega}$ is the imposed rotation rate. (Note that in this Chapter the symbol Ω stands for rotation rate and should not to be confused with enstrophy in previous Chapters.) The numerical scheme to solve Eq. 6.1 is based on a diagonal form of the system of equations in Fourier space which makes use of additional auxiliary variables and allows us to integrate both viscous and rotation terms exactly via integrating factors. The details of the algorithm and its implementation can be found in Yeung & Zhou (1998).

We note that by non-dimensionalizing the Navier-Stokes equations in a rotating frame using U and L as velocity and length scales, we obtain two nondimensional parameters: UL/ν which is a large-scale Reynolds number and $U/(\Omega L)$ which is known as the Rossby number and is a measure of inertia (nonlinear) to Coriolis effects. We note that the Rossby number can also be thought of as a ratio of the rotation time scale $(1/\Omega)$ to turbulence time scales. If we use a characteristic time for large scales (e.g. $K/\langle\epsilon\rangle$ where K is the turbulent kinetic energy) then $Ro_T = \langle\epsilon\rangle/(2K\Omega)$ is known as the turbulence Rossby number. The micro Rossby number, obtained by using Kolmogorov time scale $\tau_\eta = (\nu/\langle\epsilon\rangle)^{1/2}$, is defined as $Ro^\omega = 1/(2\tau_\eta\Omega)$.

It is well known that rotation can only affect turbulence by nonlinear mechanisms (e.g. Cambon *et al.* 1997, Jacquin *et al.* 1990). Several features are known for this flow:

- The spectral transfer from large scales to small scales is reduced as rotation rate Ω

increases. This implies that the dissipation rate (at small scales) is reduced too (e.g. Morinishi *et al.* 2001, Yeung & Zhou 1998, Jacquin *et al.* 1990).

- The energy spectrum shows a steeper slope than -5/3 (K41). Several spectral slopes from -2 to -3 were proposed in the literature (Baroud *et al.* 2002, Zeman 1994, Zhou 1995, Mahalov & Zhou 1996, Cambon *et al.* 2004) although the available data from experiments and simulations is not conclusive.

- Anisotropy develops through nonlinear interactions modified by rotation. One way anisotropy is observed is by the faster growth of length scales along the axis of rotation (e.g. Cambon *et al.* 1997, Yeung & Zhou 1998). Although the Reynolds stress tensor b_{ij} remains almost isotropic there are still anisotropies that can be studied by splitting $b_{ij} = b^e_{ij} + b^z_{ij}$ where b^e_{ij} is the *directional anisotropy* while b^z_{ij} is known as the *polarization anisotropy* (Yang & Domaradzki 2004). Anisotropy at small scales has also been observed (Yeung & Zhou 1998) although these are less known.

- There is a reduction of intermittency as measured by moments of velocity gradients especially aligned with the rotation axis (Yeung *et al.* 2003).

Due to the increase in integral length scales it is necessary to check whether the periodic boundary conditions in our simulations modify the results substantially. For this purpose we have performed simulations with similar initial conditions and several rotation rates on the usual $(2\pi)^3$ domain and a larger $(4\pi)^3$ domain. In order to keep the same resolution at small scales when the linear size of the domain is doubled the number of grid points (and the computation power required) increase by a factor of eight. Typical results for integral length scales defined as

$$L_{\alpha\alpha,\beta} = \frac{1}{\langle u_\alpha u_\alpha \rangle} \int_0^\infty \langle u_\alpha(\boldsymbol{x}) u_\alpha(\boldsymbol{x} + r\boldsymbol{e}_\beta) \rangle dr, \tag{6.2}$$

are shown in figure 6.1. Transverse length scales along the axis of rotation ($\beta = 3$ in our simulations) grow when rotation is imposed while transverse length scales perpendicular to it do not undergo significant changes. It is seen that a small domain (i.e. $(2\pi)^3$) indeed tend to suppress the growth of integral scales (line A in figure 6.1). When a larger domain is used (i.e. $(4\pi)^3$), it is clear that integral scales grow further although they do not approach a value twice as large as in the $(2\pi)^3$ domain. At lower R_λ we found that increasing the domain further did not lead to a substantial increase in integral scales and a $(4\pi)^3$ was adopted. Another advantage of a larger domain is that statistical variability is substantially reduced since a larger domain allows better sampling of the large scales which contain most of the turbulence kinetic energy.

An additional constraint in simulations of rapidly rotating flows is that the time step Δt in the integration scheme should be small enough to capture fast fluctuations imposed by rotation. We verified in our simulations that the *wave* Courant number $\Omega\Delta t$ is much less than unity (see e.g. Bartello 2002, Yeung & Xu 2004).

We have performed simulations of turbulence in a rotating frame with initial conditions being stationary, isotropic turbulence at $R_\lambda \approx 240$ aimed at extending previous results (Yeung & Zhou 1998) and understanding the observations mentioned above. The rotation vector in our simulations is defined as $\mathbf{\Omega} = (0, 0, \Omega)$ and such that the initial Rossby numbers (at the time rotation is introduced) are $Ro^\omega = 4$, 1 and 1/4.

The energy and dissipation rates provide important information about global measures of the state of the turbulence. In figure 6.2 we show the evolution of these quantities for all rotation rates in our simulations. When rotation is imposed there is no noticeable decrease in turbulent kinetic energy. On the other hand, the energy dissipation rate drops significantly as is seen in figure 6.2(b). The higher the rotation rate, the larger the decrease in $\langle\epsilon\rangle$. This observation is consistent with a reduced spectral transfer and with previous

results (Yeung & Zhou 1998).

6.2 Characterization of Anisotropy

To characterize anisotropy at large scales, integral length scales have been used extensively. In figure 6.3 we show transverse integral scales along and perpendicular to the the axis of rotation. In isotropic turbulence all six transverse components (see Eq. 6.2) are statistically identical. A comparison between length scales along the axis of rotation (part (a) in the figure) and perpendicular to it (part (b)) shows departures from isotropy at all Ro^{ω}. However, we see that anisotropy is strongest at intermediate rotation rates ($Ro^{\omega} = 1$) consistent with the results in Bartello *et al.* (1994) and Yang & Domaradzki (2004). Jacquin *et al.* (1990) suggested three different regimes in terms of Rossby numbers. If Ro_T is large then the rotation time scale is larger than all turbulent time scales and the effects of rotation are very weak. At intermediate rotation rates ($Ro_T > 1$ but $Ro^{\omega} < 1$) the rotation modifies the nonlinear interactions while at very large rotation rates (Ro^{ω} small) the nonlinear terms are completely damped. Therefore, it is at intermediate scales that rotation has the strongest effects on the structure of the turbulence. Thus, the nonlinear interactions modified by rotation seem to trigger the anisotropy at large scales.

As mentioned in Section 6.1, although the anisotropy tensor b_{ij} remains isotropic, it is known that anisotropies develop at all scales. To characterize them it is useful to divide the anisotropy tensor into different parts as follows. The second-order spectral tensor $\hat{U}_{ij}$ is defined as

$$\langle \hat{u}_i^*(\mathbf{p}, t)\hat{u}_j(\mathbf{k}, t)\rangle = \hat{U}_{ij}\delta(\mathbf{k} - \mathbf{p}) \tag{6.3}$$

and is related to the Reynolds stress tensor according to

$$R_{ij} = \langle u_i u_j \rangle = \int \Re[\hat{U}_{ij}(\mathbf{k})]d\mathbf{k} \tag{6.4}$$

where $\Re[\ldots]$ denotes the real part. It is now convenient to express the velocity field in the

so-called Craya-Herring frame which is an orthonormal basis attached to the wavenumber vector $\mathbf{k}$ (Craya 1958, Herring 1974). Due to incompressibility the velocity lies in a plane perpendicular to $\mathbf{k}$ whose local frame may be defined as

$$\mathbf{e}^{(1)}(\mathbf{k}) = \frac{\mathbf{k} \times \mathbf{\Omega}}{|\mathbf{k} \times \mathbf{\Omega}|}, \qquad \mathbf{e}^{(2)}(\mathbf{k}) = \frac{\mathbf{k} \times \mathbf{e}^{(1)}}{|\mathbf{k} \times \mathbf{e}^{(1)}|}. \tag{6.5}$$

With the additional introduction of the eigenvectors of the curl operator (Cambon & Jacquin 1989)

$$N_i(s\mathbf{k}) = e_i^{(2)}(\mathbf{k}) - ise_i^{(1)}(\mathbf{k}), \qquad s = +1, -1 \tag{6.6}$$

the real part of the second-order spectral tensor Eq. 6.3 becomes

$$\Re[\hat{U}_{ij}] = \frac{E(k)}{4\pi k^2} P_{ij} + \left(e(\mathbf{k}) - \frac{E(k)}{4\pi k^2} \right) P_{ij} + \Re[ZN_iN_j], \tag{6.7}$$

where $e(\mathbf{k})$ is the energy in a single mode $\mathbf{k}$, $E(k)$ is the usual three-dimensional spectrum so that $E(k)/4\pi k^2$ gives the average energy per mode in the shell of radius $k = |\mathbf{k}|$ and $P_{ij} = \delta_{ij} - k_ik_j/k^2$ is the solenoidal projection tensor. The vectors N_i are the orthogonal basis and $Z = \hat{U}_{ij}(\mathbf{k}, t)N_i(-\mathbf{k})N_j(-\mathbf{k})/2$ is called the complex deviator. More details about this representation can be found in Cambon *et al.* (1997), Cambon & Jacquin (1989) and Herring (1974). Because the first term on the right-hand side characterizes a pure three-dimensional isotropic state the other two terms represent departures from it. The Reynolds stress tensor can be obtained by integrating Eq. 6.7 in wavenumber space according to Eq. 6.4

$$\langle u_iu_j \rangle = q^2 \frac{\delta_{ij}}{3} + \int \left(e(\mathbf{k}) - \frac{E(k)}{4\pi k^2} \right) P_{ij} d\mathbf{k} + \int \Re[ZN_iN_j] d\mathbf{k}, \tag{6.8}$$

from which it is trivial to obtain the anisotropy tensor $b_{ij} = \langle u_iu_j \rangle / q^2 - \delta_{ij}/3$

$$b_{ij} = \int \left(e(\mathbf{k}) - \frac{E(k)}{4\pi k^2} \right) P_{ij} d\mathbf{k} + \int \Re[ZN_iN_j] d\mathbf{k} \tag{6.9}$$

$$= b_{ij}^e + b_{ij}^z. \tag{6.10}$$

The first term b^e_{ij} characterizes *directional anisotropy* as it is non trivial only if the spectrum depends on both magnitude and direction of the wavenumber vector. It measures the departure from a shell-averaged spectrum. The second term, b^z_{ij}, denotes the departure from a tensorial isotropic distribution on the plane perpendicular to the wavenumber vector and is called *polarization anisotropy* (Cambon & Jacquin 1989). It is also important to note that the information contained in b^e_{ij} and b^z_{ij} is analogous to the descriptors suggested by Kassinos & Reynolds (1994) in that they give information about both the *componentiality* and the *dimensionality* of the flow (Mansour *et al.* 1991b, Morinishi *et al.* 2001).

The evolution of b^e_{33} is shown in figure 6.4(a) (in an axisymmetric situation b_{11} and b_{22} are equal to $-b_{33}/2$). We can see that the greatest anisotropy appears at an intermediate rotation rate $Ro^\omega = 1$ (line B) which is consistent with the strongest anisotropy seen from integral length scales. The increase in b^e_{33} is related to the anisotropic distribution of energy in wavenumber space. In particular, the positive value is consistent with a concentration of energy in the equator, i.e. small k_3 (Morinishi *et al.* 2001). The polarization anisotropy is shown in figure 6.4(b). It becomes negative and the sum $b^e_{33} + b^z_{33}$ is close to zero as seen in part (c) of the figure. The rapid oscillations in b^z_{33} occur in time scales of order $O(1/\Omega)$ and are essentially due to the linear phase-scrambling effects (Mansour *et al.* 1991b) of rotation which were also observed in Yeung & Zhou (1998) and Yang & Domaradzki (2004). We can also see that the data does not support a trend towards a pure two-dimensional, two-component state (2D-2C) which is characterized by $b_{33} = -1/3$, $b^e_{33} = 1/6$ and $b^z_{33} = -1/2$. It cannot be ruled out, however, that at asymptotically long times these values could be reached. However, due to the increase in integral length scales the effect of the domain size should be addressed if contamination from the imposed boundary conditions are to be avoided. For reference, we mention that the values corresponding to a pure two-dimensional three-component state (2D-3C) are $b_{33} = b^e_{33} = 1/6$ and $b^z_{33} = 0$.

To study anisotropic features at all scales it is useful to look at the spectra of different velocity components which are shown in figure 6.5 for different rotation rates at $t/T_{E,0} \approx 4.5$. In isotropic turbulence, the three component spectra are equal and show a $k^{-5/3}$ inertial range seen as a plateau in figure 6.5(a). When rotation is introduced K41 phenomenology has to be modified due to the additional length and time scales in the spectral process. At low rotation rates (part (b)) the spectral slope is not very different from the non-rotating case altough apparent departures from isotropy are seen at intermediate scales where we see more energy in u_3 than in the components perpendicular to $\mathbf{\Omega}$. This behavior can be explained by a stronger reduction of energy transfer to components perpendicular to the axis of rotation (Yeung & Zhou 1998). We also note, however, that at the lowest wavenumbers the three component spectra are very close to each other consistent with an isotropic Reynolds stress tensor. In the figure we include $k_\Omega \equiv (\Omega^3/\langle\epsilon\rangle)^{1/2}$ below which, according to Zeman (1994), the effects of rotation are important. Note that for intermediate rotations (parts (b) and (c)) only part of the spectrum is affected whereas for strong rotation (part (d)) all the spectrum is affected ($k_\Omega > 10^3$ and is not seen). At intermediate rotation rates ($Ro^\omega = 1$) our data may be consistent with a (narrow) k^{-2} scaling as suggested by Zhou (1995). The same behavior was observed for the three-dimensional spectrum (not shown). This is consistent with previous results at lower R_λ from Yeung & Zhou (1998). At high rotation rates ($Ro^\omega = 1/4$) the spectra evolves to a k^{-3} scaling as seen in figure 6.5(d). This scaling, which holds better for components perpendicular to $\mathbf{\Omega}$, appears over a wider range of scales than the k^{-2} at a higher Rossby number. The transition between k^{-2} and k^{-3} was also observed in Yang & Domaradzki (2004). Although more elaborated derivations exist (see e.g. Cambon *et al.* 2004) a k^{-3} spectrum can be derived by dimensional analysis if we assume that, for a range of scales, Ω and k are the only relevant parameters. Comparison of spectra at different rotation rates suggest that anisotropy is strongest at intermediate

rotation rates ($Ro^{\omega} = 1$) and intermediate scales.

6.3 Intermittency and Structure

In previous simulations at a lower Reynolds number on a smaller domain, Yeung *et al.* (2003) found that as Ω is increased, intermittency is reduced and velocity gradients become less non-Gaussian. The results presented here support these conclusions at earlier times as shown in Table 6.1. Initially (isotropic turbulence) the skewness and flatness factors of longitudinal velocity gradients are known to have the values $\mu_3 \approx -0.55$ and $\mu_4 \approx 6.81$. For low rotation rate ($Ro^{\omega} = 4$) there is no significant change in either μ_3 or μ_4. However, at high rotation rates we see that at early times μ_3 is close to zero and μ_4 to 3 (which are Gaussian values). The monotonic trend with Ro^{ω} suggests that the reduced non-Gaussianity is related to the damping of the nonlinear terms as opposed to the interaction of rotation with the dynamics of the nonlinear transfer. The observed reduced spectral transfer (also monotonic with Ro^{ω}; see e.g. figure 6.2) indicates that, as rotation increases, the spectral peak for velocity gradients would move to lower wavenumbers where the forcing (with Gaussian statistics) has more influence. At later times both skewness and flatness factors increase. It is not clear whether they will reach the same stationary state values before rotation is introduced. Longer simulations have to be conducted although integral length scales can grow to unacceptable levels. For gradients along the axis of rotation the same drop in μ_3 and μ_4 was observed at early times although they seem to return to Gaussian values later. In order to obtain better statistics ensemble averaging is desired. However, due to the non-stationary nature of this flow this would require performing several simulations.

Intermittency is also commonly studied through structure functions (e.g. Monin & Yaglom 1975, Frisch 1995). If a scaling range exists, the exponents give useful information about the structure of the flow. In the case of rotating turbulence we have to distinguish between the direction along the axis of rotation (x_3) and perpendicular to it. In figure 6.6

we show the longitudinal structure function $\langle(\Delta_{r_3}u_3)^n\rangle/(\langle\epsilon\rangle r_3)^{n/3}$ (where r_3 is a separation in the x_3 direction) for $n = 2$, 3, 6 and 8 at $t/T_{E,0} \approx 4.0$. By careful examination of the third order function with no rotation, we delimited the inertial range in which power laws are to be sought. This range is indicated by the dashed vertical lines in figure 6.6. For small distances, an analytic range is seen in the figure, for all rotation rates, as the structure functions approach $r^{2n/3}$ (dashed-dotted lines). It is clear from figure 6.6(a) that the local slope of second order structure functions in the scaling range increases monotonically with Ω. The third order structure function, on the other hand, shows a decrease in its normalized value at all scales. In addition, the scaling range (plateau) is reduced and it changes signs at a smaller scale. As in Simand *et al.* (2000) and Morize *et al.* (2005) this can be interpreted as a reduction of spectral transfer and even inversion for scales larger than the zero-crossing of $\langle(\Delta_{r_3}u_3)^n\rangle$. A scaling range is not clear and no power law can be extracted unambiguously. The sixth and eighth order structure functions (figure 6.6c and d) show an interesting feature which could not be seen in lower order moments. For intermediate rotation rates, the data suggest the existence two scaling ranges. At small scales $9 \lesssim r/\eta \lesssim 30$ structure functions approach a plateau consistent with K41 phenomenology. At larger scales ($30 \lesssim r/\eta \lesssim 300$), however, the slope increases with rotation. This range of scales coincides roughly with the inertial range for the non-rotating case (vertical dashed lines). For reference, the figure also includes the scale $r_\Omega \approx 2\pi/k_\Omega$ for each rotation rate (except for $\Omega = 0$) as solid symbols. For $Ro^\omega = 4$ and 1, the sixth and eighth order structure functions are close to the non-rotating case for $r < r_\Omega$ whereas for $r > r_\Omega$ structure functions deviate from the non-rotating case and exhibit the two scaling ranges mentioned above. Therefore, the scale r_Ω obtained from the wavenumber k_Ω suggested by Zeman (1994), appears to be a good indicator of influence of rotation in physical space. At strong rotation rates ($Ro^\omega = 1/4$), all scales in our simulations are affected and no evidence of two

different scalings was found.

In figure 6.7 we show the scaling exponents obtained by fitting a power law of the form r^{ζ_n} in the "inertial range" delimited by the dashed lines in figure 6.6. As is well known, the non-rotating case (circles) shows anomalous scaling, i.e. $\zeta_n < n/3$. It is clear that as the Rossby number decreases, the exponents increase monotonically. At the strongest rotation the scaling exponents are not far from $p/2$ which was also observed in Baroud *et al.* (2002) and Simand *et al.* (2000). The linear dependence of the exponents ζ_n with n, yet anomalous (i.e. different from $n/3$), suggests a self-similar behavior of the flow (Frisch 1995). It is important to note that this self-similar behavior appears only at scales larger than some intermediate scale (within the "inertial range"). Below this length scale, structure functions may still scale according to K41. A wider range of scales (i.e. higher Reynolds number) is necessary to address this claim more conclusively. We note that for isotropic turbulence, $\zeta_n = n/2$ would imply a three-dimensional spectral slope of -2 (e.g. Monin & Yaglom 1975). However, in a strongly anisotropic situation such as the present, different scaling exponents in different directions may combine to give a different spectral slope and have to be interpreted carefully (Cambon *et al.* 2004).

To characterize the internal structure of turbulent flows, many studies have investigated the preferential alignments of different vectors which are known to be unrelated for Gaussian fields (see e.g. Tsinober 1998). It is well-known, for example, that in isotropic turbulence vorticity tends to align with the eigenvector associated with the middle eigenvalue of the strain-rate tensor (e.g. Ashurst *et al.* 1987, Tsinober *et al.* 1992). In figure 6.8 (left panels) we show, for different rotation rates, the PDF of the cosine of the angle between $\boldsymbol{\omega}$ and $\boldsymbol{\Lambda}_2$, the eigenvector associated with the middle eigenvalue λ_2. Lines A in the figures are for $t/T_{E,0} = 0$ which are the same for all Ro^{ω} and correspond to the non-rotating (isotropic) initial conditions. As already mentioned, initially there is a strong alignment between

vorticity and the middle eigenvector showing strong departures from Gaussianity (horizontal dashed line). For low rotation rates ($Ro^{\omega} = 4$), the effect of the Coriolis force on this alignment is negligible. When a stronger rotation is imposed ($Ro^{\omega} = 1$), we see that there is a fast reduction of non-Gaussianity at earlier times followed by a return to a state of preferential alignment. At later times (line E), the alignment is even stronger than in the non-rotating case. For the case with strongest rotation ($Ro^{\omega} = 1/4$), the reduction of non-Gaussian features is more pronounced but the return to a preferential alignment is apparent. Longer simulations are needed to address the asymptotic state of the PDF of $\cos(\boldsymbol{\omega}, \boldsymbol{\Lambda}_2)$.

The generation of enstrophy is known to be related to the process of vortex stretching which appears as a source term in the evolution equation for enstrophy. This term, which can be written as $\omega_i W_i$ (with $W_i = \omega_j s_{ij}$ being the vortex stretching vector), shows that the production of enstrophy depends on both the magnitude of the vectors ($\boldsymbol{\omega}$ and $\mathbf{W}$) and their relative alignment. Moreover, the observed strong tendency to be parallel (as opposed to anti-parallel) shows the predominance of enstrophy generation (as opposed to enstrophy destruction). In figure 6.8 (right panels) we show the PDF of the angle between vorticity and the vortex stretching vector. For low rotation rates, we see again a weak effect on this alignment. For high rotation rates, we see a fast departure from the preferential alignment in non-rotating turbulence (line A) and a trend towards reduction of non-Gaussianity (the dashed line shows the PDF for strictly Gaussian fields as derived in Shtilman *et al.* 1993). It is seen that the alignment between $\boldsymbol{\omega}$ and $\mathbf{W}$ approaches an asymptotic state in a short time scale whereas the alignment between $\boldsymbol{\omega}$ and $\boldsymbol{\Lambda}_2$ continues to evolve for the entire lentgh of the simulation. It is also noted that $\cos(\boldsymbol{\omega}, \mathbf{W})$ seems closer to the Gaussian prediction than $\cos(\boldsymbol{\omega}, \boldsymbol{\Lambda}_2)$. Because the PDFs for Gaussian fields are symmetric, it is clear that the mean value is zero. For example, $\cos(\boldsymbol{\omega}, \mathbf{W})$ which can also be thought of as the normalized enstrophy production $\omega_i W_i/(|\boldsymbol{\omega}||\mathbf{W}|)$, vanishes in that case. Our results at $Ro^{\omega} = 1/4$

show that in fact strong rotation symmetrizes the PDF of $\cos(\boldsymbol{\omega}, \mathbf{W})$ reducing enstrophy generation. This result is consistent with the reduced spectral transfer to small scales.

6.4 Theoretical Considerations

6.4.1 A Local Taylor-Proudman Theorem

An important theorem for rapidly rotating flows is the Taylor-Proudman theorem which was originally obtained by neglecting the unsteady, nonlinear and viscous terms and taking the curl of the Navier-Stokes equations in a rotating frame of reference. The result is (see e.g. Greenspan 1968)

$$(\boldsymbol{\Omega} \cdot \nabla)\mathbf{u} = 0 \tag{6.11}$$

which simply says that there is no variation in the velocity (*all* components) along the axis of rotation. That is to say, a two dimensional state. Although some two dimensional patterns were observed in turbulent flows no clear demonstration of a Taylor-Proudman theorem was found.

Using our DNS we compare the relative weight of the terms in Eq. 6.1 in figure 6.9 where we show the variance of the different contributions at different rotation rates and for different components of the velocity. For the non-rotating case (part (a) in the figure), we see that the local acceleration and the non-linear terms are the largest although the pressure gradients are of the same order of magnitude. The viscous terms are small and, as is well-known, their contribution decreases with Reynolds numbers. The forcing contribution in Eq. 6.1 (not shown) is found to be smaller than the all the other terms. Figures 6.9(b) and (c) show the contributions to the equations for u_1 and u_3 respectively for the strongest rotation available ($Ro^{\omega} = 1/4$). The dominant terms in the equation for u_1 are the rotation term, pressure gradient and local acceleration. It is clear that at this low Rossby number the non-linear terms are more than an order of magnitude smaller than e.g. rotation terms. The viscous terms are three orders of magnitude smaller. Since the equation for the velocity

component along the axis of rotation does not have an explicit contribution from the Coriolis term, the local acceleration is balanced by pressure gradients as is seen in figure 6.9(c). As expected, the unsteady term cannot be neglected in a turbulent flow which was a crucial step to obtain Eq. 6.11. Keeping the three dominant terms in Eq. 6.1 and taking the curl leads to

$$\frac{\partial \boldsymbol{\omega}}{\partial t} \approx 2(\boldsymbol{\Omega} \cdot \nabla)\mathbf{u} \tag{6.12}$$

which, using our choice $\boldsymbol{\Omega} = (0, 0, \Omega)$, becomes

$$\frac{\partial \omega_p}{\partial t} \approx 2\Omega \frac{\partial u_p}{\partial x_3}. \tag{6.13}$$

It is clear that regions of small velocity gradients will be those with slow time variation of vorticity. To examine this we computed the conditional expectation $\langle u_{3,3} | \omega_{3,t} \rangle$ normalized by their standard deviations. (For simplicity in notation, the argument after the comma in subscripts denote differentiation with respect to that argument. For example, $u_{3,3}$ denotes $\partial u_3/\partial x_3$ and $\omega_{3,t}$ denotes $\partial \omega_3/\partial t$.) If Eq. 6.13 is a good approximation then we would find a linear dependence of this quantity with the conditioning variable. In figure 6.10(a) we show this conditional expectation at late times ($t/T_{E,0} \approx 4.5$) for all rotation rates at an initial $R_\lambda \approx 240$. For non-rotating turbulence (line A) the conditional mean is far from the prediction given by Eq. 6.13 since the non-linear terms in the Navier-Stokes equations cannot be neglected. However, it is clear that as rotation increases, Eq. 6.13 becomes a better approximation for a wider range of fluctuations. At $Ro^\omega = 1/4$ (line D), this range extends to about ± 2 standard deviations. Therefore, in order to have two-dimensional features (i.e. small gradients along the axis of rotation) in addition to low Rossby numbers, the quantity $\omega_{3,t}$ should be small. At intermediate rotation rates, the contribution from the other terms in Eq. 6.1 are not negligible although for very small values of $\omega_{3,t}$ the linear relation Eq. 6.13 may still be a good approximation. In figure 6.10(b) we show the same quantity for even lower Rossby numbers (stronger rotation) at a lower initial Reynolds

number. At the strongest rotation (line C) Eq. 6.13 is in excellent agreement with the data. The results presented so far suggest a monotonic trend with Ro^{ω} to a state governed by Eq. 6.13.

A natural question now is regarding the volume occupied by regions where $\omega_{3,t}$ is small. To study this we show in figure 6.11(a) the PDF of $\omega_{3,t}/\sigma_{\omega_{3,t}}$ (with $\sigma_{\omega_{3,t}}$ the standard deviation of $\omega_{3,t}$) at $t/T_{E,0} \approx 4.5$. We can see that it presents wider tails at intermediate rotation rates although the effect is weak. In part (b) of the figure, we show the same PDF but using linear scales. At intermediate rotation rates ($Ro^{\omega} = 4$) the distribution shows an increased probability of small values compared to the standard deviation. For the strongest rotation, the core does not show the same narrow peak and values of order of the standard deviation are even more likely than the non-rotating case. However, the results discussed above were normalized by the *instantaneous* standard deviation which is different at different rotations. To further compare the effects of the introduction of rotation with its initial (isotropic) state, in figure 6.11(c) and (d) we show the PDF of $\omega_{3,t}/\sigma_{\omega_{3,t}}^{(t=0)}$ where $\sigma_{\omega_{3,t}}^{(t=0)}$ is the standard deviation at the beginning of the simulation (which is the same for all cases). We can see now that in terms of the initial distribution of $\omega_{3,t}$, large values become less likely as rotation increases. In figure 6.11(d) we can also see that regions with very small time variation of vorticity compared to the initial standard deviation are larger for intermediate rotation rates ($Ro^{\omega} = 1$). Under both normalizations, our results suggest a non-monotonic trend with Ro^{ω}: small values of $\omega_{3,t}$ occupy larger volumes at intermediate rotation rates. Therefore, although Eq. 6.13 becomes a better approximation at small Rossby numbers, it is at intermediate values of rotation at which larger regions of space contain small $\omega_{3,t}$. Note however, that for our data at all rotation rates, $|\omega_{3,t}|/\sigma_{\omega_{3,t}}$ is smaller than 2 (which limits the range where Eq. 6.13 is a good approximation; see figure 6.10(a)) over more than 95% of the space.

A consequence of the results above is that there is no trend towards a Taylor-Proudman state (i.e. Eq. 6.11). However, it is still possible to look for those regions in space where it does hold, that is a *local* Taylor-Proudman theorem. The topology of $\omega_{3,t}$ for late times is shown in figure 6.12 for our $R_\lambda \approx 240$ (1024^3) simulation. Non-rotating turbulence (top on the figure) shows a wide range of scales where regions of large and small values of $|\omega_{3,t}|$ are evenly distributed in space. There is no difference between planes parallel (left) and perpendicular (right) to the axis of rotation. As rotation rate increases, the data shows the disappearance of fine structures monotonically with Ro^ω which is consistent with a reduced spectral transfer. However, we also see that the difference between planes parallel and perpendicular to the axis of rotation is more pronounced at intermediate rotation rates ($Ro^\omega = 1$). At this Rossby number, long structures along the axis of rotation are apparent, consistent with increased integral length scales in that direction. Long structures aligned with $\mathbf{\Omega}$ were also observed (not show here) for the energy dissipation rate (Donzis *et al.* 2004). At the highest rotation rate in figure 6.12 we can see extended uniform regions with $\omega_{3,t}/\sigma_{\omega_{3,t}} \sim O(1)$ delimited by very low values of $\omega_{3,t}$ arranged in thin but long regions.

It is useful also to study the statistics of the right hand side of Eq. 6.13. In figure 6.13 we show the PDF of velocity gradients in different directions. The non-rotating case (line A) shows the known result that the PDF of transverse gradients (part (b)) exhibit longer tails than longitudinal gradients (part (a)). Longitudinal gradients along the axis of rotation (i.e. $u_{3,3}$) show a strong Rossby-number dependence with wider tails at intermediate rotation rates ($Ro^\omega = 1$). For stronger rotation rates ($Ro^\omega = 1/4$), we see that the PDF of $u_{3,3}$ is not far from Gaussian (included in the figure as a dashed line). The PDF of the transverse gradient $u_{3,1}$ on the other hand, shows almost no dependence on Ro^ω rate maintaining strong departures from Gaussianity at all rotation rates.

6.4.2 A Proposed Mechanism for Mixing at Low Rossby Numbers

The modified Taylor-Proudman theorem (Eq. 6.13) suggests a mechanism for the observed fact that properties are more uniform along $\mathbf{\Omega}$ as discussed above (the same was observed for passive scalars in Yeung & Xu 2004). If we write the equation for a component perpendicular to the axis of rotation (e.g. x_1) we obtain:

$$\frac{\partial \omega_1}{\partial t} \approx 2\Omega \frac{\partial u_1}{\partial x_3}. \tag{6.14}$$

which simply says that a gradient of u_1 along x_3 will be accompanied by an increase in vorticity in x_1. This would clearly tend to mix the zones of different velocities that originally generated vorticity making properties more uniform along the axis of rotation. The rate at which this process happens clearly scales with $\sim 1/\Omega$. We can also see that the equation for ω_3

$$\frac{\partial \omega_3}{\partial t} \approx 2\Omega \frac{\partial u_3}{\partial x_3}. \tag{6.15}$$

offers a different mechanism since the gradients $\partial u_3/\partial x_3$ do not decrease by an increase in ω_3. However, large scale vortices aligned with $\mathbf{\Omega}$ can be formed in regions with large longitudinal velocity gradients along x_3. These structures can indeed be seen on the left panels in figure 6.12 for intermediate and strong rotations. The different nature of this mechanism in different directions would clearly generate the kind of anisotropy observed from our DNS data. We emphasize that at the highest rotation in the present simulation, Eq. 6.13, which governs this process, is a good approximation in more than 95% of the domain.

A more quantitative analysis can be done due to the linear nature of Eq. 6.13. If a stable solution is perturbed with fluctuations of the form

$$u_i = u_i^* e^{\iota s t} e^{\iota \mathbf{k} \cdot \mathbf{x}} \tag{6.16}$$

where u_i^* is the amplitude of the perturbation and the sign of the exponent s determines whether a perturbation would grow, Eq. 6.14 can be written as

$$\iota s(k_2 u_3^* - k_2 u_3^*) = 2\Omega u_1^* k_3. \tag{6.17}$$

Solving for ιs we obtain

$$\iota s = \frac{2\Omega u_1^*}{(k_2/k_3)u_3^* - u_2^*}. \tag{6.18}$$

It is clear from Eq. 6.16 that linearly unstable modes are those with $\iota s > 0$ which according to Eq. 6.18 implies

$$k_3 < (u_3^*/u_2^*)k_2 \tag{6.19}$$

However, if the perturbation amplitude is assumed the same for all components (i.e. $u_1^* = u_2^* = u_3^*$), then the most unstable modes are those with $k_3 \sim k_2$ (but still $k_3 < k_2$). The same linear stability analysis applied to Eq. 6.13 for $p = 2$ and 3, results in $k_3 \sim k_1$ ($k_3 > k_1$) and $k_1 \sim k_2$ ($k_1 > k_2$) respectively being the most unstable modes. It is seen that the modified Taylor-Proudman theorem in Eq. 6.13 suggests that perturbations of the form Eq. 6.16 with comparable wavenumbers will grow in the three directions. Therefore, for very strong rotations (in which case Eq. 6.13 is a better approximation), linear perturbations of the type in Eq. 6.16 do not appear to have any preferential direction. This is in agreement with results in previous Sections in that the strongest anisotropies are found at intermediate rotation rates and decrease as Ω is increased.

6.4.3 Refined Similarity Hypothesis at Low Rossby Numbers

In Section 6.3 we investigated the scaling of structure functions to obtain more information about the behavior of the flow. We now would like to use Eq. 6.13 to help understand those results. Note that one can integrate Eq. 6.13 along x_3 from say $x_3^{(0)}$ to $x_3^{(0)} + r$. The result is

$$r_3 \frac{\partial(\omega_p)_{r_3}}{\partial t} \approx 2\Omega(\Delta_{r_3} u_p) \tag{6.20}$$

where

$$(\omega_p)_{r_3} = \frac{1}{r_3} \int_{x_3^{(0)}}^{x_3^{(0)}+r_3} \omega_p \, dr_3' \tag{6.21}$$

is a one-dimensional local average and $\Delta_{r_3} u_p$ is a structure function, both along the axis of rotation (x_3). We can now take the n-th power and ensemble average to obtain:

$$\langle (\Delta_{r_3} u_p)^n \rangle \approx \frac{1}{(2\Omega)^n} \left\langle (\dot{\omega}_p)^n_{r_3} \right\rangle r_3^n \tag{6.22}$$

where, for simplicity, $\dot{\omega}_p$ stands for $\partial \omega_p / \partial t$. It is interesting to compare this result to the refined similarity hypothesis of Kolmogorov (1962) for isotropic turbulence:

$$\langle (\Delta_r u)^n \rangle = C_n \langle \epsilon_r^{n/3} \rangle r^{n/3}. \tag{6.23}$$

We first note that although Eq. 6.22 is only valid for structure functions along the axis of rotation they can be both longitudinal and transverse. Second, Eq. 6.22 was derived from the Navier-Stokes equations as opposed to Eq. 6.23. The only known result from the Navier-Stokes equations for isotropic turbulence is the third-order longitudinal structure function which scales linearly with r and for which the proportionality coefficient is known (Kolmogorov 1941a, see Eq. 4.1). However, high order moments depart from results following this reasoning and Eq. 6.23 was proposed instead although it cannot be derived strictly from the governing equations and the prefactors C_n are not known a priori. For rotating turbulence, on the other hand, all the coefficients are known and velocity differences are seen to depend on the (one dimensional) local average of the time variation of vorticity instead of dissipation. For isotropic turbulence, Chen *et al.* (1997b) proposed a refined similarity hypothesis for transverse structure functions which differ from longitudinal ones in that they scale with local averages of enstrophy instead of dissipation. Both longitudinal and transverse structure functions under strong solid-body rotation, however, scale with vorticity along the axis of rotation. Is it clear that, as in Kolmogorov (1962),

expression 6.22 connects small scale activity (through $\dot{\omega}_p$) with the dynamics at other scales (through $\Delta_{r_3} u_p$).

As discussed in Section 6.3, there is a range of scales for which the scaling exponents are approximately $\zeta_n = n/2$ (see figure 6.7) consistent with Baroud *et al.* (2002) and Simand *et al.* (2000). This would imply according to Eq. 6.22 that $\langle (\dot{\omega}_p)^n_{r_3} \rangle \sim r_3^{-n/2}$. We also found that there is range of scales (for scales smaller than those in which we observe $\zeta_n = n/2$) in which the scaling predicted by K41 (i.e. $\zeta_n = n/3$) may hold for intermediate rotation rates (see again figure 6.7 and the text). In that range Eq. 6.22 implies $\langle (\dot{\omega}_p)^n_{r_3} \rangle \sim r_3^{-2n/3}$. The computation of both sides of Eq. 6.22 would be very useful to test the refined similarity hypothesis for strongly rotating flows proposed here. Also, simulations at higher Reynolds numbers are highly desirable to obtain wider scaling ranges and address more unambiguously scaling exponents.

6.5 Conclusions, Discussion and Future Issues

In this Chapter we have investigated the scaling of initially isotropic turbulence subject to solid-body rotation which is important in engineering, geophysics and astrophysics. Two further constrains appear in simulations when the equations are solved in a rotating frame. First, integral length scales grow along the axis of rotation and contamination from periodic boundary conditions may be of some concern. To investigate this, simulations on larger than usual domain sizes were performed. It was found that the size of the box was indeed constraining the growth of integral length scales. Doubling the linear size of the domain requires the use of twice as many grid points in each direction to keep the same resolution at small scales, increasing the computational costs by a factor of eight. A domain of size $(4\pi)^3$ instead of the usual $(2\pi)^3$ was found satisfactory. The second constraint is that for strong rotation rates, the time step should be small enough as to capture fast fluctuations due to the imposed rotation.

We have performed simulations at 1024^3 resolution on larger than usual domains (i.e. $(4\pi)^3$) of initially isotropic turbulence at $R_\lambda \approx 240$ and $Ro^\omega = \infty$ (no rotation), 4, 1 and 1/4. Integral length scales along the axis of rotation are larger than those perpendicular to it indicating stronger correlation in that direction. The strongest anisotropy appears at intermediate rotation rates ($Ro^\omega = 1$). To further characterize anisotropy we have computed the anisotropy tensor b_{ij} and its components b^e_{ij} and b^z_{ij} to evaluate the so-called directional and polarization anisotropy. Although the Reynolds stress tensor remains isotropic, that is $b_{ij} = 0$, the components b^e_{ij} and b^z_{ij} both depart from zero when rotation is introduced. Larger values of b^e_{ij} are found at $Ro^\omega = 1$. Since the initial Reynolds number is high enough to display a (narrow) inertial range, velocity component spectra display a $k^{-5/3}$ scaling at $t/T_{E,0} = 0$. When rotation is introduced, energy content in the velocity component parallel to $\mathbf{\Omega}$ is larger than in the plane perpendicular to it at all scales. The difference appears to be greatest at intermediate scales and at $Ro^\omega = 1$ and is consistent with reduced spectral transfer to velocity components perpendicular to $\mathbf{\Omega}$. Since, following Jacquin *et al.* (1990), rotation modifies the nonlinear interactions (the so-called coupling effect) only at intermediate rotation rates, our results suggest that this coupling is responsible for the anisotropies observed at all scales.

Intermittency was also found to be affected by solid-body rotation. Longitudinal velocity gradients along the axis of rotation approach Gaussian statistics when rotation is introduced and the effect is stronger at low Ro^ω. At later times, departures from Gaussianity reappear. Longer simulations and multiple realizations of the flow are desirable to address whether the flow would return to the non-rotating values or will approach an asymptotic state which scales with Ro^ω. Those future simulations will have to address the issue of contamination from boundary conditions since integral length scales are seen to continue to grow.

More information about the scaling of the flow was obtained by investigating the scaling

of structure functions. As rotation increases the third-order structure function changes sign at smaller scales indicating a reduced energy transfer and even a reversal at large scales. Two scaling ranges were observed especially for the sixth and eighth order structure functions. For scales in the range $9 \lesssim r/\eta \lesssim 30$ the data appears to be consistent with Kolmogorov (1941a) scaling, i.e. $\zeta_n = n/3$. The second scaling range $30 \lesssim r/\eta \lesssim 300$ displays anomalous scaling although a self-similar behavior is still observed with scaling exponents $\zeta_n = n/2$ consistent with recent experimental evidence. Simulations at higher Reynolds numbers and a wider range of Rossby numbers would be desirable. While the former would allow for wider scaling ranges, the latter would enable us to address more accurately the transition to the two-scaling-range state.

Two dimensional features have been observed and compared with the Taylor-Proudman theorem for rapidly rotating flows. We investigated this results using our DNS data and proposed a *local* version of the theorem. Specifically, we derived Eq. 6.13 and tested its validity as Ro^{ω} is decreased. We found that at $Ro^{\omega} = 1/4$, our result is in good agreement with DNS data in more than 95% of the domain. The implication is that the Taylor-Proudman theorem Eq. 6.11 holds only when $\omega_{t,3}$ is small. By looking at its PDF, we find that values close to zero are more likely at intermediate rotation rates. The topology of $\omega_{t,3}$ was also observed to present stronger anisotropies at this intermediate rotation rate. As Ro^{ω} is decreased, one observes the disappearance of small scales consistent with a reduced spectral transfer.

Equation 6.13 also helps explain the mechanisms underlying the observed fact that properties are more uniform along the axis of rotation. A theoretical result was obtained for the scaling of both longitudinal and transverse structure functions along $\mathbf{\Omega}$. The final expression, Eq. 6.22, which contains no unknown coefficients, was compared to classical results by Kolmogorov (1962) derived from phenomenological arguments. It is interesting

that Eq. 6.13 shows that the scaling of structure functions in one direction are determined by the component of vorticity in that direction which, by definition, contains velocity gradients only along the other two directions. It will be interesting to explore the implications of such scaling on the componentiality and dimensionality of rapidly rotating flows.

Table 6.1: Skewness (μ_3) and flatness factor (μ_4) of longitudinal velocity gradients perpendicular to the axis of rotation for three different rotations rates.

	Initial Ro^{ω}	4	1	1/4
$t/T_{E,0} = 1.5$	μ_3	-0.56	-0.18	-0.05
	μ_4	7.00	3.94	3.07
$t/T_{E,0} = 3.0$	μ_3	-0.60	-0.14	0.06
	μ_4	8.61	5.34	4.34
$t/T_{E,0} \approx 4.5$	μ_3	-0.62	-0.15	-0.07
	μ_4	8.52	7.07	6.03

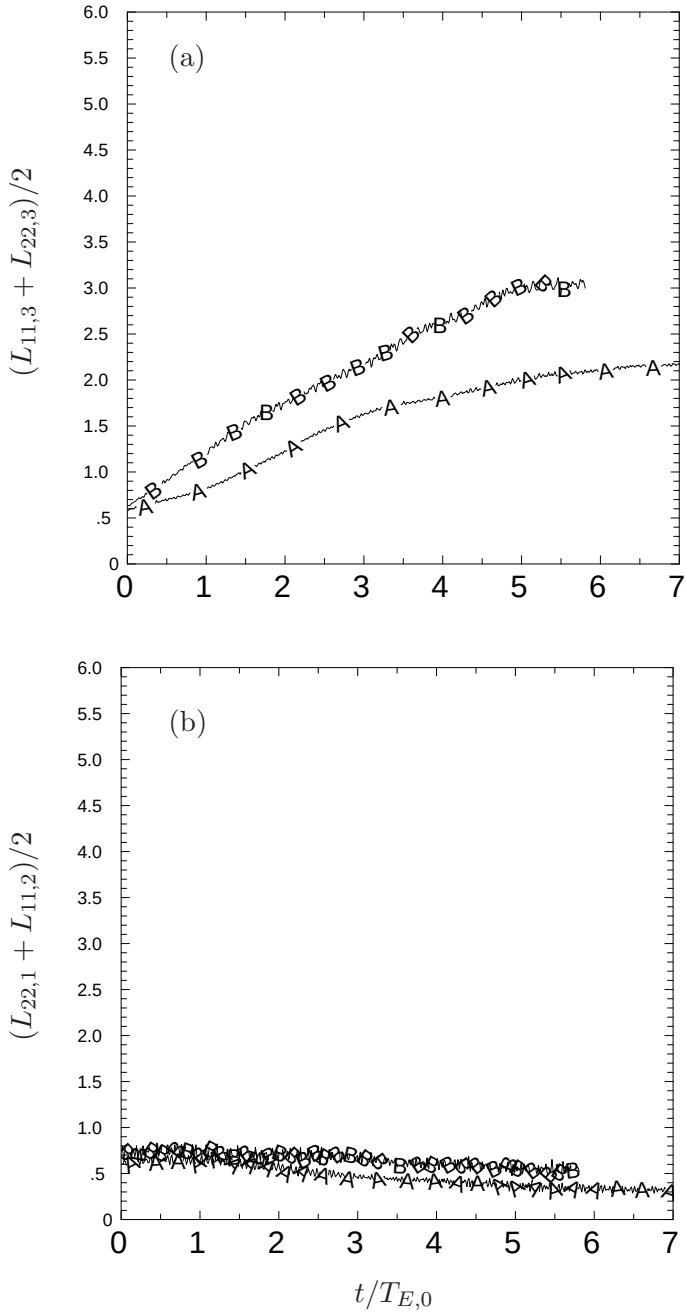

Figure 6.1: Transverse integral length scales parallel (a) and perpendicular (b) to the axis of rotation for initial $Ro^{\omega} \approx 0.2$ and $R_{\lambda} \approx 140$. A: $(2\pi)^3$, 256^3; B: $(4\pi)^3$, 512^3.

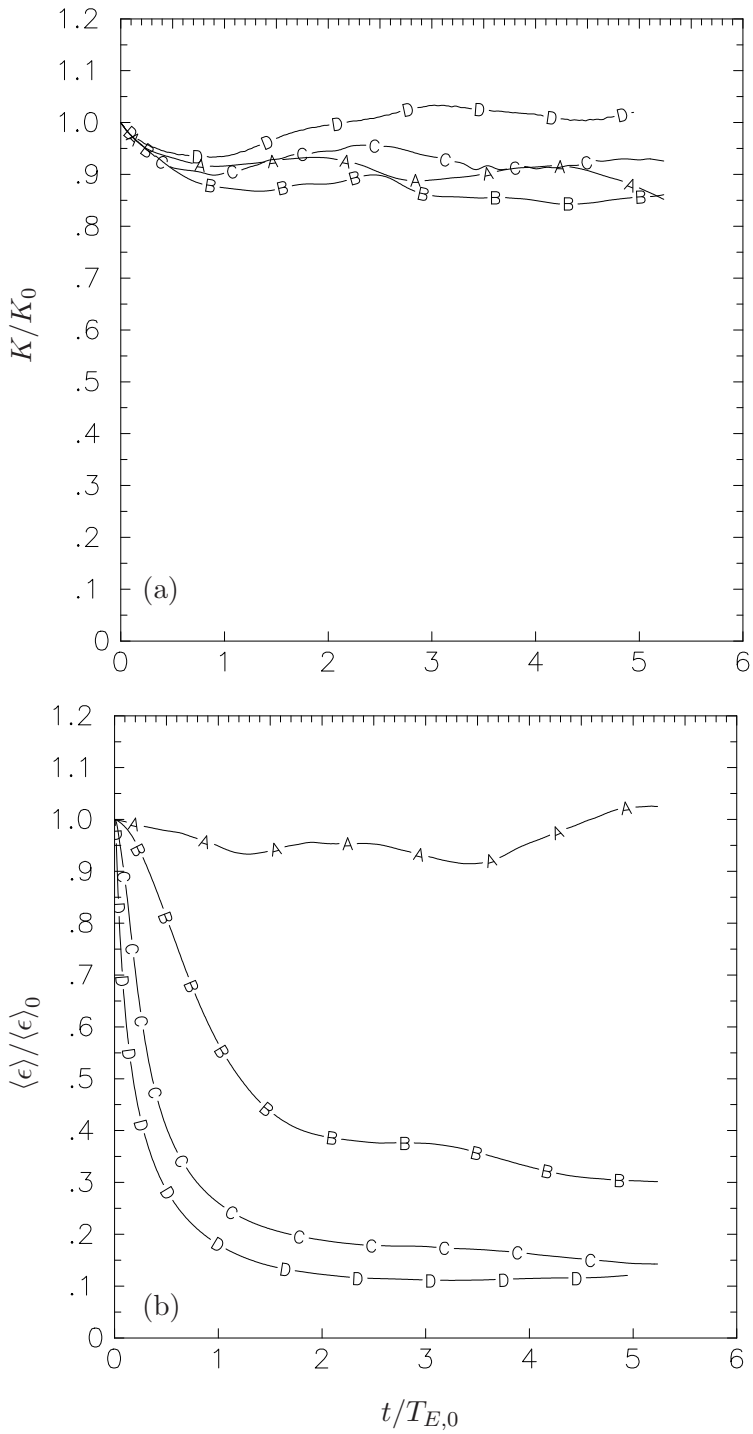

Figure 6.2: Evolution of turbulent kinetic energy (a) and mean energy dissipation rate (b) normalized by their initial values. Initial $R_\lambda \approx 240$. Line A: no rotation; lines B-D: initial $Ro^\omega = 4$, 1 and 1/4.

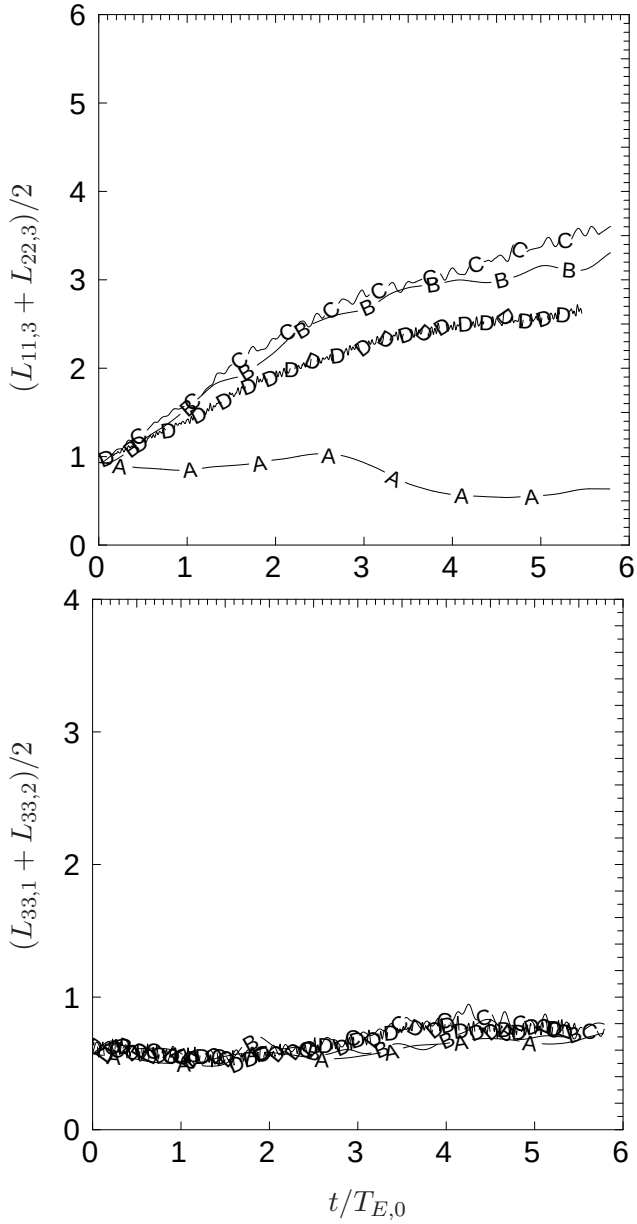

Figure 6.3: Transverse integral length scales as a function of time. Initial $R_\lambda \approx 240$ (1024^3) in a $(4\pi)^3$ domain. Line A: no rotation; lines B-D: initial $Ro^\omega = 4$, 1 and 1/4.

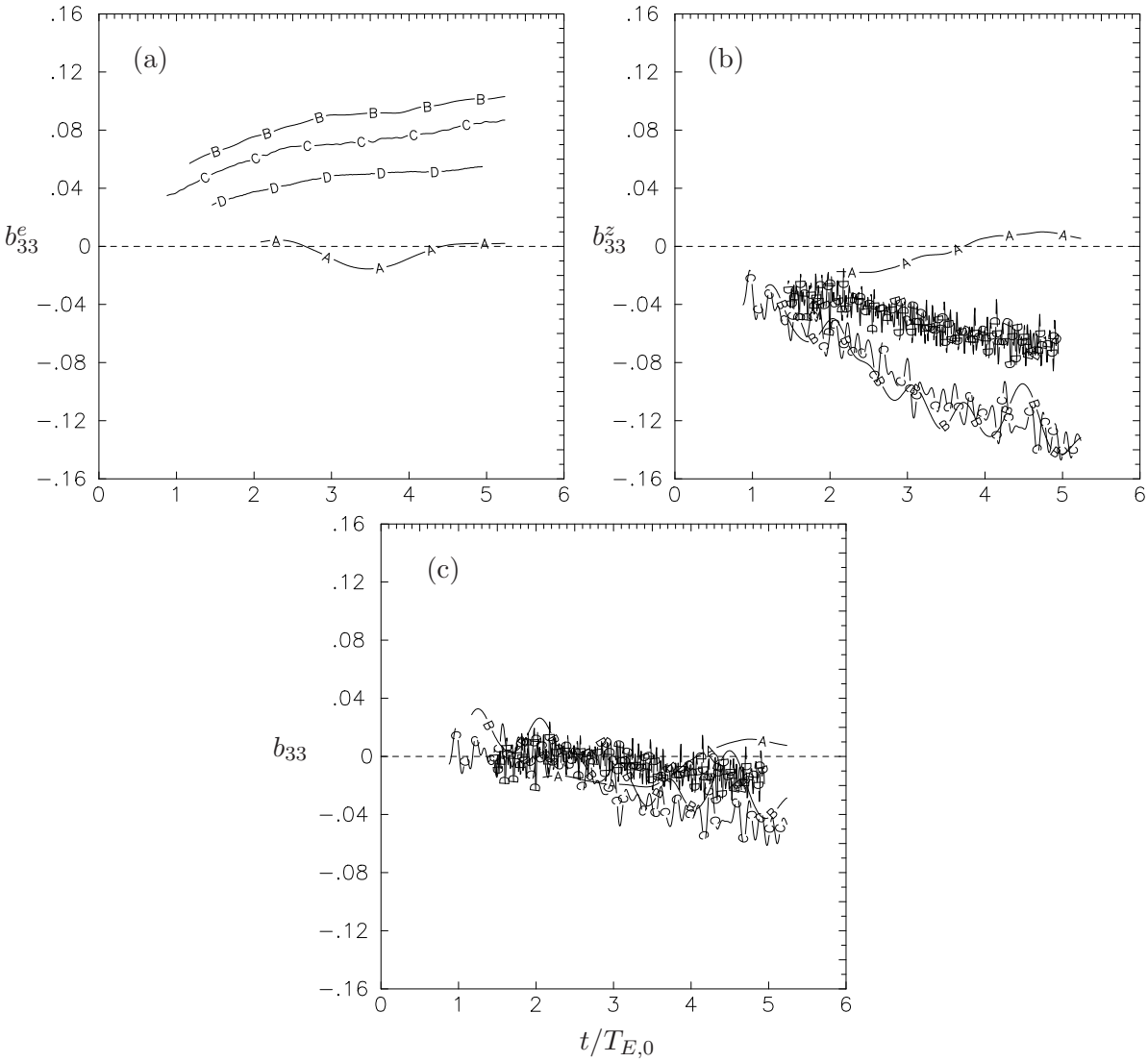

Figure 6.4: Evolution of anisotropy measures b^e_{33} (a), b^z_{33} (b) and b_{33} (c) for an initial $R_\lambda \approx 240$ (1024^3). Line A: no rotation; lines B-D: initial $Ro^\omega = 4$, 1 and 1/4.

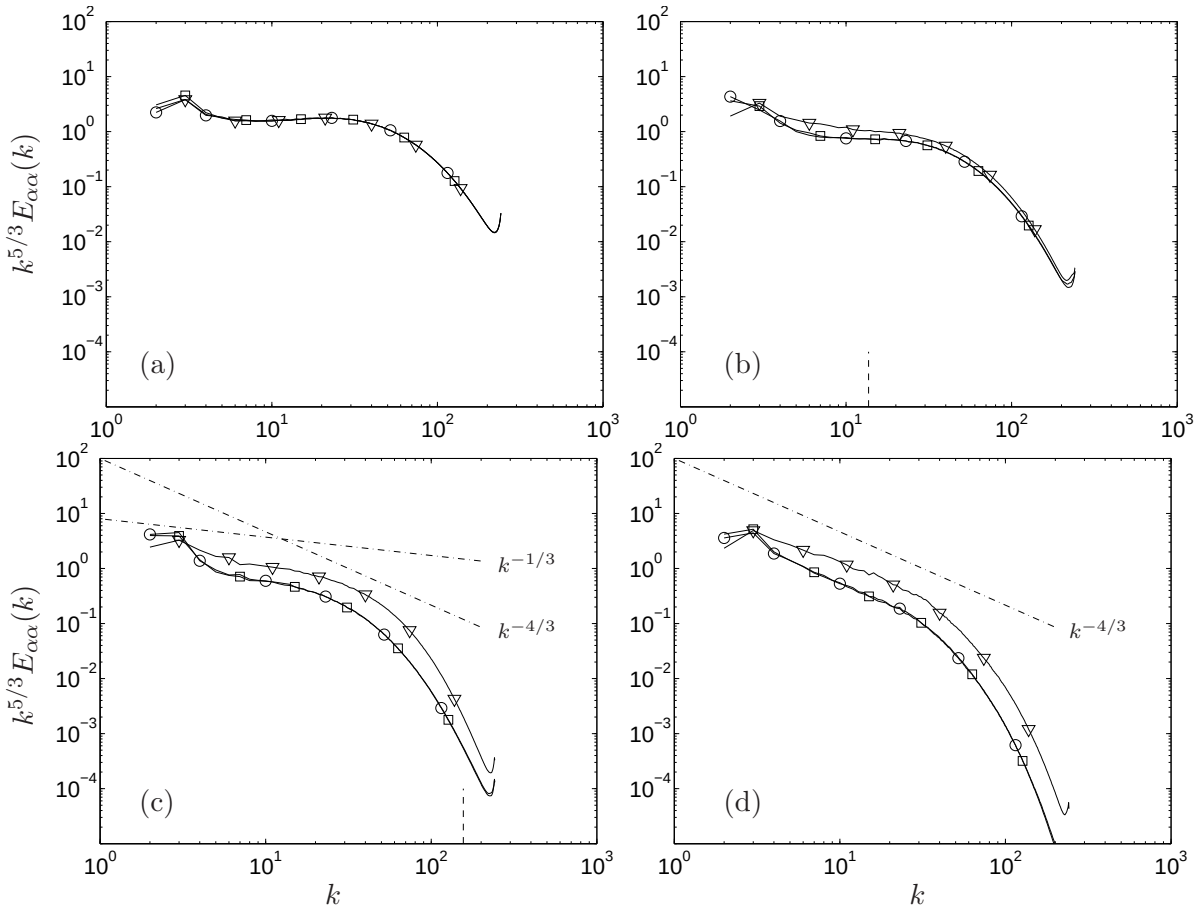

Figure 6.5: Energy component spectrum for different rotation rates at $t/T_{E,0} \approx 4.5$. Circles: $\alpha = 1$; Squares: $\alpha = 2$; Triangles: $\alpha = 3$. (a) no rotation; (b), (c) and (d) for $Ro^{\omega} = 4$, 1 and 1/4 respectively. Dashed-dotted lines: slopes $-1/3$ which corresponds to k^{-2}, and $-4/3$ which correspond to k^{-3}. Vertical dashed lines: scale $k_{\Omega} = (\Omega^3/\langle\epsilon\rangle)^{1/2}$.

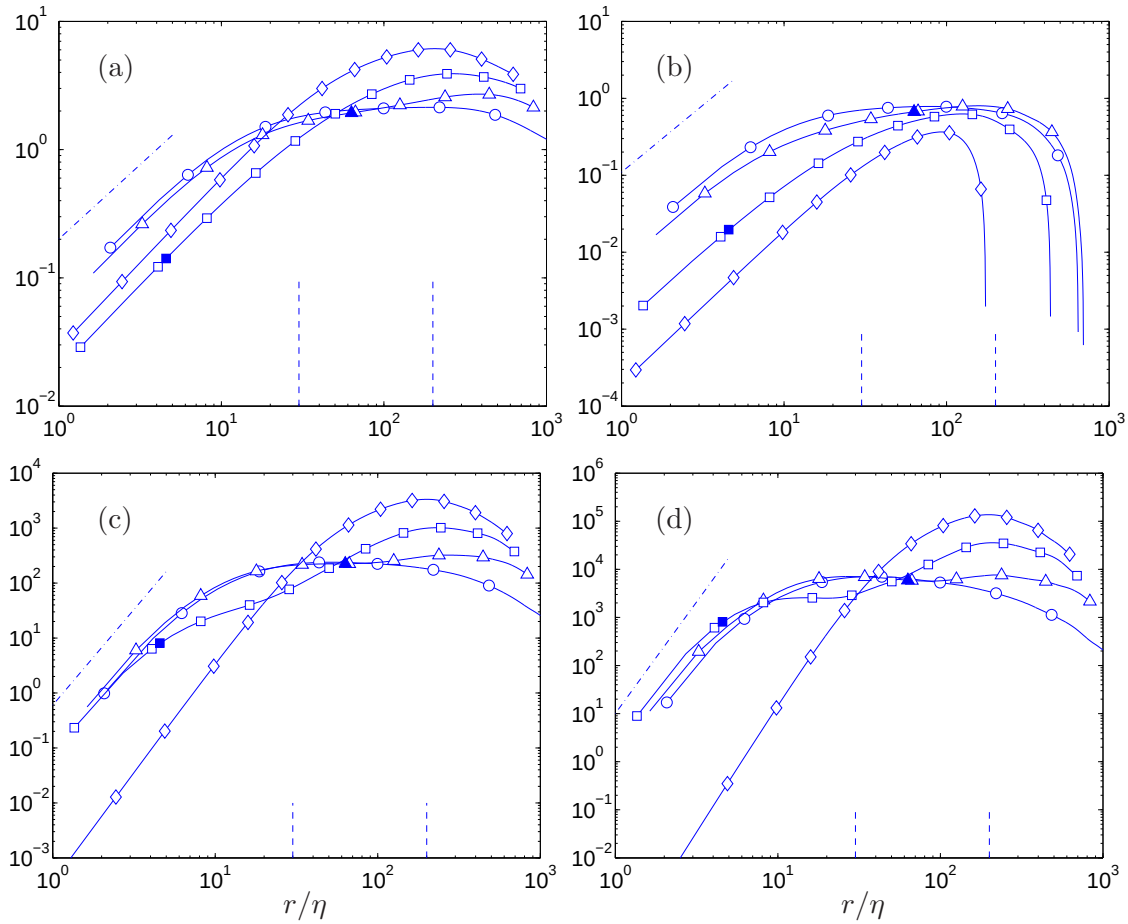

Figure 6.6: Longitudinal structure functions along x_3 (axis of rotation) normalized according to K41 at $t/T_{E,0} \approx 4.0$: $\langle(\Delta_{r_3} u_3)^n\rangle/(\langle\epsilon\rangle r)^{n/3}$ with $n = 2$ (a), 3 (b), 6 (c) and 8 (d). Initial $R_\lambda \approx 240$ (1024^3). Symbols are ◯: no rotation, △: $Ro^\omega = 4$, □: $Ro^\omega = 1$ and ◇: $Ro^\omega = 1/4$. Vertical dashed lines: inertial range for the non-rotating case. Dashed-dotted line on the left: analytic range $\sim r^{2n/3}$. Bold symbols: scale $r_\Omega = 2\pi/k_\Omega$ for each rotation rate.

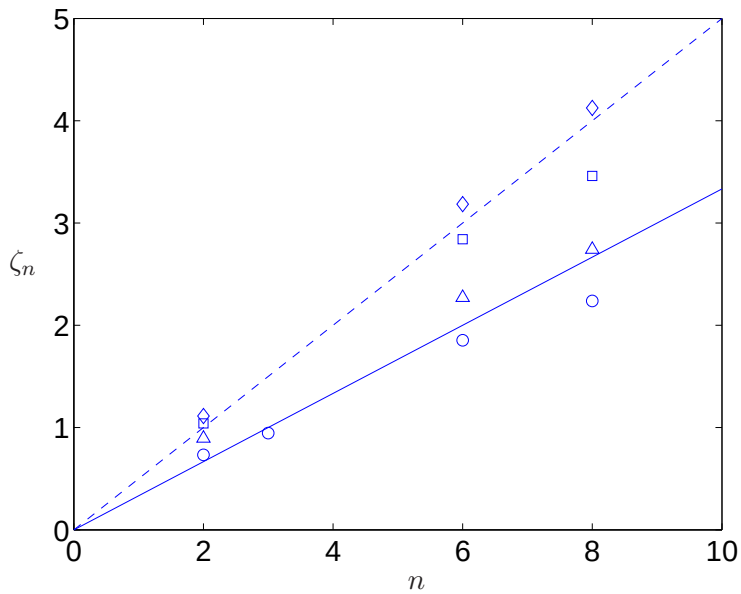

Figure 6.7: Scaling exponents for longitudinal structure functions along the axis of rotation. Symbols are ◯: no rotation, △: $Ro^\omega = 4$, □: $Ro^\omega = 1$ and ◇: $Ro^\omega = 1/4$. Solid line: $p/3$. Dashed line: $p/2$.

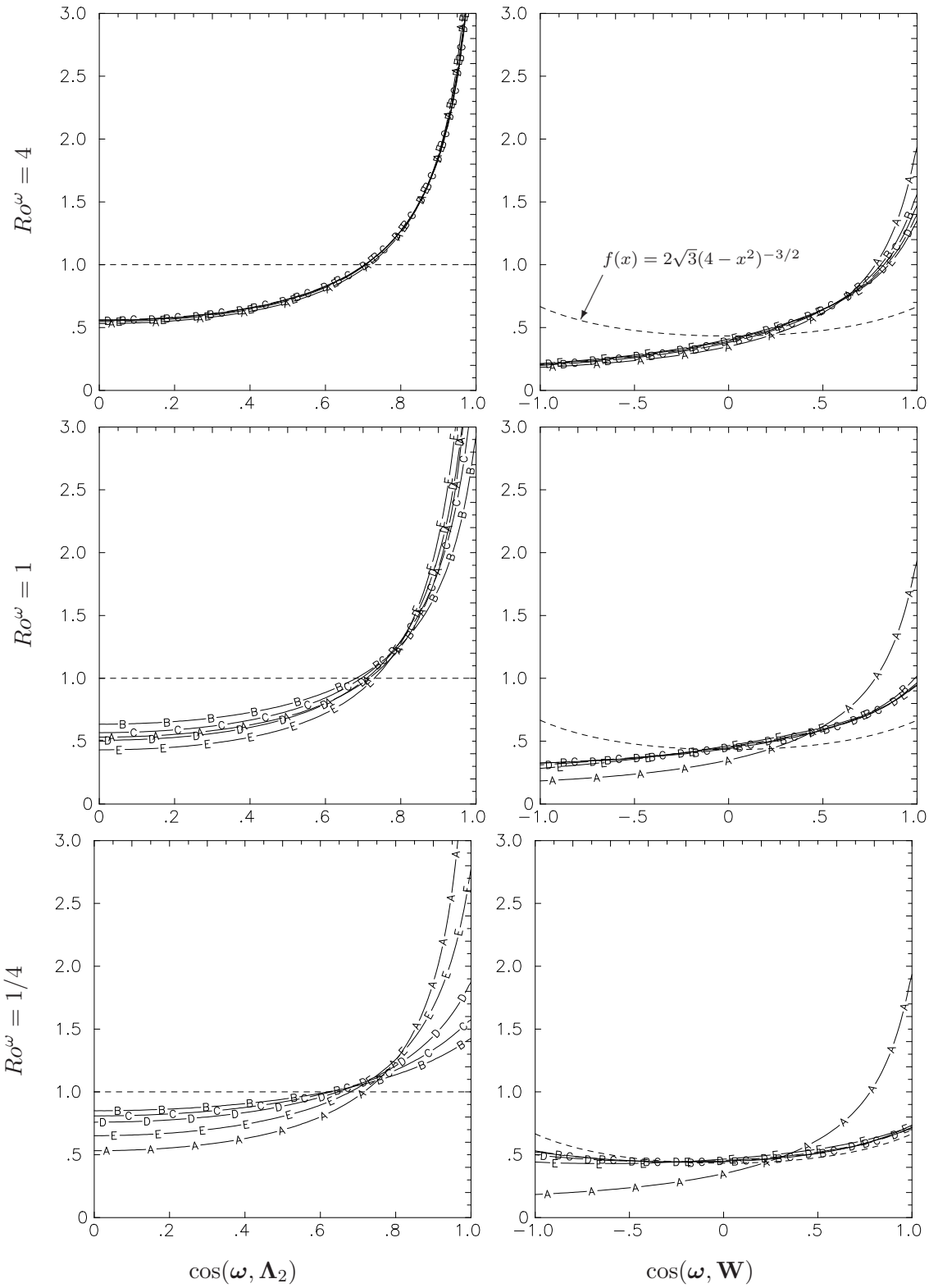

Figure 6.8: PDFs of the cosine of the angle between $\boldsymbol{\omega}$ and $\boldsymbol{\Lambda}_2$ (left panels) and $\boldsymbol{\omega}$ and $\mathbf{W}$ (right panels) for different rotation rates. Lines A to E correspond to $t/T_{E,0} = 0$, 0.6, 1.3, 2.2 and 4.4. Dashed lines are Gaussian results.

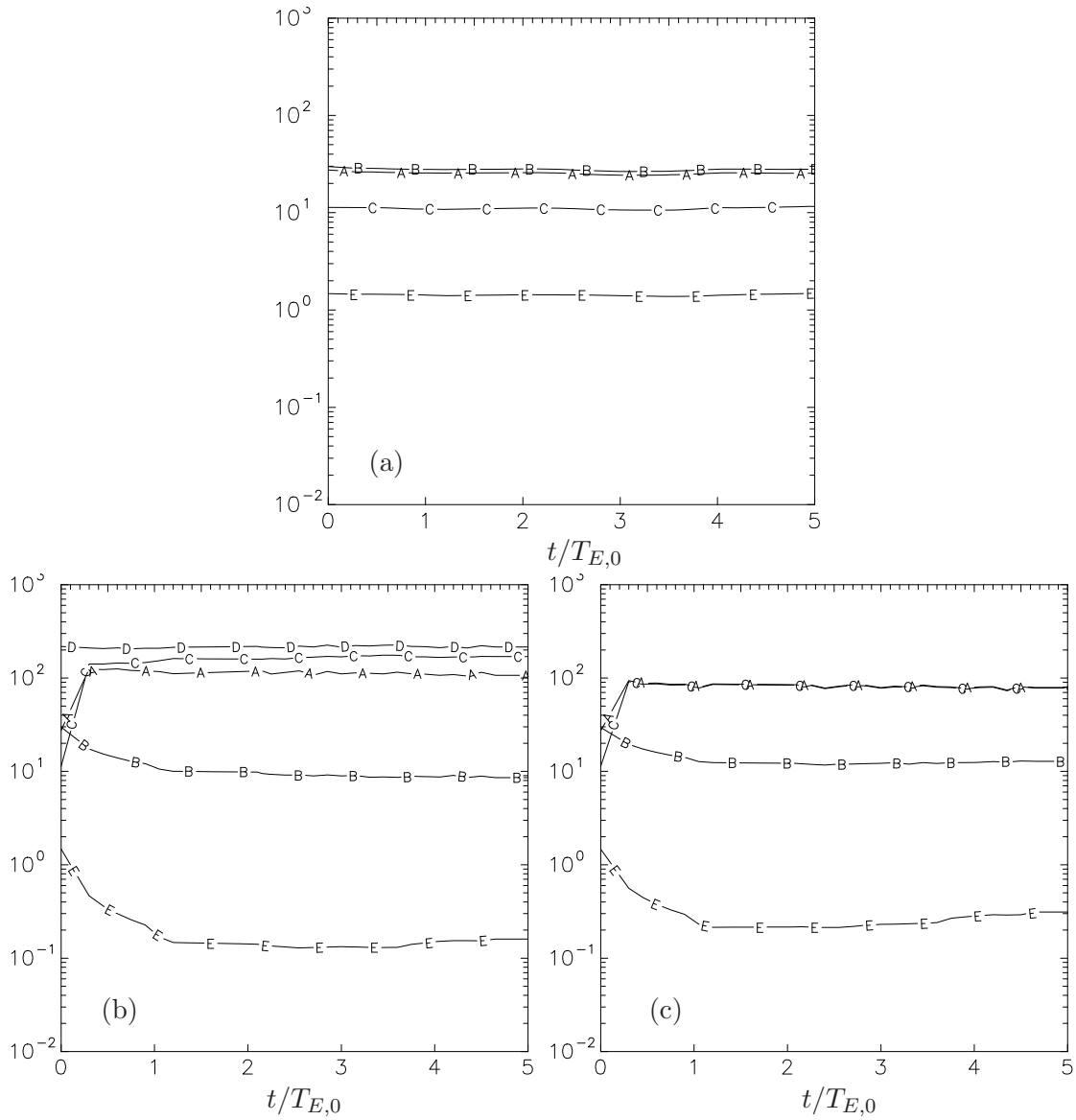

Figure 6.9: Variance of terms in Eq. 6.1 for (a) u_1 with no rotation, (b) u_1 at $Ro^{\omega} = 1/4$ and (c) u_3 at $Ro^{\omega} = 1/4$. Lines are local acceleration (A), non-linear terms (B), pressure gradient (C), rotation term (D) and viscous term (E).

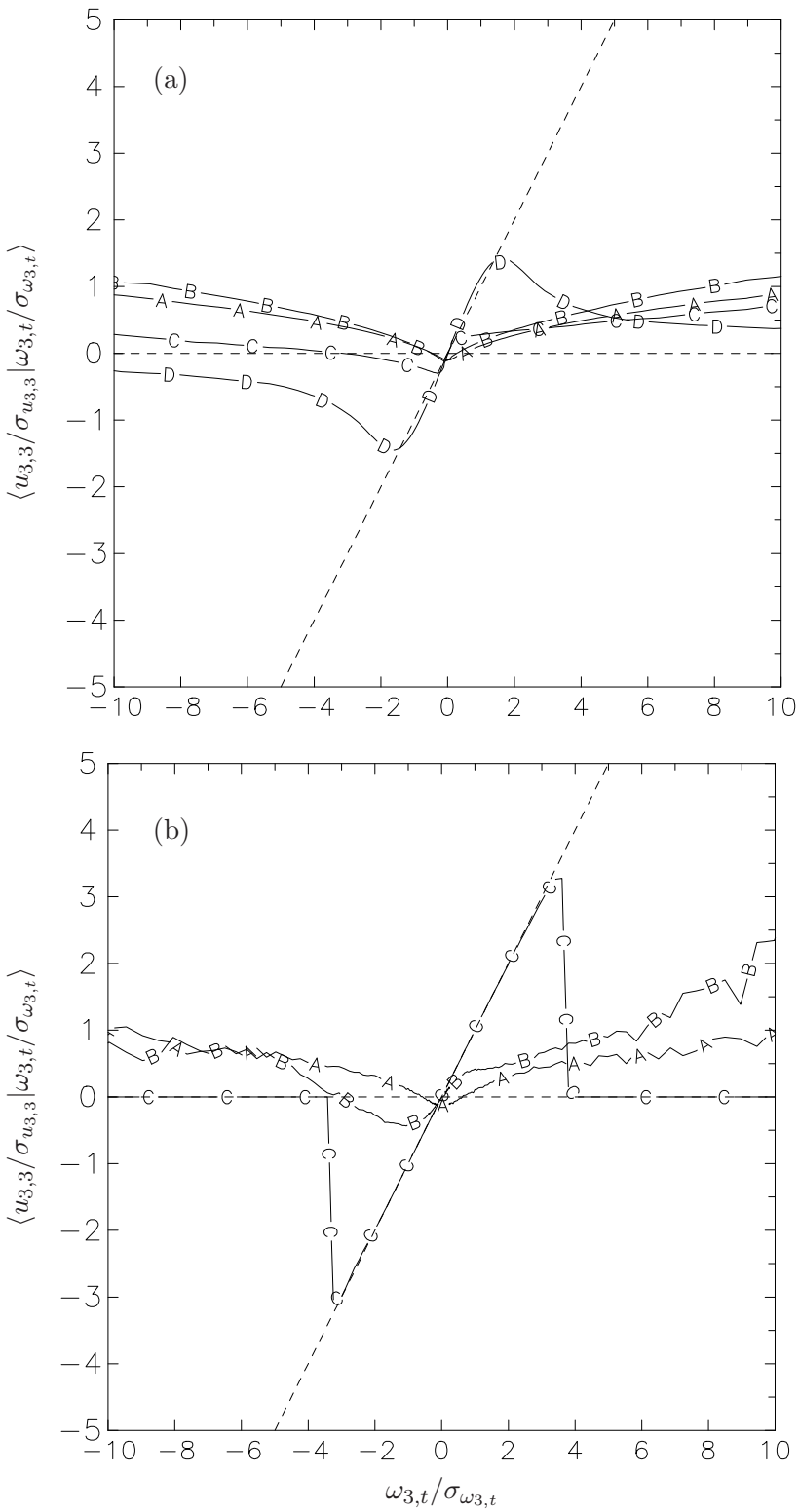

Figure 6.10: Conditional mean $\langle u_{3,3}/\sigma_{u_{3,3}}|\omega_{3,t}/\sigma_{\omega_{3,t}}\rangle$ (σ_α is the standard deviation of α). (a) Initial Reynolds number of $R_\lambda \approx 240$ (1024^3) with A: no rotation, B-D increasing rotation with $Ro^\omega = 4$, 1 and 1/4. (b) Initial Reynolds number of $R_\lambda \approx 38$ (512^3) with A: no rotation, B-C: $Ro^\omega = 1$ and 1/16. Dashed lines: slope 1 (according to Eq. 6.13).

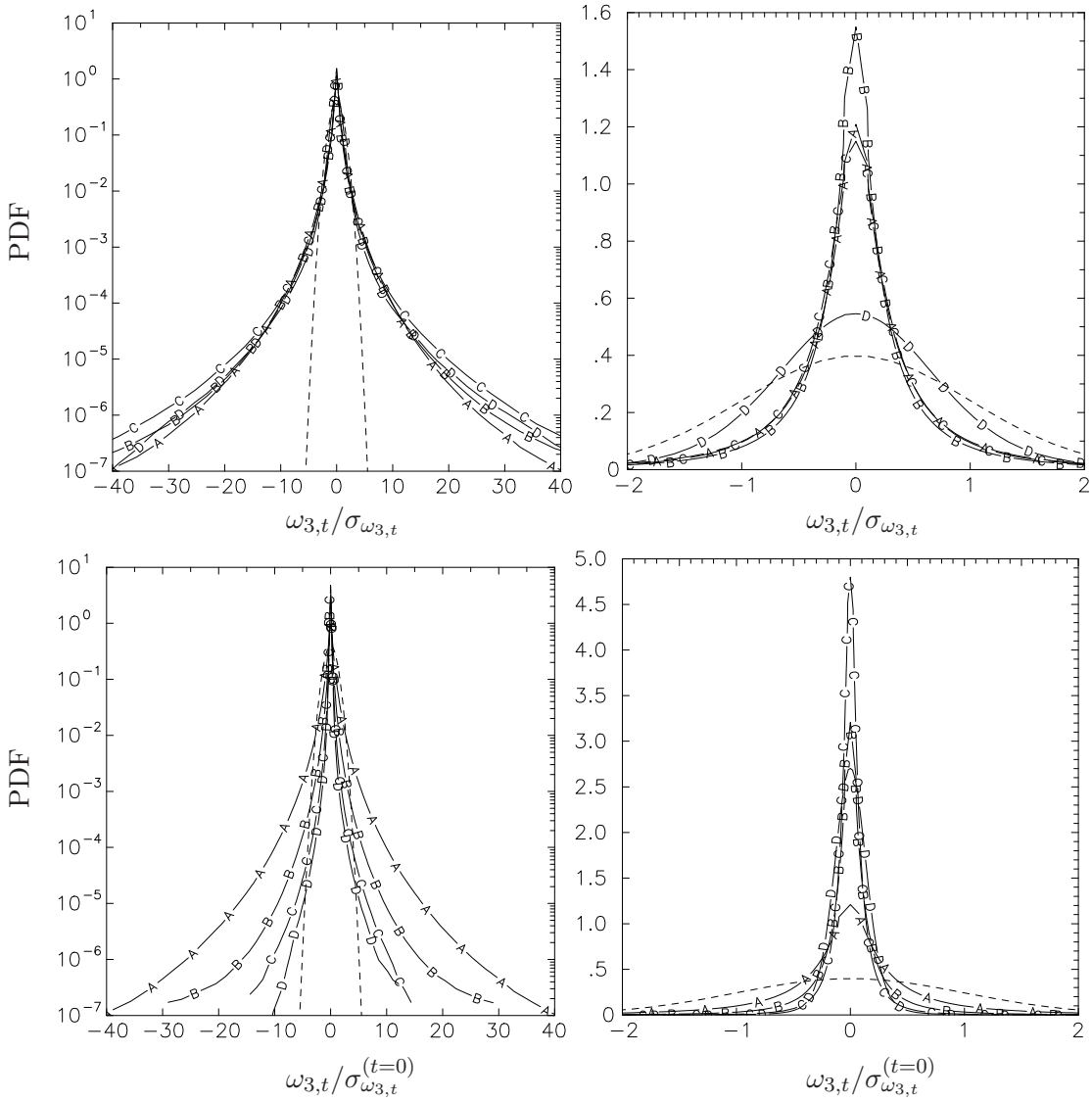

Figure 6.11: PDF of $\omega_{3,t}$ at $t/T_{E,0} \approx 4.5$ normalized by the standard deviation $\sigma_{\omega_{3,t}}$ at the same instant of time in log-linear (a) and linear-linear scales (b). Panels (c) and (d) are the same as (a) and (b) but normalized by the *initial* standard deviation $\omega_{3,t}^{(t=0)}$ (at the beginning of the simulations). A: no rotation, B-D increasing rotation with $Ro^{\omega} = 4$, 1 and 1/4. time. Dashed line: Gaussian distribution.

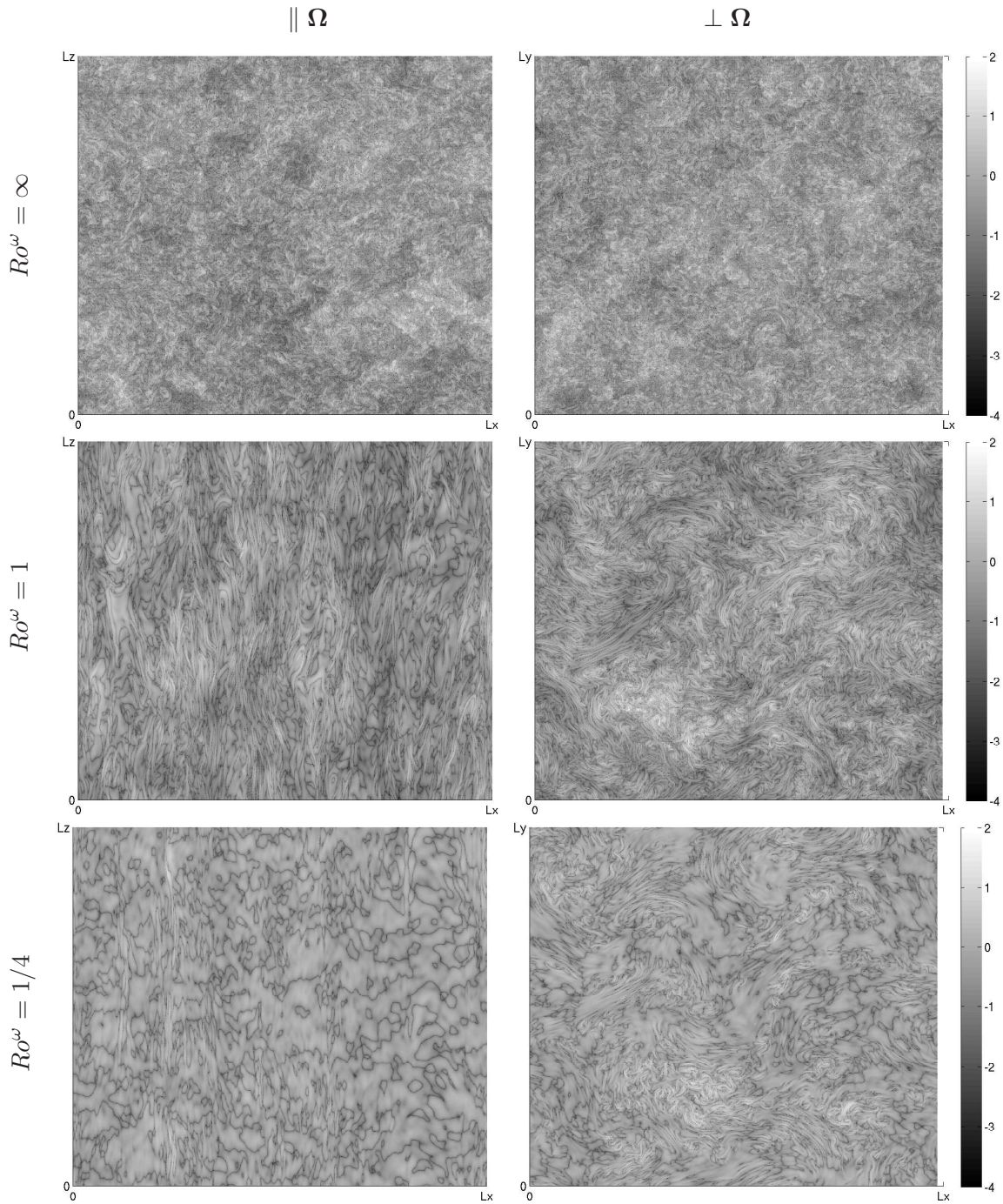

Figure 6.12: Contours of $|\omega_{3,t}|/\sigma_{\omega_{3,t}}$ from DNS at $R_\lambda \approx 240$ on a $(4\pi)^3$ domain (2048^3). Left: planes parallel to the axis of rotation. Right: planes perpendicular to axis of rotation. From top to bottom: no rotation, $Ro^{\omega} = 1$ and $1/4$. The color map is given in terms of $\log_{10}(|\omega_{3,t}|/\sigma_{\omega_{3,t}})$.

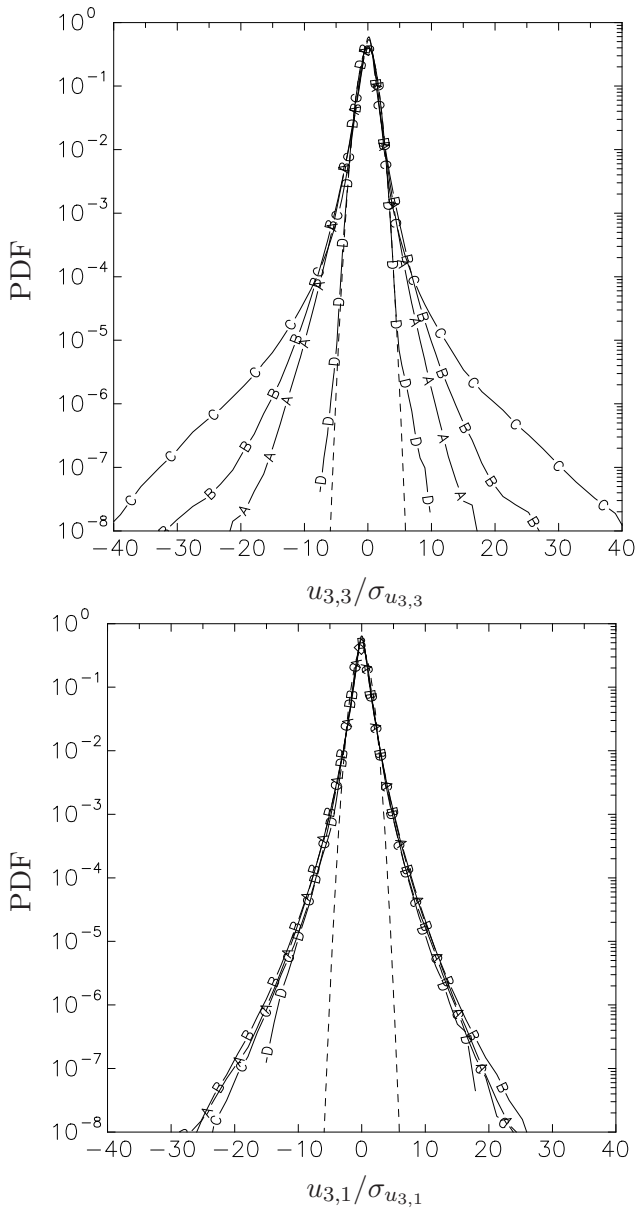

Figure 6.13: (a) PDF of $u_{3,3}$ at $t/T_{E,0} \approx 4.5$ normalized by the standard deviation $\sigma_{u_{3,3}}$. (B) PDF or $u_{3,1}/\sigma_{u_{3,1}}$ at the same instant of time. A: no rotation, B-D increasing rotation with $Ro^{\omega} = 4$, 1 and 1/4. time. Dashed line: Gaussian distribution.

CHAPTER VII

CONCLUSIONS

In this thesis we have studied the scaling of turbulence and turbulent mixing using direct numerical simulations, at up to 2048^3 resolutions of stationary isotropic turbulence at Taylor-scale Reynolds numbers up to 650, and scalars with Schmidt numbers ranging from 1/8 to 1024. To achieve Reynolds numbers comparable or in some cases larger than those found in typical experimental setups we have made use of the most powerful supercomputers available to the research community capable of sustained performance in the Teraflop range.

The velocity field is maintained in a stationary state by the addition of stochastic forcing at the large scales. Stationarity in scalar fluctuations is obtained also, via production by an imposed uniform mean gradient that acts against molecular dissipation. The tremendous detail provided by our simulations allows us to compute quantities which are very difficult to measure in experiments. In addition, the possibility of systematic variation of parameters helps us address a number of important scaling issues, such as intermittency for the velocity and scalar fields and the effects of solid body rotation.

The rest of this Chapter consists of two sections. First, we summarize the computational aspects of our CPU and memory intensive simulations followed by a discussion of the physical understanding obtained from those simulations. In the last section we discuss future work and challenges in terms of both the computing and the physics of turbulence.

7.1 Principal Findings

7.1.1 Numerical and Computational Aspects

In Chapter 2 we described the pseudo-spectral method used in our direct numerical simulations. In order to investigate the scaling of turbulence and turbulent mixing in different physical regimes (e.g. higher Reynolds and Schmidt numbers or lower Rossby number in rotating turbulence), high resolutions are needed with the consequent increase in computational power required. The parallel algorithm used to generate most of our database was described. A new scheme has been developed based on a two-dimensional domain decomposition in which each processor holds a *pencil* of data. To transpose the data across processors, the *pencils* code requires twice as many collective communication calls as the *slabs* code . However, fewer processors (of the order of $\sqrt{N_P}$) are involved in each communication. The *pencils* code has been benchmarked for resolutions up to 4096^3 on up to 32768 processors on BlueGene's at SDSC and IBM Watson Research Center. We showed results with resolutions ranging from 512^3 to 4096^3 and with processor counts in the range 2048 to 32768 showing that the code presents good weak and strong scaling. For example, the CPU time per step per processor for a 4096^3 is 20 secs on 32768 processors versus 39 secs on 16384 processors which represents almost perfect strong scaling (see e.g. figure 2.3).

In our simulations velocity fields are saved at regular time intervals for post-processing and/or checkpointing. Severe bottlenecks were observed when the original I/O scheme, which consists of all processors writing simultaneously individual files, was used at large processor counts. For example, writing restart files for a 4096^3 problem (which represents 768 GB of data) on 32768 processors took about 3 hours on BlueGene/W. A new scheme using knowledge about the underlying architecture was developed to alleviate the bottlenecks generated when many processors try to access shared resources (e.g. network, disks, I/O nodes). In this scheme, processors are scheduled in batches so that these bottlenecks

are minimized. This solution, which is particular to BlueGene's architectures, reduced the I/O time by a factor of more than 7 to about 25 minutes.

In addition to the computing issues mentioned above, we also discussed the importance of initial conditions for very large simulations. For example, a 4096^3 simulation starting from an initial Gaussian field with a given spectrum may take millions of CPU hours to reach a stationary state. Therefore, it is important to reduce the transient time between the start of the simulation and the attainment of a stationary state. We developed a new scheme that uses an *instantaneous* velocity field from a lower resolution simulation. The rest of the modes are initialized with a Gaussian field. The resulting Fourier coefficients are multiplied by appropriate factors so that a "target" spectrum is obtained. This scheme also avoids the initial decay of kinetic energy due to the lack of correlation between initial forcing and velocity fields. Tests at lower resolutions indicate that a fully developed stationary state can be reached in about one eddy-turnover time compared with 4 or 5 required by an initialization with a Gaussian field.

In Chapter 3, we studied the effect of finite resolution in direct numerical simulations on the study of intermittency in isotropic turbulence. We compared moments of both dissipation and enstrophy at different resolutions (up to 2048^3) but the same Reynolds numbers (140 and 240). It was found that simulations at the usual resolution criterion of $k_{max}\eta \approx 1.5$ underestimate high-order moments but a a value of $k_{max}\eta \approx 3$ (which corresponds to a grid spacing equal to Kolmogorov length scale) appears to be sufficient to obtain grid independent moments up to fourth order at $R_\lambda \approx 240$. This result is achieved although no clear analytic range was observed for structure functions at the corresponding order predicted recently by Yakhot & Sreenivasan (2005). Using Taylor-series expansions, we quantify the degree of departure from analytic range in structure functions as a function of order and Reynolds number. Our predictions are less restrictive than Yakhot & Sreenivasan (2005)

for low orders but similar for high orders. Inertial-range statistics were found to be weakly dependent on resolution at the small scales. Ratios of normalized moments of the same order (e.g. $\langle(\epsilon')^p\rangle/\langle(\Omega')^p\rangle$) are also less dependent on resolution and may be inferred with reasonable accuracy from simulations at $k_{max}\eta \approx 1.5$ (used in most DNS aimed at reaching high Reynolds number).

7.1.2 Physical Understanding

In Chapter 4 we studied the scaling of intermittency at small scales through fluctuations in energy dissipation and enstrophy. The tails of their PDFs are found to be well represented by stretched-exponential fits for values up to 100 times the mean. However, our data at the two highest Reynolds available (400 and 650) show the existence of extreme fluctuations of the order of several thousand times the mean. The tails of these PDFs can be described by a sum of two stretched exponentials which dominate respectively for intermediate and very large values of dissipation and enstrophy. For extreme values, the PDFs of dissipation and enstrophy coincide within statistical error suggesting a possible universal behavior of very strong fluctuations although low order statistics may still differ. Conditional statistics show that large values of dissipation are usually accompanied by large enstrophy although the converse is not necessarily true. Nevertheless, at extreme values of dissipation and enstrophy there is a significant degree of overlap. These extreme fluctuations appear in clusters whose size depends on (decreases with) the value of the threshold used to define the cluster. The nature of extreme fluctuations was studied further by decomposing dissipation and enstrophy into longitudinal, transverse and cross terms. The relative contribution of these components suggest a state of local isotropy but only in very intense regions (with dissipation and enstrophy beyond 1000 times the mean) which may help understand the similar scaling seen in the far tails of their PDFs.

The scaling of passive scalars was studied in Section 5 where we used our DNS database

with Sc from 1/8 to 1024 and R_λ from 8 to 650. Results from our simulations at $R_\lambda \approx 650$ (2048^3) and $Sc = 1/8$ and 1 show a clear $k^{-5/3}$ inertial-convective scaling. This result extends for about a decade for $Sc = 1/8$ and a slightly narrower range at $Sc = 1$ due to a spectral bump around $k\eta \approx 0.1$ (similar to the one observed for the velocity field) which can be interpreted as a precursor of a k^{-1} scaling. The Obukhov-Corrsin constant obtained from these results is in excellent agreement with experimental results. For weakly diffusive scalars ($Sc \gg 1$), our results at $R_\lambda \approx 8$, 38 and 140 support a trend towards a k^{-1} scaling as Sc is increased. Batchelor's expression for the scalar spectrum is found to underestimate the high wavenumber content at all Sc and R_λ. Kraichnan's expression on the other hand, which takes into account fluctuations of strain rates, provides a better representation of the data. When normalized according to Batchelor scaling, the spectrum appear to show some degree of universality at high wavenumbers ($k\eta_B \gtrsim 0.1$) for all R_λ and Sc including both low and high Schmidt number scalars. This result suggests that mechanisms different from those assumed by Batchelor and Kraichnan (which find theoretical support for high-Sc scalars) may be involved in turbulent mixing.

A basic premise in the phenomenology of turbulence is the concept of dissipative anomaly, where the mean dissipation rate is independent of viscosity at high Reynolds numbers. The same assumption about the mean scalar dissipation rate also has an important role in the extensions of K41 to passive scalars. The scaling of the mean scalar dissipation $\langle\chi\rangle$ was discussed in Section 5.2 using comprehensive data from DNS and experiments. It was found that $\langle\chi\rangle$ is independent of molecular properties if in addition to the Reynolds number being large, $\ln(Sc)/R_\lambda$ is small for $Sc > 1$ and $R_\lambda Sc^{1/2}$ is large for $Sc < 1$. We further obtained limits which provide a basis for evaluating whether a given flow can be considered in the asymptotic state in terms of R_λ and Sc. A new Reynolds number was proposed

$R_{L'} = (u'L^2/\lambda)/\nu$ which appears to provide a universal scaling for the mean scalar dissipation.

Scalar intermittency at small scales was investigated through the tail in the PDF of scalar dissipation. Intermittency is found to increase with both R_λ and Sc but reaches an asymptotic state in the high-Sc limit. This asymptotic state seems to require higher Sc when R_λ is small. This was also observed from moments of scalar gradient fluctuations in different directions. In the high-Sc limit, the flatness factor of gradients along the mean scalar gradient approaches the value of 10, 12 and 20 for $R_\lambda \approx 8$, 38 and 140 respectively. A phenomenological argument was given which suggests that saturation of intermittency occurs according to the condition ${R_\lambda}^2 Sc \gg 1$. Scaling exponents of local averages of scalar dissipation show that intermittency at inertial-convective scales decreases with Sc when $Sc > 1$. The skewness of scalar gradient fluctuations along the mean gradient was used to address departures from local isotropy. Consistent with previous results, persistent anisotropy is found at the highest Reynolds numbers achieved in our simulations. The less understood scaling with Sc was also investigated at different R_λ. Anisotropy at small scales decreases as Sc is increased and this return to isotropy is faster when R_λ is large.

In Chapter 6 we studied the effect of solid-body rotation on initially isotropic turbulence. To control contaminations from boundary conditions we have performed simulations on larger-than-usual domains. The initial Reynolds number was $R_\lambda \approx 240$ (at 1024^3 resolution) and three different microscale Rossby numbers ($Ro^\omega = 4$, 1 and 1/4) were imposed. Departures from isotropy are observed at all scales and are strongest at intermediate rotation rates. Results include unequal growth of integral scales (figure 6.1), non-zero values of components of the anisotropy tensor (figure 6.4 and Eq. 6.10), and different scaling of component spectra in different directions (figure 6.5). The spectral slope is close to -2 for intermediate rotation rates but close to -3 for strong rotation. Intermittency was found to

decrease monotonically with rotation rates at early times suggesting that it is caused by the damping of nonlinear terms. The skewness and flatness factors of velocity gradients approach Gaussian values at small times but departures from Gaussianity are apparent at later times. Structure functions present anomalous scaling (i.e. departures from K41) although at low Rossby numbers, the scaling exponents are linear in the order (i.e. $\zeta_n = n/2$) suggesting a self-similar state for a range of scales. At intermediate rotation rates two scaling ranges are observed for high-order structure functions. At smaller scales, K41 scaling ($\zeta_n = n/3$) may still apply whereas at larger scales the scaling exponents behave as $\zeta_n = n/2$. The small-scale structure of rotating turbulence was further studied through alignments between vorticity ($\boldsymbol{\omega}$) and the middle eigenvector of the strain-rate tensor ($\boldsymbol{\Lambda}_2$) and between vorticity and the vortex stretching vector ($\mathbf{W}$). At early times, the preferential alignment between $\boldsymbol{\omega}$ and $\boldsymbol{\Lambda}_2$ is reduced but it is restored at later times. On the other hand, the reduction in alignment observed at early times between $\mathbf{W}$ and $\boldsymbol{\omega}$ does not evolve in time and approaches an asymptotic distribution not far from Gaussian predictions. This implies a reduction of enstrophy generation through vortex stretching in rapidly rotating flows. The classical Taylor-Proudman theorem was investigated for rotating turbulence. An alternative version is proposed by keeping the unsteady terms in the governing equations which allows us to explain the observed homogeneity along the axis of rotation. A refined similarity hypothesis similar to that proposed by Kolmogorov (1962) is suggested implying that structure functions along the axis of rotation scale with local averages of the time-derivative of vorticity.

7.2 Future Research Directions

In this concluding section, we discuss possible extensions to the research presented in this work. As in the previous section we divide the discussion into computational issues and those concerning the physical understanding.

The computational power available to the research community has increased tremendously over time allowing us to be close to achieving resolutions of 4096^3. As described in this thesis, the original code had to be changed from a 1D to a 2D domain decomposition (i.e. the *slabs* code and *pencils* code respectively) to make use of very large number of processors. Issues such as I/O performance or even disk space have to be taken into account for very large simulations. In this work we discussed a solution to poor I/O performance on BlueGene's architectures but similar issues may also arise in new or next-generation machines. With the present *pencils* code a 4096^3 simulation at $R_\lambda \approx 1100$ has been started from initial conditions developed using the new scheme described in Chapter 2. Continuing this simulation (which at present spans only a fraction of Kolmogorov time scale) is part of future work. It is also desirable to include moderately diffusive scalars in such simulations although memory and time constraints would increase. It is interesting to note that the detailed study of passive scalars at $Sc \sim O(1)$ at these Reynolds numbers could also be useful to improve models that can be used in, e.g., large-eddy simulation of engineering devices at realistic conditions (see e.g. Peters 2000).

The scaling of intermittency is still an active field of study. Simulations have provided valuable input for models and basic understanding. Accurate determination of, for example, high-order moments is crucial to compare between competing theories. Our work presented here provides resolution requirements which depend on the order of the moment. Our results, however, were tested against data at $R_\lambda \approx 140$ and 240. The influence of smaller scales at higher Reynolds numbers is yet to be discovered. Our theoretical developments relating structure functions and velocity gradients may be useful for experiments as well and we hope they can help disentangle resolution effects from real trends.

Results on extreme fluctuations of dissipation and enstrophy observed at high R_λ provide support for a universal behavior. The study of these strong fluctuations is important not

only from a theoretical standpoint but also for practical problems such as combustion and dispersion. Therefore, it is necessary to obtain reliable statistics of strong fluctuations which require very long simulations at higher-than-usual resolutions. The increase of available computer power can help resolve these issues in the near future. Detailed studies comparing the structure of extreme fluctuations (such as that by Moisy & Jiménez 2004, for moderate fluctuation levels) can also provide further insight into the nature of intermittency at small scales. The study of dissipation and enstrophy through different gradients (longitudinal, transverse, and cross terms) proved to be useful to investigate the relation between them. It will also be interesting to decompose gradients in frames of reference intrinsic to the turbulent structure, such as the eigenframe of the strain-rate tensor or a system of axes attached to the vorticity vector.

Besides characterizing intermittency, it will be very interesting to investigate its origins (e.g. Li & Meneveau 2005). In particular, the role of large scales in the appearance of extreme fluctuations is an interesting problem that has not been addressed carefully (e.g. Sreenivasan 2004). This also raises the natural question about the origins of intermittency for passive scalars and its relation with large scales.

An interesting problem with practical significance is the effect of intermittency on reacting flows. For example, it is important to address the role of extreme values of energy dissipation, enstrophy and scalar dissipation on reaction rates. Local Damköhler numbers (Da) can vary considerably in a given flow as values of dissipation are three or four orders of magnitude larger than the mean. Thus, although reactions can be considered fast on average, they may be fast in some regions and slow in others. Quantifying the effects of intermittency in reacting flows using DNS with complex chemistry is an interesting and important topic for future research.

Many issues about the scaling of turbulent mixing are still not completely understood.

In particular, the good collapse of spectra at both low and high Schmidt number is an interesting issue yet to be resolved. Mechanisms for mixing at small scales different from those proposed by classical theories (by e.g. Obukhov, Corrsin, Batchelor, Kraichnan) may be dominant. Detailed studies of small-scale mixing are therefore necessary. The tremendous detail available in DNS suggests that it could be the best tool in this respect.

A crude estimate based on the assumption that large scales are responsible for strong gradients in the scalar field yield the condition $Sc \sim 5000/{R_\lambda}^2$ for the Schmidt number at which intermittency attain an asymptotic level. This prediction is shown in in figure 7.1 where we also show our DNS database of turbulent mixing (above the dashed line the estimate predicts that flow is in the asymptotic state). This rough guide could help design simulations and experimental setups to address some of these fundamental issues. For example, the study of mixing at very low Sc may give hints on the phenomenon of saturation of intermittency as well as e.g. the scaling of the spectrum. However, since scalar integral scales are larger at low Sc (see figure 5.12) larger domains may be necessary. We found that the forcing scheme used in this thesis, produces an artificial "jump" in the spectrum at $k = k_f$ in large domains. The reason for this effect is in the use of a Heavyside function for the forcing (wavenumbers in the range $k \leq k_f$ are forced with equal strength). Different "shape" functions were tested to distribute the input of energy from the forcing among low wavenumber modes. A smooth function of the form $[\cos(\pi k/k_f) + 1]/2$ (with $k \leq k_f$) eliminates the "jump" and can be used for these future simulations in large domains.

It would also be interesting to use DNS to study turbulence in conducting fluids (the so-called magnetohydrodynamics or MHD). The coupling between velocity and magnetic field fluctuations through the additional Lorentz force in the governing equations give rise to a variety of new phenomena which is still to be understood. In particular, the $k^{-5/3}$ scaling observed in the spectrum of the magnetic field may give some hint about the underlying

physics not only for conducting fluids but also for normal hydrodynamic turbulence. The detailed interaction of fluctuations of the velocity and magnetic fields at different scales may be worth exploring. The scaling of quantum turbulence which according to the current understanding, can be thought of as a two-fluid model (one viscous normal fluid coexisting with an inviscid superfluid) is also an interesting topic for future work.

Recent experimental data of the cosmic microwave background (CMB) radiation (e.g. from the Wilkinson Microwave Anisotropy Probe or WMAP) have revealed that the observed fluctuations of temperature (which are believed to be the remnant of the early universe) are themselves Gaussian. However, moments of temperature increments (structure functions) show the same multiscaling behavior as in hydrodynamic turbulence (Bershadskii & Sreenivasan 2002, 2003). A simulation of the so-called primordial turbulence (which is estimated to have occurred ~ 14 billion years ago) could help explain the scaling found not only for structure functions but for the spectrum (Donzis *et al.* 2005a). In such a simulation a spherical geometry with periodic boundary conditions may be the most appropriate in which spherical harmonics should be used instead of the typical Fourier representation used for isotropic turbulence.

We conclude this work with a positive note. It is an exciting time for the study of turbulence using large scale numerical simulations. The computational power that allows simulations at Reynolds and Schmidt numbers necessary to address long standing problems are now available to the research community. And the trend to build even larger supercomputers shows no sign of decline or saturation. Simulations of isotropic turbulence at asymptotically large Reynolds numbers, turbulent flows in complex geometries at reasonably large Reynolds numbers or simulations including more physical processes (e.g. combustion, or MHD) at realistic conditions may be only a decade away.

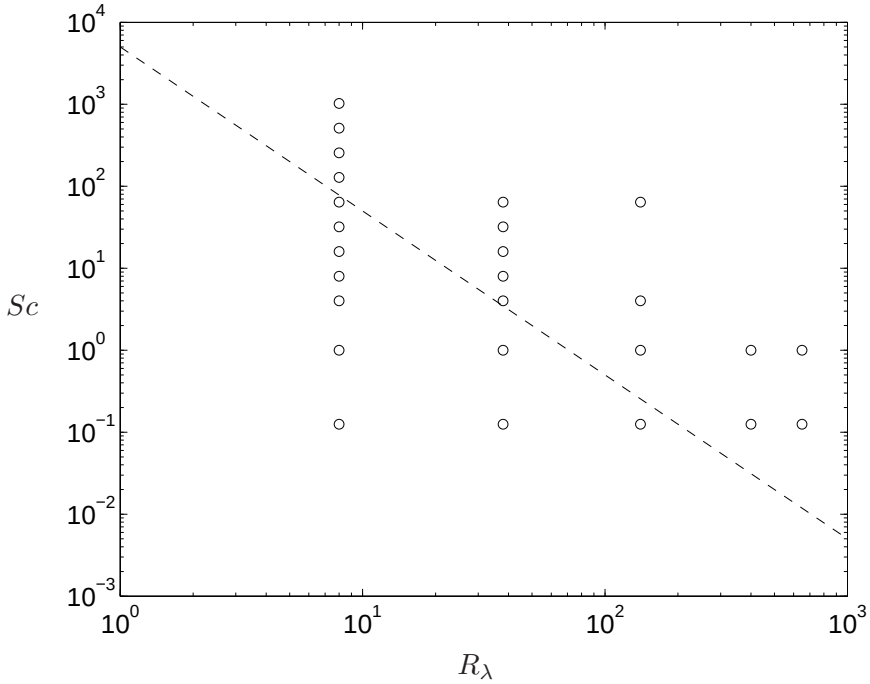

Figure 7.1: Our DNS database in the R_λ-Sc plane. The dashed line is $5000/{R_\lambda}^2$.

APPENDIX A

A LOCAL ISOTROPY RESULT FOR LONGITUDINAL VELOCITY GRADIENTS

We present here a theoretical derivation for Eq. (4.12) which is supported by the observed behavior of the quantity $\langle L|\epsilon\rangle$ as in Figs. 4.10 and 4.11. The starting point is that local isotropy requires that the fourth-order tensor $\langle u_{i,j}u_{k,l}\rangle$ take the form

$$\langle u_{i,j}u_{k,l}\rangle = \alpha\delta_{ij}\delta_{kl} + \beta\delta_{ik}\delta_{jl} + \gamma\delta_{il}\delta_{jk} \tag{A-1}$$

where the scalar coefficients α, β, γ can, with the use of incompressibility, be expressed in terms of longitudinal and transverse velocity gradient variances (Pope 2000), $\langle(u_{1,1})^2\rangle$ and $\langle(u_{1,2})^2\rangle$. We propose that the same basic relation applies to conditional averages given a scalar variable which is itself statistically homogeneous in space. Accordingly we write

$$\langle u_{i,j}u_{k,l}|\epsilon\rangle = \alpha(\epsilon)\delta_{ij}\delta_{kl} + \beta(\epsilon)\delta_{ik}\delta_{jl} + \gamma(\epsilon)\delta_{il}\delta_{jk} \tag{A-2}$$

Contracting the subscripts i and j and using incompressibility gives

$$3\alpha + \beta + \gamma = 0 \tag{A-3}$$

where for brevity we henceforth omit the dependence on ϵ in α, β, γ in the notation. For longitudinal gradients setting $i = j = 1$ gives

$$\langle(u_{1,1})^2|\epsilon\rangle = \alpha + \beta + \gamma \tag{A-4}$$

whereas for transverse gradients setting $i = 1$ and $j = 2$ gives

$$\langle(u_{1,2})^2|\epsilon\rangle = \beta\ . \tag{A-5}$$

By solving the above for α, β and γ, and using the simple isotropy results $\langle L|\epsilon\rangle = 6\langle(u_{1,1})^2|\epsilon\rangle$, $\langle T|\epsilon\rangle = 6\langle(u_{1,2})^2|\epsilon\rangle$, we can re-write Eq. (A-2) as

$$\langle u_{i,j}u_{k,l}|\epsilon\rangle = -\frac{\langle L|\epsilon\rangle}{12}(\delta_{ij}\delta_{kl} - 3\delta_{il}\delta_{jk}) + \frac{\langle T|\epsilon\rangle}{6}(\delta_{ik}\delta_{jl} - \delta_{il}\delta_{jk}) \ . \tag{A-6}$$

For the cross-terms, therefore, we have

$$\langle u_{1,2}u_{2,1}|\epsilon\rangle = \frac{1}{4}\langle L|\epsilon\rangle - \frac{1}{6}\langle T|\epsilon\rangle \tag{A-7}$$

and hence

$$\langle C|\epsilon\rangle = \frac{3}{2}\langle L|\epsilon\rangle - \langle T|\epsilon\rangle \tag{A-8}$$

Since by definition $\langle L|\epsilon\rangle + \langle T|\epsilon\rangle + \langle C|\epsilon\rangle = \epsilon/\nu$ substitution from Eq. (A-8) now produces the result $\epsilon/\nu = (5/2)\langle L|\epsilon\rangle$ and hence Eq. (4.12) for the behavior of $\langle L|\epsilon\rangle$ as claimed in Eq. (4.12) and confirmed to within sampling error in our DNS data.

It should be noted that an exact result as shown here is available only for $\langle L|\epsilon\rangle$ but not $\langle T|\epsilon\rangle$ or $\langle C|\epsilon\rangle$ separately (which would have to involve additional assumptions not well supported by the numerical data). Furthermore, whereas conditioning by the enstrophy leads to a relation similar to Eq. (A-8), since the contributions of T and C to Ω are different, no corresponding result can be derived for $\langle L|\Omega\rangle$.

APPENDIX B

SIMULATIONS OF THREE-DIMENSIONAL TURBULENT MIXING FOR SCHMIDT NUMBERS OF THE ORDER 1000

P.K. Yeung, S. Xu, D.A. Donzis and K.R. Sreenivasan. *Flow, Turbulence and Combustion* **72** (2004), (333-347).

Abstract

We report basic results from newnumerical simulations of passive scalar mixing at Schmidt numbers (Sc) of the order of 1000 in isotropic turbulence. The required high grid-resolution is made possible by simulating turbulence at very low Reynolds numbers, which nevertheless possesses universality in dissipative scales of motion. The results obtained are qualitatively consistent with those based on another study (Yeung et al., Phys. Fluids 14 (2002) 4178-4191) with a less extended Schmidt number range and a higher Reynolds number. In the stationary state maintained by a uniform mean scalar gradient, the scalar variance increases slightly with Sc but scalar dissipation is nearly constant. As the Schmidt number increases, there is an increasing trend towards k^{-1} scaling predicted by Batchelor (Batchelor, J. Fluid Mech. 5 (1959) 113-133) for the viscous-convective range of the scalar spectrum; the scalar gradient skewness approaches zero; and the intermittency measured by the scalar gradient flatness approaches its asymptotic state. However, the value of Sc needed for the asymptotic behavior to emerge appears to increase with decreasing Reynolds number of the turbulence. In the viscous-diffusive range, the scalar spectrum is in better agreement with Kraichnan's (Kraichnan, Phys. Fluids 11 (1968) 945-953) result than with Batchelor's.

APPENDIX C

HIGH SCHMIDT NUMBER SCALARS IN TURBULENCE: STRUCTURE FUNCTIONS AND LAGRANGIAN THEORY

M. Borgas, B. L. Sawford, S. Xu, D.A. Donzis and P.K. Yeung. *Physics of Fluids* **16** (2004), (3888-3899).

Abstract

We demonstrate the existence of Batchelor's viscous-convective subrange using direct numerical simulation (DNS) results to confirm the logarithmic dependence of the scalar structure function on the separation for the scalar field generated by stationary isotropic turbulence acting on a uniform mean scalar gradient. From these data we estimate the Batchelor constant $\tilde{B}_\theta \approx 5$. By integrating a piecewise continuous representation of the scalar variance spectrum we calculate the steady-state scalar variance as a function of Reynolds number and Schmidt number. Comparison with DNS results confirms the ${R_\lambda}^{-1}$ behavior predicted from the spectral integration, but with a coefficient about 60% too small. In the large Reynolds number limit the data give a value of 2.5 for the mechanical-to-scalar time scale ratio. The dependence of the data for the scalar variance on Schmidt number agrees very well with the spectral integration using the values of the Batchelor constant estimated from the structure function. We also carry out an exact Lagrangian analysis of the scalar variance and structure function, explicitly relating the Batchelor constant to the Lyapunov exponent for the separation of pairs of fluid particles within the turbulence dissipation subrange. Our results, particularly for the scalar variance, illustrate explicitly the singular nature of the zero diffusivity limit. For finite values of the Schmidt number

and Reynolds number the viscous-convective subrange contribution to the variance can be significant even at moderate values of the Reynolds number.

APPENDIX D

SCALAR DISSIPATION RATE AND DISSIPATIVE ANOMALY IN ISOTROPIC TURBULENCE

D.A. Donzis, K.R. Sreenivasan and P.K. Yeung. *Journal of Fluid Mechanics* **532** (2005), (199-216).

Abstract

We examine available data from experiment and recent numerical simulations to explore the supposition that the scalar dissipation rate in turbulence becomes independent of the fluid viscosity when the viscosity is small and of scalar diffusivity when the diffusivity is small. The data are interpreted in the context of semi-empirical spectral theory of Obukhov and Corrsin when the Schmidt number, Sc, is below unity, and of Batchelor's theory when Sc is above unity. Practical limits in terms of the Taylor-microscale Reynolds number, R_λ, as well as Sc, are deduced for scalar dissipation to become sensibly independent of molecular properties. In particular, we show that such an asymptotic state is reached if $R_\lambda Sc^{1/2}$ for $Sc < 1$, and if $\ln(Sc)/R_\lambda$ for $Sc > 1$.

APPENDIX E

HIGH-REYNOLDS-NUMBER SIMULATION OF TURBULENT MIXING

P.K. Yeung, D.A. Donzis and K.R. Sreenivasan. *Physics of Fluids* **17** (2005), (081703).

Abstract

A brief report is given of a new 2048^3 direct numerical simulation of the mixing of passive scalars with uniform mean gradients in forced, stationary isotropic turbulence. The Taylor-scale Reynolds number is close to 700 and Schmidt numbers of 1 and 1/8 are considered. The data provide the most convincing evidence to date for the inertial-convective scaling. Significant departures from small-scale isotropy are sustained in conventional measures. Subject to some stringent resolution requirements, the data suggest that commonly observed differences between the intermittency of energy and scalar dissipation rates may in part be a finite-Reynolds-number effect.

APPENDIX F

ACCELERATION AND DISSIPATION STATISTICS OF NUMERICALLY SIMULATED ISOTROPIC TURBULENCE

P.K. Yeung, S.B. Pope, A.G. Lamorgese and D.A. Donzis. *Physics of Fluids* **18** (2006), (065103).

Abstract

Direct numerical simulation (DNS) data at grid resolution up to 2048^3 in isotropic turbulence are used to investigate the statistics of acceleration in a Eulerian frame. A major emphasis is on the use of conditional averaging to relate the intermittency of acceleration to fluctuations of dissipation, enstrophy, and pseudodissipation representing local relative motion in the flow. Pseudodissipation (the second invariant of the velocity gradient tensor) has the same intermittency exponent as dissipation and is closest to log-normal. Conditional acceleration variances increase with each conditioning variable, consistent with the scenario of rapid changes in velocity for fluid particles moving in local regions of large velocity gradient, but in a manner departing from Kolmogorov's refined similarity theory. Acceleration conditioned on the pseudodissipation is closest to Gaussian, and well represented by a novel "cubic Gaussian" distribution. Overall the simulation data suggest that, with the aid of appropriate parameterizations, Lagrangian stochastic modeling with pseudodissipation as the conditioning variable is likely to produce superior results. Reduced intermittency of conditional acceleration also makes the present results less sensitive to resolution concerns in DNS.

Bibliography

Abraham, E. R. (1998). The generation of plankton patchiness by turbulent stirring. *Nature*, 391:477–580.

Anselmet, F., Gagne, Y., Hopfinger, E. J., and Antonia, R. A. (1984). High-order velocity structure functions in turbulent shear flows. *J. Fluid Mech.*, 140:63–89.

Antonia, R. A. and Orlandi, P. (2003). Effect of Schmidt number on small-scale passive scalar turbulence. *Appl. Mech. Rev.*, 56:615–632.

Antonia, R. A., Zhou, T., and Xu, G. (2000). Second-order temperature and velocity structure functions: Reynolds number dependence. *Phys. Fluids*, 12:1509–1517.

Ashurst, W. T., Kerstein, A. R., Kerr, R. R., and Gibson, C. C. (1987). Alignment of vorticity and scalar gradient with strain rate in simulated navier-stokes turbulence. *Phys. Fluids*, 30:2343–2353.

Balkovsky, E. and Fouxon, A. (1999). Universal long-time properties of Lagrangian statistics in the Batchelor regime and their application to the passive scalar problem. *Phys. Rev. E.*, 60:4164–4174.

Baroud, C. N., Plapp, B. B., She, Z., and Swinney, H. L. (2002). Anomalous self-similarity in a turbulent rapidly rotating fluid. *Phys. Rev. Lett.*, 88:114501.

Bartello, P. (2002). A comparison of time discretization schemes for two-timescale problems in geophysical fluid dynamics. *J. Comp. Phys.*, 179:268–285.

Bartello, P., Metais, O., and Lesieur, M. (1994). Coherent structures in rotating 3-dimensional turbulence. *J. Fluid Mech.*, 273:1–29.

Batchelor, G. K. (1953). *The Theory of Homogeneous Turbulence*. Cambridge University Press.

Batchelor, G. K. (1959). Small-scale variation of convected quantities like temperature in turbulent fluid. *J. Fluid Mech.*, 5:113–139.

Bershadskii, A., Kit, E., and Tsinober, A. (1993). On universality of geometrical invariants in turbulence—experimental results. *Phys. Fluids*, 5:1523–1525.

Bershadskii, A. and Sreenivasan, K. R. (2002). Multiscaling of cosmic microwave background radiation. *Phys. Lett. A*, 299:149–152.

Bershadskii, A. and Sreenivasan, K. R. (2003). Extended self-similarity of the small-scale cosmic microwave background anisotropy. *Phys. Lett. A*, 319:21–23.

Biferale, L., Boffetta, G., Celani, A., Devenish, B. J., Lanotte, A., and Toschi, F. (2004). Multifractal statistics of lagrangian velocity and acceleration in turbulence. *Phys. Rev. Lett.*, 93:064502.

Biferale, L. and Procaccia, I. (2005). Anisotropy in turbulent flows and in turbulent transport. *Phys. Rep.*, 414:43–164.

Bilger, R. W. (2004). Some aspects of scalar dissipation. *Flow Turb. Combust.*, 72:93–114.

Birouk, M. and Gokalp, I. (2006). Current status of droplet evaporation in turbulent flows. *Prog. Energy Combust. Sci.*, 32:408–423.

Bogucki, D., Domaradzki, J. A., and Yeung, P. K. (1997). Direct numerical simulations of passive scalars with $Pr > 1$ advected by turbulent flow. *J. Fluid Mech.*, 343:111–130.

Borgas, M. S., Sawford, B. L., Xu, S., Donzis, D. A., and Yeung, P. K. (2004). High Schmidt number scalars in turbulence: structure functions and lagrangian theory. *Phys. Fluids*, 16:3888–3899.

Borgas, M. S. and Yeung, P. K. (2004). Relative dispersion in isotropic turbulence. part 2. a new stochastic model with Reynolds-number dependence. *J. Fluid Mech.*, 503:125–160.

Brethouwer, G., Hunt, J. C. R., and Nieuwstadt, F. T. M. (2003). Micro structure and lagrangian statistics of the scalar field with a mean gradient in isotropic turbulence. *J. Fluid Mech.*, 474:193–225.

Cambon, C. and Jacquin, L. (1989). Spectral approach to non-isotropic turbulence subjected to rotation. *J. Fluid Mech.*, 202:295–317.

Cambon, C., Mansour, N. N., and Godeferd, F. S. (1997). Energy transfer in rotating turbulence. *J. Fluid Mech.*, 337:303–332.

Cambon, C., Rubinstein, R., and Godeferd, F. S. (2004). Advances in wave turbulence: rapidly rotating flows. *New J. Phys.*, 6:73.

Chen, S., Dhruva, B., Kurien, S., Sreenivasan, K. R., and Taylor, M. A. (2005). Anomalous scaling of low-order structure functions of turbulent velocity. *J. Fluid Mech.*, 533:183–192.

Chen, S., Sreenivasan, K. R., and Nelkin, M. (1997a). Inertial range scalings of dissipation and enstrophy in isotropic turbulence. *Phys. Rev. Lett.*, 79(7):1253–1256.

Chen, S., Sreenivasan, K. R., Nelkin, M., and Cao, N. (1997b). Refined similarity hypothesis for transverse structure functions in fluid turbulence. *Phys. Rev. Lett.*, 79(12):2253–2256.

Chertkov, M., Falkovich, G., and Kolokolov, I. (1998a). Intermittent dissipation of a passive scalar in turbulence. *Phys. Rev. Lett.*, 80:2121–2124.

Chertkov, M., Kolokolov, I., and Vergassola, M. (1998b). Inverse versus direct cascades in turbulent advection. *Phys. Rev. Lett.*, 80:512–515.

Constantin, P. (1994). Geometric statistics in turbulence. *SIAM Rev.*, 36:73–98.

Corrsin, S. (1951). On the spectrum of isotropic temperature fluctuations in isotropic turbulence. *J. Appl. Phys.*, 22:469–473.

Craya, A. (1958). Contribution à l'analyse de la turbulence associée à des vitesses moyennes. 345, P.S.T. Ministère de l'Air.

Dasi, L. P. (2004). *The small-scale structure of passive scalar mixing in turbulent boundary layers*. PhD thesis, Gerogia Institute of Technology.

Dhruva, B., Tsuji, Y., and Sreenivasan, K. R. (1997). Transverse structure functions in high-Reynolds-number turbulence. *Phys. Rev. E.*, 56(5):R4928–R4930.

Dimotakis, P. E. (2005). Turbulent mixing. *Annu. Rev. Fluid Mech.*, 37:329–356.

Doering, C. R. and Foias, C. (2002). Energy dissipation in body-forced turbulence. *J. Fluid Mech.*, 467:289–306.

Donzis, D. A., Bershadskii, A., Sreenivasan, K. R., and Yeung, P. K. (2005a). Toward high-resolution dns of primordial turbulence. In *Nonlinear Cosmology: Turbulence and Fields*, ICTP, Trieste, Italy.

Donzis, D. A., Sreenivasan, K. R., and Yeung, P. K. (2005b). Scalar dissipation rate and dissipative anomaly in isotropic turbulence. *J. Fluid Mech.*, 532:199–216.

Donzis, D. A., Yeung, P. K., and Sreenivasan, K. R. (2004). Scaling and domain size effects in numerical simulations of rotating turbulence. *Bull. Am. Phys. Soc.*, 49(22):193.

Eckhardt, B., Schneider, T. M., Hof, B., and Westerweel, J. (2007). Turbulence transition in pipe flow. *Annu. Rev. Fluid Mech.*, 39:447–468.

Eswaran, V. and Pope, S. B. (1988). An examination of forcing in direct numerical simulations of turbulence. *Comput. Fluids*, 16:257–278.

Falkovich, G., Gawedzki, K., and Vargassola, M. (2001). Particles and fields in fluid turbulence. *Rev. Mod. Phys.*, 73:913–975.

Fox, R. O. (2003). *Computational Models for Turbulent Reacting Flows*. Cambridge University Press.

Franks, P. (2005). Plankton patchiness, turbulent transport and spatial spectra. *Marine ecology-progress series*, 294:295–309.

Frisch, U. (1995). *Turbulence*. Cambridge University Press.

Gamba, A. and Kolokolov, I. V. (1998). Dissipation statistics of a passive scalar in a multidimensional smooth flow. *J. Stat. Phys.*, 94:759–777.

Garrett, A. E. (1985). Evolution of scalar spectra with the decay of turbulence in a stratified fluid. *J. Fluid Mech.*, 159:379–407.

Garrett, C. (2006). Turbulent dispersion in the ocean. *Prog. Ocean.*, 70:113–125.

Gibson, C. H. (1968). Fine structure of scalar field mixed by turbulence i. zero-gradients points and minimal gradient surfaces. *Phys. Fluids*, 11:2305–2315.

Gibson, C. H., Ashurst, W. T., and Kerstein, A. E. (1988). Mixing of strongly diffusive passive scalars like temperature by turbulence. *J. Fluid Mech.*, 194:261–293.

Gibson, C. H. and Schwarz, W. H. (1963). The universal equilibrium spectra of turbulent velocity and scalar fields. *J. Fluid Mech.*, 16:365–384.

Gotoh, T., Fukayama, D., and Nakano, T. (2002). Velocity field statistics in homogeneous steady turbulence obtained using a high-resolution direct numerical simulation. *Phys. Fluids*, 14:1065–1081.

Greenspan, H. (1968). *The theory of rotating fluids.* Cambridge University Press.

He, G., Chen, S., Kraichnan, R. H., Zhang, R., and Zhou, Y. (1998). Statistics of dissipation and enstrophy induced by localized vortices. *Phys. Rev. Lett.*, 81(21):4636–4639.

Hentschel, H. G. E. and Procaccia, I. (1983). The infinite number of generalized dimensions of fractals and strange attractors. *Physica D*, 8:435–444.

Herring, J. R. (1974). Approach to axisymmertric turbulence to isotropy. *Phys. Fluids*, 17:859–872.

Holzer, M. and Siggia, E. (1994). Turbulent mixing of a passive scalar. *Phys. Fluids*, 6:1820–1837.

Hosokawa, I. (1991). Turbulence models and probability distributions of dissipation and relevant quantities in isotropic turbulence. *Phys. Rev. Lett.*, 66(8):1054–1057.

Hoyas, S. and Jiménez, J. (2006). Scaling of the velocity fluctuations in turbulent channels up to $\mathrm{Re}_\tau = 2003$. *Phys. Fluids*, 18:011702.

Jackson, D. and Launder, B. E. (2007). Osborne Reynolds and the publication of his papers on turbulent flow. *Annu. Rev. Fluid Mech.*, 39:19–35.

Jacquin, L., Leuchter, O., Cambon, C., and Mathieu, J. (1990). Homogeneous turbulence in the presence of rotation. *J. Fluid Mech.*, 220:1–52.

Jiménez, J. (2003). Computing high-Reynolds-number turbulence: will simulations ever replace experiments? *J. of Turb.*, 4:022.

Jiménez, J. (2004). Turbulent flows over rough walls. *Annu. Rev. Fluid Mech.*, 36:173–196.

Kaneda, Y., Ishihara, T., Yokokawa, M., Itakura, K., and Uno, A. (2003). Energy dissipation rate and energy spectrum in high resolution direct numerical simulations of turbulence in a periodic box. *Phys. Fluids*, 15:L21–L24.

Kassinos, S. C. and Reynolds, W. C. (1994). A structure-based model for the rapid ditortion of homogeneous turbulence. Tech. Rep. TF-61, Stanford University.

Kerr, R. M. (1985). Higher-order derivative correlations and the alignment of small-scale structures in isotropic numerical turbulence. *J. Fluid Mech.*, 153:31–58.

Kolmogorov, A. N. (1962). A refinement of previous hypothesis concerning the local structure of turbulence in viscous incompressible fluid at high Reynolds number. *J. Fluid Mech.*, 13:82–85.

Kolmogorov, A. N. (1941a). Local structure of turbulence in an incompressible fluid for very large Reynolds numbers. *Dokl. Akad. Nauk. SSSR*, 30:299–303.

Kolmogorov, A. N. (1941b). Dissipation of energy in the locally isotropic turbulence. *Dokl. Akad. Nauk. SSSR*, 32:16–18.

Kraichnan, R. H. (1968). Small-scale structure of a scalar field convected by turbulence. *Phys. Fluids*, 11:945–953.

Li, Y. and Meneveau, C. (2005). Origin of non-gaussian statistics in hydrodynamic turbulence. *Phys. Rev. E.*, 95:164502.

Lumley, J. and Yaglom, A. (2001). A century of turbulence. *Flow Turb. Combust.*, 66:241–286.

L'vov, V. and Procaccia, I. (1996). The universal scaling exponents of anisotropy in turbulence and their measurements. *Phys. Fluids*, 8:2565–2567.

Mahalov, A. and Zhou, Y. (1996). Analytical and phenomenological studies of rotating turbulence. *Phys. Fluids*, 8:2138–2152.

Mansour, N. N., Cambon, C., and Speziale, C. G. (1991a). Single-point modeling of initially isotropic turbulence under uniform rotation. Annual Research Briefs, Center for Turbulence Research, Stanford University.

Mansour, N. N., Shih, T.-H., and Reynolds, W. C. (1991b). The effects of rotation on initially anisotropic homogeneous flows. *Phys. Fluids*, 3:2421–2425.

Meneveau, C. and Sreenivasan, K. R. (1987). Simple multifractal cascade model for fully developed turbulence. *Phys. Rev. Lett.*, 59(13):1424–1427.

Meneveau, C. and Sreenivasan, K. R. (1991). The multifractal nature of turbulent energy dissipation. *J. Fluid Mech.*, 224:429–484.

Miller, P. L. and Dimotakis, P. E. (1996). Measurements of scalar power spectra in high Schmidt number turbulent jets. *J. Fluid Mech.*, 308:129–146.

Mills, R., Kistler, A., O'Brien, V., and Corrsin, S. (1958). Turbulence and temperature fluctuations behind a heated grid. TN 4288, NACA.

Moin, P. and Kim, J. (1997). Tackling turbulence with supercomputers. *Scientific American*, 276:62–68.

Moin, P. and Mahesh, K. (1998). Direct numerical simulation: A tool in turbulence research. *Annu. Rev. Fluid Mech.*, 30:539–578.

Moisy, F. and Jiménez, J. (2004). Geometry and clustering of intense structures in isotropic turbulence. *J. Fluid Mech.*, 512:111–133.

Monin, A. and Yaglom, A. (1975). *Statistical Fluid Mechanics*, volume 2. MIT Press.

Morinishi, Y., Nakabayashi, K., and Ren, S. (2001). Dynamics of anisotropy on decaying homogeneous turbulence subjected to system rotation. *Phys. Fluids*, 13:2912–2922.

Morize, C., Moisy, F., and Rabaud, M. (2005). Decaying grid-generated turbulence in a rotating tank. *Phys. Fluids*, 17:095105.

Mydlarski, L. and Warhaft, Z. (1998). Passive scalar statistics in high-peclet number grid turbulence. *J. Fluid Mech.*, 358:135–175.

Nelkin, M. (1992). In what sense is turbulence an unsolved problem. *Science*, 255:566–570.

Nelkin, M. (1994). Universality and scaling in fully developed turbulence. *Adv. Phys.*, 43:143–181.

Nelkin, M. (1999). Enstrophy and dissipation must have the same scaling exponents in the high Reynolds number limit of fluid turbulence. *Phys. Fluids*, 11:2202–2204.

Nimela, J. J. and Sreenivasan, K. R. (2006). The use of cryogenic helium for classical turbulence: Promises and hurdles. *J. Low Temp. Phys.*, 143:163–212.

Obukhov, A. M. (1949). The structure of the temperature field in a turbulent flow. *Izv. Akad. Nauk. SSRR, Ser. Geophys.*, 13:77–81.

Obukhov, A. M. (1962). Some specific features of atmospheric turbulence. *J. Fluid Mech.*, 13:58–69.

Orszag, S. A. (1969). Numerical methods for the simulation of turbulence. *Phys. Fluids*, 12:250–257.

Orszag, S. A. (1971). Numerical simulations of incompressible flows within simple boundaries: accuracy. *J. Fluid Mech.*, 49:75–112.

Orszag, S. A. and Patterson, G. S. (1972). Numerical simulation of three-dimensional homogeneous isotropic turbulence. *Phys. Rev. Lett.*, 28(2):76–79.

Overholt, M. R. and Pope, S. B. (1996). Direct numerical simulation of a passive scalar with imposed mean gradient in isotropic turbulence. *Phys. Fluids*, 8:3128–3148.

Overholt, M. R. and Pope, S. B. (1998). A deterministic forcing scheme for direct numerical simulations of turbulence. *Computers & Fluids*, 27:11–28.

Pekurovsky, D., Yeung, P. K., Donzis, D. A., Kumar, S., Pfeiffer, W. A., and Chukkapalli, G. (2006). DNS turbulence code with 2D domain decomposition on Power4+/Federation and Blue Gene systems. In *SP SciComp, Boulder CO*.

Peters, N. (2000). *Turbulent combustion*. Cambridge University Press.

Peyret, R. and Taylor, T. D. (1983). *Computational Methods for Fluid Flow*. Springer, New York.

Pope, S. B. (2000). *Turbulent Flows*. Cambridge University Press.

Prasad, R. R., Meneveau, C., and Sreenivasan, K. R. (1988). Multifractal nature of the dissipation field of passive scalars in fully turbulent flows. *Phys. Rev. Lett.*, 61(1):74–77.

Prasad, R. R. and Sreenivasan, K. R. (1990). Quantitative 3-dimensional imaging and the structure of passive scalar fields in fully turbulent flows. *J. Fluid Mech.*, 256:1–34.

Pullin, D. I. and Saffman, P. G. (1998). Vortex dynamics in turbulence. *Annu. Rev. Fluid Mech.*, 30:31–51.

Pumir, A. (1994). A numerical study of the mixing of a passive scalar in three dimensions in the presence of a mean gradient. *Phys. Fluids*, 6:2118–2132.

Qian, J. (1995). Viscous range of turbulent scalar of large Prandtl number. *Fluid. Dyn.Res.*, 15:103–112.

Rogallo, R. S. (1981). Numerical experiments in homogeneous turbulence. NASA TM 81315, NASA Ames Research Center, Moffett Field, CA.

Rogallo, R. S. and Moin, P. (1984). Numerical-simulation of turbulent flows. *Annu. Rev. Fluid Mech.*, 16:99–137.

Rosales, C. and Meneveau, C. (2006). A minimal multiscale Lagrangian map approach to synthesize non-Gaussian turbulent vector fields. *Phys. Fluids*, 18:075104.

Ruetsch, G. R. and Maxey, M. R. (1991). Small-scale features of vorticity and passive scalar fields in homogeneous turbulence. *Phys. Fluids*, 3:1587–1597.

Sanford, L. P. (1997). Turbulent mixing in experimental ecosystem studies. *Mar. Ecol. Prog. Ser.*, 161:265–293.

Schumacher, J., Sreenivasan, K. R., and Yeung, P. K. (2003). Schmidt number dependence of derivative moments for quasi-static straining motion. *J. Fluid Mech.*, 479:221–230.

Shtilman, L., Spector, M., and Tsinober, A. (1993). On some kinematic versus dynamic properties of homogeneous turbulence. *J. Fluid Mech.*, 247:65–77.

Siggia, E. (1981). Numerical study of small-scale intermittency in 3-dimensional turbulence. *J. Fluid Mech.*, 107:375–406.

Simand, C., Chilla, F., and Pinton, J. F. (2000). Inhomogeneous turbulence in the vicinity of a large-scale coherent vortex. *Europhys. Lett.*, 49:336–342.

Sirivat, A. and Warhaft, Z. (1983). The effect of a passive cross-stream temperature gradient on the evolution of temperature variance and heat flux in grid turbulence. *J. Fluid Mech.*, 128:323–346.

Sreenivasan, K. R. (1984). On the scaling of the turbulence energy-dissipation rate. *Phys. Fluids*, 27:1048–1051.

Sreenivasan, K. R. (1991). On local isotropy of passive scalars in turbulent shear flows. *Proc. Roy. Soc. Lond.*, 434:165–182.

Sreenivasan, K. R. (1995). The energy dissipation rate in turbulent shear flows. In Deshpande, S., Prabhu, A., Sreenivasan, K., and Viswanath, P., editors, *Developments in Fluid Mechanics and Aerospace Sciences*, pages 159–190. Interline Publishers.

Sreenivasan, K. R. (1996). The passive scalar spectrum and the obukhov-corrsin constant. *Phys. Fluids*, 8:189–196.

Sreenivasan, K. R. (1998). An update on the energy dissipation rate in isotropic turbulence. *Phys. Fluids*, 10:528–529.

Sreenivasan, K. R. (1999). Fluid turbulence. *Rev. Mod. Phys.*, 71:s383–s395.

Sreenivasan, K. R. (2004). Possible effects of small-scale intermittency in turbulent reacting flows. *Flow Turb. Combust.*, 72:115–131.

Sreenivasan, K. R. and Antonia, R. A. (1997). The phenomenology of small-scale turbulence. *Annu. Rev. Fluid Mech.*, 29:435–472.

Sreenivasan, K. R., Juneja, A., and Suri, A. (1995). Scaling properties of circulation in moderate-Reynolds-number turbulent wakes. *Phys. Rev. Lett.*, 75:433.

Sreenivasan, K. R. and Prasad, R. R. (1989). New results on the fractal and multifractal structure of the large Schmidt number passive scalars in fully turbulent flows. *Physica D*, 38:322–329.

Sreenivasan, K. R., Tavoularis, S., Henry, R., and Corrsin, S. (1980). Temperature fluctuations and scales in grid-generated turbulence. *J. Fluid Mech.*, 100:597–621.

Sreenivasan, K. R. and Yeung, P. K. (2000). Dissipation anomaly in passive scalars. *Bull. Amer. Phys. Soc.*, 45(9):107.

Stolovitzky, G. and Sreenivasan, K. R. (1993). Scaling of structure functions. *Phys. Rev. E*, 48(1):R33–R36.

Tavoularis, S. and Corrsin, S. (1981). Experiments in nearly homogeneous shear flow with a uniform mean temperature gradient. part 1. *J. Fluid Mech.*, 104:311–347.

Taylor, G. I. (1938). Production and dissipation of vorticity in a turbulent fluid. *Proc. Roy. Soc. Lond.*, 918:15–23.

Tennekes, H. and Lumley, J. L. (1972). *A First Course in Turbulence*. MIT Press.

Tsinober, A. (1998). Is concentrated vorticity that important? *Euro. J. Mech. B.*, 17:421–449.

Tsinober, A., Kit, E., and Dracos, T. (1992). Experimental investigation of the field of velocity gradients in turbulent flows. *J. Fluid Mech.*, 242:169–192.

Vedula, P. and Yeung, P. K. (1999). Similarity scaling of acceleration and pressure statistics in numerical simulations of isotropic turbulence. *Phys. Fluids*, 11:1208–1220.

Veynante, D. and Vervisch, L. (2002). Turbulent combustion modeling. *Prog. Energy Combust. Sci.*, 28:193–266.

Villermaux, E., Innocenti, C., and Duplat, J. (2001). Short circuits in the corrsin-obukhov cascade. *Phys. Fluids*, 13:284–289.

Vinen, W. F. and Niemela, J. J. (2002). Quantum turbulence. *J. Low Temp. Phys.*, 128:167–231.

Wang, L. P., Chen, S., and Brasseur, J. G. (1999). Examination of hypotheses in the kolmogorov refined turbulence theory through high-resolution simulations. part 2. passive scalar field. *J. Fluid Mech.*, 400:163–197.

Wang, L. P., Chen, S., Brasseur, J. G., and Wyngaard, J. C. (1996). Examination of hypotheses in the kolmogorov refined turbulence theory through high-resolution simulations. part 1. velocity field. *J. Fluid Mech.*, 309:113–156.

Warhaft, Z. (2000). Passive scalars in turbulent flows. *Annu. Rev. Fluid Mech.*, 32:203–240.

Warhaft, Z. and Lumley, J. L. (1978). An experimental study of the decay of temperature fluctuations in grid-generated turbulence. *J. Fluid Mech.*, 88:659–684.

Watanabe, T. and Gotoh, T. (2004). Statistics of passive scalar in homogeneous turbulence. *New J. Phys.*, 6:40.

Williams, B. S., Marteau, D., and Gollub, J. P. (1997). Mixing of a passive scalar in magnetically forced two-dimensional turbulenc. *Phys. Fluids*, 9:2061–2080.

Xu, G., Antonia, R. A., and Rajagopalan, S. (2000). Scaling of mean temperature dissipation rate. *Phys. Fluids*, 12:3090–3093.

Yakhot, V. and Sreenivasan, K. R. (2005). Anomalous scaling of structure functions and dynamic constraints on turbulence simulations. *J. Stat. Physics*, 121:823.

Yang, X. and Domaradzki, J. A. (2004). Large eddy simulations of decaying rotating turbulence. *Phys. Fluids*, 16:4088–4104.

Yeh, T. T. and Van Atta, C. W. (1973). Spectral transfer of scalar and velocity fields in heated-grid turbulence. *J. Fluid Mech.*, 58:233–261.

Yeung, P. K., Donzis, D. A., and Sreenivasan, K. R. (2005). High-Reynolds-number simulation of turbulent mixing. *Phys. Fluids*, 17:081703.

Yeung, P. K. and Pope, S. B. (1989). Lagrangian statistics from direct numerical simulations of isotropic turbulence. *J. Fluid Mech.*, 207:531–586.

Yeung, P. K., Pope, S. B., Kurth, E. A., and Lamorgese, A. G. (2007). Lagrangian conditional statistics, acceleration and local relative motion in numerically simulated isotropic turbulence. *J. Fluid Mech.*, 582:399–422.

Yeung, P. K., Pope, S. B., Lamorgese, A. G., and Donzis, D. A. (2006). Acceleration and dissipation statistics of numerically simulated isotropic turbulence. *Phys. Fluids*, 18:065103.

Yeung, P. K. and Sawford, B. L. (2002). Random sweeping hypothesis for passive scalars in isotropic turbulence. *J. Fluid Mech.*, 459:129–138.

Yeung, P. K. and Xu, J. (2004). Effects of rotation on turbulent mixing: non-premixed passive scalars. *Phys. Fluids*, 16:93–103.

Yeung, P. K., Xu, J., and Sreenivasan, K. R. (2003). Scaling properties of rotating homogeneous turbulence. In *Symposium on Modeling and Simulation of Turbulent Flows*, Honolulu, HI. ASME Fluid Engineering Division Summer Meeting.

Yeung, P. K., Xu, S., Donzis, D. A., and Sreenivasan, K. R. (2004). Simulations of three-dimensional turbulent mixing for Schmidt numbers of the order 1000. *Flow Turb. Combust.*, 72:333–347.

Yeung, P. K., Xu, S., and Sreenivasan, K. R. (2002). Schmidt number effects on turbulent transport with uniform mean scalar gradient. *Phys. Fluids*, 14:4178–4191.

Yeung, P. K. and Zhou, Y. (1997). Universality of the kolmogorov constant in numerical simulations of turbulence. *Phys. Rev. E*, 56(2):1746–1752.

Yeung, P. K. and Zhou, Y. (1998). Numerical study of rotating turbulence with external forcing. *Phys. Fluids*, 10:2895–2909.

Zeff, B. W., Lanterman, D. D., McAllister, R., Roy, R., Kostelich, E. J., and Lathrop, P. (2003). Measuring intense rotation and dissipation in turbulent flows. *Nature*, 421:146–149.

Zeman, O. (1994). A note on the spectra and decay of rotating homogeneous turbulence. *Phys. Fluids*, 6:3221–3223.

Zhou, T. and Antonia, R. A. (2000). Reynolds number dependence of the small-scale structure if grid turbulence. *J. Fluid Mech.*, 406:81–107.

Zhou, T., Antonia, R. A., and Chua, L. P. (2005a). Flow and Reynolds number dependencies of one-dimensional vorticity fluctuations. *J. Turb.*, 6:28.

Zhou, T., Hao, Z., Chua, L. P., and Yu, S. C. M. (2005b). Scaling of longitudinal and transverse velocity increments in a cylinder wake. *Phys. Rev. E.*, 71:066307.

Zhou, Y. (1995). A phenomenological treatment of rotating turbulence. *Phys. Fluids*, 7:2092–2094.

Zhou, Y., Matthaeus, W., and Dmitruk, P. (2004). Magnetohydrodynamic turbulence and time scales in astrophysical and space plasmas. *Rev. Mod. Phys.*, 76:1015–1035.

Zocchi, G., Tabeling, P., Maurer, J., and Willaime, H. (1994). Measurement of the scaling of the dissipation at high Reynolds numbers. *Phys. Rev. E.*, 50:3693–3700.